

Technische Universität München  
Fakultät für Physik



Max-Planck-Institut für Biochemie  
Abteilung für Molekulare Strukturbiologie



# IN SITU ARCHITECTURE AND CELLULAR INTERACTIONS OF POLYQ INCLUSIONS

**Felix Jan Benedict Bäuerlein**

Vollständiger Abdruck der von der Fakultät für Physik  
der Technischen Universität München  
zur Erlangung des akademischen Grades eines  
Doktors der Naturwissenschaften (Dr. rer. nat.)  
genehmigten Dissertation.

Vorsitzender:

Prof. Dr. Martin Zacharias

Prüfer der Dissertation:

1. Hon.-Prof. Dr. Wolfgang Baumeister
2. Prof. Dr. Andreas Bausch
3. Prof. Dr. Johannes Buchner

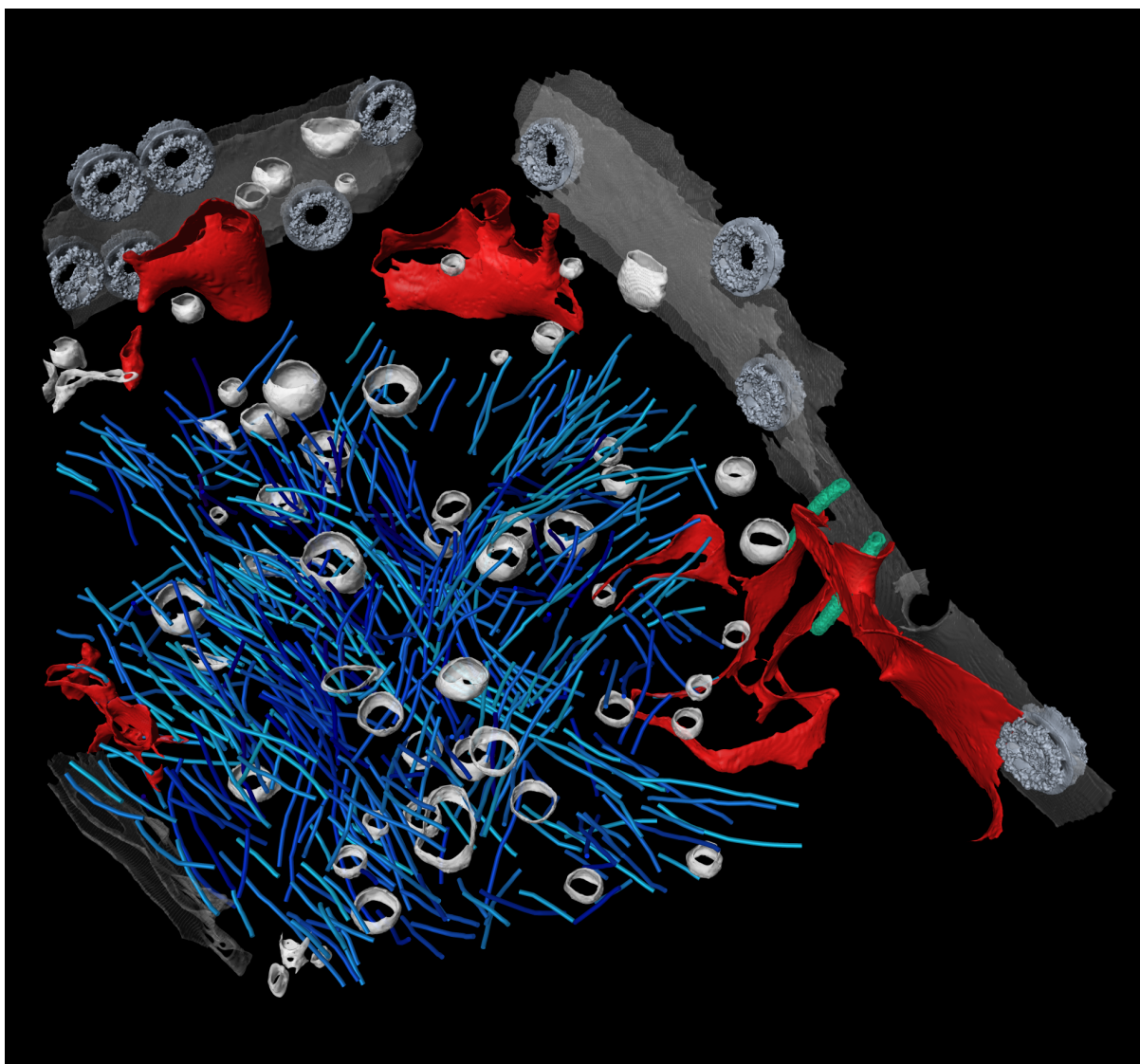
Die Dissertation wurde am 06.02.2018 an der Technischen Universität München eingereicht und durch die Fakultät für Physik am 09.07.2018 angenommen.





To my parents Cornelia and Edmund  
and my dear grandmother Mumum





### Preview

Inclusions of misfolded proteins are found in the brain of patients of many neurodegenerative diseases, but the contribution of these aggregates to cytotoxicity remains poorly understood. In this PhD thesis, cryo-electron tomography is employed to analyze at unprecedented resolution the architecture of neuronal polyQ inclusions within their cellular environment. Cytoplasmic polyQ inclusions contain fibrils that strongly interact with cellular endomembranes, particularly those of the ER. These interactions alter ER organization and dynamics, and may even lead to ER membrane rupture. This preview image shows how the polyQ fibrils (cyan) of an inclusion body at the vicinity of the nucleus (grey) interact with the ER membranes (red). Vesicles (white) are abundant both within the inclusion and at its periphery.



# CONTENT

<b>Abstract.....</b>	<b>x</b>
<b>Video Abstract.....</b>	<b>x</b>
<b>Publications of Felix J.B. Bäuerlein .....</b>	<b>xii</b>
<b>1. Introduction.....</b>	<b>2</b>
<b>1.1 Neurodegeneration.....</b>	<b>2</b>
<b>1.2 Protein Aggregation .....</b>	<b>3</b>
A Glance at Protein Aggregation and Proteostasis.....	3
Protein Aggregation in Neurodegeneration.....	4
<b>1.3 Huntington’s Disease (HD) .....</b>	<b>6</b>
Epidemiology.....	6
Signs and Symptoms.....	6
Neuropathology of HD.....	7
Non-Neurological Features of HD.....	7
Pharmacological Therapy.....	8
HD Genetics.....	9
<b>1.4 Aggregation in HD .....</b>	<b>10</b>
Huntingtin (Htt) as a model example of Aggregation in Neurodegeneration .....	10
Experimental Systems for HD Investigation.....	11
State-of-the-Art: Ultrastructural Imaging of Inclusion Bodies in HD .....	12
<b>1.5 Other Neurodegenerative Diseases.....</b>	<b>15</b>
Other polyQ-Diseases .....	15
Alzheimer’s Disease (AD) .....	15
Parkinson’s Disease (PD).....	16
Amyotrophic Lateral Sclerosis (ALS) .....	17
<b>2. Cryo-Electron Microscopy Techniques .....</b>	<b>18</b>
<b>2.1 Electron Microscopy of Biological Samples .....</b>	<b>18</b>
<b>2.2 The Transmission Electron Microscope (TEM).....</b>	<b>20</b>
<b>2.3 Cryo-Electron Microscopy .....</b>	<b>23</b>
Aqueous Nature of Biological Samples.....	23
The Idea of Cryo-Electron Microscopy.....	23
Vitrification of Biological Samples .....	23
Plunge Freezing .....	24
High-Pressure Freezing.....	25
Challenges of Cryo-EM.....	26
Electron-Sample Interactions and the Contrast Transfer Function .....	28
<b>2.4 Cryo Electron Tomography (CET).....</b>	<b>32</b>
Tilt Series and Frame Alignment.....	32
Tomogram Reconstruction .....	34
<b>2.5 Cryo-Focused Ion Beam Technology (Cryo-FIB) .....</b>	<b>36</b>
Thickness-Limitation in TEM .....	36
The Cryo-FIB Instrument.....	36
The Cryo-FIB Method.....	38
<b>2.6 Correlative Microscopy .....</b>	<b>40</b>
<b>2.7 How to improve SNR .....</b>	<b>43</b>
The Volta Phase Plate (VPP).....	43



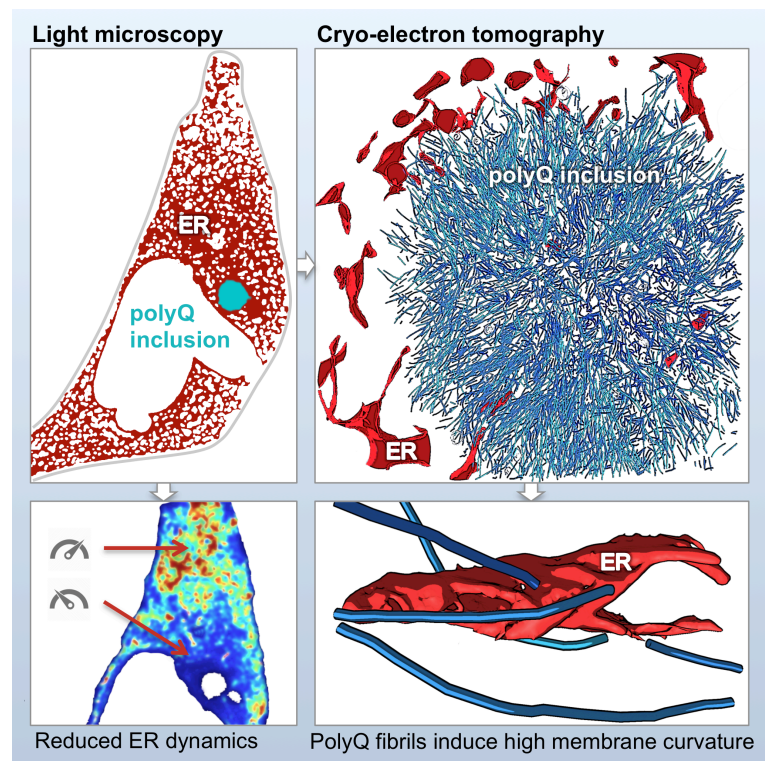
The Direct Detection Device (DDD) .....	45
<b>2.8 Segmentation of Cellular Components.....</b>	<b>47</b>
Membrane Segmentation.....	47
Filament Tracing.....	48
Protein Localization (Template Matching).....	49
<b>3. Results .....</b>	<b>52</b>
<b>3.1 Improvements of the Cryo-ET Method.....</b>	<b>52</b>
3.1.1 Vitrification.....	52
Problem: Imperfect Vitrification in HeLa .....	53
Solution: Control of Vitrification by short time exposure to Glycerol .....	53
3.1.2 Finding the Inclusion Body .....	55
Targeting of GFP-labeled IBs.....	55
Targeting of mCherry-Ubiquitin marked IBs.....	55
Secondary High-Precision Depth Targeting of IBs in the FIB/SEM (Z-Targeting).....	55
3.1.3 Platinum-Coating & Induced Artifact-Cleaning.....	57
Problem: Cryo FIB-Lamellas interfere with VPP imaging .....	57
Solution: Conductive Lamella-coating .....	58
Artifact Cleaning Procedure.....	58
3.1.4 New Generation Cryo-ET Workflow.....	60
3.1.5 Neuro-2a .....	63
<b>3.2 IB Architecture .....</b>	<b>64</b>
3.2.1 IB structure on the meso scale .....	64
Location and shape .....	64
Aggregated species .....	65
3.2.2 Filament characterization.....	66
Htt97Q-GFP in neurons and HeLa .....	66
Htt97Q in HeLa.....	67
Htt64Q-GFP in HeLa .....	67
3.2.3 Volume occupation of IBs.....	68
3.2.4 Persistence Length of IB Filaments .....	68
<b>3.3 Cellular Interactions of IBs .....</b>	<b>69</b>
3.3.1 Structural Association of IBs with Endomembranes.....	70
Interaction of IBs with the Endoplasmic Reticulum .....	70
Interaction of IBs with other organelles.....	72
PolyQ repeat length has no strong influence on membrane interactions.....	73
3.3.2 Filament-Membrane Interactions.....	74
3.3.3 Dependence of ER-Deformation on Filaments.....	75
3.3.4 ER-Dynamics at IBs Periphery.....	79
3.3.5 Relocalization of ERAD components and other ER Proteins.....	81
ER chaperones (Calnexin, Calreticulin, BiP, PDI) .....	81
ERAD (ERLIN-2, Sel1L, p97, OS9) .....	81
Other ER proteins (Sec61, SERCA).....	81
3.3.6 Depletion of membrane bound Ribosomes at IB-ER interface.....	82
<b>3.4 Huntingtin Aggregation in Primary Hippocampal Neurons .....</b>	<b>84</b>
3.4.1 Cellular Interactions of IBs in Neurons.....	84
3.4.2 Nuclear IBs.....	86
<b>4. Discussion .....</b>	<b>88</b>
<b>4.1 PolyQ Expanded Huntingtin Exon 1 Forms Fibrillary IB's.....</b>	<b>88</b>
How is the molecular arrangement in IB's? Are IB's structured or amorphous? .....	88
What is the impact of the polyQ repeat length on IB formation and fibril properties? .....	89
What can be derived from the architecture of IBs ? .....	90
<b>4.2 Cellular Interactions of IBs .....</b>	<b>91</b>

Do IBs interact with their cellular environment and which cellular structures are affected?.....	91
What are the consequences of the IB-membrane interaction? .....	93
How do nuclear and cytosolic IBs differ in their cellular interaction? .....	95
Can proteins be trapped inside IB's? .....	95
<b>4.4 Improvements of the New-Generation Cryo-EM Methods.....</b>	<b>97</b>
How apt is vitrification by plunge freezing and how far could it be improved?.....	97
How far is VPP imaging compatible with FIB-Lamellas? .....	98
<b>5. Methods .....</b>	<b>100</b>
<b>5.1 Experimental Model.....</b>	<b>101</b>
HeLa Cell Culture (performed by Itika Saha) .....	101
Hippocampal Neuron Culture and Transfection (performed by Archana Mishra) .....	101
<b>5.2 Method Details .....</b>	<b>101</b>
Plasmids and Antibodies (applied by Itika Saha) .....	101
Immunofluorescence.....	102
Correlative Light Microscopy and Live Cell Imaging .....	102
Cell Vitrification.....	103
Cryo-Focused Ion Beam Milling.....	103
Cryo-Electron Tomography .....	104
Tomogram Reconstruction and Analysis.....	104
<b>5.3 Quantification and Statistical Analysis .....</b>	<b>105</b>
Persistence Length Analysis .....	105
Ribosome Template Matching and Calculation of ER-bound Ribosome Density (performed by Maria Kalemanov with support of Antonio Martínez-Sánchez) .....	105
Determination of ER Membrane Curvature (with Maria Kalemanov) .....	106
Statistical Analysis .....	107
<b>5.4 Data and Software Availability.....</b>	<b>107</b>
<b>5.5 Key Resources Table.....</b>	<b>107</b>
<b>6. Appendix .....</b>	<b>110</b>
<b>6.1 Aggregate Detection Algorithm (AGDA) .....</b>	<b>110</b>
<b>6.2 Ring Shape Detection Algorithm (RSDA) .....</b>	<b>110</b>
<b>6.3 Persistence Length Calculation of Fibrils .....</b>	<b>111</b>
Persistence Length Calculation.....	111
Amira Lineset Conversion .....	111
<b>6.4 Measurement of local ER Dynamics/Mobility .....</b>	<b>111</b>
ER Mobility Analysis Package .....	111
Individual Traces.....	112
<b>Acronyms .....</b>	<b>114</b>
<b>Bibliography.....</b>	<b>116</b>
<b>Curriculum Vitae .....</b>	<b>134</b>
<b>Acknowledgements .....</b>	<b>136</b>



## ABSTRACT

Expression of many disease-related aggregation-prone proteins results in cytotoxicity and the formation of large intracellular inclusion bodies. To gain insight into the role of inclusions in pathology and the in situ structure of protein aggregates inside cells, we employ advanced cryo-electron tomography methods to analyze the structure of inclusions formed by polyglutamine (polyQ)-expanded huntingtin exon 1 within their intact cellular context. In primary mouse neurons and immortalized human cells, polyQ inclusions consist of amyloid-like fibrils that interact with cellular endomembranes, particularly of the endoplasmic reticulum (ER). Interactions with these fibrils lead to membrane deformation, the local impairment of ER organization, and profound alterations in ER membrane dynamics at the inclusion periphery. These results suggest that aberrant interactions between fibrils and endomembranes contribute to the deleterious cellular effects of protein aggregation.



### Graphical abstract

(Reprinted from Bäuerlein et al. 2017, with permission from Elsevier.)

## VIDEO ABSTRACT

A video abstract, demonstrating cryo-FIB technology and cryo-electron tomography applied on cells with Huntingtin Exon 1 aggregates and the main results of this study is accessible here:  
CELL Video Abstracts Youtube Channel : [https://youtu.be/r\\_mVjaM\\_cyw](https://youtu.be/r_mVjaM_cyw)



# PUBLICATIONS OF FELIX J.B. BÄUERLEIN

Title: **In Situ Architecture and Cellular Interactions of PolyQ Inclusions.**  
 Authors: **Felix J.B. Bäuerlein**, Itika Saha, Archana Mishra, Maria Kalemánov, Antonio Martínez-Sánchez, Rüdiger Klein, Irina Dudanova, Mark S. Hipp, F. Ulrich Hartl, Wolfgang Baumeister and Rubén Fernández-Busnadiego.  
 Journal: **Cell**  
 Issue/Pages: 171 (1): 179-187.e10  
 DOI: 10.1016/j.cell.2017.08.009  
 Date: 2017, September 21

*Highlighted by Leading Edge Preview Article in the same Issue:*  
 Pedro Guedes-Dias and Erika L. F. Holzbaaur. (September 21, 2017)  
**Huntingtin Fibrils Poke Membranes.**  
**Cell** 171 (1): 32–33. doi: 10.1016/j.cell.2017.09.009.

Title: **Removing Contamination-Induced Reconstruction Artifacts from Cryo-Electron Tomograms.**  
 Authors: Jose-Jesus Fernandez, Ulrike Laugks, Miroslava Schaffer, **Felix J.B. Bäuerlein**, Maryam Khoshouei, Wolfgang Baumeister and Vladan Lucic.  
 Journal: **Biophysical Journal**  
 Issue/Pages: 110 (4): 850–59  
 DOI: 10.1016/j.bpj.2015.10.043  
 Date: 2016, February 23

Title: **Structural Basis of Vesicle Formation at the Inner Nuclear Membrane.**  
 Authors: Hagen C., Dent K.C., Zeev-Ben-Mordehai T., Grange M., Bosse J.B., Whittle C., Klupp B.G., Siebert C.A., Vasishtan D., **Bäuerlein F.J.B.**, Cheleski J., Werner S., Guttmann P., Rehbein S., Henzler K., Demmerle J., Adler B., Koszinowski U., Schermelleh L., Schneider G., Enquist L.W., Plitzko J.M., Mettenleiter T.C., Grünewald K.  
 Journal: **Cell**  
 Issue/Pages: 163 (7): 1692–1701  
 DOI: 10.1016/j.cell.2015.11.029  
 Date: 2015, December 17

Title: **Focused Ion Beam Micromachining of Eukaryotic Cells for Cryoelectron Tomography.**  
 Authors: Alexander Rigort\* & **Felix J.B. Bäuerlein\***, Elizabeth Villa, Matthias Eibauer, Tim Laugks, Wolfgang Baumeister and Jürgen M. Plitzko.  
 Journal: **PNAS**  
 Issue/Pages: 109 (12): 4449–54  
 DOI: 10.1073/pnas.1201333109  
 Date: 2012, March 20

\* these authors contributed equally



# 1

## INTRODUCTION

### 1.1 NEURODEGENERATION

Neurodegeneration is characterized by a progressive loss of structure of neuronal tissue on the microscopic as well as on the macroscopic level, accompanied by a loss of function of neurons and connectivity of neuronal circuits. These neurodegenerative processes lead to diverse typical syndromes like dementia, movement disorders (dystonia) and behavioral abnormalities as an expression of the so far incurable and lethal neurological diseases: Alzheimer's (AD), Parkinson's (PD), Huntington's (HD), amyotrophic lateral sclerosis (ALS) and other rare forms. The etiology of these diseases is predominantly sporadic and not understood, while a small fraction of the patients has a genetically based variant. An exception is the inherited Huntington's disease, which is explicitly determined by a mutation in the Huntingtin gene.

A common histopathological hallmark of many neurodegenerative diseases is the presence of pathognomonic protein aggregates. Commonly, one or two disease-specific proteins are observed to aggregate intra- or extracellularly. In the early stages of neurodegeneration these pathological alterations are found in disease-specific confined regions of the post-mortem brain. In vivo, functional decline of these regions can be measured by neuroimaging for neuronal activity with functional magnetic-resonance imaging (fMRI) as well as positron-emission tomography (PET) and for axonal integrity and connectivity with diffusion-tensor imaging (DTI). In the course of these diseases, protein aggregation seems to spread across the cortex along anatomical connections made by neurons and appears in large parts of the brain (Aguzzi and Rajendran, 2009; Brettschneider et al., 2015; Polymenidou and Cleveland, 2012). In an advanced stage, the degeneration of neuronal tissue becomes



macroscopically apparent by a loss of grey matter of the disease-specific regions deep inside the brain, but also by a gross atrophy of the cortex and a consecutive enlargement of the cerebrospinal fluid spaces.

Despite the genetic or sporadic etiology of these diseases and massive research efforts, conclusive insights into the disease mechanisms fail to appear so far. Although an enormous amount of 162.756 publications<sup>1</sup> to date (AD: 79.765, PD: 56.381, HD: 10.758, ALS: 15.852) investigated these diseases, none could offer a solution to the problem of neurodegeneration.

The lack of mechanistic insights is the reason, why FDA- and EMA-approved therapeutic options are restricted to symptomatic therapy-regimens. So far, no available substance has been able to change neither the survival nor the progression of the mentioned neurodegenerative diseases, only the progression of symptoms can be palliated.

## 1.2 PROTEIN AGGREGATION

### A GLANCE AT PROTEIN AGGREGATION AND PROTEOSTASIS

Proteins are involved in almost every cellular function. While in bacteria 4.000-5.000 proteins are found, mammalian cells express 10.000-20.000 different proteins. These are synthesized as a linear chain of amino acids by ribosomes. The proper functionality of most synthesized proteins depends on one defined three-dimensional folding (native state). **Figure 1.1A** shows schematically the Gibbs free-energy landscape for native protein folding (green) and also aberrant intermolecular interactions (red) that lead to protein aggregation (Balchin et al., 2016). The thermodynamically favorable native folding state is often reached by chaperone-assisted folding via intermediate folding states. However, the native state of a protein is only marginally stable and constantly under risk of misfolding. In a non-native conformation, these species are prone for unspecific intermolecular contacts that lead to protein aggregation. Not only misfolded proteins can lead to aggregation, but about 30% of proteins of the mammalians' proteome contain extensive intrinsically unstructured regions (Balchin et al., 2016; Dunker et al., 2008; Hipp et al., 2014) – aggregation of such proteins is associated with AD and PD. Possible deleterious effects of protein aggregation can be mediated either by a loss-of-physiological-function or by a gain-of-toxic-function. Aggregates cover a range of morphologies: from small soluble assemblies (oligomers) to larger insoluble protein deposits (inclusion bodies) that can be unstructured, amorphous aggregates or highly ordered amyloid fibrils with cross-beta structure. The cross- $\beta$  structure of amyloid fibrils is defined by  $\beta$ -strands, oriented perpendicular to the fibrils' axis.

To perpetuate the integrity of its proteome (proteostasis), mammalian cells maintain an extensive proteostasis network (**Figure 1.1B**, (Hipp et al., 2014)) that accounts for ~1400 proteins (Kim, 2013; Powers et al., 2009). This quality control network mediates correct protein folding and conformational repair with molecular chaperones – important are also mechanisms to degrade terminally misfolded proteins and aggregates by the ubiquitin-proteasome system (UPS) and autophagy. An imbalance of the proteostasis network or lack of capacity is associated with protein aggregation (Balchin et al., 2016;

---

<sup>1</sup> PubMed-search for MeSH-Terms: „Alzheimers disease“, Parkinsons disease“, „Huntingtons disease“ and „Amyotrophic lateral sclerosis“ on 17.11.2017

Hipp et al., 2014). A decline of the proteostasis networks' capacity is associated with aging (Labbadia and Morimoto, 2015) and thus facilitating aging-diseases associated with aggregation like neurodegeneration, type II diabetes, heart disease and certain forms of cancer (Balchin et al., 2016).

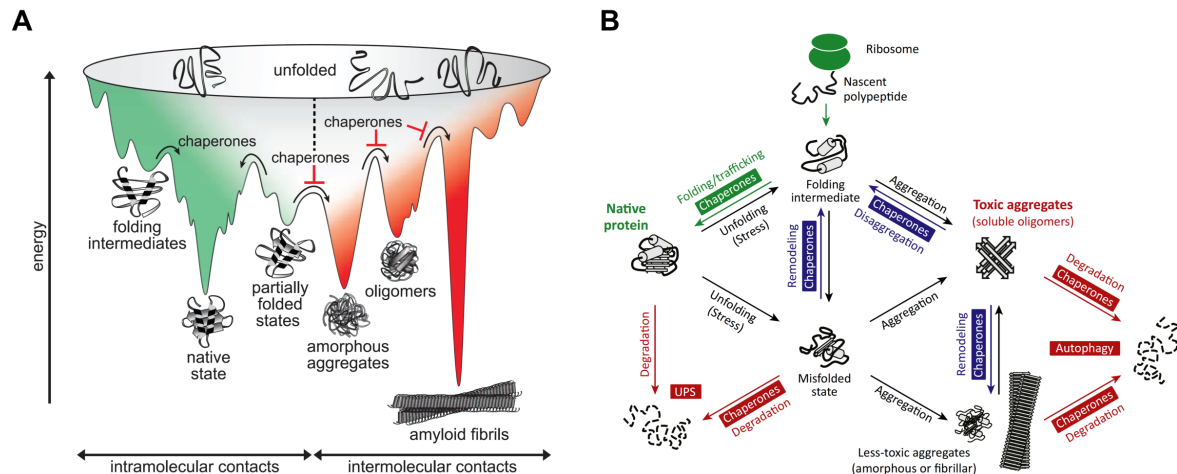


**Figure 1.1: Protein Aggregation**

**A: Protein aggregation competes with folding.** During folding, protein molecules sample various conformations while traveling downhill on a potential free-energy surface (green) toward the thermodynamically favorable native state. Kinetically trapped on- or off-pathway intermediates occupy low-energy wells (folding intermediates and partially folded states). Molecular chaperones provide assistance to folding by lowering free-energy barriers and preventing aberrant intermolecular interactions (red), which can lead to various forms of aggregates (amorphous, oligomeric, fibrillar). Fibrillar (amyloid-like) aggregates maybe thermodynamically the most stable. (from (Balchin et al., 2016), with permission)

**B: The proteostasis network (PN).** The PN maintains protein homeostasis by controlling the levels of functional proteins and preventing the formation of toxic aggregates. This is achieved by integrating three branches of the PN: (i) protein synthesis, the chaperone pathways for the folding of newly synthesized proteins and intracellular trafficking (PN branch of biogenesis; green); (ii) the chaperone pathways for the remodeling of misfolded proteins and protein disaggregation (PN branch of conformational maintenance; blue); and (iii) the pathways of protein degradation by the ubiquitin–proteasome system (UPS) and autophagy (PN branch of degradation; red). Toxic aggregates (mainly diffusible, oligomeric states) may be converted to less toxic, insoluble inclusions of amorphous or fibrillar (amyloid-like) structure. (from (Hipp et al., 2014), with permission)

## PROTEIN AGGREGATION IN NEURODEGENERATION

A conspicuous commonality of neurodegenerative diseases is the propensity of the disease proteins to aggregate in the brains (**Figure 1.2**) and other tissues of patients. Inclusion bodies (IB) are a hallmark of AD, PD, HD and ALS. Also common to most of these diseases is the observation that the aggregated species are structurally characterized as amyloids, which can be tested by staining for Congo red, Thioflavin S and by x-ray diffraction showing a general  $\beta$ -sheet structure (Rochet and Lansbury, 2000). Although aggregates of the various neurodegenerative diseases consist of very different proteins, they do share a common structural feature: the cross  $\beta$ -sheet conformation. It is intensely debated whether these aggregates contribute to the disease's pathology – if so, the structural commonality in the different neurodegenerative proteinopathies could be based on a common pathogenesis.

So far, soluble oligomeric aggregates have been linked to toxicity in many of these proteinopathies (Arrasate and Finkbeiner, 2012; Finkbeiner, 2011; MacDonald et al., 1993; Scherzinger et al., 1997). The large insoluble IBs found histologically in patients' brains and in animal and cellular models are diversely discussed and their role in disease is unclear. The studies interpreting IBs as protective entities propose the sequestration of the toxic oligomers into the IBs structure (Arrasate and Finkbeiner, 2012; Bucciantini et al., 2002; Haass and Selkoe, 2007; Leitman et al., 2013). In contrast, other studies interpret IBs to be involved in the disease mechanism and thus toxic to cells (DiFiglia et al., 1997; Pieri et al., 2012; Stefani and Dobson, 2003).

However, the significance of inclusion bodies in pathology is not well understood, and the in situ structure of protein aggregates and their interaction with cellular structures has not yet been determined. Structural studies with classical electron microscopy could not solve this question, as fixation of the sample and heavy-metal staining are procedures that very likely induce artifacts and are not compatible with high resolution imaging, what is reflected by inconsistent characterizations of aggregates in these studies. Thus, it remains unclear to what extent inclusion bodies are involved in pathological cellular interactions. Cryo-electron tomography experienced major developments in the last years that make it uniquely capable to investigate pathological features in situ at molecular resolution and thus enables to investigate inclusion bodies in their unperturbed cellular environment.

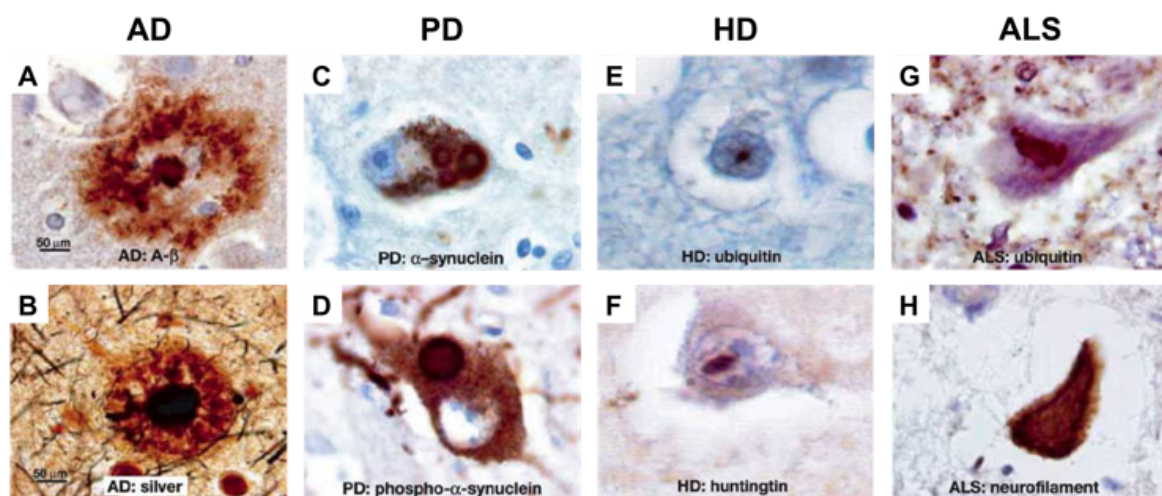


**Figure 1.2: Aggregation in Neurodegeneration**

Characteristic neurodegenerative disease neuropathological lesions involve deposition of abnormal proteins, which can be intranuclear, cytoplasmic or extracellular. All are labeled with antibodies (except D), as indicated.

**A:** AD, neuritic plaque labeled for  $A\beta$  (cerebral cortex). **B:** AD, neuritic plaque, silver stained (Hirano method). **C:** PD, Lewy bodies labeled for  $\alpha$ -synuclein (fine granular brown label in this and the next panel represent neuromelanin) (substantia nigra). **D:** PD, Lewy body labeled for phosphorylated  $\alpha$ -synuclein (substantia nigra). **E:** HD, intranuclear inclusion labeled for ubiquitin (cerebral cortex) **F:** HD, intranuclear inclusion labeled for huntingtin (cerebral cortex). **G:** ALS, cytoplasmic skein of neurofilaments labeled with ubiquitin (medulla oblongata). **H:** ALS, cytoplasmic skein of neurofilaments labeled with neurofilament (medulla oblongata). (modified from (Ross and Poirier, 2004), with permission)

## 1.3 HUNTINGTON'S DISEASE (HD)

The disease has already been known since the Middle Ages. It was termed “Veitstanz” (german) or “chorea” (greek word for ‘dance’), since patients affected by HD present jerky dance-like movements. The first thorough, scientific investigation of HD was published in 1872 by George Huntington – since then the disorder is called Huntington's disease. HD is typically diagnosed around the age of 30-50, whereupon the disease can occur at any age, from juvenile to advanced age. The disease is characterized by a movement disorder with unwanted movements, accompanied by neuropsychiatric manifestations and cognitive impairment with regular development of dementia.

### EPIDEMIOLOGY

Huntington's disease is an autosomal dominant inherited disorder. The prevalence of HD is about 5-7/100.000 (Walker, 2007) – similar for both genders and worldwide stable in countries with Caucasian ethnicity. In Japan the prevalence is about a magnitude lower with 0.5/100.000 (Walker, 2007) and also very low in the rest of Asia and similar in African populations (Wright et al., 1981). The higher prevalence of HD seems to depend on European ancestry (Bates et al., 2015). The incidence of HD in Western populations is about 0.5-0.7/100.000 (Bates et al., 2015). Only 5-8% of HD cases are de novo mutations (Almqvist et al., 2001; Ramos-Arroyo et al., 2005), without any family history of HD.

### SIGNS AND SYMPTOMS

The most prominent physical symptoms are random, uncontrollable movements of the extremities called ‘chorea’ that make it impossible for the patient to sit still in a chair, often accompanied with abnormal face expressions that the individual is unable to control. Further physical symptoms are saccadic eye movements, difficulties speaking, chewing and swallowing.

Besides the motor symptoms, neuropsychiatric manifestations are common in HD: 40% of HD patients experience severe psychiatric problems such as suicide and suicidal attempts (16-32% depending on disease state), psychosis and aggression (Orth et al., 2010). The majority of HD patients (87%) had psychiatric abnormalities like anxiety, depression, obsessive and compulsive behavior, apathy or irritability (Orth et al., 2010).

Cognitive decline is another major presentation of HD. With 40%, a large portion of HD patients show mild cognitive impairment (MCI) already before onset of motor symptoms (Duff et al., 2010). The features of cognitive decline in HD are unlike Alzheimer's disease, but comparable to subcortical pathologies, as seen in vascular dementia or Parkinson's disease

Survival after diagnosis is about 15-20 years - after 15 years 1/3 of HD patients are still alive. The leading cause of death with 30-50% of HD patients is pneumonia predominantly caused by aspiration, followed by cardio-vascular diseases and the third most common cause of death with 7% is suicide (Haines et al., 1986; Heemskerk and Roos, 2010; Walker, 2007).

## NEUROPATHOLOGY OF HD

For the investigation of aggregation in HD, it is of interest where the neurodegenerative processes are affecting the brain. Characteristic for HD is an early and extensive atrophy of the striatum – a part of the basal ganglia, composed of the caudate nucleus and the putamen. The striatum is importantly involved in the initiation and inhibition of movements – this regulatory function is impaired in Huntington's Disease. Nuclear magnetic resonance imaging (MRI) shows grey matter loss, primarily in the striatum but also in some other subcortical regions (Pallidum) and the cortex (Domínguez et al., 2013; Georgiou-Karistianis et al., 2013; Jernigan et al., 1991). Diffusion-weighted imaging (DTI), with its scalar measures of fractional anisotropy and mean diffusivity, shows early degeneration of these grey matter regions but also in white matter – it is sensitive to microstructural damages (axonal degeneration, demyelination) (Liu et al., 2016). These alterations are detectable more than 15 years before clinical onset of disease symptoms.

## NON-NEUROLOGICAL FEATURES OF HD

The core symptoms of Huntington's Disease include motor deficits like hyperkinesia aside of cognitive impairment and psychopathological changes like depression, anxiety, apathy, OCD and psychotic episodes. Neurodegeneration of the basal ganglia and the neocortex has been linked to these symptoms.

The most outstanding symptoms of HD are of neuropathological nature, but HD is complicated by peripheral abnormalities like muscle atrophy, cardiac failure, impaired glucose tolerance, osteoporosis, testicular atrophy and weight loss (**Figure 1.3**). These peripheral abnormalities seem to occur independently from the neurological dysfunction (van der Burg et al., 2009). Indeed, huntingtin is not only expressed in neurons, but ubiquitarily in all tissues (Hoogeveen et al., 1993; Li et al., 1993; Trottier et al., 1995). It was shown in studies with knock-out mice that huntingtin is essential for most tissues, as the absence of huntingtin causes apoptosis in all three germ-layers (endoderm, mesoderm and ectoderm) and causes embryonal lethality (Zeitlin et al., 1995). Furthermore, the ubiquitous expression of mutant huntingtin in HD causes damage in heart, pancreas and muscles; aggregates are also found in these tissues (Cisbani and Cicchetti, 2012). A particular sensitivity of neurons may be the reason for the highly distinctive symptoms of HD, which are caused by degeneration of neurons, in contrast to other consequences of tissue damage: a study comparing neurons with the other three cell-types of brain-tissue (astrocytes, oligodendrocytes and microglia) showed that neurons were by far more vulnerable to inclusion body formation, with microglia being the least sensitive one, although the expression-level of mutant huntingtin was similar for all cell-types (Jansen et al., 2017).

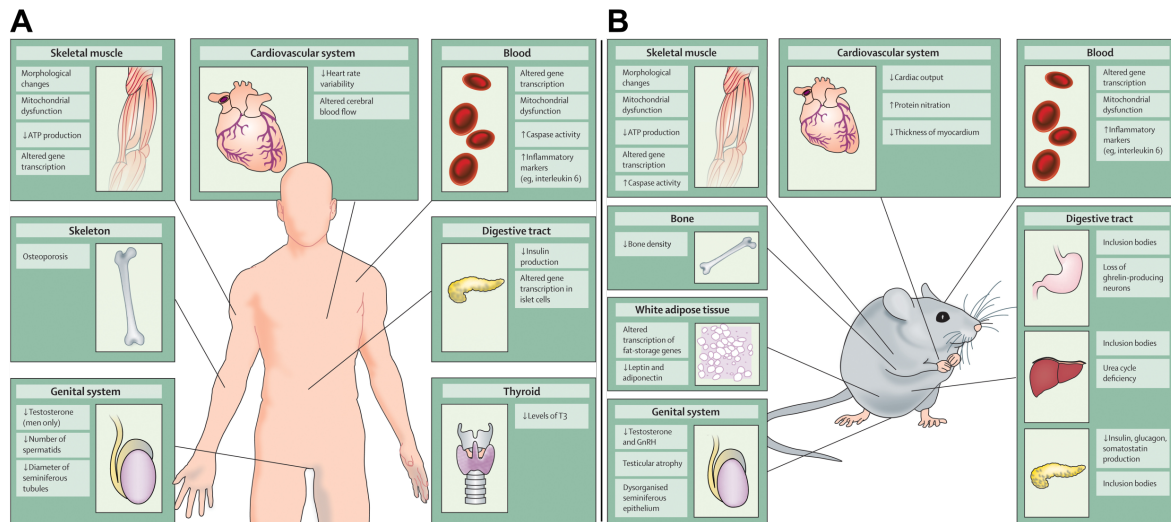


**Figure 1.3: Peripheral Pathology of Huntington's Disease**

**A:** Peripheral pathology observed in patients with Huntington's disease. **B:** Peripheral pathology found in animal models of Huntington's disease. (from (van der Burg et al., 2009), with permission)

## PHARMACOLOGICAL THERAPY

As for all other neurodegenerative diseases, there is no causative therapy available. Pharmacological strategies are restricted to symptomatic treatments. The hyperkinesia is treated by dopaminergic substances like Tiaprid or Tetrabenazine, alternative the atypical neuroleptic Olanzapin is used. But non FDA- or EMA-approved substance so far is able to change the progression of the disease.

A potential new substance (IONIS HTT<sub>Rx</sub>) investigated by the company IONIS Pharmaceuticals showed a dose-dependent reduction of mutant and wildtype Huntingtin levels, when administered intrathecally to 46 patients with early manifested HD in a Phase IIa proof of concept study (ClinicalTrials.gov Identifier: NCT02519036). However, it remains to be proven in a large-scale Phase III study, if this substance is finally able to modify disease progression.

## HD GENETICS

A mutation in the HTT-gene causes the disease. The HTT-gene is located on the short arm of chromosome four at position 16.3 and its expression product is the huntingtin protein. The mutation in the HTT-gene affects a repetitive CAG-sequence at the 5'-end that codes for the amino acid glutamine. People with 35 or less CAG-repeats will not get HD in a normal lifetime, people with 35-40 repeats have a reduced penetrance and individuals with an expansion of >40 counts will get Huntington's disease (**Figure 1.4A**). The CAG-repeat length correlates inversely with the age at onset of the disease-symptoms (**Figure 1.4B,D**) – with more than 60 CAG-repeats, the disease affects juvenile patients. While the CAG-repeat length determines the speed of the disease development, it does not affect the kinetics of the metabolic decline in HD patients: cell death is best fit by a constant risk model and independent of the CAG-repeat length (**Figure 1.4C**).

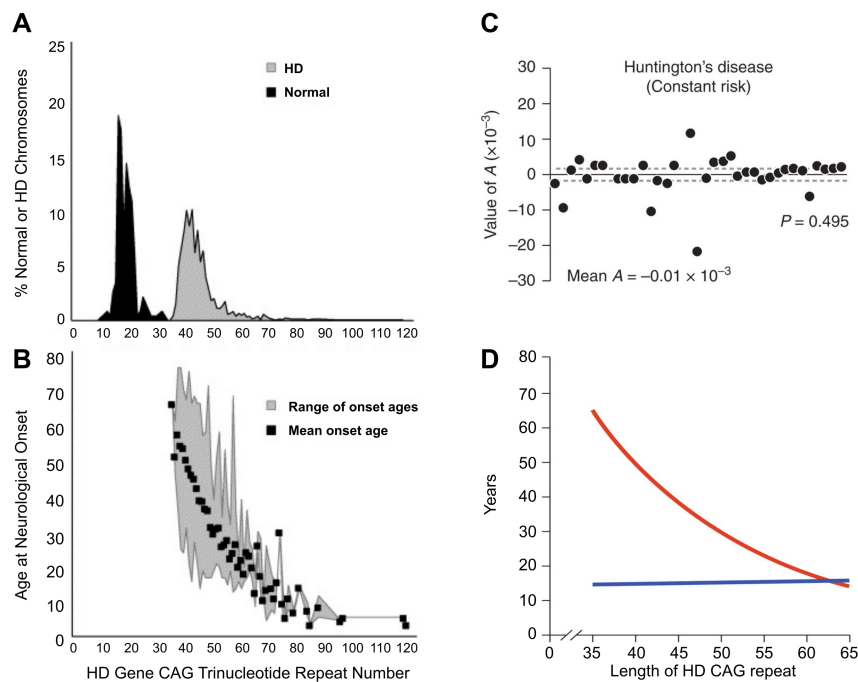


**Figure 1.4: The Role of the CAG Expansion in the HTT-Gene on HD Pathogenesis.**

**A:** The range of the HD CAG repeat sizes observed on normal and HD chromosomes as each allele's percentage of the total. **B:** The mean age at neurological onset and the range of ages at onset associated with different HD expanded CAG repeats. (A and B: from (Gusella and MacDonald, 2007), with permission) **C:** The kinetics of metabolic decline in Huntington's disease patients is best fit by a constant risk of cell loss. Values of A, the exponent of an equation relating longitudinal metabolic changes to time, do not differ significantly from zero ( $P = 0.495$ , Student's t-test). Each point represents the estimated A for an individual patient. Solid line, mean A (mean  $\pm$  s.d.:  $-0.01 \times 10^{-3} \pm 5.3 \times 10^{-3} \text{ mMh}^{-1}$ ,  $n=38$  patients) across patient population; dashed lines, 95% confidence interval for the mean value of A ( $-1.7 \times 10^{-3}$ ,  $1.7 \times 10^{-3}$ ). (from (Clarke et al., 2000), with permission) **D:** Aggregation of the data from (B) and (C): Correlation of HD CAG-repeat length with age at onset. Best-fit curves for age at neurological onset (red) and duration of disease from onset to death (blue), plotted against CAG repeat length for the expanded mutant allele from Huntington disease (HD) patients. Age at onset is strongly correlated with the CAG-repeat length ( $r^2=0.54$ ;  $p < 0.001$ ), and duration of disease shows no correlation with the CAG-repeat length, suggesting that, after onset of HD, factors independent of the original trigger of pathogenesis determine the rate of progression. (C and D: from (Finkbeiner, 2011), with permission).

## 1.4 AGGREGATION IN HD

### HUNTINGTIN (HTT) AS A MODEL EXAMPLE OF AGGREGATION IN NEURODEGENERATION

The very high penetrance shows that the genetic mutation is sufficient and causative for the disease. This makes the aggregation of huntingtin (Htt) especially interesting as a model example for neurodegenerative proteinopathies to investigate the interaction of inclusion bodies within their cellular context.

The Htt protein is 3144 amino acids long with a mass of 348 kDa. The N-terminal region carries the poly-glutamine (polyQ) repeat that determines the aptness to aggregate. The physiological function of Htt in humans and animals is not clear but it seems to be essential for the cell and is involved in critical processes, like vesicle transport, protein trafficking and transcription (Cattaneo et al., 2005). The structure of the full length Htt protein was just recently solved by single-particle cryo-EM (Guo et al., 2018) – however the N-terminal polyQ-domain could not be resolved.

In HD patients' postmortem brains, inclusion bodies are only detected by antibodies to the N-terminus of the full length protein (Becher et al., 1998; DiFiglia et al., 1997; Gourfinkel-an et al., 1998; Gutekunst et al., 1999) caused by aberrant splicing (Neueder et al., 2017; Sathasivam et al., 2013) of the 67 exons of the HTT-gene and/or by proteolytic cleavage (Bates et al., 2015), resulting in a short exon 1 product (**Figure 1.5A**). Furthermore, it has been shown that full length huntingtin does not aggregate (Gutekunst et al., 1999). Moreover, exon 1 alone is sufficient to cause HD-like phenotype in transgenic mice (Mangiarini et al., 1996) and is in the literature<sup>2</sup> widely used. **Figure 1.5B** shows a model of the pathological cellular mechanisms of Huntingtin exon 1 in HD.

While the role of the large insoluble inclusion bodies is unclear (protective: (Arrasate and Finkbeiner, 2012; Bucciantini et al., 2002; Haass and Selkoe, 2007; Leitman et al., 2013), toxic: (DiFiglia et al., 1997; Pieri et al., 2012; Stefani and Dobson, 2003)), the presence of soluble oligomeric aggregates is clearly associated with cytotoxicity in several studies (Arrasate and Finkbeiner, 2012; Finkbeiner, 2011; Kim et al., 2016; Leitman et al., 2013; MacDonald et al., 1993; Sánchez et al., 2003; Schaffar et al., 2004; Scherzinger et al., 1997)). Soluble oligomeric species have been shown to interfere with several cellular functions: transcriptional regulation, disruption of axonal transport, mitochondrial/bioenergetic dysfunction and protein quality control (Bence et al., 2001; Kim et al., 2016; Orr and Zoghbi, 2007). A proteome-wide screening showed a plethora of aberrant protein interactions with oligomeric aggregates (Kim et al., 2016): affected classes of proteins are found in the pathways of translation, chromatin-assembly, RNA-binding/processing, transcription, ribosome biogenesis, chaperones, ubiquitin-proteasome-system, cytoskeleton, vesicle transport – several of these interaction classes support previous findings of impaired cellular function in HD.

---

<sup>2</sup> A PubMed search for the term “huntingtin exon 1” results in 440 articles.



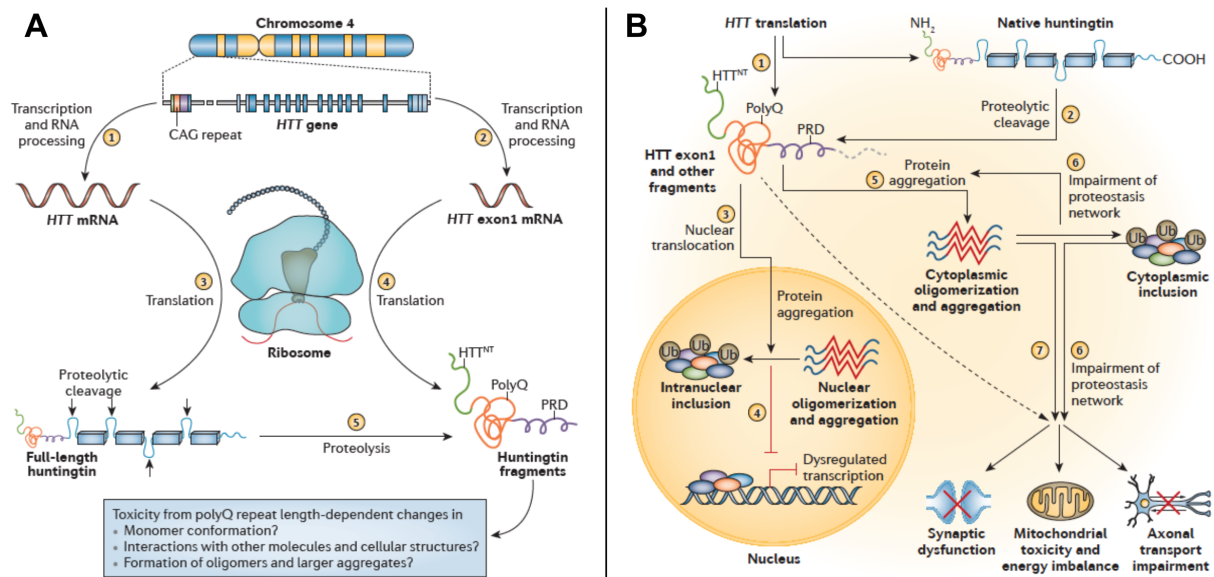


**Figure 1.5: Huntingtin**

**A:** Expression of HTT generates an initial RNA transcript that is normally processed into an mRNA encoding the full-length huntingtin protein (label 1), but it can also be aberrantly processed into an mRNA encoding only exon1 if the gene contains an expanded CAG repeat (label 2). Translation generates either the full-length huntingtin protein (label 3) or the HTT exon1 protein (label 4). The HTT exon1 fragment consists of the 17-amino-acid mixed sequence HTTNT, the polyglutamine (polyQ) sequence encoded by the CAG repeat and a proline-rich domain (PRD). The full-length huntingtin protein consists of this exon1 sequence followed by a series of ordered (boxes) and disordered (loops) protein segments. Proteolytic cleavage (label 5; cleavage sites indicated by arrows) mediated by recognition sequences located in the disordered segments generates a series of products, including HTT exon1-like fragments. Such fragments containing expanded polyQ segments have important roles in triggering Huntington disease by molecular mechanisms that are yet to be elucidated. (from (Bates et al., 2015), with permission)

**B:** (1) HTT is translated to produce the full-length huntingtin protein as well as an amino-terminal HTT exon1 fragment (the result of aberrant splicing). The length of the polyglutamine (polyQ) tract in these proteins depends on the extent of somatic instability. (2) Full-length native huntingtin is cleaved through proteolysis to generate additional protein fragments. (3) Protein fragments enter the nucleus. (4) Fragments are retained in the nucleus through self-association, oligomerization and aggregation — leading to the formation of inclusions, a process that causes transcriptional dysregulation through the sequestration of other proteins and through other incompletely defined mechanisms. (5) Huntingtin fragments oligomerize and aggregate in the cytoplasm. (6) The aggregation of huntingtin is exacerbated through the disease-related impairment of the proteostasis network, which also leads to global cellular impairments. (7) The aberrant forms of huntingtin result in additional global cellular impairments, including synaptic dysfunction, mitochondrial toxicity and a decreased rate of axonal transport. PRD, proline-rich domain; Ub, ubiquitin. (from (Bates et al., 2015), with permission)

## EXPERIMENTAL SYSTEMS FOR HD INVESTIGATION

HD is a neurodegenerative disorder of the human species. Thus research-efforts are preferentially focused on the gold-standard: the human brain. Noninvasive neuroimaging methods like MRI, DTI, fMRI, CT and PET yield valuable information about structural, functional and network-connectivity alterations in HD patients (e.g.: (Domínguez et al., 2013; Georgiou-Karistianis et al., 2013; Jernigan et al., 1991; Liu et al., 2016)) that couldn't be acquired differently – however their resolution is limited to the sub-millimeter range. For studies that aim for cellular resolution, only avital brain-tissue from

deceased patients is available, since it is extremely difficult to obtain human vital neurons from patients. This is primarily due to ethical considerations: in the Hippocratic tradition the upmost ambition of the physicians' action is "primum non nocere"<sup>3</sup>, which strongly restricts the options to obtain live neuronal tissue from the human brain to therapeutic conditions (e.g. tumor resections, resections in therapy refractory epilepsy).

Studies with other mammalian species like mice and rats however provide invasive insights. The R 6/2 mouse is the first and most extensively investigated mouse model for HD (Mangiarini et al., 1996) – expressing exon 1 of human Htt with 144 CAG repeats. Several further transgenic mouse models have been established (Ferrante, 2009) also with polyQ-expanded full length Htt like the YAC (Slow et al., 2003) and BAC (Gray et al., 2008) mice. All these models recapitulate many but not all disease symptoms but the Htt aggregates have been observed to be indistinguishable (Davies et al., 1997) to the ones in human brains. Furthermore, the disease progression in the mouse models is observable in a much shorter time-span (weeks to months, (Ferrante, 2009)).

However, although HD is a predominantly neurodegenerative disorder, mutant huntingtin is expressed ubiquitarily in all human tissues (see chapter 1.3), thus human non-neuronal/peripheral cell types can therefore be used, in addition to tissue from animals (van der Burg et al., 2009). Several inducible cell lines have been established (Cisbani and Cicchetti, 2012) with different Htt constructs and also transient transfection of cell lines or primary cultures have been used to model the pathological features of HD.

These models have revealed that cultured cells are more susceptible to the presence of the pathological form of Htt when the latter is overexpressed, whereas physiological expression leads to more subtle changes (Cisbani and Cicchetti, 2012).

## STATE-OF-THE-ART: ULTRASTRUCTURAL IMAGING OF INCLUSION BODIES IN HD

It was shown that polyQ-expanded Htt exon 1 forms fibrils in vitro (Scherzinger et al., 1997). Structural investigations of in vitro Htt exon 1 fibrils with nuclear magnetic resonance spectroscopy (Hoop et al., 2016; Isas et al., 2015) revealed the presence of  $\beta$ -hairpin-containing  $\beta$ -sheets that are connected through interdigitating extended side chains. (Isas et al., 2015) propose a bottlebrush model, in which the polyQ domains form the fibril core and the proline-rich domains the bristles of the bottlebrush.

Several research efforts attempted to reveal the 'ultrastructural' architecture of huntingtin inclusion bodies in humans HD brain, animal models and cell cultures by classical electron microscopy (**Figure 1.6**): it has remained controversial for decades whether Htt in cellular IBs is present in granular or fibrillar form (Davies et al., 1997; DiFiglia et al., 1997; Finkbeiner, 2011; Miller et al., 2010; Petrasch-Parwez et al., 2007; Qin et al., 2004; Waelter et al., 2001).

These studies investigated Htt inclusion bodies in human HD brain (DiFiglia et al., 1997), in transgenic animal models (Davies et al., 1997; Miller et al., 2010; Petrasch-Parwez et al., 2007) and in transfected cell lines (Qin et al., 2004; Waelter et al., 2001). Both, nuclear and cytosolic IBs were found in the human HD brain (DiFiglia et al., 1997) as well as in the other studies.

---

<sup>3</sup> „primum non nocere“ (latin) means translated into English: “first, do not harm”. It is a fundamental principle in medical ethics derived from the Hippocratic oath and the Corpus Hippocraticum Epidemics, Book I (Lloyd et al. 1984, Wegner et al. 2004), where is stated: "Practice two things in your dealings with disease: either help or do not harm the patient".

Study	System	construct	IB appearance (classical EM)
Miller et al. 2010	-Primary striatal culture (rat)	HttQ64,72,97-GFP exon 1	granular / amorphous
Petrasch-Parwez et al. 2007	-tgHD rats -R6/2 mice	Q51 Htt exon 1-15 Q141-157 Htt exon 1	granular & fibrillar
Qin et al. 2004	-MCF-7	FH969-100Q	granular & fibrillar
Waelter et al. 2001	-293 Tet-Off	HDQ83 exon 1	fibrillar
DiFiglia et al. 1997	-HD patients	endogenous Htt	granular & fibrillar
Davies et al. 1997	-R6/2 mice	Q141-157 Htt exon 1	granular (occasional fibrillar)

**Table 1.1: Overview of studies investigating the molecular structure of IBs**

The before mentioned hypothesis that IBs in HD contain only short N-terminal fragments of the full length Htt protein is supported by the observation by DiFiglia et al. that the ultrastructure of IBs in HD patient brain is indistinguishable from that of IBs found in HD mice expressing only exon 1 (Davies et al., 1997), as DiFiglia et al. remark in their paper.

However, the characterizations of the ‘ultrastructure’ of the IBs in the different studies is inconsistent: several studies described the IBs substantially as amorphous granular and only minor fibrillar structures (Davies et al., 1997; DiFiglia et al., 1997; Miller et al., 2010; Petrasch-Parwez et al., 2007), while others put forward the observation of fibrils (Qin et al., 2004; Waelter et al., 2001).

All these studies show EM images of samples that were dehydrated, plastic-embedded and stained with heavy metals, a series of procedures that are very likely to induce structural alterations, particularly at the molecular level. Thus, classical electron microscopy is in general incompatible with high-resolution imaging of biological specimens. However, cryo-electron microscopy is capable of imaging cellular structures at molecular resolution, while preserving the sample in its native, unperturbed, close-to-native state.

#### Figure 1.6: State-of-the Art of Ultrastructural Imaging in HD by Classical Electron Microscopy (p. 14)

**A&B:** From DiFiglia et al. 1997. Human neuronal intranuclear IB (hNII) in the HD cortex with immunoperoxidase labeling. **A:** hNII in a cortical neuron appears as a dense aggregate with no limiting membrane separating it from the nucleoplasm.

**B:** Higher magnification of NII in (A) shows the presence of labeled granules and filaments within the inclusion.

**C&D:** From Davies et al. 1997. Huntingtin within the neuronal nucleus of transgenic mice. Discrete deposition of huntingtin within two neuronal intranuclear IBs with antibodies to huntingtin.

**E&F:** From Petrasch-Parwez et al 2007. Intranuclear aggregates as documented by conventional transmission electron microscopy. **E:** A medium-sized striatal neuron shows a round intranuclear aggregate (large arrow) slightly larger than the neighbored nucleolus (N). **F:** At higher magnification, the membraneless aggregate reveals a granular and fibrillar (arrowheads) appearance.

**G&H:** From Waelter et al. 2001. Transfected 293 Tet-Off cells containing Htt83Q exon 1 aggregates, after expression for 3–5 d. **G:** Cell containing a typical perinuclear inclusion body. **H:** At higher magnifications, Htt83Q exon 1 fibrils with a diameter of roughly 10 nm can be observed.

**I&J:** From Qin et al. 2004. Huntingtin IBs. MCF-7 cells were transiently transfected with FH969–100Q and immunostained for FLAG using the immunoperoxidase method. **I:** This cell contains one Flag-labeled huntingtin body. Note the radiating fibrils in the core (C) and the less defined structure in the shell (S). Multilamellar-type autophagic bodies (a) about the shell.

**J:** Higher magnification of htt body in (I). The dashed line is the approximate boundary between the shell (S), which is heavily labeled for Flag, and the core (C), which is not. There are radiating fibrils in the core (arrows).

**K&L:** From Petrasch-Parwez et al 2007. Dendritic aggregates as documented by conventional transmission electron microscopy. **K:** The aggregate localized in a cross-sectioned dendrite (large arrow) is surrounded by numerous mitochondria (small arrows). **L:** At higher magnification, the dendritic aggregate exhibits granular and fibrillar (arrowheads) composition as seen for nuclear IBs in the same study in (E,F).

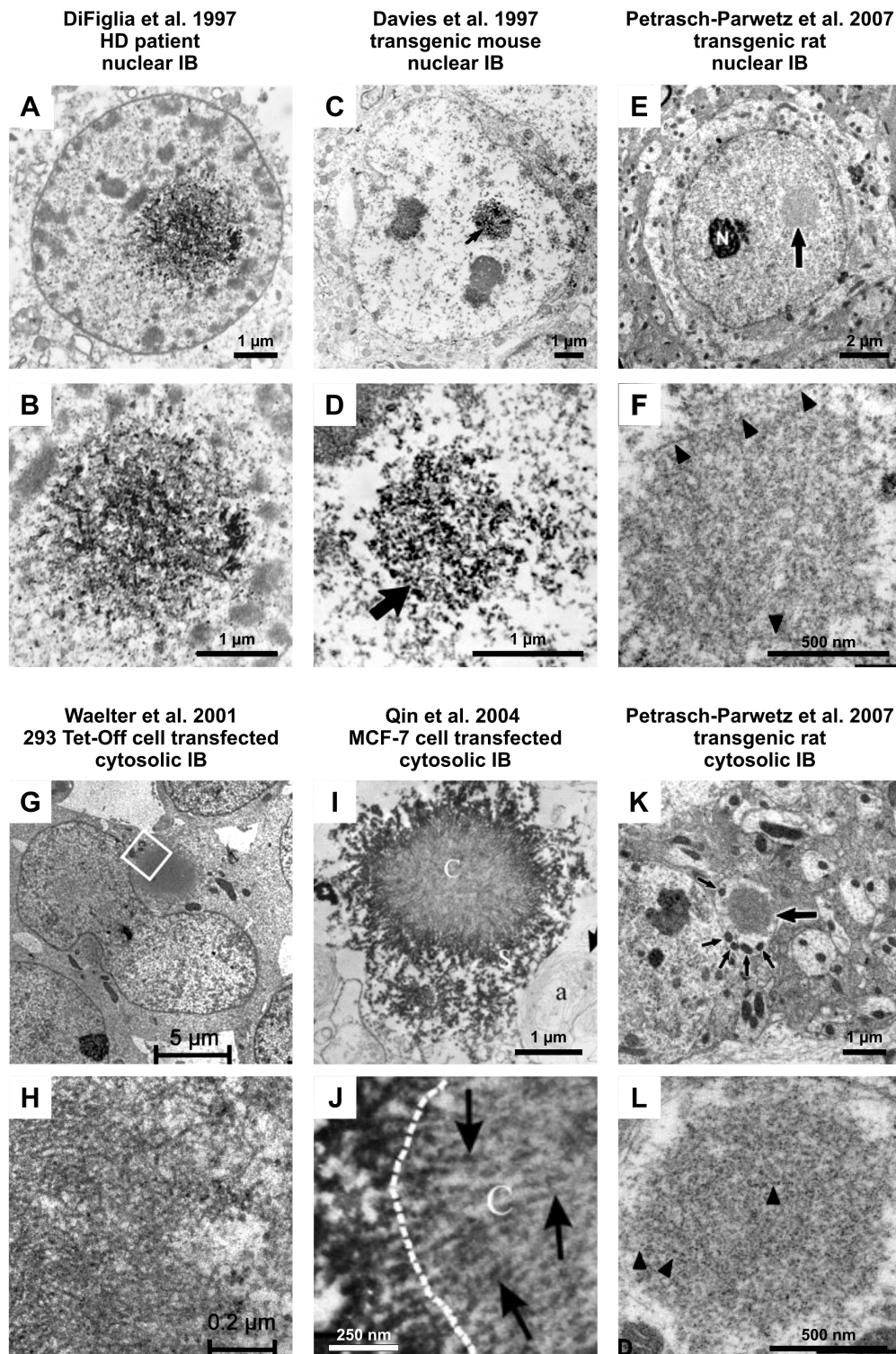


Figure 1.6: State-of-the-Art of Ultrastructural Imaging in HD by Classical Electron Microscopy

## 1.5 OTHER NEURODEGENERATIVE DISEASES

The aggregation of disease-proteins is a communality for most neurodegenerative diseases. In this chapter the other three main neurodegenerative diseases AD, PD and ALS and further polyQ diseases are presented, to exemplify the divergence of their disease presentation, while chapter 1.2 focuses on the microscopic common features.

### OTHER POLYQ-DISEASES

Besides HD, seven other trinucleotide diseases with (CAG)<sub>n</sub> repeats coding for glutamine are known (**Table 1.2**). These mutations are associated with inclusion bodies in several of these diseases as found in HD. The occurrence of inclusions roughly correspond to the regions of neuronal degradation (Ross and Poirier, 2004). A communality of polyQ diseases is a progressive degeneration of neurons in the central nervous system – the main region affected by atrophy is defined by the name of the disease (except HD).

Disease	Normal range (CAG repeats)	Disease range (CAG repeats)	Presence of inclusions
Huntington's disease (HD)	6–35	36–121	Yes
Dentatorubral-pallidoluysian atrophy (DRPLA)	3–35	49–85	Yes
Spinobulbar muscular atrophy (SBMA)	11–33	38–62	Not assessed
Spinocerebellar ataxia 1 (SCA1)	6–44	40–81	Yes
Spinocerebellar ataxia 2 (SCA2)	15–29	35–59	Not assessed
Spinocerebellar ataxia 3 (SCA3)	12–41	55–84	Yes
Spinocerebellar ataxia 6 (SCA6)	4–17	20–30	Not assessed
Spinocerebellar ataxia 7 (SCA7)	4–35	37–200	Yes

**Table 1.2: Trinucleotide repeat diseases that are caused by a CAG/polyglutamine repeat expansion in the relevant protein.** (from (Rubinsztein et al., 1999), with permission)

### ALZHEIMER'S DISEASE (AD)

Alzheimer's Disease is a devastating neurodegenerative pathology characterized by a progressive mental decline typically affecting patients above 65 years of age. It is the most common cause of dementia worldwide. In 1906, the psychiatrist and neuropathologist Professor Alois Alzheimer described for the first time the neurohistological characteristics in the brain of his diseased, demented patient Auguste Deter at the psychiatric clinic of the Ludwig-Maximilians-University Munich.

**Epidemiology:** In 2015, 46 million people were diagnosed with dementia (0.6% of world population), of which about 30 million patients have Alzheimer's Disease (Global Burden of Disease Study 2015, 2016). The prevalence of AD in 2015 shows a 38% increase compared to 2005, demonstrating that dementia caused by neurodegeneration is an emerging 'pandemic'<sup>4</sup> problem. Models to forecast the prevalence of AD project a four-fold increase until 2050 (Brookmeyer et al., 2007; Ferri et al., 2005; Wimo et al., 2003), predominantly in low- and middle-income countries because of their increasing

<sup>4</sup> The term pandemic should express the massive global increase of dementias – but should not state that there is an infectious cause, as the term is often used for.

life-expectancy. The global annual incidence is 750/100.000 and it rises exponentially with age.

Only a very rare fraction (< 1%) of AD is autosomal inherited, where a genetic mutation in at least one of the three genes Presenilin-1 (PSEN1), Presenilin-2 (PSEN2) or Amyloid precursor protein (APP) causes the disease. The etiology for the most common form of AD (sporadic AD) is not understood, although there is some evidence for genetic factors (Bertram et al., 2010) like the APOE4-variant, which acts as a vulnerability-gene for the predominantly sporadic form of AD. Age is the greatest risk factor for the development of AD.

**Signs and Symptoms:** AD is characterized by a massive cognitive decline, predominantly a deterioration of memory, and leads to death within 3 to 9 years after diagnosis (Querfurth and LaFerla, 2010). Characteristic is the inability to memorize new facts or memories, but not all memory domains are affected similarly: older memories, like the episodic, semantic and implicit memory, are preserved longer, while the disease progresses. Other typical symptoms are difficulties with orientation (time, place, person, situation), amnesic aphasia, depression, apathy, aggression or illusion, but also paranoid ideas like delusion of jealousy, theft and being poisoned. The cause of death are usually external factors like pneumonia and other infections, because most patients are bedridden in the end, physically weak and therefore prone to get sick.

**Aggregating protein:** In AD two proteins are observed to aggregate:  $\beta$ -amyloid ( $A\beta$ ) is found in extracellular neuritic plaques and hyperphosphorylated tau protein is found as neurofibrillary tangles cytosolically in the cell body of neurons.  $A\beta$  peptides originate from the sequential proteolytic cleavage of the amyloid precursor protein by a  $\beta$ - and  $\gamma$ -secretase.  $A\beta$  peptides are natural products of metabolism with a length of 36-43 amino acids, in which  $A\beta_{40}$  is much more prevalent than the more aggregation-prone  $A\beta_{42}$  – in AD this ratio is disturbed and  $A\beta_{42}$  is found to aggregate. The tau protein is a microtubule-stabilizing protein and tends to aggregate in the cytosol of cells when hyperphosphorylated as seen in AD.

## PARKINSON'S DISEASE (PD)

Parkinson's Disease is the most common neurodegenerative disorder after AD. It was already known in the ancient world, but the first written account dates from 1817 by James Parkinson, while a histopathological description by Friedrich Lewy followed in 1912.

**Epidemiology:** In 2015, 6.2 million people are diagnosed with Parkinson's disease (Global Burden of Disease Study 2015, 2016). In Europe the prevalence of PD is approximately 108-256/100.000 with an annually incidence of 11-19/100.000 (von Campenhausen et al., 2005). The etiology for PD is unclear and seems to be a product of a complex interaction of environmental and genetic factors (Kalia and Lang, 2015). Thus the majority of PD cases are sporadic forms, but up to 10% of the patients have single mutations determining the disease (Lesage and Brice, 2009). As for AD, for PD the age is the greatest risk factor for the development of the disease and increases exponentially with age (Driver et al., 2009).

**Signs and Symptoms:** Parkinson's disease is predominantly characterized as a movement disorder, but regularly accompanied by neuropsychiatric symptoms and a common course of dementia.

Typical motor-symptoms of PD are the delay of initiation of movements, small movement amplitudes (bradykinesia) like micrographia, a 4-6 Hz resting tremor, muscular rigidity, difficulties walking and postural instability. Besides motor-symptoms, sleep disturbances are regular and neuropsychiatric manifestations are common: up to 40% of patients suffer from visual hallucinations, illusions and delusions (Onofrij et al., 2007) - also depression, anxiety and apathy occur frequently. Typically,

dementia is developing in to up to 80% of PD patients over the course of the disease (Hely et al., 2008).

**Aggregating protein:** A characteristic of PD is the massive cell death in the substantia nigra (pars compacta) of the mid brain (mesencephalon). Symptoms occur when up to 70% of the dopaminergic cells have been lost. In these cells and other parts of the brain, pathognomonic Lewy bodies (Goedert, 2001) are found in the cell body, which are highly immunoreactive for  $\alpha$ -Synuclein (Spillantini et al., 1997).

### AMYOTROPHIC LATERAL SCLEROSIS (ALS)

ALS is a rapidly progressing, lethal neurodegenerative disease affecting motor neurons with the consequence of muscle atrophy and weakness throughout the body, ultimately resulting in a lethal respiratory insufficiency. The term amyotrophic lateral sclerosis was introduced by Jean-Martin Charcot, who published a paper in 1874, in which he deduced the relationship between the clinical signs and the histopathological findings (Rowland, 2001).

**Epidemiology:** ALS is a rare disease – declared by the FDA as an “orphan disease” with a typical onset between the 6<sup>th</sup> to 8<sup>th</sup> decade and a prevalence of 4-5/100.000 in the USA (Mehta, 2016). The incidence in Europe and USA is about 2/100.000 per year (Kiernan et al., 2011). The majority (>90%) of ALS cases are sporadic with an unclear etiology, but 5-10% of ALS cases are familial: gene-mutations in the SOD1 gene cause 5%/20% of the sporadic/familial cases, a mutation in the TDP-43/FUS/ANG genes causes 5-10%/5%/1% of the familial cases. Recent evidence (Majounie et al., 2012) shows an interesting association of patients that carry a hexanucleotide repeat expansion in C9orf72 with sporadic (7%) and familial (39%) ALS and also with sporadic (6%) and familial (25%) frontotemporal dementia (FTD). The penetrance for this genetic lesion rises from 0% at 35 years to 50% at 50 years to full penetrance at 80 years of age.

**Signs and Symptoms:** The symptoms show progressive paralyzes and atrophy of skeletal muscles. Patients lose the ability to initiate voluntary movements, until in the final stage the muscles responsible for breathing fail.

**Aggregating protein:** In ALS several proteins are found to aggregate in inclusion bodies (TDP-43, c9orf72, FUS, SOD1), but in almost all cases of ALS, cytoplasmic IBs were positive for TDP-43 (Kiernan et al., 2011). In FTD half of the patients showed TDP-43 positive IBs, what indicates a certain overlap of ALS and FTD.

## 2

# CRYO-ELECTRON MICROSCOPY TECHNIQUES

## 2.1 ELECTRON MICROSCOPY OF BIOLOGICAL SAMPLES

In order to get the most detailed data, the investigation of physiological and pathological processes and their structural correlates in biology and medicine needs to be performed at highest resolution. There are several suitable methods to visualize structural or functional aspects at different levels of resolution (**Figure 2.1**).

### **Why doing TEM on biological samples?**

Transmission electron microscopy (TEM) is able to investigate the structure of cells and tissues at nanoscale and is positioned in between high-resolution methods like NMR or x-ray crystallography and the lower-resolution techniques of light and fluorescence microscopy. In the field of light microscopy, the super-resolution techniques like STED (Hell and Wichmann, 1994; Klar et al., 2001) work around Abbe's diffraction limit and reach resolutions three to four magnitudes higher. Although these are great advances in modern fluorescence light microscopy and offer the possibility to investigate dynamic processes at resolutions way below 100 nm (Lidke and Lidke, 2012), these methods require a presumption and the visualization remains restricted to fluorescently labeled structures. On the contrary TEM microscopy of biological samples is independent of structure-specific labels and allows imaging any structure inside a cell, that would be hidden in fluorescence microscopy except the labeled structure(s) of interest.



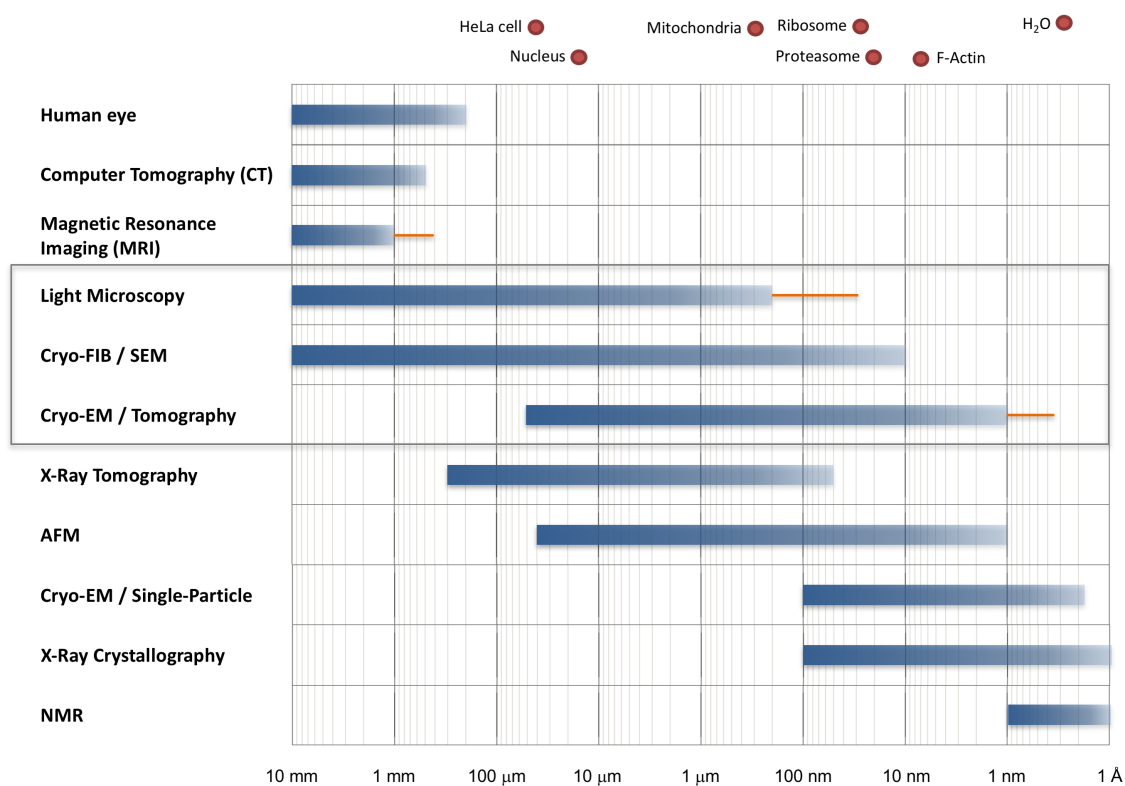


**Figure 2.1: Resolution Ranges of Biological Imaging Techniques**

General overview of imaging techniques applied on biological specimens. The blue bars indicate the resolution range of each method. The orange lines show recent developments or strategies that overcome the previous resolution limit of the specific method. At the top of the figure, typical sizes of biological structures are indicated (red circles).

Thus, TEM gives the opportunity, to investigate the complexity of the cellular landscape from larger structures like organelles down to macromolecules. Furthermore, the structure of macromolecules can be determined by single-particle TEM. However, conventional TEM has beside these benefits also disadvantages like dehydration, chemical fixation and staining of the sample. Cryo-electron microscopy overcomes these disadvantages, bears molecular resolution and can be pushed further towards atomic resolution by sub-tomogram averaging.

However, none of these techniques are able to depict the full range of spatial information. Hence it is necessary to combine the qualities of the different techniques in a hybrid approach.

In this study we combined three microscopy techniques: light microscopy, to target cells of interest and gain dynamic information on a larger scale but with lower resolution (~200 nm); cryo-FIB/SEM, to precisely prepare electron-transparent lamellas at medium resolution (~20 nm), guided by correlation with the targeting information of the LM data; and cryo-electron tomography (cryo-ET) to visualize the three-dimensional intra-cellular architecture in high resolution (~1 nm).

Tomography is ideally suited to investigate biological questions and provides unprecedented insights into the 3D-organization of cells in their native state on the structural level at molecular resolution.

## 2.2 THE TRANSMISSION ELECTRON MICROSCOPE (TEM)

Transmission electron microscopy was developed by Ernst Ruska and Max Knoll in the early 1930s (Knoll and Ruska, 1932). The first prototype proved a resolution greater than light in 1933 and the first commercial TEM was produced under Ruska's guidance at Siemens in 1939. In 1986 Ernst Ruska was awarded with the Nobel Prize in physics for the development of transmission electron microscopy. TEM images are 2D projections of the three-dimensional sample. The grey scale image can be directly interpreted as the intensity of the transmitted electrons through the sample at the corresponding position with full amplitude and phase information.

This section should give an overview on the essential components of the TEM: the electron source, a lens system with apertures, the energy filter and finally the detector.

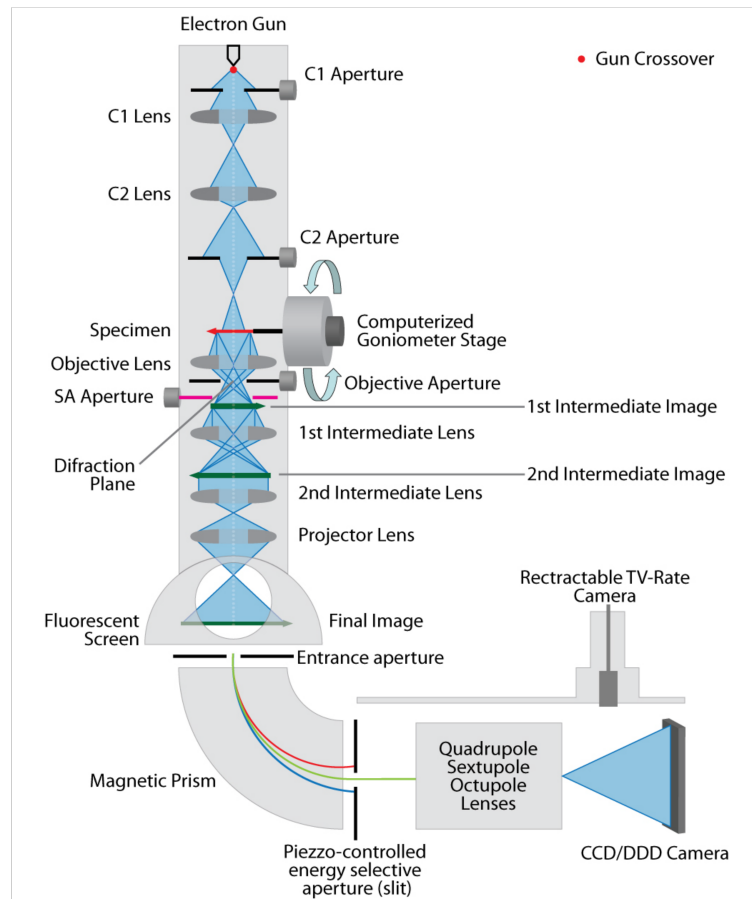


**Figure 2.2: The Transmission Electron Microscope**

Schematic representation of a transmission electron microscope. The electron beam is indicated in blue, generated by the electron gun, then passing through a lens and aperture system. For tomography, the sample is tilted in the goniometer stage. The post column energy filter reduces the chromatic aberration by filtering out inelastically scattered electrons. The image is detected by the detector – a CCD or preferentially a direct electron detector (DDD). (from Kochovski 2014, with permission)

At atmospheric pressure ( $10^3$  mbar), the mean free path of gas molecules is about 60 nm, which would lead to the scattering of all electrons before they would have reached the sample. Thus the gas pressure needs to be lowered substantially in the electron microscope: in a final vacuum of usually  $10^{-7}$  to  $10^{-9}$  mbar, the mean free path<sup>5</sup> is 0.6-60 km.

### Electron Source

The electron source is a crucial element of the TEM: it is required to produce an electron beam that is of high brightness as well as high temporal and spatial coherence. The brightness of the electron source is reliant on the current density. The coherence of the electron-beam correlates with the resolution-limit. The temporal coherence length  $\lambda_c = v\hbar/\Delta E$  with velocity  $v$  depends on the energy spread (= chromatic aberration), which should be minimal for high temporal coherence. The spatial coherence  $d_c = \lambda/2\alpha$  on the other hand depends on the aperture angle  $\alpha$  of the source.

Two types of electron-sources are used in TEM: field emission guns (FEG) and thermionic electron guns.

The FEG is a modern type electron source that is typically used and is superior to the classical thermionic electron guns in all qualities: the gun brightness is  $10^2$ - $10^3$  higher and the energy spread is 0.2-0.7 eV versus 1-2 eV. The conduction electrons in metals or compounds have to overcome the work function to be emitted into the vacuum. For thermionic electron guns, this is reached by heating the source to 1400-2000 K. FEG sources can be operated at room temperature (300 K) because of a very strong electrical field ( $10^9$  V/m) of the highly curved tungsten tip (0.1  $\mu\text{m}$  curvature), so that electrons can quantum-mechanically tunnel from the metal into the vacuum.

### Lens system, Apertures and Specimen Stage

The electrons are accelerated up to 300 kV and a series of electromagnetic lenses and apertures guide the beam down the microscope axis to form a defined illumination of the sample area. The strength of the electromagnetic lenses is tuned by the amount of current in the lens coil, creating a magnetic field deflecting the electrons to magnify or focus the beam. Typically, two condenser lenses (C1 and C2) and corresponding apertures are used in TEM, to optimize illumination: The Titan Krios FEG (Thermo Fisher Scientific), which was used in this study, is equipped with a third condenser lens (C3) to ensure an ideal parallel illumination of the specimen.

The specimen is installed on the sample-stage, a goniometer, to subsequently tilt the sample for tomographic acquisition. The EM-grid is grabbed by a cooled grid-gripping arm that allows additionally to rotate the sample around its  $z$ -axis.

After the beam has interacted and passed the sample, the objective lens focuses the beam in the back focal plane, where either the objective aperture filters out highly scattered electrons that would contribute to noise, or instead a Volta phase plate is positioned to create an additional phase shift that causes phase contrast.

Hereafter the beam is magnified by intermediate lenses and the projection lens to the final magnification and can be displayed on the fluorescent phosphor screen for revision or finally on the detector.

---

<sup>5</sup> Calculated for nitrogen by  $MFP = k_B T / \sqrt{2} \pi p d_m$ . (Edelmann, 1988, p. 38)

### **Energy Filter**

Inelastically scattered electrons are relevant noise contributors (this will be discussed in detail in the section “Electron-sample Interactions”) – their scattering angles are rather small, so that the objective aperture is not blocking these. Thus a post column energy filter is used to identify electrons with an energy loss and filters them out to improve amplitude contrast. The essential part of this filter is a prism spectrometer (Reimer and Kohl, 2008) that deflects electrons of different energies to different locations on the ‘energy dispersive plane’. With a slit in this plane, electrons of a defined energy range can be selected and the rest is blocked. In the ‘zero-loss mode’ electrons with a range of 10-20 eV around the acceleration energy of 80-300 kV are selected for detection, filtering out most of the relevant inelastically scattered electrons (see **Figure 2.5**).

### **Detectors**

Finally, the image needs to be recorded to further process it. In the beginning of electron microscopy photographic film was used to detect the image formed by the electron beam. In 1986 CCD cameras were first explored in electron microscopy (Mochel and Mochel, 1986) and became commercially available in the early 1990s (Krivanek and Mooney, 1993) for the cryo electron microscopy field. They were an attractive alternative to film, since they made the images readily available for data acquisition and analysis. No time consuming handling of the photographic film (~2d for film development and scanning of a tilt-series) was necessary.

## 2.3 CRYO-ELECTRON MICROSCOPY

### AQUEOUS NATURE OF BIOLOGICAL SAMPLES

Biological samples are intrinsically aqueous and the liquid water content is not compatible with the vacuum of an electron microscope. In classical transmission electron microscopy (TEM) this problem is often solved by chemical fixation, dehydration and resin embedding of the cells or tissue. Additionally, samples are stained with heavy metals to increase contrast. All these procedures are very likely to induce structural artifacts that are not compatible with high resolution imaging of biological samples, as they cause the removal of the hydration shell of cellular components and denaturation of proteins.

### THE IDEA OF CRYO-ELECTRON MICROSCOPY

By way of contrast, in cryo-electron microscopy cells are kept in their aqueous environment. To prevent the water from evaporation in the microscopes vacuum, physical fixation through very rapid freezing ( $10^4$ - $10^5$  K/s) results in the formation of amorphous ice (Moor, 1964; Moor and Riehle, 1968; Riehle and Höchli, 1973). This process is called vitrification and transforms liquid water into a glass-like solid body, without water molecules reorganizing into crystals. The latter would damage and/or distort biological structures due to the volume expansion as well as the exclusion of solvents and cause imaging artifacts. On the other hand, vitrification preserves cellular samples in a close to native state, fully hydrated, unstained, with halted Brownian motion and therefore allows high resolution imaging at molecular resolution.

Cellular structures are well preserved in their physiological state, shape and conformation when properly vitrified – in contrast to all classical fixation methods that strongly alter the structure on the molecular level.

### VITRIFICATION OF BIOLOGICAL SAMPLES

While vitrification, molecules lose their translational and rotational freedom and a liquid becomes an amorphous solid without the molecules arranging into a crystal lattice (glass transition). Vitreous ice is a type of ice that is not found on earth naturally, but only occurs in extraterrestrial space when water vapor freezes on very cold surfaces. Vitrification means in practical terms that the Brownian or any energy-dependent motion – of the biological sample, which is in its physiological, aqueous environment – are halted instantaneously in a millisecond timeframe. The diffusion coefficient<sup>6</sup> of water is reduced over ten magnitudes from liquid water at 25 °C to -150 °C (Smith et al., 2000) and is modeled to decrease further below the glass transition temperature of ~137 °C (Debenedetti, 2003). The heat of the specimen needs to be transferred through its surface into the cryogen.

---

<sup>6</sup> The Stokes-Einstein-Stokes relation  $D = \frac{k_B T}{6\pi\eta r}$  shows that the dynamic viscosity  $\eta$  is indirectly proportional to the diffusion coefficient  $D$ . That means that with a decreasing diffusion coefficient, the viscosity of water increases over 10 magnitudes and more upon vitrification.

The sample thickness is critical, as the heat transfer rate decelerates hyperbolically with increasing depth:

$$\frac{dQ}{dt} = \lambda \cdot A \cdot \frac{dT}{dx}$$

(Q: Heat, t: time,  $\lambda$ : thermal conductivity, A: Area, T: Temperature, x: distance).

Amorphous ice, kept below  $\sim 136$  °C, is in a metastable state (DeBenedetti, 2003; Watanabe and Kouchi, 2008). Heating the sample to warmer temperatures (devitrification) will cause a first order phase transition to crystalline ice, which strongly diffracts electrons obliterating the biological information and causes a volume expansion and distortion of cellular structures. (However imperfect vitrification vs. devitrification is not so obvious, since ice crystals have less time to grow.) Hence it is crucial that vitrified samples are kept well below 136 °C.

Several vitrification methods have been explored in the past: plunge-freezing (Dubochet and McDowell, 1981) is the gold-standard for single cells or protein solutions, and high-pressure freezing (Moor and Riehle, 1968) is often used for tissues. Slam-freezing (Harreveld et al., 1965; van Harreveld and Crowell, 1964) as well as propane-jet freezing (Moor et al., 1976; Müller et al., 1980) should only be mentioned here, since they play only a minor role in modern cryo-EM.

## PLUNGE FREEZING

Plunge freezing is the most widely used vitrification-method in the field of cryo-electron microscopy. Cells are seeded on EM-grids in culture medium (**Figure 2.3A**). For vitrification, excess medium is removed by blotting the EM-grid to minimize the thickness of the sample (**Figure 2.3B**).

In the plunge freezing process the sample is immersed into a cryogen to freeze it rapidly (**Figure 2.3C**). Cooling rates<sup>7</sup> of  $10^4$ - $10^5$  K/s are necessary to immobilize water molecules quick enough, in order to reach the glass transition temperature before nucleation occurs (Moor, 1964; Moor and Riehle, 1968; Riehle and Höchli, 1973). Typically, either ethane or propane is used as a cryogen, cooled to slightly above its freezing point ( $-183$  °C and  $-188$  °C respectively). We used an improved cryogen: a eutectic mixture of propane (63%)/ethane (37%) (Tivol et al., 2008) that is liquid at  $-196$  °C – the boiling point of LN<sub>2</sub>.

---

<sup>7</sup> In this chapter, temperatures are indicated in °C and to clearly distinguish T-differences or cooling-rates - these are indicated in K.

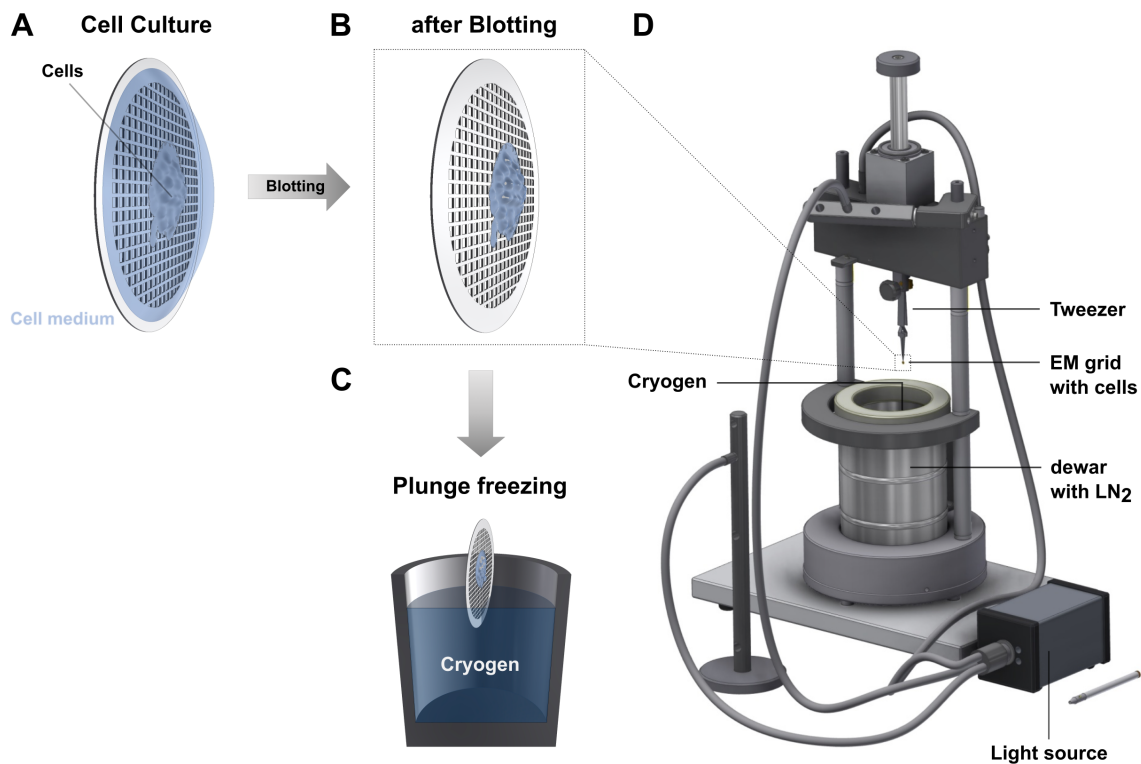


**Figure 2.3: Plunge Freezing**

**A:** EM grid (gold,  $\varnothing$  3 mm) with attached cells, in medium. **B:** The EM grid of (A) after blotting – here most of the medium is removed, so that only a thin film of water remains, surrounding the cells. **C:** Immediately after blotting, the grid is immersed into the cryogen. **D:** The cryo Plunger 2010 (designed in the Baumeister Dept.). The grid is held in place with a tweezer for blotting in place. For subsequent plunging, a magnetic switch releases the gravity propelled movement, that immerses the grid into the cryogen. The cryogen is a eutectic mixture of propane (63%)/ethane (37%) (Tivoli et al. 2008) that is cooled by liquid nitrogen at  $-196^{\circ}\text{C}$ . (illustrated by Tim Laugks, with permission)

Plunge freezing is well established for the vitrification of thin films of water containing proteins for single-particle analysis and also extensively used to vitrify pro- and eukaryotic cells. That pure liquid water can be vitrified ( $\sim 1 \mu\text{m}$  thickness) was shown for the first time 37 years ago (Brüggeller and Mayer, 1980; Dubochet and McDowell, 1981). Due to the molecular crowding in cells, the cryoprotective potential of these macromolecules lead to the expectation that substantially thicker volumes of cytosol ( $\sim 10 \mu\text{m}$  thickness) can be vitrified as pure water (Dubochet et al., 1988).

## HIGH-PRESSURE FREEZING

The idea behind high-pressure freezing is the principle of Le Chatelier: water increases its volume by 8-9% while freezing. High pressure opposes this expansion, and thus crystallization is hindered. This idea is explained by the phase diagram of water (**Figure 2.4**): at 2099 bar the freezing temperature of water reaches a minimum with  $-22^{\circ}\text{C}$ , lowering the temperature-difference to the glass-transition temperature by 16%. Liquids can be super-cooled below their freezing point, remaining liquid if no nucleation sites are present. This is possible till a temperature where the whole sample will homogeneously crystallize, known as the homogenous nucleation temperature ( $T_{\text{H}}$ ). The most critical

phase for ice crystal formation is between the  $T_H$  and the glass transition temperature. At normal pressure the temperature-difference that needs to be overcome till glass transition are 95 K with a  $T_H$  of  $-41^\circ\text{C}$  (Moore and Molinero, 2011). Interestingly,  $T_H$  at 2099 bar is reduced to  $-92^\circ\text{C}$ , which lowers the temperature difference to just 44K. If the cooling rate is high enough, samples of thicknesses between 100-300  $\mu\text{m}$  can be vitrified at high pressure.

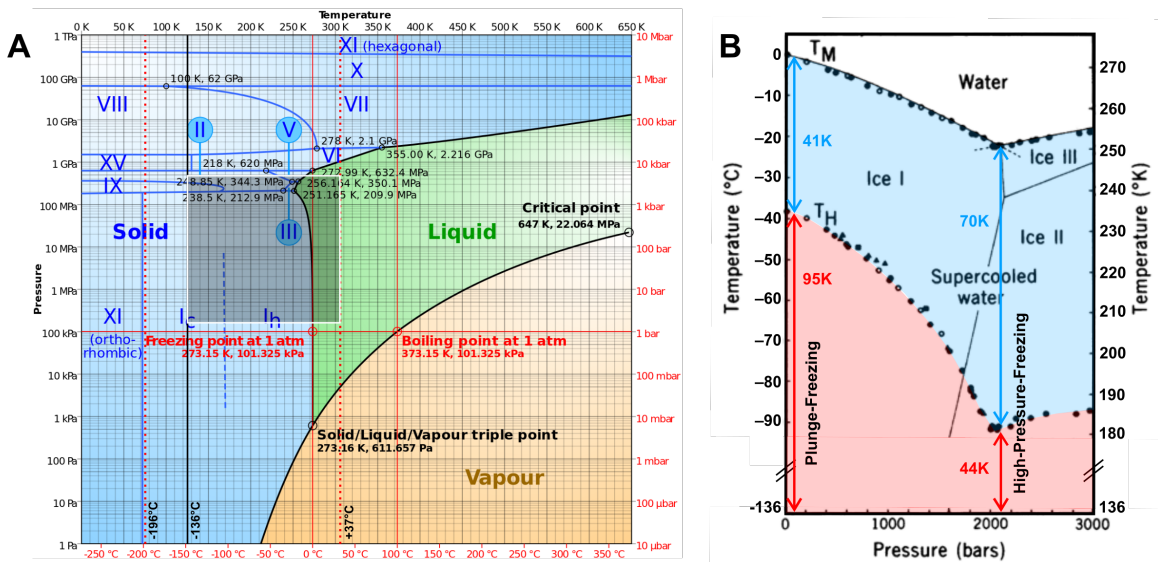


**Figure 2.4: Phase diagram of water**

**A:** Phase diagram of water ranging from 0-650 K temperature and  $10^{-5}$ - $10^7$  bar pressure. The red dotted lines indicate physiological temperature at  $+37^\circ\text{C}$  and LN2 boiling point at  $-196^\circ\text{C}$ . The solid black line indicates the glass transition temperature of water at  $-136^\circ\text{C}$ . The grey boxed region is magnified in (B). (modified from (Zhang et al., 2015), with permission) **B:** Magnification of the grey boxed region in (A), to visualize the vitrification process for plunge-freezing and high-pressure freezing (notice that the axes are switched). Plunge-freezing is the rapid cooling of the specimen at atmospheric pressure (1 bar) below the glass transition temperature at  $-136^\circ\text{C}$ . High-pressure freezing is performed at 2099 bar.  $T_M$  is the melting temperature and  $T_H$  is the homogenous crystallization temperature. Below the  $T_M$  water can remain liquid in a super-cooled state (blue marked region). Below the  $T_H$  the sample will start to homogeneously crystallize (red marked region). Notice the remarkable drop of the  $T_M$  and specially the  $T_H$  at 2099 bar. (modified from (Kanno et al., 1975), with permission)

## CHALLENGES OF CRYO-EM

### Dose-Limitation

In most imaging techniques contrast-formation is based on the interaction of the incoming radiation (electrons or light) with the sample. Consequently, an increasing radiation dose can be expected to improve the contrast. The interactions with the sample can be elastic or inelastic. In the latter case for TEM the energy of the incident electrons is deposited in the sample and causes radiation damage.

In biological TEM the incoming electrons have an energy of 80.000-300.000 eV and the main energy loss ranges around only a few tens eV (Figure 2.5C). But this deposited energy suffices to break ionic and covalent bonds (radiolysis), since their binding energy is in the mentioned range, and also to heat the sample, if the dose rate exceeds its heat dissipation. Radiolysis of especially organic compounds



leads ultimately to the formation of hydrogen-gas filled cavities (Leapman and Sun, 1995) that appear as “bubbling” effect in the TEM and locally destroy and deform the sample (Karuppasamy et al., 2011; Meents et al., 2010). Heating of the sample due to a high electron dose rate ( $\sim 50 \text{ e}/\text{\AA}^2 \text{ s}^{-1}$ ) can cause ice crystallization (Karuppasamy et al., 2011). These effects caused by inelastic scattering lead to a strong limitation of the acceptable electron dose for biological samples.

This prevents improving contrast substantially by simply increasing dose. Cooling of the sample not only prevents the water from evaporation in the vacuum, but also slows down radiation damage – better at liquid nitrogen temperature at 77 K than Helium at 4 K (Bammes et al., 2010). The upper bound of the acceptable electron-exposure for cryo-electron tomography at 300 keV electron energy can be roughly accounted to greater than  $200 \text{ e}/\text{\AA}^2$ , which is the equivalent to a dose of  $\sim 200 \text{ MGy}$ <sup>8</sup>. At higher doses, the ionization of organic molecules typically causes the formation of hydrogen (Leapman and Sun, 1995), that accumulates in gas-cavities (gas-bubbles) in the specimen, causing local deformations. This effect depends on the composition and thickness of the sample and can already appear at much lower doses, for example in the case of prokaryotes at around  $110 \text{ e}/\text{\AA}^2$  (Comolli and Downing, 2005). However, it has to be considered that structural damage on the molecular scale already occurs with doses  $> 20\text{-}30 \text{ e}/\text{\AA}^2$  (Baker et al., 2010; Owen et al., 2006). Among other features of radiation damage, it leads to the destruction of high resolution features like amino-acid side chains as well as the blurring of macromolecules. But these radiation damage effects are only relevant, when it is the intention to average structures in the tomogram. If the foremost aim is instead to interpret structures in their cellular context and not to average sub-tomograms for high-resolution approaches, electron exposures of  $100\text{-}150 \text{ e}/\text{\AA}^2$  can result in high quality tomograms. Due to the radiation sensitivity of frozen hydrated specimens, the electron exposure needs to be limited and a low-dose scheme is essential.

### Contrast

Besides resolution, contrast is the main property of an image to recognize structures. In cryo-electron microscopy the contrast suffers from the low signal-to-noise ratio due to the limited electron-dose that is acceptable.

Contrast is generated in two distinct ways: on the one hand there is amplitude contrast that is achieved by attenuating the amplitude of the electron-beam, by removing inelastic scattered electrons with an energy filter. On the other hand, there is phase contrast that has its origin in the phase-shift of the electrons’ wave function while being elastically scattered in the sample. Inelastic scattering rather contributes to noise (in the absence of chromatic aberration correction), whereas elastic scattering carries valuable information. Amplitude contrast is very weak for biological samples and in classical electron microscopy, heavy-metal staining is used to increase the amplitude contrast - but this is not compatible with high-resolution imaging. In total, amplitude contrast accounts only 14% of that due to phase contrast (Langmore and Smith, 1992). Thus, only the use of phase contrast bears further structural information. It can be achieved by negative defocusing, that implies phase contrast but with the disadvantage of loss of resolution.

---

<sup>8</sup> Natural radiation per year:  $2 \cdot 10^{-9} \text{ MGy}$ ,  $\text{LD}_{50}$  for human radiation poisoning  $4.8 \cdot 10^{-6} \text{ MGy}$

## ELECTRON-SAMPLE INTERACTIONS AND THE CONTRAST TRANSFER FUNCTION

The intensity differences between different regions of the image, respectively the contrast are caused by interactions of electrons with the sample. Two types of interactions can be distinguished (**Figure 2.5A**): inelastic scattering, where electrons deposit energy in the sample and contribute to noise, and elastic scattering, where the incident electrons keep their energy, but shift their phase and thus carry valuable information.

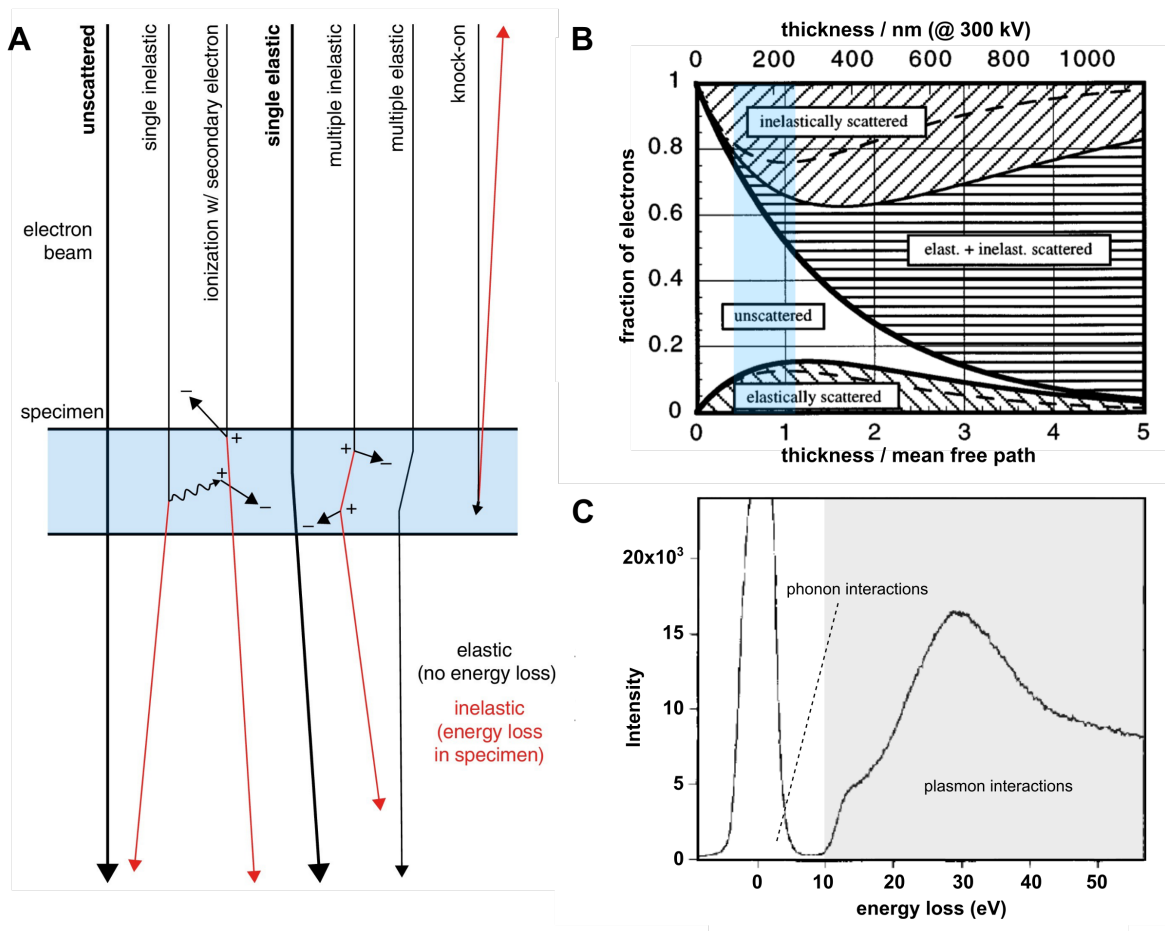


**Figure 2.5: Electron-energy histogram**

**A:** Diagram of high-energy electron scattering in a thin layer of ice, with types of events shown in order of decreasing probability from left to right. Only the unscattered and single elastic scattering events (bold) contribute to typical phase contrast imaging; the remainder damage the specimen (inelastic) or contribute noise to the image. The relative probability of these events is described by their scattering cross sections (further explained in the text). (for details, see (Russo and Passmore, 2016)) **B:** Distribution of scattered electrons for vitreous ice over the elastic (lower diagonally hatched area), inelastic (upper diagonally hatched area), and mixed (horizontally hatched area) scattering channels for vitreous ice as a function of thickness (in multiples of the total mean free path and, for 300 kV, in nm). The dashed lines mark fractions of single (elastic or inelastic) scattering. The light blue area indicates the typical thickness range of FIB-prepared lamellas. (modified from (Koster et al., 1997)) **C:** Energy-loss spectrum of electrons with 80 keV incident energy transmitted through a layer of vitreous ice about 140 nm thick through an objective aperture. In 'zero-loss' mode, electrons with higher energy loss can be filtered out (grey region), that only the 'zero-loss' peak is used for imaging. (modified from (Langmore and Smith, 1992), with permission)

### Elastic Scattering

When incoming electrons are deflected electrostatically by the Coulomb field of an atoms nucleus, the energy state and momentum of the electron are conserved so that this process represents an elastic scattering (**Figure 2.5A&B**). This interaction is the most important aspect that contributes to contrast in biological cryo-EM.

The total cross section for the elastic scatter process is defined by (Reimer and Kohl, 2008):

$$\sigma_{el} = \frac{h^2 Z^{3/4}}{\pi E_0^2 \beta^2} \propto Z^{4/3}$$

The incoming electron follows a hyperbolic trajectory caused by the attractive force between the electron and the nucleus. These electrons experience a phase shift unlike the unscattered ones while interacting with the nuclear Coulomb field. In the image plane, the superposition of the elastically scattered and thus phase-shifted electron-waves interfere with unscattered ones and thus create phase-contrast. The intensity of the image is then governed by constructive or destructive interference of the electron waves that is furthermore dependent on the frequency of the imaged object. Typical for biological samples, the low  $Z$  environment determines these to be weak phase objects with a phase shift of  $90^\circ$  ( $\pi/2$ ), that results in a minimal change of the amplitude of the superimposed waves and consequently also the intensity. The objective lens is in charge of focusing and responsible for transferring the contrast to the resulting image. This is described by the ‘contrast transfer function’ (CTF):

$$CTF(k, \Delta z) = -2\sin\left[\pi\left(-\Delta z\lambda k^2 + \frac{1}{2}C_s\lambda^3 k^4\right)\right]$$

The CTF depends on two parameters: the spatial frequency  $k$  and the defocus  $\Delta z$ . Two constants are defined by microscope characteristics –  $C_s$ , the spherical aberration of the objective lens and  $\lambda$ , the electrons wavelength determined by the acceleration voltage ( $\lambda=1.97$  pm @ 300 kV). The CTF describes, how defocusing induces additional phase shift. **Figure 2.6** demonstrates how the contrast is transferred by the microscope to the detector and visualizes the dependency on the defocus.

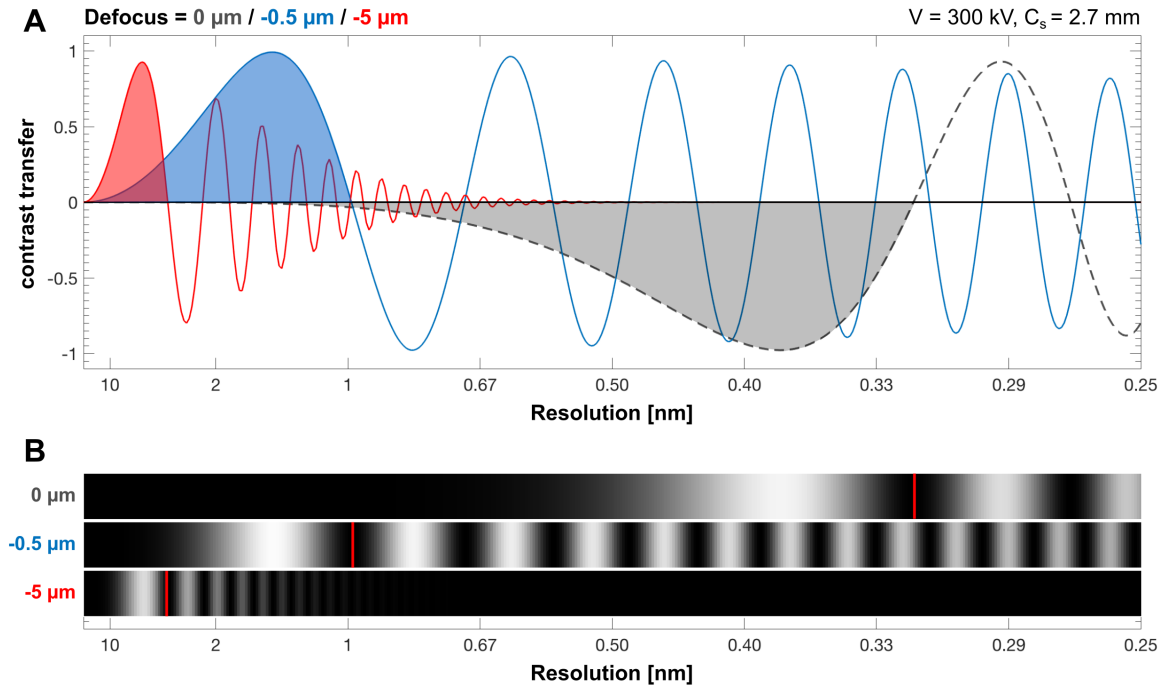


**Figure 2.6: Contrast transfer function**

**A:** The contrast-transfer function (CTF) describes how the microscope modifies the real image dependent on the defocus and the spatial frequency. The spatial frequency is in principle the size of an object to be imaged. The CTF is an oscillating sinus-function that transfers the contrast optimally if it is 1, and no information is transferred when the CTF crosses 0. If the CTF becomes negative, the contrast is inverted. The point-resolution (directly interpretable resolution) is defined by the first zero of the CTF, beyond this resolution the contrast oscillates and information is not continuously transferred. Phase contrast can be induced by defocusing. Three defocus values are visualized here: 0  $\mu\text{m}$  (grey), -0.50  $\mu\text{m}$  (blue) and -5.0  $\mu\text{m}$  (red). For 0  $\mu\text{m}$  defocus (grey area) low frequencies are almost completely lost and mainly high frequencies are transferred, what causes a strongly blurred image. Increasing defocus improves the contrast for low frequencies (blue and red areas) but with the disadvantage of the loss of resolution. This is due to an intensified dampening of the CTF for higher frequencies – well visible for the red curve ( $\Delta f$  -5.0  $\mu\text{m}$ ) – here the oscillations vanish quickly. **B:** The probability of the information transfer is visualized here as an intensity scale (0...1 equals black...white) in relation to the spatial frequency. Frequencies with a white or grey tone are transferred, while in black regions the information is lost. The big information loss of low frequencies for 0 defocus explains the unfavorable image quality. The red lines indicate the point-resolution limit that decreases with increasing defocus: 0.32 nm / 1.0 nm / 3.1 nm for defocus values of 0  $\mu\text{m}$  / -0.50  $\mu\text{m}$  / -5.0  $\mu\text{m}$ .

As mentioned earlier, temporal and spatial coherence determines the resolution limit: temporal and spatial incoherence diminish resolution by amplifying the exponential decrease of the CTF for higher frequencies – the temporal and spatial coherence envelope functions  $E_t$  and  $E_c$ .

$$E_t(k) = \exp \left[ -\frac{1}{2} \pi^2 \lambda^2 k^4 C_c^2 \left( 4 \left( \frac{\Delta I}{I_0} \right)^2 + \left( \frac{\Delta V}{V_0} \right)^2 + \left( \frac{\Delta E}{E_0} \right)^2 \right) \right]$$

The temporal-coherence envelope function  $E_t$  depends on the instabilities of the objective lens  $\Delta I/I_0$ , the overall energy spread of the incident electron beam  $\Delta V/V_0$ , the incident electron energy  $\Delta E/E_0$  and the chromatic aberration of the objective lens  $C_c$ , the electrons wavelength  $\lambda$  and the spatial frequency  $k$ .

$$E_c(k) = \exp \left[ -\frac{(-\pi\Delta z k + \pi C_s \lambda^2 k^3)^2 \alpha_i^2}{\ln 2} \right]$$

The spatial-coherence envelope function  $E_c$  depends on the spherical aberration  $C_s$ , the illumination aperture  $\alpha_i$  and the defocus  $\Delta z$ . The influence of the defocus on the resolution limit can be seen in **Figure 2.6A**.

### Inelastic Scattering

When incoming electrons interact with the shell electrons of the samples atoms, the excitation of energy states results in energy losses (**Figure 2.5A**) of the incoming electron and thus represents an inelastic scattering process (**Figure 2.5B**). **Figure 2.5C** shows the histogram of the electron energy loss spectrum - three excitation mechanisms (Reimer and Kohl, 2008) can be distinguished:

- **Phonon excitations** cause a minimal  $\Delta E$  of 0.02-1 eV (**Figure 2.5C**). This energy loss is smaller than the energy spread of the electron source and thus can't be filtered out.
- **Plasmon excitations** as well as intra- and interband excitations of outer atomic electrons cause a  $\Delta E$  of a few to several ten eV (**Figure 2.5C**). This is the prominent, critical fraction of inelastically scattered electrons that provokes dose-limiting damage to the sample!
- **Ionization** of core electrons in inner atomic shells are rather rare and cause a  $\Delta E$  of  $\gg 100$  eV (e.g.: C: 277 eV, N: 392 eV, O: 525 eV). This fraction can easily be filtered out, but can also be used due to the characteristic values, for elemental analysis by electron energy loss spectroscopy (EELS).

Disadvantageous of inelastically scattered electrons is on one side the damaging nature, due to the amount of deposited energy and on the other side, the poor localization of this species, that derives from the non-localized plasmon interaction volume. Thus inelastically scattered electrons contribute to noise besides the chromatic aberration effect and need to be removed. While strongly scattered electrons are effectively removed by the objective aperture, the typically small scattering angle of inelastically scattered electrons leaves them unfiltered by this measure. But their energy loss makes them distinguishable from unscattered and elastically scattered electrons and can thus be filtered by a post-column energy filter. The filter can be used in 'zero-loss' mode, in which electrons that differ more than 10-20 eV from their acceleration energy are filtered out.

The total cross section for the inelastic scatter process is defined by (Robenek, 1995):

$$\sigma_{inel} = \frac{1.5 \cdot 10^{-20}}{\beta^2} Z^{1/3} \ln \left( \frac{2}{\theta_E} \right) \propto Z^{1/3}$$

with the atomic number  $Z$ ,  $\beta=v/c$  to correct for relativistic speed and  $\theta_E \approx 13.5 Z/mv^2$ .

Filtering of inelastically scattered electrons causes amplitude contrast, since the amplitude of the incoming electron beam is reduced by blocking these species. In biological specimens, amplitude contrast ultimately accounts only for 14% of that due to phase contrast (Langmore and Smith, 1992).

This results from the low difference of the atomic numbers of the solvent water and the common atoms in biological matter (C, N, O). The dependence of the total cross section for inelastic scattering on  $Z^{1/3}$  explains the low contribution to contrast. Thus the usage of phase contrast has high potential in terms of contrast.

Inelastic scatter processes are the dominating interactions for biological samples due to the low  $Z$  environment. The ratio between inelastic and elastic scatter processes is theoretically described by the simple ratio  $\frac{\sigma_{inel}}{\sigma_{el}} \approx \frac{26}{Z}$  and is experimentally determined to be rather  $\frac{\sigma_{inel}}{\sigma_{el}} \approx \frac{20}{Z}$  (Reimer and Kohl, 2008). This means that in biological samples, with the most relevant interactor, carbon ( $Z=6$ ), inelastic scattering occurs three times more often than the energy-loss free interaction. Meaning on the one hand that for biological specimens, phase contrast is about 20x ( $\sim 3/0.14$ ) more efficient than amplitude contrast (Langmore and Smith, 1992).

## 2.4 CRYO ELECTRON TOMOGRAPHY (CET)

In structural biology, the field of cryo-electron microscopy has two major domains: the single particle analysis (SPA) and cryo-electron tomography (CET).

The intention of SPA is the structure-determination of proteins and some larger biological entities like viruses. A large number (typically  $10^3$ - $10^5$ ) of identical particles, that are ideally randomly oriented in the vitrified sample, are imaged to be averaged, what improves the SNR and reconstructed into a 3D tomogram. Due to the resolution-revolution (Kühlbrandt, 2014a, 2014b) near-atomic resolution are possible (Bartesaghi et al., 2015; Merk et al., 2016). The classical method for the structure-determination of proteins is x-ray crystallography. A great advantage of SPA over x-ray crystallography is firstly the possibility to investigate different conformational states of a protein (e.g.: (Asano et al., 2015)) and secondly proteins can be analyzed, that are not crystallizable.

The aim of CET is the visualization of the unperturbed intracellular landscape with its full complexity at molecular resolution (Baumeister, 2005a). Cellular processes, macromolecules and their interaction as well as pathological conditions can be observed in their native cellular environment. In contrast to SPA, a single individual sample is sufficient to obtain a tomogram. The resolution is about a magnitude lower than in SPA, however recurrent structures in the tomogram can be averaged analogous to SPA by sub-tomogram-averaging (Bartesaghi and Subramaniam, 2009; Förster and Hegerl, 2007) and thus improving SNR and resolution.

### TILT SERIES AND FRAME ALIGNMENT

Electron micrographs are essentially two-dimensional projections of the entire three-dimensional object in the electron-beam due to the large focus depth. Thus, features from different layers are superimposed, making it difficult to interpret these images in their third dimension. Radon published in 1917 the mathematical principle behind tomography (Radon, 1917). The practical implications of the Radon transformation are the following: a series of projections that visualize the object from different angles can be synthesized into a three-dimensional density map. The central slice theorem

describes that each projection is represented as a planar slice in the 3D Fourier transform. Thus reconstructing a tomogram from a tilt-series means filling the 3D Fourier space with a series of planar slices around the tilt-axis, representing the individual projections of the tilt-series (Crowther et al., 1970; De Rosier and Klug, 1968; Hoppe, 1969).

In clinical computer tomography the instrument turns completely around the ‘specimen’ – the patient. In electron microscopy the instrument remains static, but instead the specimen is tilted incrementally under the electron-beam. However, the geometry of the specimen-holder only allows a reduced tilt-range of typically  $\pm 70^\circ$  instead of  $\pm 90^\circ$  and the sample-thickness reduces the tilt-range further to about  $\pm 60^\circ$ . Thus projections are solely available in a certain angle-range and consequently lack some information in space, called the missing wedge. This is causing distortions and especially an elongation of structures in the electron beam axis. A way to gather parts of the missing information is to tilt the sample not only around the x-axis but also around the y-axis, what is termed dual-tilt acquisition (Mastronarde, 1997; Penczek et al., 1995; Taylor et al., 1984).

A tilt-series can be acquired in different schemes (**Figure 2.7**): unidirectional, bidirectional and dose-symmetric, all each with a constant angle increment. A tilt scheme with decreasing angle increments for higher tilts, the Saxton-scheme (Saxton et al., 1984), was proposed to reduce resolution-anisotropy, which occurs due to increasing sample thickness at higher tilt angles. However, a constant angle increment between the different tilts appeared to perform better in the presence of noise.

Crowther defined the maximum reachable resolution  $d$  (Crowther et al., 1970) by:

$$d = \frac{\pi D}{N} = \Delta\alpha \cdot D$$

This relationship shows that, in order to reconstruct a particle of diameter  $D$ , the resolution ameliorates with the increasing number of projections  $N$ , equivalent to a smaller angle increment  $\Delta\alpha$ . However, this definition applies only for cylindrical objects over a full tilt-series ( $\pm 90^\circ$ ). It does not account for limiting factors like noise, the missing wedge and the dose-dependent resolution-impairment, but it emphasizes the importance of a fine-spaced angle-increment.

Since the applicable dose is limited, before radiation damage becomes relevant, the entire dose needs to be distributed over the full tilt series. Fortunately, the signal-to-noise ratio of the resulting tomogram does not differ from a single projection, if it is acquired with the same cumulative dose. Additionally, it offers the major advantage of the third dimension. This was proven by (Hegerl and Hoppe, 1976) and is known as the dose fractionation theorem.

Several software packages were developed to setup and control an automated acquisition scheme, including SerialEM (Mastronarde, 2005), TOM Toolbox (Nickell et al., 2005), UCSF Tomography (Zheng et al., 2004) and FEI Xplore3D™ Tomography Suite (Thermo Fisher Scientific).

The electron beam needs to travel a larger distance through the sample with increasing tilt angle. To keep the contribution of each tilt equivalent to the final reconstruction, the signal-to-noise ratio needs to be kept constant. Thus a higher dose needs to be applied for projections at higher tilt angles. It is usual to adapt the electron dose for each tilted projection to  $1/\cos(\alpha)$ . This guarantees control over the maximal electron dose, but this correction does not account for the exponential decay of the beam intensity due to inelastic scattering. With FIB-prepared lamellas the situation is more difficult, as they have a pre-tilt, so that the smallest dose needs to be applied at a stage angle different from  $0^\circ$ . These

problems can be solved by using an alternative option in SerialEM ('keep counts constant') that tries to keep the intensity of the electron beam on the detector constant for all tilts by estimating the expected change in intensity for the following projection.

The goniometer (the sample-stage that controls the sample position) is not performing at a very precise level. Thus the position and the focus need to be controlled and corrected after each tilt increment. To keep the radiation damage minimal in the area of the tomogram acquisition, the tracking (x-y position) and the auto-focusing (z-position) are shifted along the tilt-axis outside the area of the tomogram-acquisition to correct these movement errors.

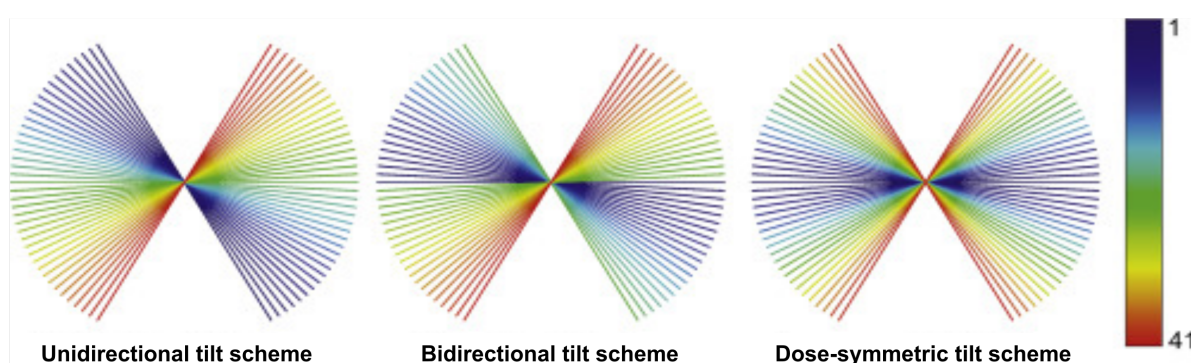


**Figure 2.7: Tilt-Acquisition**

Schematic showing the order in which tilts are collected in unidirectional, bidirectional, and “dual-walkup” tilt schemes. Tilts are shown from 60 to +60 degrees in 3 degree increments for a total of 41 tilts. Grey values/colors correspond to the collection order of each tilt according to the color map shown on the right. When tilts are collected with constant exposure times, the tilt order is directly related to the accumulated electron dose on each image. The unidirectional tilt scheme shows a linear sweep from one angular extreme to the other. The bidirectional tilt scheme shows a discontinuity, when the tilt-increment direction is changed. The dual-walkup tilt scheme shows a near-symmetric accumulated electron dose. (from (Hagen et al., 2017), with permission)

A resolution- and sharpness-limiting factor is drift and beam-induced movements of the sample, causing a smearing of the image while the several seconds lasting exposure. A big advantage of the direct detectors is the ability to fractionate the dose on multiple shortly exposed micrographs (“frames”), that can be aligned afterwards to reduce motion-induced artifacts, what explicitly improves the resolution and sharpness of the resulting image.

Every individual projection of the tilt-series is thus acquired in a stroboscopic way also called frame-movie, in which the several seconds lasting exposure is subdivided in ~200 ms short frames. For each tilt-projection these frames can be aligned and the integration of the noisy frames then results in a sharper image.

## TOMOGRAM RECONSTRUCTION

The so acquired tilt-series of projections need to be reconstructed into the desired three-dimensional density map – the tomogram. For reconstruction, the individual projections of the tilt-series need to be well aligned to each other, that the back-projection of the same structure coincides in the same spot. The conventional approach uses spherical nanometer-sized gold-beads, which are suspended with the



sample and are used to align the individual projections. However, these gold markers have not been successfully delivered into a cell so far and are thus almost exclusively suitable for prokaryotic cells or the very periphery of a larger cell, but not for deep intracellular investigations like in this study. The alternative approach is using structural features of the sample itself to align the projections – this is called ‘patch tracking’ in SerialEM – here, the image is divided in overlapping sub regions (patches), and the tilt-series is correlated in each patch separately (Castaño-Díez et al., 2007).

The aligned projections need to be transformed into 3D space. The most commonly used algorithm in cryo-electron tomography is currently the weighted back-projection (WBP) (**Figure 2.8A**). A simple back-projection would result into a very blurry reconstruction (**Figure 2.8B**). This is due to an overestimation of low frequencies, while higher frequencies are underestimated. This problem can be prevented by the application of a filter in Fourier space that down-weights the contribution of low frequencies – this is the weighting in the WBP – developed almost 50 years ago (Bracewell and Riddle, 1967; Crowther et al., 1970; Gilbert, 1972) (**Figure 2.8C**).

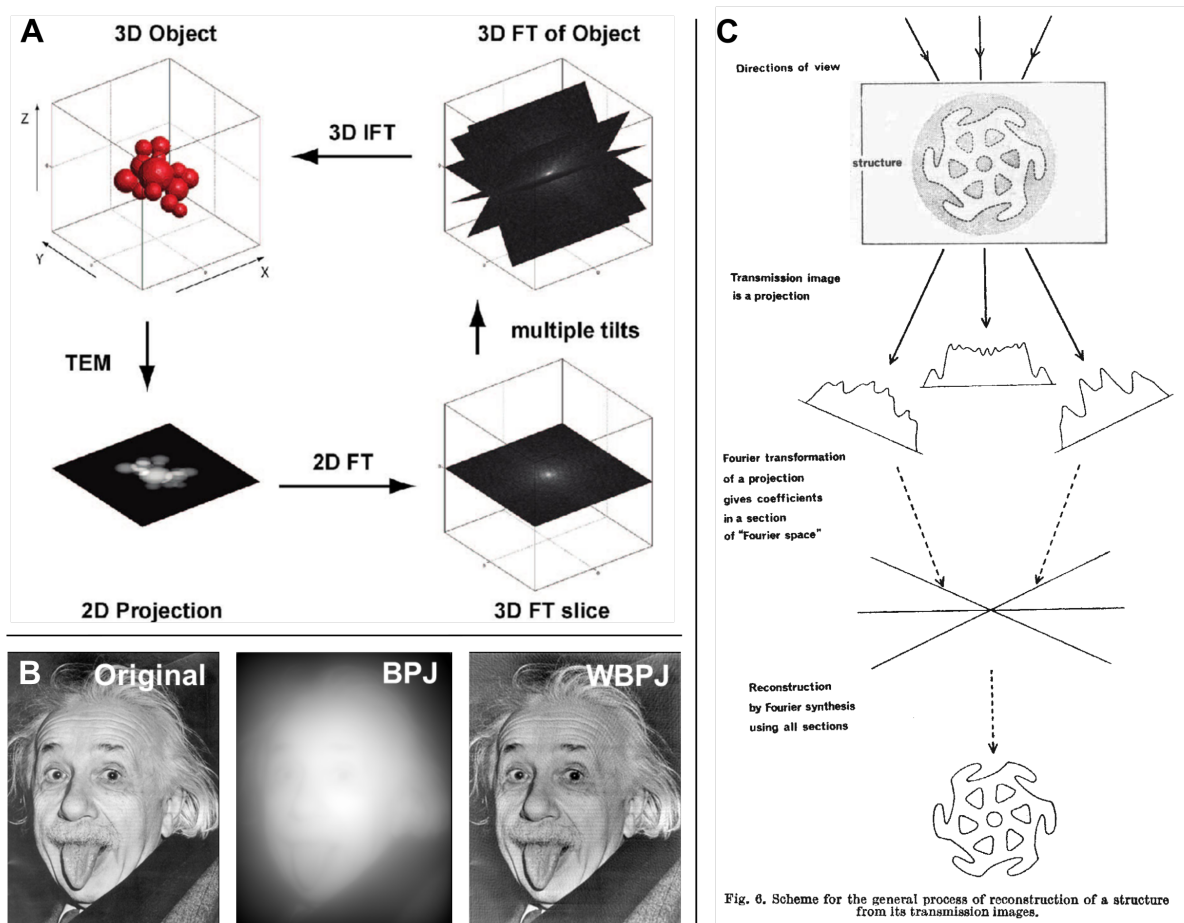


**Figure 2.8: Reconstruction**

**A:** Reconstruction scheme using the Projection-Slice theorem. FT denotes the Fourier transform, and IFT denotes the inverse Fourier transform. By combining projections recorded at multiple tilts around the x-axis, the 3D FT of the object is probed. An inverse Fourier transform then reconstructs the 3D object. (from (Friedrich et al., 2009) , with permission) **B:** Visualization of a simple back projection (BPJ) from the original, versus a weighted back-projection, showing an explicit improved result. (modified from <https://www.int.kit.edu/1731.php>) **C:** Original figure from DeRosier and Klug (De Rosier and Klug, 1968) explaining the reconstruction shown in (A).

## 2.5 CRYO-FOCUSED ION BEAM TECHNOLOGY (CRYO-FIB)

### THICKNESS-LIMITATION IN TEM

The main limitation of cryo-ET is the thickness of the sample. With today's intermediate-voltage electron microscopes, high-resolution data can only be acquired with a sample thickness below 500 nm – ideally in a range of 100-250 nm. Since eukaryotic cells are typically about a magnitude thicker, most of the cell's volume is inaccessible by cryo-ET. Imaging between 500-1000 nm is still possible in principle, but the fraction of electrons – of the anyway limited dose – drops in this range quickly to a few percent, since the vast majority of electrons were scattered inelastically in the sample and thus can't be used for imaging. At the same time the amount of beam-damage rises higher than the amount of electrons that are lost.

This means that only very peripheral regions of eukaryotic cells that are thin enough could be acquired by cryo-electron tomography. Key to overcome this limitation is a sufficiently thin preparation of the sample.

#### **The classical approach: CEMOVIS**

An earlier approach to solve the thickness problem used cryo-ultramicrotomy (Al-Amoudi et al., 2005; Hsieh et al., 2006; McDowall et al., 1983) to create 50-200 nm thin sections of the sample: this strategy is called “cryo-EM of vitreous sections” (CEMOVIS). CEMOVIS suffers from major artifacts due to the mechanical cutting-forces, such as compression (>30%), scatter and knife marks. Artifacts that distort irregularly the cellular structures in the resulting sections. Moreover, it is not possible to precisely target and prepare thin sections of a specific region of interest inside single cells. Despite considerable efforts to make cryo-sectioning a routine technique, it remained a challenge to its practitioners to prepare and handle these sections, especially the thermal and electrical contact on EM-grids in the cryo-TEM.

#### **Opening Windows into the Cell: Cryo-FIB**

A pioneering work from (Marko et al., 2006) showed the proof-of-principle that a new non-mechanical approach - using a focused-ion-beam - can be used to prepare thin vitreous sections in prokaryotes. In 2009 we developed the cryo-FIB technology for single cells on EM-grids (Bäuerlein, 2010; Rigort and Bäuerlein et al., 2012) that is now used as a routine preparation-technique for in-situ cryo-TEM studies in eukaryotes and prokaryotes (Arnold et al., 2016; Asano et al., 2015; Böck et al., 2017; Bollschweiler et al., 2017; Engel et al., 2015b, 2015a; Fukuda et al., 2017; Hagen et al., 2015; Jasnin et al., 2016; Mahamid et al., 2016; Pfeiffer et al., 2017; Schaffer et al., 2015) as well as in this work (Bäuerlein et al., 2017).

### THE CRYO-FIB INSTRUMENT

The FIB/SEM Dual-Beam Microscope is equipped with an electron-beam (SEM), a focused ion-beam (FIB), a cryo-transfer system, a cryo-stage and a nitrogen-gas cooling-system.

The (SEM) is used to visualize the sample in a nondestructive way: variation of the beam voltage (up to 30 kV) modifies the contrast between EM grid, ice, cells and even intra-cellular structures.

Image-formation in TEM and SEM is fundamentally different: in TEM the electron-beam (80-300 keV) passes widened through the sample - elastic and inelastic scattering of the incident electrons in

the sample is responsible for the contrast (see section 2.2). In SEM the image of the sample is formed by scanning the surface with a focused electron-beam (1-30 keV). Inelastic scattered electrons cause the emission of low-energy secondary electrons ( $<50$  eV) from the k-shell of excited atoms - collected by an Everhart-Thornley detector (a scintillator-photomultiplier system). The amount of emitted secondary electrons depends among other parameters mainly on the surface geometry and thus visualizes the sample surfaces' topography - this is the most common SEM-mode. Elastically scattered electrons that are reflected by the sample are called backscatter electrons (BSE) – another electron-entity to visualize the sample. The contrast here is formed between areas of different chemical composition, since heavy elements backscatter electrons stronger than light elements.

The focused ion-beam (FIB) is used to precisely ablate site-specifically parts of the cell, so that an electron-transparent lamella of the cells' volume remains containing the structure of interest.

FIB-systems typically use a Gallium-source – low beam currents allow imaging of the sample - high beam currents are used to locally sputter material. The impact of the heavy, high-energetic (1-30 keV) ions on the samples surface cause collision cascades, that eject an atom if the cascade reaches the target surface and the energy is greater than the surface binding energy.

With the gas-injection system (GIS), an organometallic platinum compound is deposited on the sample to prevent the successive erosion of the lamella front during milling (Hayles et al., 2007).

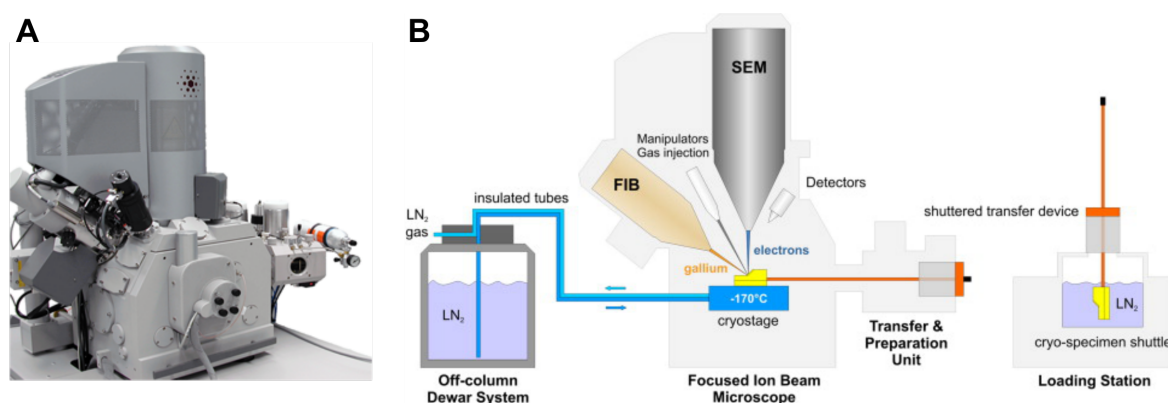


**Figure 2.9:** cryo-FIB/SEM Dual-Beam Microscope

**A:** Photograph of the FEI Quanta 3D FEG SEM/FIB dual-beam microscope used in this study – adapted to cryo-applications. **B:** Schematic representation of the cryo-SEM/FIB microscope in the middle with the electron-beam (SEM), the ion-beam (FIB) and the gas-injection system (GIS). On the left, the Dewar-System, cooling down gaseous nitrogen, that is conducted (vacuum-tight) to the cryostage in the microscope carrying the shuttle with the specimen. In the loading station on the right side, the sample is positioned – under liquid nitrogen (LN<sub>2</sub>) – in the transfer-shuttle, that is introduced into the microscopes vacuum via the transfer & preparation unit. This additionally contains a sputter unit, to apply metallic platinum on the sample for conductivity and compatibility with Volta phase plate imaging. (for details of B, see (Rigort et al., 2012c), with permission)

## THE CRYO-FIB METHOD

**Figure 2.10A** gives a tilted overview of the cellular ‘landscape’ of the entire EM grid - imaged with the ion-beam and the electron-beam (**Figure 2.10B**).

The focused ion-beam has a Gaussian-shaped cross section, meaning that aside from the focus center (in the distribution tails) material is also removed to a lesser extent, but causing a successive erosion of the lamella front. Before starting the FIB-preparation, the sample is covered with an organometallic platinum-compound<sup>9</sup> using a gas-injection system (Hayles et al., 2007), in order to protect the lamella front with a more beam-resistant material.

A cell of interest is then selected and visualized in higher magnification to plan the FIB-milling by the electron- beam (**Figure 2.10C**) and ion-beam (**Figure 2.10D**).

The removal of material with the ion-beam is conducted in three steps, starting with higher beam-currents to speed up the process and continuing subsequently with lower beam-currents to achieve with a high precision:

**1) Rough milling**

In this first step, larger volumes of material are removed with a higher beam-current of 500-1000 pA, but at the same time with lower precision (beam-diameter 35-44 nm). The aim is to remove bulk material quickly, producing a lamella of 2  $\mu\text{m}$  thickness (**Figure 2.10E-G**). The large beam-diameter does not allow the precise production of thin lamellas in the range of 100-250 nm. Therefore, fine-milling is necessary.

**2) Fine milling**

In this step, the 2  $\mu\text{m}$  thick lamella is thinned down to 800 nm with a beam-current of 300 pA (beam-diameter 31 nm). (**Figure 2.10H**)

**3) Polishing**

The polishing step is intended to precisely thin down the lamella to its final thickness of 100-250 nm with a beam-current of 30-50 pA (beam-diameter 17-19 nm). (**Figure 2.10I-J**)

The lower cross section of higher energy electrons (5-10 kV) allows estimating the thickness-profile of the entire thin lamella. Areas with differing thicknesses can now be eventually corrected (**Figure 2.10I**).

---

<sup>9</sup> Trimethyl(methylcyclopentadienyl)platinum(IV):  $\text{C}_5\text{H}_4\text{CH}_3\text{Pt}(\text{CH}_3)_3$  (CAS-No.: 94442-22-5)

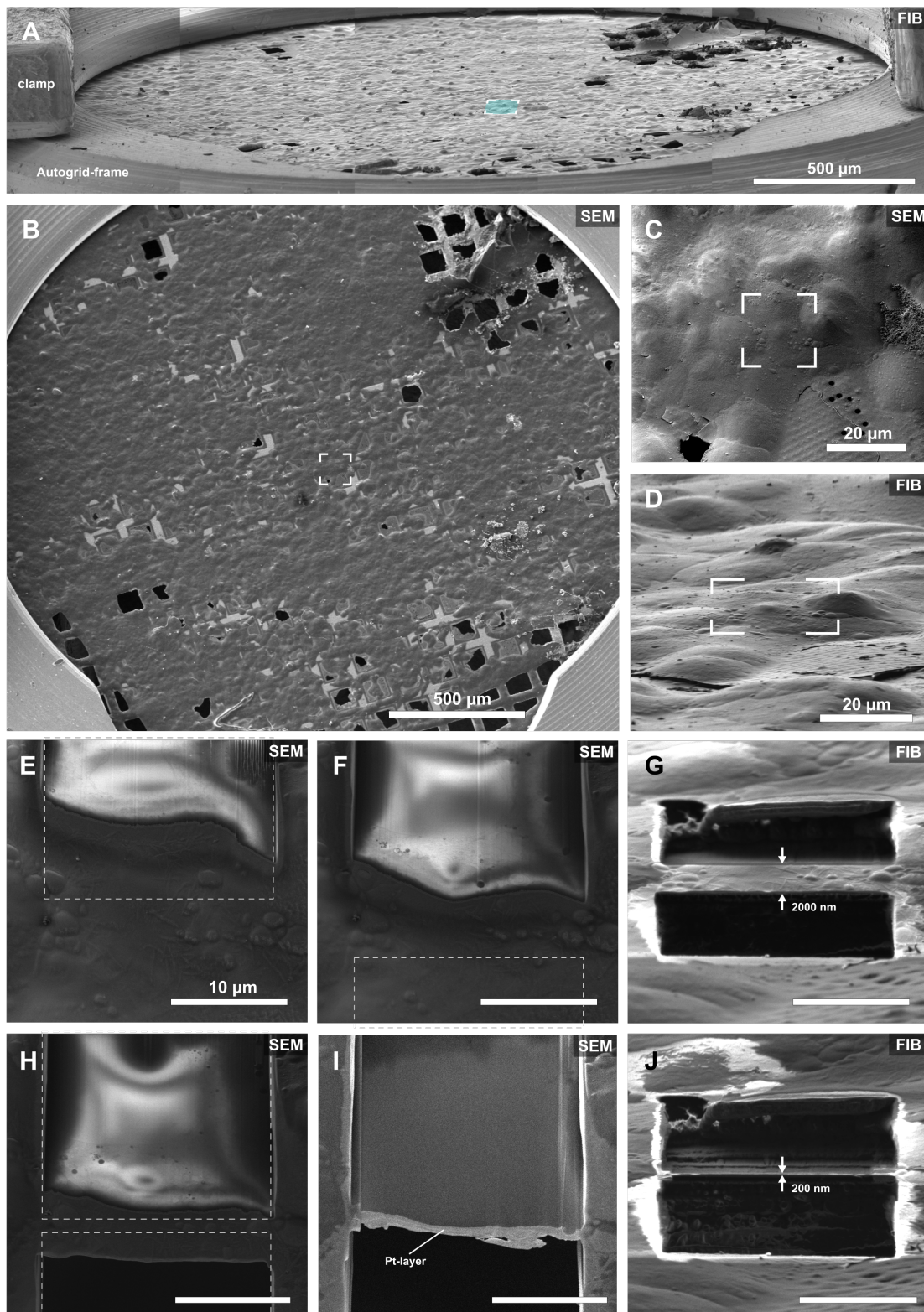


Figure 2.10: Cryo-FIB Technique

**Figure 2.10: cryo-FIB Technique (p. 39)**

**A:** FIB micrograph showing an overview of the entire EM grid under 13° angle of view to the surface. Such low angles are typically used for lamella-preparation. For handling, the EM grid is protected in a modified Autogrid™ and a clamp of the transfer-shuttle is holding it in position. The marked region shows a cell of interest. **B:** SEM-overview of the EM-grid. The boxed region shows the same area marked in (A). **C:** (SEM) – magnification of the boxed region in (B). **D:** (FIB) – The boxed region marks the identical region in (C). **E-J:** FIB-preparation of an electron-transparent lamella through the cell visualized in (C/D). **E:** (SEM) – initial step, ablating the top of the cell boxed in (D) to expose the cytoplasm to screen for the structure of interest. A further layer is planned to be removed by the ion-beam – indicated by the dotted box. **F:** (SEM) – Result after the removal of the layer, indicated in (E). To produce a lamella, now the inferior part of the cell is ablated by the ion-beam – indicated by the dotted box. **G:** (FIB) – Result of the Rough milling step (see text) after the inferior part of the cell was removed. The intermediate lamella is 2000 nm thick and will be further thinned down in the following. **H:** SEM micrograph of the lamella in (G). The dotted boxes summarize the following steps of fine milling and polishing. **I:** (SEM) – Visualization of the final lamella with a higher voltage (5 kV), to prove a homogenous thickness. The bright ribbon in the front is the remaining organic Pt-layer that partially converted to metallic Pt, thus the brighter intensity. **J:** (FIB) – Conclusive imaging of the finally 200 nm thin, electron transparent lamella, ready to be investigated in the TEM.

## 2.6 CORRELATIVE MICROSCOPY

To investigate deep intracellular structures in cells by cryo-ET, it is often necessary to thin down eukaryotic cells by cryo-FIB technology to a few 100 nm due to the thickness limitation < 500 nm. Depending on the research question, either the majority of cells can contain the structure/feature of interest or just a small percentage of them. In the latter case, it is essential to identify the cells of interest before starting the cryo-FIB preparation, since only the surface is visible in the cryo-FIB/SEM microscope and not these intracellular features. Another crucial challenge is to determine the precise location and size of the structure of interest inside the cell, as it should end up in the final - few hundreds nm thin - lamella of the cryo-FIB preparation. Thus, another imaging-method is necessary, to identify cells of interest:

The idea of the correlative approach came up in the late 1970s (Webster et al., 1978): it utilizes complementary visual microscopy techniques that allow to capture the entire population of cells, identify certain cells with features of interest and then consecutively acquire high-resolution data of the structures and cellular events. The first approaches in cryo-EM came 30 years later (Sartori et al., 2007; Schwartz et al., 2007).

### Correlative Cryo-EM Workflow

**Figure 2.11** shows the correlative cryo-EM workflow, in which cells are identified by correlative light-microscopy and thin sections of cells are prepared by cryo-FIB.

After the cells have been seeded onto the EM grids and have developed their physiological or pathological phenotype in culture (**Figure 2.11 ‘Cell-Culture’**), the EM-grids need to be imaged in a light microscope (**Figure 2.11 ‘LM’**) – but before that, the following has to be considered:

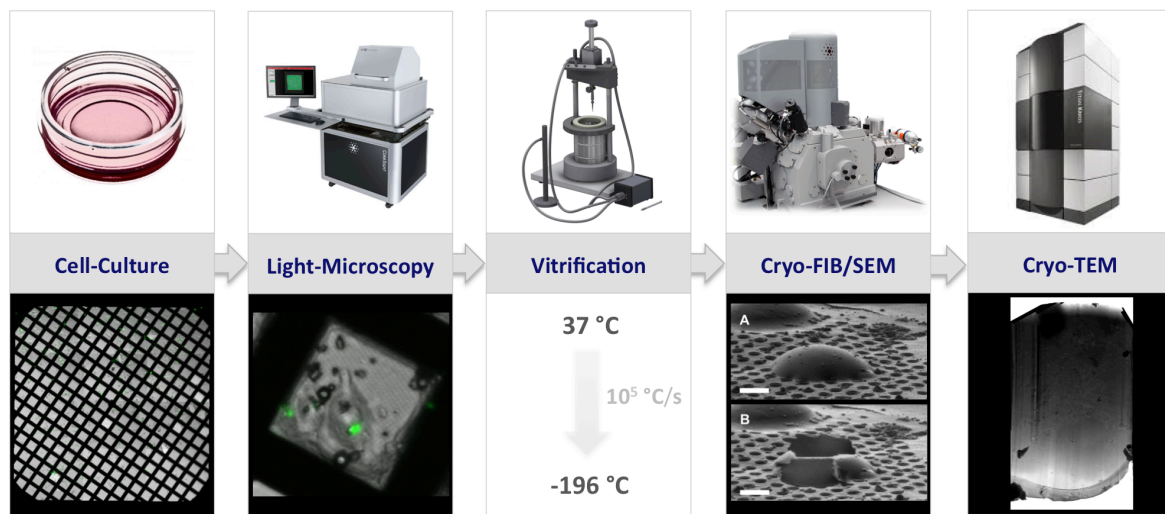


**Figure 2.11: Correlative Microscopy**

Preparation-pipeline for correlative cryo-electron microscopy. The upper images represent the location of action / the instrument where the individual step in the preparation-pipeline takes place. The lower images show a typical example of each step. Primarily cells are cultured and the imaged in the light-microscope to find sites of interest, that are then – after vitrification – targeted in the FIB/SEM, to be thinned down. Finally, the sample with the electron-transparent lamella, produced by the FIB-technology is transferred to the TEM and there, tilt-series of regions of interest are acquired and then reconstructed into three-dimensional tomograms.

For the cryo-FIB preparation and cryo-TEM microscopy the sample needs to be vitrified. This can be achieved either before or after the correlative light microscopy:

LM imaging after vitrification requires a cryo-LM setup - with the advantage of very precise correlation (good for small and motile structures), but the disadvantages of being time consuming, more challenging in handling (risk for ice-contamination) and not suitable for high throughput. An algorithm and a cryo-setup were developed (Arnold et al., 2016) that allow a precision of 200-300 nm in 60% of the cases.

LM imaging before vitrification merely needs a setup for physiological conditions - with the advantages of easy/quick handling and high throughput, but the requirement of a spatially rather stable structure of interest. The decision of which strategy should be used depends on the motility of the cell type and the structure of interest. In the here presented workflow, cells are vitrified after being imaged in the LM: To target specific cells in the entire population with the fluorescently labeled structure of interest, the whole grid is imaged by fluorescence and bright field light microscopy.

The sample is then vitrified (**Figure 2.11 'Vitrification'**) and transferred to the cryo-FIB/SEM (**Figure 2.11 'Cryo-FIB/SEM'**).

An overview map of the sample is acquired with the SEM. At the cryo-FIB/SEM microscope the SEM and LM bright field micrographs are correlated by converting the coordinates of the LM imaging into the SEM space. Since the coordinates of the fluorescence and bright field data are in the same coordinate space, the fluorescence data can be then superimposed on the SEM micrograph (**Figure 2.12A**). Accordingly, single cells that contain the structure of interest can be targeted (**Figure 2.12B**). Usually not all cells with a structure of interest are suitable for tomography, since the geometry of the

grid bars of the EM grid shadows  $\sim 20\%$  of the transparent grid area during the tilt series-acquisition. The selected cells are further processed with the focused ion-beam by preparing an electron-transparent lamella (**Figure 2.12C,D**).

In the TEM an overview of the lamella is acquired (**Figure 2.12E**), to identify sites-of-interest in the cell (**Figure 2.12F**) and to plan, where to take tomograms (**Figure 2.12G**).

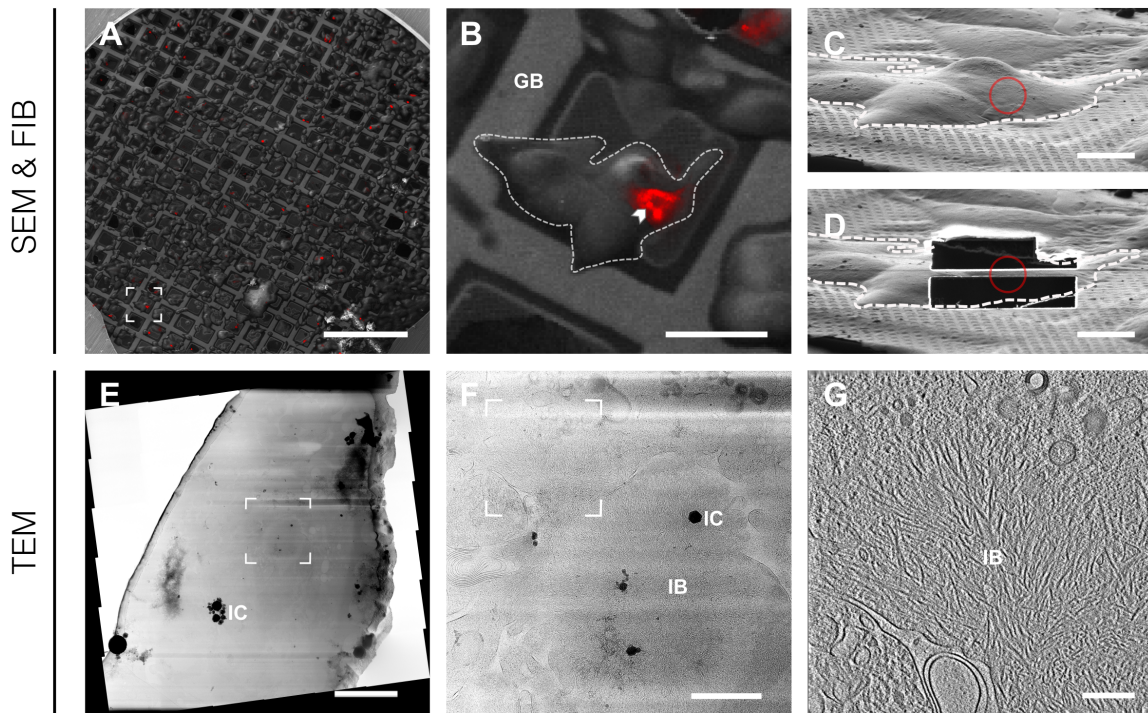


**Figure 2.12: Correlation of LM and SEM/FIB for guided Lamella-Preparation**

**A:** Overlay of live cell imaging and cryo-scanning electron microscope (SEM) images of HeLa cells growing on an EM grid and co-expressing mHtt and mCherry-ubiquitin (red). Ubiquitin puncta mark the location of mHtt IBs so that they can be targeted for focused ion beam (FIB) milling. Scale bar, 500  $\mu\text{m}$ . **B:** cryo-SEM magnification of the region boxed in (A): group of cells (dotted line), one of which contains an IB (white arrowhead). GB, grid bar. Scale bar, 50  $\mu\text{m}$ . Side view of (B) imaged with the ion beam before **C:** and after **D:** lamella preparation. Scale bar, 15  $\mu\text{m}$ . **E:** cryo-transmission electron microscope (TEM) overview of the lamella shown in (D). IC, ice crystal contamination deposited on top of the lamella. Scale bar, 5  $\mu\text{m}$ . **F:** Magnification of the region boxed in (E) containing the mHtt IB. Scale bar, 1  $\mu\text{m}$ . **(G)** 1.7 nm-thick slice of a tomogram recorded in the region boxed in (F). Scale bar, 250 nm.

After being transferred to the cryo-TEM, the lamellas are imaged to explore the captured cellular volume and to plan the tomography acquisition. For each site of interest, a series of 60-70 tilted high-resolution projections is acquired to be reconstructed into the final 3D tomogram.



## 2.7 HOW TO IMPROVE SNR

### Phase Contrast in TEM

Imaging vitreous biological specimens in focus yields only very poor contrast, typically not sufficient to recognize structures. Thus defocus is typically applied to induce phase contrast, but this measure corrupts the contrast transfer at high spatial frequencies, since the CTF-envelope function is damping these frequencies stronger with increasing defocus. Additionally, the contrast transfer at low spatial frequencies continues to be rather poor (**Figure 2.11A**).

Phase plates however are intended to apply a uniform quarter-wave phase shift to the scattered electrons relative to the unscattered beam. In light microscopy they already have been established for decades. But considerable attempts in electron microscopy with the Zernike phase plate weren't successful (Danev et al., 2009; Zernike, 1955). This was mainly due to ageing and contamination of the used carbon films, which resulted in uncontrolled phase shifts by charging and strong image artifacts, technical difficulties that prevented this type and also others to become established as a routine-method (Glaeser, 2013).

A new approach has been recently proven to be successful: the Volta-Phase-Plate (Danev et al., 2014).

### THE VOLTA PHASE PLATE (VPP)

The Volta Phase Plate is a continuous carbon film, which is positioned in the back focal plane of the microscope at the position of the objective aperture, so that the beam is maximally condensed to around 25 nm diameter on the phase plate (**Figure 2.13B**). This is called on-plane condition. An initial 'conditioning' exposure of a freshly selected phase plate position induces the development of a phase-shift to the unscattered beam relative to the scattered electrons. The exact mechanism has not yet been terminally proven. However, experimental data indicate that non beam-induced electrostatic charging causes the phase-shift. The most probable hypothesis explains the phenomenon in relation to the surface chemistry: Danev et al. state that "the beam irradiation causes local desorption of chemisorbed species, which leads to a local change in the work function and thus the Volta potential." (Danev et al., 2014). Essential is the heating of the VPP to prevent beam-induced contamination and charging that lead to a deterioration of the VPP performance.

The VPP adds the first term in the following equation to the CTF:

$$CTF(k, \Delta z) = -2\sin \left[ -\varphi \left( 1 - e^{-\frac{k^2}{2s^2}} \right) + \pi \left( -\Delta z \lambda k^2 + \frac{1}{2} C_s \lambda^3 k^4 \right) \right]$$

$\varphi$  is the phase shift of the VPP in radians,  $k$  is the spatial frequency,  $s$  is the radius of the VPP spot in reciprocal space ( $0.05 \text{ nm}^{-1}$ ). The term describing the phase-shift causes the sinus function to be equivalent to a cosine of the second term. This means that low frequencies, which were only poorly transferred without the phase plate, are now being transferred very well (**Figure 2.13C**). This illustrates the impressive visual gain of contrast using the VPP.

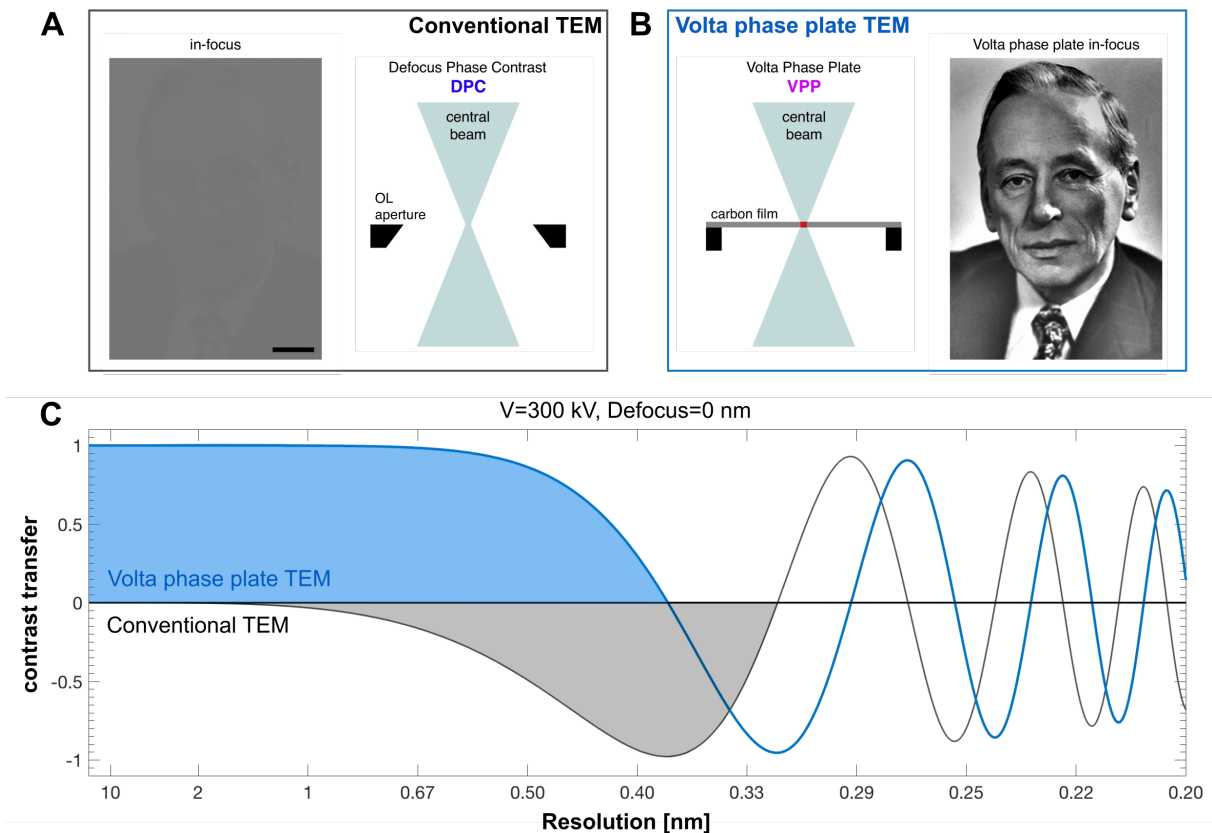


**Figure 2.13: The Volta phase plate**

**A-B:** Simulation of a weak-phase object imaging in an electron microscope. The simulation was performed using a portrait of Frits Zernike (1888–1966), the inventor of phase contrast microscopy, as a model object with a maximum phase shift of  $0.2\pi$ . Scale bar: 20 nm. **A:** An in-focus image of a weak-phase object shows almost no contrast. Defocus phase contrast uses an aperture at the back-focal plane. **B:** The Volta phase plate comprises a continuous amorphous carbon film. The phase shift is generated by the modification of the surface properties of the film by the central diffraction beam. A Volta phase plate image of a weak-phase object is a close-to-original representation of the model object. (A and B: modified from (Danev and Baumeister, 2017), with permission) **C:** Contrast transfer function (CTF) at 300 kV,  $\Delta f=0$  nm for conventional TEM (grey curve) and Volta phase plate TEM (blue curve). The essential difference is clearly visible for low frequencies – while the contrast transfer is vanishing with conventional TEM (grey area), there is a significant transfer of contrast with the Volta phase plate (blue area). At high frequencies, the CTF is comparable.

### Disadvantages of Classical Detectors

CCD cameras are commercially available since the early 1990s (Krivanek and Mooney, 1993) and are the standard detector for the cryo electron microscopy field. Nevertheless, CCD cameras have a major disadvantage: the incident electrons have to be converted by a scintillator layer into photons that are then detected by the CCD chip. The scintillator typically needs more than one electron to produce enough signal and thus the detector is characterized by a very low detection quantum efficiency (DQE) – even lower than photographic film. Additionally, drift and beam-induced movements of the sample cause a smearing of the image during the exposure comparable to longer exposures in sports-

photography. Thus neither photographic film nor CCD-cameras are ideally suited for high-resolution cryo-electron tomography. The idea arose for an electrical device that is able to directly detect electrons without the need for conversion: Direct Detection Devices.

### THE DIRECT DETECTION DEVICE (DDD)

The classical detection methods (photographic film and CCD cameras) work well for electron energies of 80-120 keV, but for higher electron energies they are considerably less efficient (McMullan et al., 2009). The reason for this is the decreased interaction cross section at higher electron energies. Higher acceleration voltages (300 kV) are necessary for thicker samples due to the same reason, but in this case the reduced inelastic interaction with the sample is advantageous. A new type of sensor was developed - the direct electron detectors – that were supposed to perform better because of their capacity to directly detect electrons without experiencing conversion losses like the interaction with the silver-halides of the photographic film or the scintillator of CCDs. Initial commercial prototypes released in 2008 lead to the first publications (Bammes et al., 2012; Brilot et al., 2012; Campbell et al., 2012; Faruqi, 2009) and were further improved.

The detector efficiency is of particular importance for the radiation-sensitive samples in cryo-electron microscopy, especially when the images suffer from an already low signal-to-noise ratio.

The performance of imaging detectors is measured by the amount of additional noise they add to the image. This is quantified by the ‘detective quantum efficiency’ (DQE) that describes the proportion of detected to incidental information as a function of the spatial frequency. An ideal detector would have a DQE of 1.0 for all frequencies. Three companies offer direct electron detectors: K2 Summit (Gatan Inc.), Falcon II (Thermo Fisher Scientific) and DE-Series (Direct Electron). Improved versions are available soon (K3, Falcon III). **Figure 2.14** shows the detector-principles and compares the DQE of the three direct electron detectors, of a CCD and of photographic film. The K2 Summit direct electron detector performs clearly superior in comparison to all other detectors and especially to CCD cameras. It is particularly better for low and middle spatial frequencies, which are essential for tomography, and is only slightly outperformed by the Falcon-II for high spatial frequencies. Thus, direct electron detectors do considerably improve the signal-to-noise ratio.

Another major advantage of DDDs is the ability to fractionate the dose on multiple shortly exposed micrographs that can be aligned afterwards to reduce motion-induced artifacts, what explicitly reduces blurring of the resulting image.

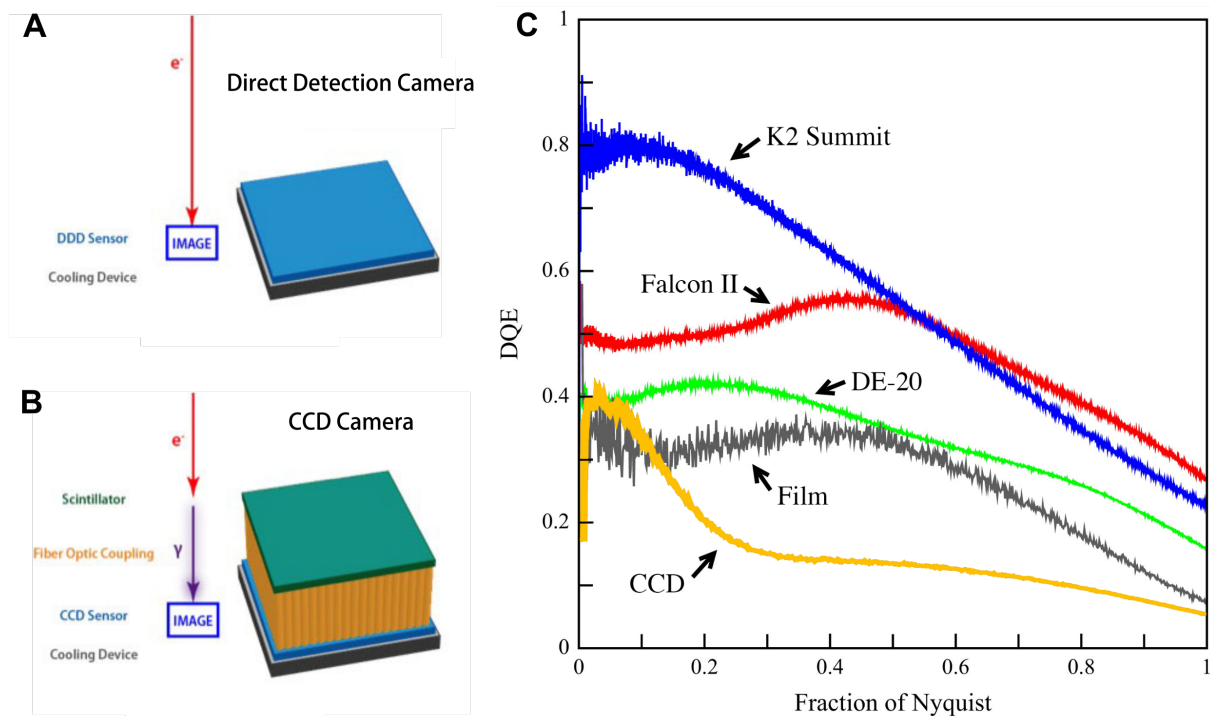


**Figure 2.14: Direct electron detectors in comparison to classical detectors**

**A:** Schematic representation of a direct detection camera. Electrons are directly detected in the semiconductor material; thus no degradation of the signal occurs due to conversion losses. To reduce thermal noise, the sensor is cooled on the distal side by a Peltier-element. **B:** Schematic representation of a CCD sensor. Electrons are first converted by a scintillator into photons, that propagate through fiber-optics to the CCD sensor, that detects the photons and converts them back to electrons. (A and B are modified from [www.directelectron.com](http://www.directelectron.com)) **C:** Comparison of the detector-performance, quantified by the DQE as a function of spatial frequency. Three direct electron detectors – K2 Summit (blue), Falcon II (red) and DE-20 (green) – are compared with photographic film (grey) and the CCD TVIPS 224 (yellow). (modified from (McMullan et al., 2014, 2009), with permission)

## 2.8 SEGMENTATION OF CELLULAR COMPONENTS

For several reasons it can be interesting to segment and identify certain structures in the final tomogram:

- **3D-Visualization:** the tomogram itself can only be visualized in one plane at the same time, so one needs to scroll through the other layers to get an impression of the entire tomogram. In order to analyze the three-dimensional organization of organelles, filaments or even the distribution of protein species, one therefore needs a 3D-representation that highlights these features and leaves out the other structures for visibility.
- **Calculation of biophysical parameters:** The segmentation of membranes yields their coordinates that can then be used to calculate for example its local curvature or surface. The segmentation of filaments by filament tracing for example opens the possibility to calculate elastic parameters like their persistence length and consecutively their stiffness.
- **Searching for certain proteins:** Certain structures like defined protein species whose structure is known can be searched in the entire tomogram and mapped with template matching. This offers possibilities to describe distribution patterns, protein orientations for example on membranes, concentrations or distances to neighbors. It finally allows calculating an averaged structure that shows high-resolution features.

### MEMBRANE SEGMENTATION

Furthermore, it can be of interest to segment membranes, for example the membranes of organelles like the endoplasmic reticulum that were studied here. With the knowledge of its exact coordinates, it is possible to calculate local membrane-curvatures as well as the density of proteins, like ribosomes for example, on its surface.

Identification and detection of structures in a tomogram are of high interest and extensively explored in the field of CET as well as MRI, but most approaches are not fully satisfying in their result in terms of sensitivity and specially specificity.

The membrane can be manually segmented by marking the structures of interest in each layer of the tomogram, but this method suffers from intra-operator variability and is time-consuming. A fully automated and standardized method to segment membrane structures is preferable. Significant advances in the computational detection were made in the last decade (Lebbink et al., 2007; Moussavi et al., 2010; Sandberg and Brega, 2007). These methods rely on template-matching, which has, however, difficulties with membrane-regions like highly curved membrane parts that deviate from the template. A new approach bases on anisotropic propagation of the local structural information using the tensor voting algorithm (Martinez-Sanchez et al., 2014) and is therefore particularly suited for membranes. This new robust local membrane detector disregards protein-structures emerging from membranes and is more robust against low signal-to-noise ratio. We based our membrane-segmentations on this semi-automated method and manually corrected regions with very high curvature, which the algorithm was not able to detect.

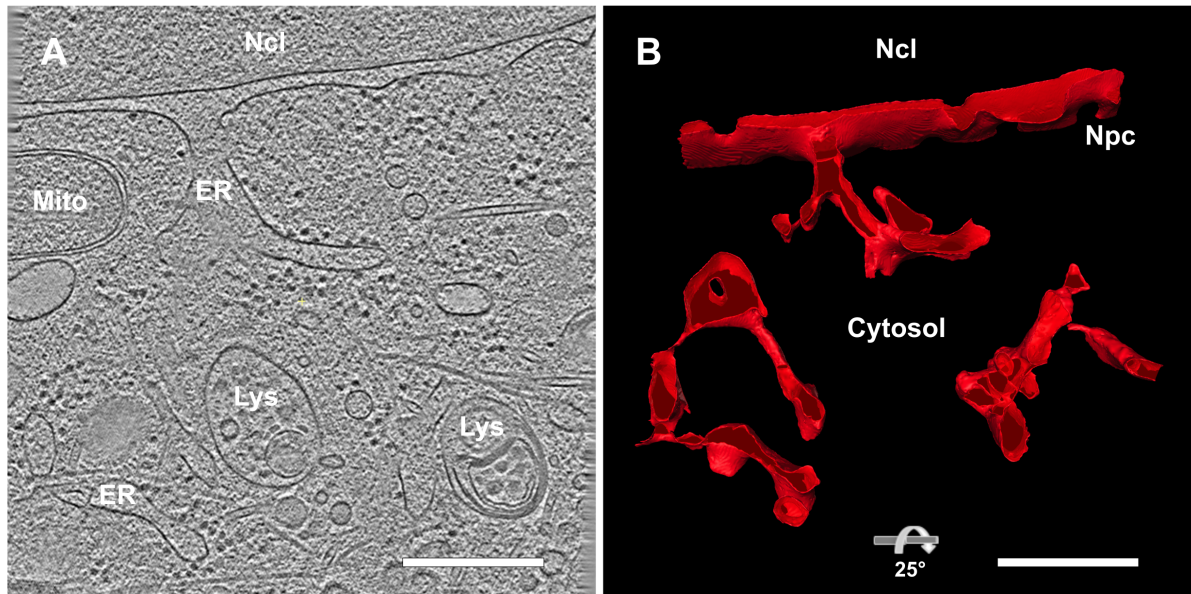


**Figure 2.15: Membrane-Segmentation**

**A:** Tomogram of a perinuclear region in a HeLa cell. The tomogram is 1610x1610x160 nm in size. The presented slice is 2.5 nm thick and thus only 1.6% of the total volume are immediately apparent. Many structures and organelles are visible and their three-dimensional organization is difficult to follow. **B:** Three-dimensional representation segmentation of the nuclear envelope and the endoplasmic reticulum. The selective segmentation of the mentioned structures, make it possible to visualize these in 3D. ER, Endoplasmic reticulum; Lys, Lysosome; Mito, Mitochondria; Ncl, Nucleus, Npc: nuclear pore complex. Scale bars, 400 nm.

## FILAMENT TRACING

Filamentous structures are especially difficult to manually segment in 3D, so that an automated approach is preferable here as well. Methods were developed to detect microtubules and actin (Nurgaliev et al., 2010; Rigort et al., 2012b; Rusu et al., 2012; Weber et al., 2012) and these are based on template matching of a massive or hollow cylinder. An extended approach (Rigort et al., 2012b) combines template matching with a new tracing algorithm that sets boundary conditions, which guide the tracing process meaningfully.

Using the coordinates of the filaments centerline, they can be further characterized concerning length distribution, orientation, density. Furthermore, elastic parameters can be derived, for example persistence length and bending stiffness. Especially the persistence length is appealing to derive from cryo-TEM tomograms, since the filaments are in their cellular context, hydrated and halted in their movement at physiological temperature in the cryo-fixed state.

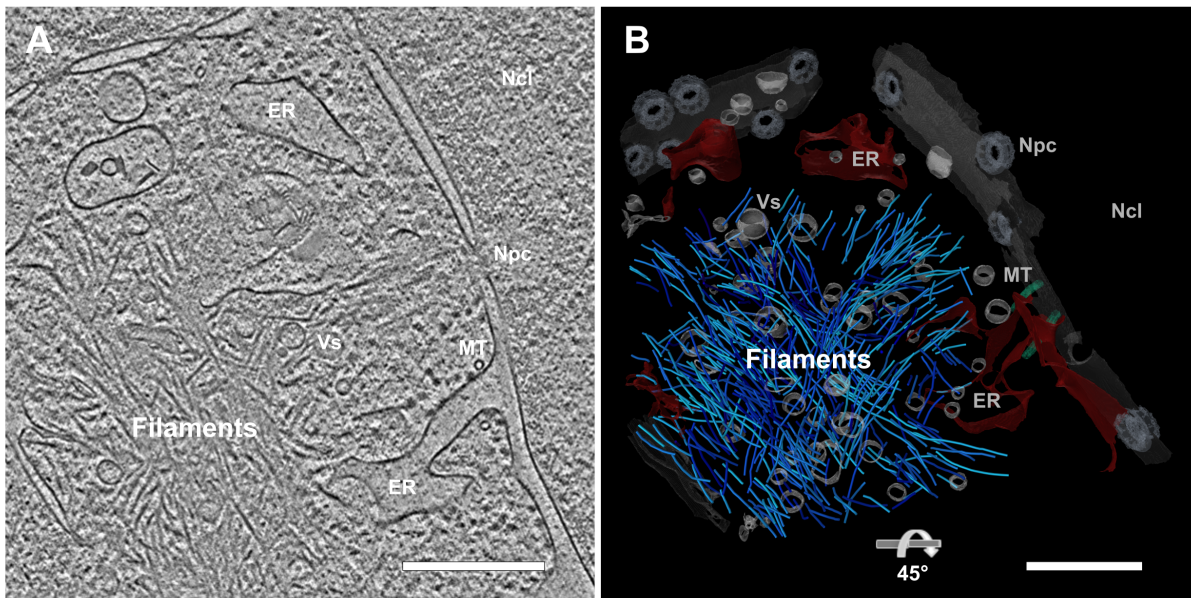


**Figure 2.16: Filament-Tracing**

**A:** Tomogram of a perinuclear region in a HeLa cell. The tomogram is 1610x1610x215 nm in size. Many filaments and several structures and organelles are visible. **B:** Three-dimensional representation of the filament tracing – the blue color shading indicates the different orientations of the filaments in the xy-plane. The segmentation of the nuclear envelope, nuclear pores, the endoplasmic reticulum, vesicles and microtubules are shown in dim colors. ER, Endoplasmic reticulum; Lys, Lysosome; Vs, Vesicles; Ncl, Nucleus, Npc: nuclear pore complex. Scale bars, 400 nm.

### PROTEIN LOCALIZATION (TEMPLATE MATCHING)

Single proteins can be detected in a tomogram by template matching: using cross-correlation, the tomogram can be screened for macromolecules, whose structure (size, shape) is known. This can be done for free as well as membrane-bound proteins. The coordinates of the detected macromolecules can be used to determine their distribution, concentration and orientation, but they can also help to calculate the density of membrane-bound proteins like the ER-bound ribosomes in this study. Furthermore, it is possible to calculate an average of the detected macromolecules and attribute the individual proteins a specific functional state (e.g.: (Asano et al., 2015; Pfeffer et al., 2012)).

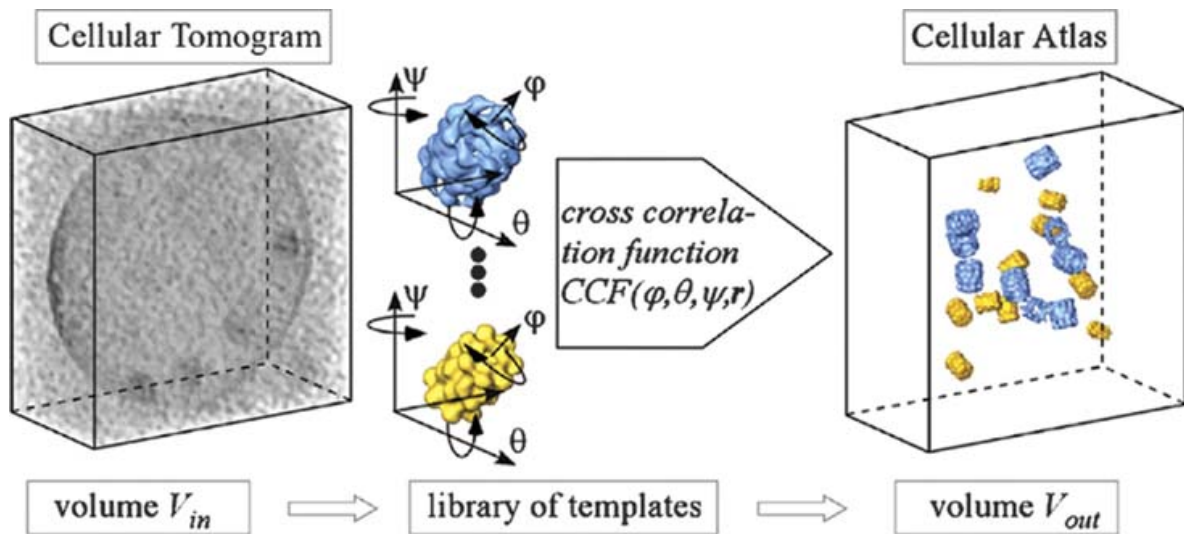


**Figure 2.17: Template-Matching**

Strategy for the detection and identification of macromolecules in cellular volumes. Because of the crowded nature of cells and the high noise levels in tomograms (left), an interactive segmentation and feature extraction is, in most cases, not feasible. It requires automated pattern recognition techniques to exploit the rich information content of such tomograms. An approach that has been demonstrated to work is based on the recognition of the structural signature (size, shape) of molecules by template matching. Templates of the investigated macromolecules are obtained by high- or medium-resolution techniques. These templates are then used to systematically search the tomograms ( $V_{in}$ ) for matching structures by cross-correlation. The tomogram has to be scanned with all possible Eulerian angles around three different axes for templates of all the different protein structures of interest. The search is computationally demanding, but can be parallelized efficiently. The output information ( $V_{out}$ ) is a set of coordinates that describes the positions and orientation of all the molecules found in the tomogram. (from (Baumeister, 2005a, 2005b; Frangakis et al., 2002), with permission)





# 3

## RESULTS

### 3.1 IMPROVEMENTS OF THE CRYO-ET METHOD

In the recent past, three major technological advances refined Cryo-Electron-Tomography and thereby made new ways of studying cellular processes possible: firstly, the development of the cryo-FIB technology (Bauerlein, 2010; Rigort and Bauerlein et al., 2012), secondly, the development of the Volta-Phase-Plate (Danev et al., 2014) and finally, the Direct Detection Devices (Bammes et al., 2012; McMullan et al., 2009).

These technological developments were essential to conduct the presented research project. At the same time their practical implementation uncovered new challenges that had to be dealt with in the early phase of this project.

#### 3.1.1 VITRIFICATION

A complete vitrified specimen is characterized by the absence of crystalline ice. This can be monitored in TEM: crystalline structures show a characteristic diffraction pattern, that can be visualized in the diffraction mode of the TEM (=Fourier-space). A single ice-crystal shows characteristic diffraction-spots – in the case of multiple randomly oriented crystals, these spots merge to a sharp ring known from the Debye-Scherrer powder diffraction method. Typical for a not entirely vitrified sample is a

polycrystalline picture, that is represented by sharp rings in the diffraction pattern. In the absence of crystalline ice, these rings are diffuse at the same location in Fourier-space. A not entirely vitrified sample contains partially crystalline and partially vitrified sub-volumes. However, the sensitivity is good for middle and larger ice crystals but is maybe limited for small crystallites: The intensity of the crystalline (sharp ring) and amorphous (diffuse ring) diffraction signal superimposes, thus it depends on the amount and size of the ice-crystals, if crystallinity can be detected.

### PROBLEM: IMPERFECT VITRIFICATION IN HELA

Vitrification did not fully succeed with HeLa cells: not a single lamella was free of crystalline diffraction patterns in the TEM, proving crystalline ice. Regions 1-2  $\mu\text{m}$  close to the cell surface seemed to be vitrified, while deeper parts showed regularly diffraction patterns. This was only discovered owing to the cryo-FIB method (Bäuerlein, 2010; Rigort and Bäuerlein et al., 2012).

Aggravating is the discovery that using diffraction to test vitrification does not seem to be sensitive enough for small crystal growth. Sometimes diffraction did not show crystalline ice, when cellular structures were obviously distorted: two cytosolic structures were massively changed due to failed vitrification and initially lead to wrong conclusions. Firstly, polyQ IB fibrils appeared to be present in more than one conformation (**Figure 3.1A, B**), diffraction detected in this case no crystal growth. Secondly, the closer mitochondria are located to an IB, wrinkling of the outer mitochondrial membrane increased gradually (**Figure 3.1D, E**). But this finding was confounded by the fact that IBs are also typically very deep inside the cell or in some cases the vicinity of the large IBs is the thickest part of the cell and vitrification is worse in deeper layers.

### SOLUTION: CONTROL OF VITRIFICATION BY SHORT TIME EXPOSURE TO GLYCEROL

Since none of the parameters of Eq. 3.1 can be changed ( $\lambda$ ,  $A$ ,  $x$  are intrinsic;  $T$  is lowest possible for organic liquid), the speed of heat transfer inside the cell is invariant of further external influences in the case of plunge freezing. Thus the strategy was to use a penetrating cryo-protectant: two substances that are established in cryobiology were tested: DMSO and glycerol. Concentrations of 2%, 5% and 10% in DMEM medium were tested for overt toxicity (cell detachment from the substrate, blebbing) vitrification improvement. DMSO caused extensive toxicity after few minutes of exposure, which was not recovered by exchange with DMSO-free medium (**Figure 3.1F**). Most cells appeared to tolerate glycerol well over >10min (**Figure 3.1G**). This time-frame is relevant, since the sample is plunge-frozen 1-2 min after the incubation. Glycerol diffuses very rapidly via Aquaporin 3 into the cell at 37°C (Kantha, 1985, p. 33), thus cells are only exposed for 2-3 min prior plunge freezing.

Finally, 10% glycerol in DMEM medium guaranteed vitrification of the entire cell: no crystalline diffraction patterns were detected. Moreover, the structural cellular alterations that had been observed upon failed vitrification without cryoprotection in fibrils (**Figure 3.1C**) and the outer mitochondrial membrane, did not occur for cells incubated with glycerol (N=130 tomograms). In this study, all structural features, that were found to be caused by IBs' fibrils in cells incubated in cell medium with 10% glycerol have been also observed in not cryoprotected cells, thus glycerol was not tempering with these observations.

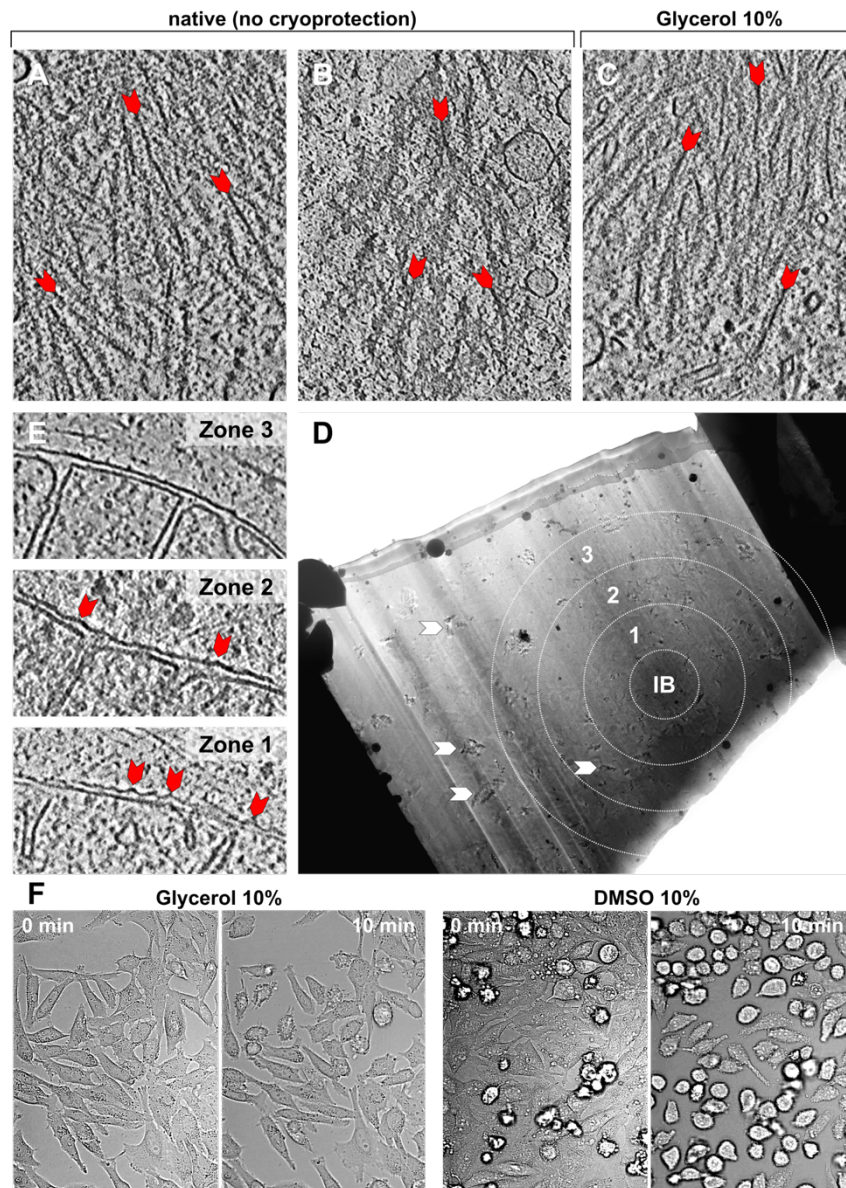


**Figure 3.1: Vitrification problem deep inside HeLa cells.**

**A:** Htt97Q fibrils of an IB close to the cells surface. **B:** Htt97Q fibrils of an IB deep inside another cell. The fibrils appear very different to the ones in (A). While the fibrils in (A) impose uniform with a fibril-backbone covered by globular domains, the fibrils in (B) are heterogeneous, also a reticular pattern is visible in the cytosol. **C:** Htt97Q fibrils of an IB in a cell, incubated in 10% glycerol for ~4 min before vitrification. **D:** Lamella of a HeLa cell containing an Htt97Q IB deep inside the cell. Tomograms of mitochondria were acquired in zones of different distance in respect to the IB (zones 1,2,3). **E:** Three examples of mitochondria imaged in the lamella of (D) in the different zones relative to the IB. The mitochondrion in zone 1 is close to the IB and shows strong wrinkling of the outer mitochondrial membrane, as others in the same zone. The mitochondrion in zone 2 (more distant from the IB) shows wrinkling too, but to a lesser extent. A mitochondrion in zone 3 has smooth mitochondrial membranes, as other mitochondria in that zone. Incomplete vitrification seems to be responsible for this artifact.

**F:** Tolerance test of Glycerol and DMSO as cryo-protectants. DMSO causes almost all cells to round-up and detach – this is not reversible in 24h after immediate change of medium, suggesting cellular death. Glycerol seems better tolerated by most of the cells in the timeframe of the experiment.

### 3.1.2 FINDING THE INCLUSION BODY

The formation of IBs is rather rare in the human brain (Jansen et al., 2017) as well as under the here used transfection conditions: the probability for IB occurrence is  $< 1\%$ , with  $\sim 5$ -15 cells containing IBs per 2000-4000 HeLa cells, which is the optimal cell density on EM-grids. Due to this low number of cells of interest, a correlative approach between LM and FIB/SEM is necessary to identify cells with IBs, as they are not directly discernible in the FIB/SEM. For different experiments the IBs were formed by either polyQ-expanded Htt exon 1 covalently labeled with GFP or non-fluorescently labeled polyQ-expanded Htt exon 1 co-expressed with mCherry-Ubiquitin, which accumulates in a ring-shape around polyQ IBs (Hipp et al., 2012).

#### TARGETING OF GFP-LABELED IBS

For the approach of correlative microscopy, a map (35 micrographs: 7168x6720 px) of the EM grid with living cells was acquired with 20x magnification (OPS 323 nm) in spinning disc confocal mode and correlated with the SEM map upon vitrification. To facilitate and optimize the selection of usable cells with IBs, a Matlab script was developed – the “Aggregate Detection Algorithm” (AGDA **s. Appendix 6.1**): it reliably identifies cells with IBs and calculates the size of the IBs. The distance of the IB to the next grid bar is measured, since it is not possible to collect tomographic tilt series of cells placed too close to the grid bars due to shadowing ( $\sim 20\%$  of the mesh area is not usable<sup>10</sup> for a tilt range  $> \pm 50^\circ$ ). These parameters are accumulated in a table and the corresponding IBs are visually labeled in the LM micrographs that are then correlated with the SEM map. In this way, it is possible to quickly identify suitable cells with IBs that presumably will be amenable to the entire time-expensive cryo-EM pipeline.

#### TARGETING OF MCHERRY-UBIQUITIN MARKED IBS

Although mCherry-Ubiquitin accumulates in a ring around polyQ IBs, a large fraction ( $\sim 97\%$ ) of fluorescent signals are false positives (no ring-shape) and massively complicate the search for IBs. To optimize the success rate, the AGDA script was modified to detect ring structures in the fluorescent micrographs – the “Ring Detection Algorithm” (RDA **s. Appendix 6.2**).

#### SECONDARY HIGH-PRECISION DEPTH TARGETING OF IBS IN THE FIB/SEM (Z-TARGETING)

The precision of the xy-correlation to target an IB of  $\sim 3 \mu\text{m}$  size with a xy-pixel-size of 323 nm is adequate. The cells were imaged at physiological temperature and the cell movement in the timeframe ( $\sim 10$  min) between the start of imaging and vitrification was small enough that the distances of IB movements are in the range of the imaging-resolution. To prepare a lamella that contains central parts of the IB, an accurate targeting in the z-dimension in the same resolution range is necessary.

---

<sup>10</sup> Due to geometric reasons, the three-dimensional gridbars will shadow parts of the grid-area at higher tilts, that are transparent at  $0^\circ$  tilt.

The precision of the correlation of the SEM and LM imaging faces three challenges:

- ***Structures move between LM imaging and vitrification***  
This problem can be solved by vitrifying the sample before imaging with the light microscope, which poses on the other hand the challenge of handling the cryo-setup and the consecutive low throughput. Nevertheless, regarding larger structures that are rather immobile this approach offers the advantages of a higher efficiency and a more comfortable processing.
- ***Local irregular distortion of the EM grid due to mechanical handling***  
Involuntary bending is almost unavoidable while handling the EM grid. This problem cannot be solved by affine registration approaches as offered in the available software products. It is only solvable with non-linear registration concepts. This is especially important, if larger parts of the sample or even the whole sample should be correlated.
- ***No correlation in z-direction***  
Even if the light microscopic data is acquired with three-dimensional information (confocal microscopy), the SEM data only offers surface information – thus correlation bears a difficult problem, because the surface in the LM is not trivially identifiable. A new approach to solve this issue was developed by Arnold et al. 2016 by using fluorescent beads for the 3D-correlation and an algorithm that superimposes the 3D-fluorescent information on the FIB-micrograph for subsequent processing. This enables a precision of up to 200-300 nm, which is sufficient to capture the structure of interest in the lamella in ~60 % of the cases.

I developed an alternative easy approach to increase the precision of targeting cellular structures in 3D: the correlation of the LM and SEM data is still used to select cells that contain the structure of interest, but the exact location of the correlation is not crucial. If the structure of interest is large enough (several hundred nanometers), a visual targeting approach surpasses the limited resolution of the correlation. With the focused ion-beam, thin layers of the cell (100-500 nm) are sequentially removed (**Figure 3.2A**), beginning from the top, until the structure of interest is reached. To verify whether this objective is reached, each newly exposed layer of cytosol is imaged by SEM (**Figure 3.2B-D**) after every step with particular settings<sup>11</sup> of the electron beam, which allow visualizing cellular structures with a resolution of tens of nanometers in the xy-plane. In the z-dimension the targeting precision depends on the thickness of the removed layers and the elongation of the structure of interest, but can be down to ~200 nm. In this study, knowing the diameter of the inclusion bodies from the fluorescent signal, the equatorial plane of the inclusion body could easily be captured in the lamella.

---

<sup>11</sup> Imaging-parameters (SEM) to visualize cellular content of a freshly exposed layer of a cell: Voltage: 2.5kV – Current: 4.1 pA – Dwell time: 300ns – Integration-mode: 128.

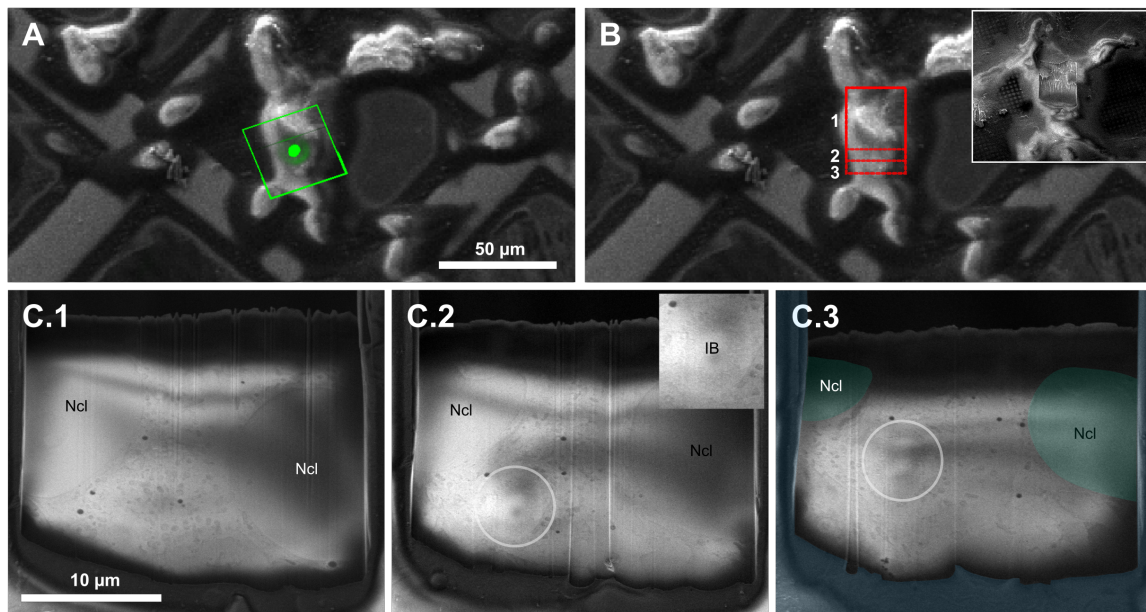


**Figure 3.2: High-Precision z-Targeting by cryo-FIB**

**A:** SEM-micrograph of a region on an EM-grid with several HeLa cells, superimposed with the fluorescence information (GFP) from correlative light-microscopy, indicating a cell with an inclusion body. The green square marks an inclusion body selected as good candidate by an algorithm introduced in section 3.1.2. **B:** The cell tagged in (A) by the green fluorescent signal is iteratively sliced (red rectangles) beginning from the top and subsequently imaged with specific parameters with the SEM to target the structure of interest. In this case, three layers were exposed – each spaced 1  $\mu\text{m}$  in the z-dimension (SEM-imaging shown in (C)). The inset shows the first FIB-slicing at the top of the cell.

**C:** SEM-micrographs representing the iterative FIB-slicing indicated in (B) by the red marked areas. C.1/2/3 corresponds to the red marked region 1/2/3 in (B). In **C.1**, cytosol is visible centrally with organelles and peripherally the nucleus but no inclusion body. In **C.2** the structure of interest – the inclusion body – becomes visible with a diameter of 3.8  $\mu\text{m}$ . The size from the fluorescent imaging is measured to 5  $\mu\text{m}$ , and an equatorial cut is preferred - so another slice is removed and in **C.3** the diameter is around 4.8  $\mu\text{m}$ .

### 3.1.3 PLATINUM-COATING & INDUCED ARTIFACT-CLEANING

#### PROBLEM: CRYO FIB-LAMELLAS INTERFERE WITH VPP IMAGING

The phase plate imaging of FIB-prepared lamellas often results in a micrograph with a contrast-rich center with distortions and low contrast in the periphery, comparable to a “tunnel-vision” or contrast-vignetting effect (**Figure 3.3A**). The central area of the image seems to take advantage of the VPP contrast enhancement, while the rest of the image appears low in contrast, as known from conventional TEM-imaging close to focus. The center of the contrast-rich part of the image moves with changing tilt of the lamella and was mainly observed when conductive structures (C-film, Pt-Layer on cell surface) were  $>2 \mu\text{m}$  distant from the area imaged.

The mechanism for this finding may be the following: The lamella is non-conductive<sup>12</sup> and due to the inelastic interaction with the electron beam, the material charges positively and builds up an electrical field. This acts as an additional electro-static lens (**Figure 3.3B**) and causes the electron beam to be out of focus instead of being focused in the back-focal plane on the phase plate. This explains why only a part of the micrograph is affected by phase contrast, causing this “contrast-vignetting” effect.

### SOLUTION: CONDUCTIVE LAMELLA-COATING

Key to overcome the problem of charging, the electrical resistance of the lamella needs to be lowered. The FIB/SEM microscope is equipped with a Pt sputtering unit. So we tried to sputter a few nm thin conductive metallic Pt-layer on the vitrified lamella. This reproducibly resolved the problem of contrast-vignetting (**Figure 3.3C**). Titrating the amount of Pt shows at the lower level bad reproducibility. Upon TEM imaging, the Pt-coat appeared to be inhomogeneous (**Figure 3.3D**) suggesting the idea of a non-linear thickness-resistance relationship. Therefore, Pt-amounts 2-3 times above the minimum dose (that worked in 50% of lamellas) were used for the coat to achieve a sufficiently low resistance of the conductive coat.

### ARTIFACT CLEANING PROCEDURE

On the other hand the discontinuous Platinum-coat induces artifacts in the tomogram that change their frequency depending on the spatial location relative to the coat-layer and are clearly visible as a horizontal line in Fourier space (**Figure 3.3E,F**). These artifacts are caused by strong contrast differences between the platinum islands and the space in between, which cause ‘rays’ emerging from these areas in an angle corresponding to the maximum tilt angle. Recently a cleaning procedure was developed (Fernandez et al., 2016) that iteratively removes both ice-contamination and the platinum-coat from the 3D-reconstruction and significantly improves tomogram quality (**Figure 3.3G**).

---

<sup>12</sup> Vitrified biological samples are dielectrics: electrolytes (e.g. K<sup>+</sup>) and other charged molecules (e.g. proteins) are immobilized due to vitrification.



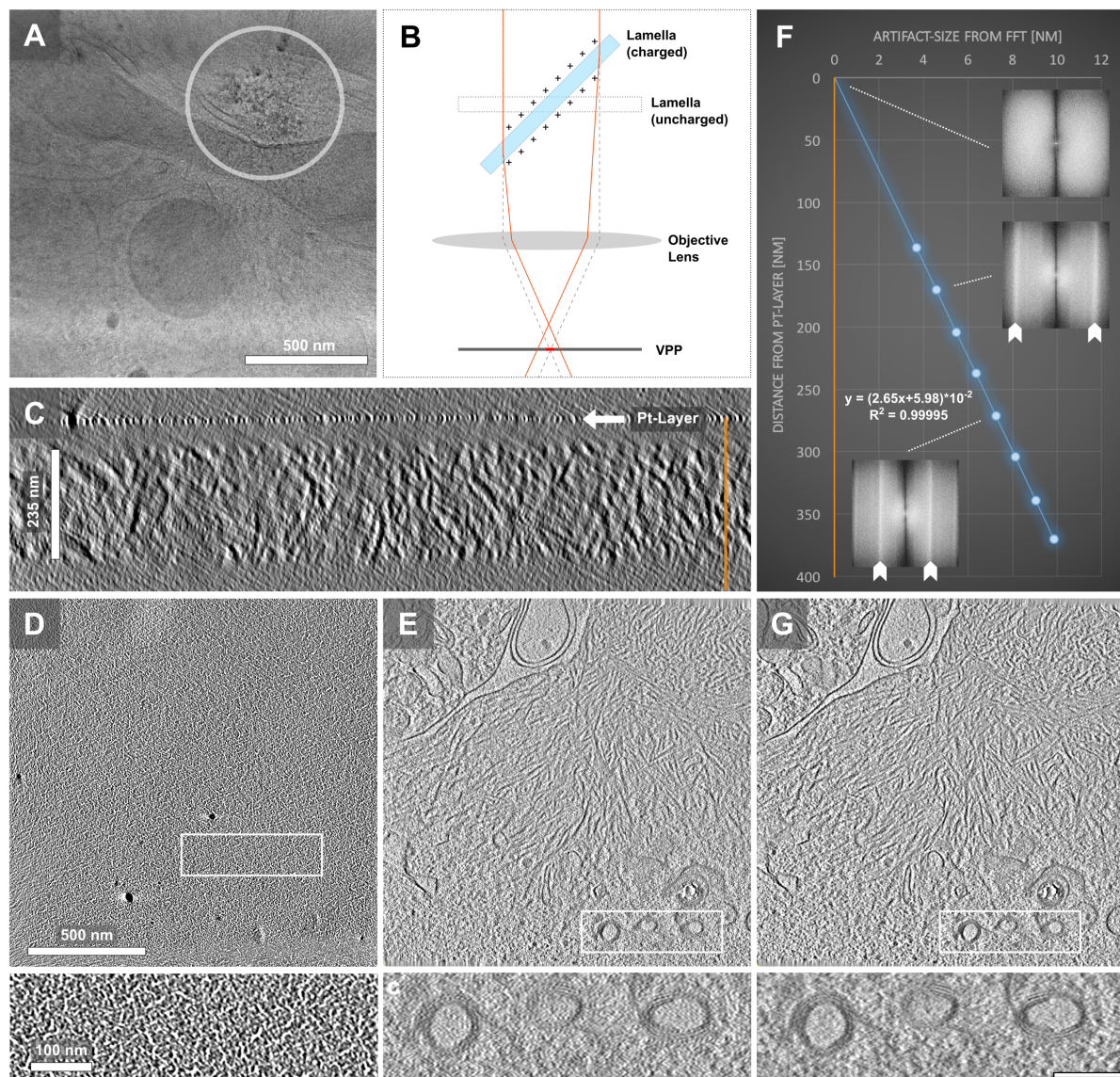


**Figure 3.3: Platinum-coating of lamellas and artifact-cleaning.**

**A:** TEM projection of a native lamella acquired with the VPP at  $-0.5 \mu\text{m}$  defocus without conductive Pt-layer. In large part the micrograph appears weak in contrast, roughly equivalent to conventional TEM at  $-0.5 \mu\text{m}$  defocus, Only a region in the upper right quadrant shows stronger contrast (marked by circle) – cytosolic structures and the mitochondrial membrane are well visible. **B:** The mechanism for the ‘contrast-tunnel-vision’ effect shown in (A). Only a sub-region of the beam is affected by the phase plate spot – equivalent to the marked region in (A). **C:** xz-slice of the tomogram, showing the Pt-layer. Artifacts become more intense distal from the Pt-layer. **D:** xy-slice visualizing the Pt-layer. The sputtered platinum doesn’t form a homogenous layer but instead nanometer-sized islands (see magnification of boxed area below). **E:** The conductive Pt-layer prevents the ‘contrast-tunnel-vision’ effect but causes artifacts in the tomogram, spatially dependent of the Pt-layer (see magnification of boxed area below). **F:** The graph visualizes the artifact-size (1/frequency) in relation to the distance to the Pt-layer. The orange line in (C) corresponds to the orange axis and indicates the measurement range along the z-dimension of the tomogram. Insets show the FFT of the corresponding xy-slice in the tomogram – arrows indicate the horizontal lines representing the artifact frequency. **G:** The same tomographic slice of (E) showing the result after the cleaning-procedure (see magnification of boxed area below). Tomographic slices are (E,G) 2.5 nm thick and averaged over 20.2 nm in (D). (magnifications of boxed regions in E&G from (Fernandez et al., 2016), with permission)

### 3.1.4 NEW GENERATION CRYO-ET WORKFLOW

Here we combined the recent developments in the cryo-EM field and the method improvements described so far in this chapter into a “New Generation cryo-EM Pipeline” and applied this to investigate the role of inclusion bodies in their cellular environment.

The schematic overview in **Figure 3.4** shows the full workflow from the cell culture until the final 3D tomogram and its post-processing analysis. The figure illustrates three entities: the physical steps of sample handling/treatment and microscopy, the data acquisition and processing and finally the scales of critical parameters during the process. This section will give an overview of the whole pipeline with focus on the method improvements, illuminated in orange font in the figure.

At first the cells of interest are cultured under physiological conditions (**Cell Culture**).

To identify cells that contain an inclusion body, we used fluorescence light microscopy (**Light Microscopy**) to create a map of the sample (**LM Map**). Thereby it is possible to identify cells that offer a fluorescent signal of the labeled structure of interest and map their precise intracellular location.

For the cryo-FIB preparation and cryo-TEM microscopy, the sample needs to be vitrified (**Vitrification**): the sample is rapidly frozen to  $-196^{\circ}\text{C}$ . This can be achieved either before or after the correlative light microscopy ( $\Leftrightarrow$ ). In this study, the motility of the used cell types (HeLa cells and primary neurons) was rather low and the movement between imaging and vitrification of the structure of interest (the inclusion body) was below the correlation precision. Thus we vitrified the sample after light microscopy. We showed in chapter 3.1.1 that large cells like HeLa are regularly not fully vitrified by plunge freezing – solely the upper  $1\text{-}2\ \mu\text{m}$  close to the surface. Thus we optimized vitrification by a short-time exposure to 10% glycerol in the medium.

In the cryo-FIB/SEM microscope (**Cryo-FIB/SEM**) a further map (**FIB/SEM Map**) is acquired and correlated with the spatial information from the light microscope (**SEM-LM Correlation  $\Sigma$** ), in order to subsequently target these cells and thin them down. To facilitate the identification in the large whole-sample imaging and to select meaningful candidates, the **XY-Correlation** was improved by two algorithms (chapter 3.1.2). Furthermore, a new method was established in this work to localize larger structures like inclusion bodies in the third dimension (**Z-Targeting**, chapter 3.1.2).

The sample is coated in the cryo-FIB by a conductive organometallic platinum layer (**Protective GIS-Pt-Layer**). Subsequently, the cell is thinned down with the focused ion-beam, so that the structure of interest is located in the final resulting electron-transparent lamella (**Lamella Preparation**).

In chapter 3.1.3 it was shown that these lamellas typically accumulate electrical charge in regions not close to the conductive carbon film, strongly interfering with Volta-Phase-Plate imaging. This problem was solved by covering the sample with a thin layer of metallic platinum (**Conductive Pt-Layer**) by sputter-coating to enhance conductivity, so that the sample is compatible for imaging with the Volta phase plate in the cryo-TEM.

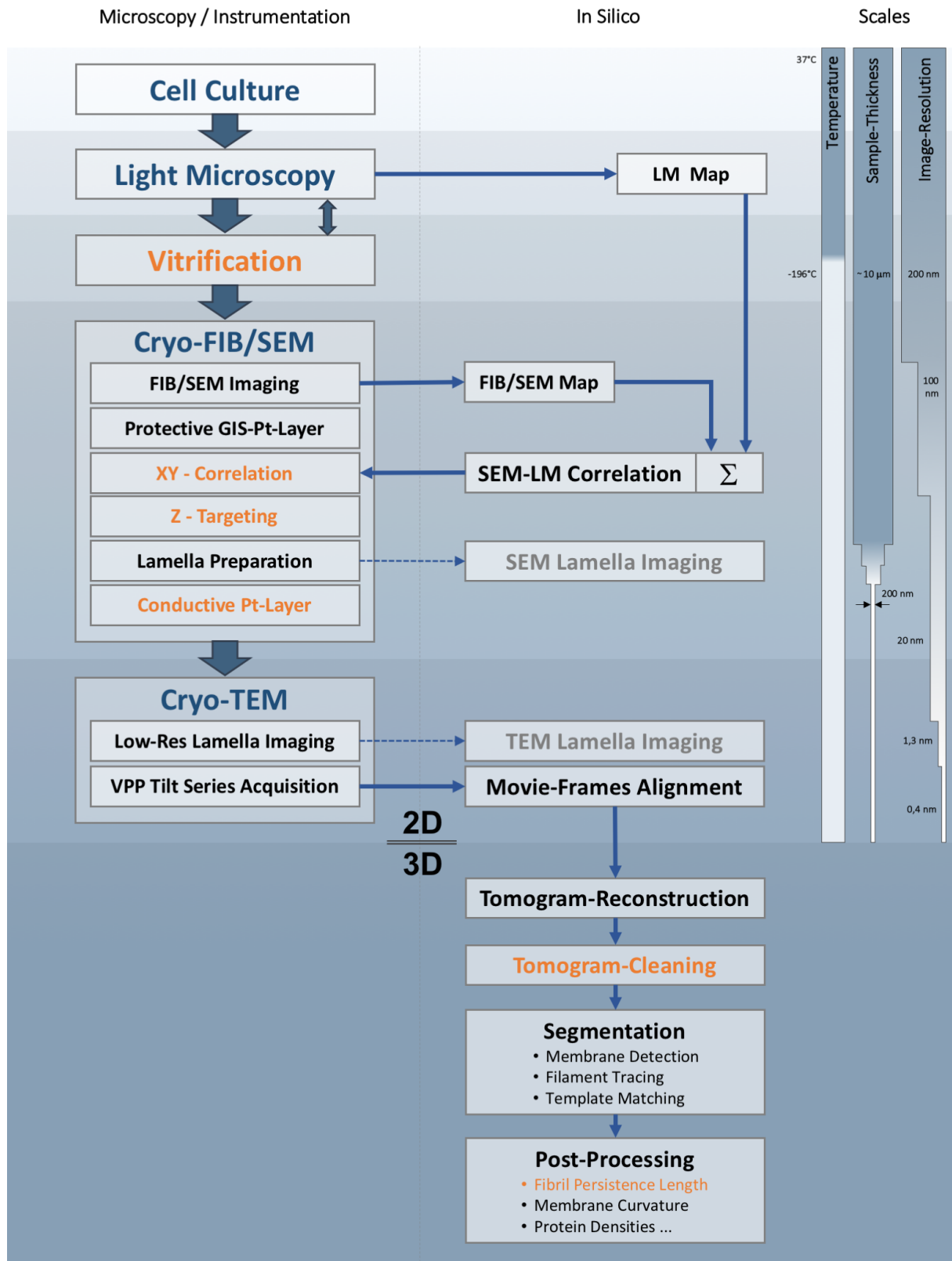
After being transferred to the **cryo-TEM**, the lamellas are imaged (**‘Low-Res Lamella Imaging’**) to explore the captured cellular volume and to plan the tomography acquisition. For each site of interest, a series of 60-70 tilted high-resolution projections is acquired (**‘VPP Tilt Series Acquisition’**) with the direct detector and contrast-enhancement by the Volta phase-plate.

These projections are computationally adjusted for drift and beam-induced movements (**‘Movie-Frames Alignment’**). In a next step the 2D micrographs are reconstructed into a 3D-tomogram (**‘Tomogram-Reconstruction’**). The conductive platinum-layer forms inhomogeneous islands, which cause artifacts in the tomogram (chapter 3.1.3). These can effectively be reduced by a computational cleaning-procedure (**‘Tomogram-Cleaning’**). Specific structures like membranes, filaments or macromolecules can be computationally selected and rendered in 3D (**‘Segmentation’**). This helps to understand the spatial configuration better, but also aids to perform biophysical calculations (**‘Post-Processing’**) like the fibril persistence length, membrane curvature, or protein densities. An algorithm was developed in this work to calculate the persistence length on the basis of the fibril segmentation and to derive elasticity parameters from the IBs’ fibrils in the static tomograms (Appendix 6.3).

#### Figure 3.4: New Generation Cryo-EM Pipeline (p. 62)

This figure shows the schematic overview of the new generation cryo-EM pipeline from the cell culture until the final 3D tomogram with subsequent biophysical analyses. The scheme is divided in three segments: the left column ‘Microscopy/Instrumentation’ visualizes all physical steps of handling/treatment and microscopy of the sample. The middle column ‘In Silico’ shows the 2D data acquisition and processing of all the necessary steps until the final tomogram and the post-processing of the 3D data. And the right column ‘Scales’ illustrates the scales of the temperature, sample-thickness and the image-resolution reached at each step in the pipeline. Grey text indicates imaging steps just for documentation, that are not essential for the final outcome. (When individual operations of this scheme are mentioned in the text, they are indicated as following: e.g. (**‘Cryo-TEM’**))

## New Generation Cryo-EM Pipeline



### 3.1.5 NEURO-2A

Initially experiments were performed using a neuroblastoma cell line (Neuro-2a) stably expressing Htt150Q-GFP in an inducible manner, hence most of the cells showed an IB after induction. This procedure would have facilitated the lamella preparation enormously, since a correlation step would have been unnecessary. Unfortunately, these cells also showed an enormous amount of membrane enclosed (probably ER) vesicular structures that had a narrow size distribution ( $\sim 100$  nm) and appeared to be virus particles (**Figure 3.5**). The attempt to identify these prominent structures by mass spectrometry did not yield an obvious result. Therefore, this cell line was not further used. However, it will later support support findings in HeLa cells and primary neurons.

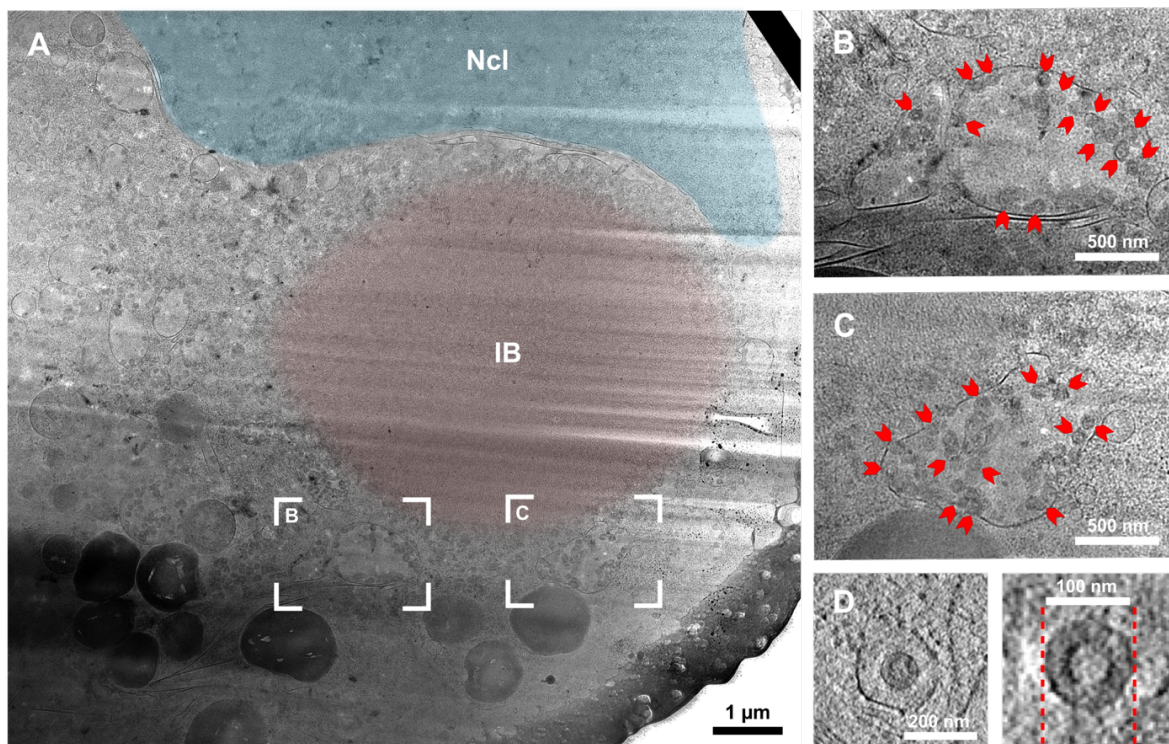


**Figure 3.5: Inducible Neuro-2a cell line with Htt150Q-GFP IB.**

**A:** TEM projection of a lamella, presenting a Htt150Q-GFP inclusion body in an inducible Neuro-2a cell line. The nucleus (Ncl) is marked in blue, the inclusion body (IB) in red. Noticeable is an enormous amount of membrane enclosed (probably ER) spherical structures in this cell. Two examples are magnified in (B) and (C). **B:** Magnification of the area marked in (A). A membrane-structure, separated from the cytosol embodies at least 30 of these particles (red arrowheads) in the 200 nm thin slice. **C:** Magnification of (A) presenting another example like in (B). **D:** Two examples of tomographic reconstructions of these particles in different cells. The particles' size is about 100 nm diameter. The particle has a 50 nm measuring core part and a 25 nm electron-denser shell.

## 3.2 IB ARCHITECTURE

This section describes the overall three-dimensional architecture of Htt97Q±GFP inclusion bodies (IBs) on a mesoscopic scale and the microscopic structure of the polymerized species in HeLa cells and primary hippocampal neurons.

### 3.2.1 IB STRUCTURE ON THE MESO SCALE

#### LOCATION AND SHAPE

HeLa cells expressing Htt97Q-GFP develop IBs - 24-48h after transfection - in only < 1% of the population. After 10-20 h after transfection cells show diffuse fluorescence – at some point the soluble species aggregate in a time frame of 15-30 min in a single IB, but in ~ 13% (28/221) of these cases a second or more rarely a third IB can be observed. IBs are roughly spherical and ~ 3  $\mu\text{m}$  in diameter in neurons and ~ 6  $\mu\text{m}$  in HeLa cells. Htt97Q-GFP IBs are mostly cytosolic and typically observed close to the nucleus (**Figure 3.6**), although intra-nuclear IBs were also found. This was previously described e.g. by (Liu et al., 2015) (Htt97Q-GFP in HEK cells) with 82% peri-nuclear, only 5% of IBs were more distant and 13% intra-nuclear, recapitulating the occurrence in this study: low-resolution EM micrographs of the IB containing lamellas revealed that IBs are 90% cytosolic and that the nucleus is partially embracing the IB in differing extent (**Figure 3.6**), indicating an adhesion force between IB and nucleus. Nevertheless, a gap of 100-200 nm between the IB's periphery and the nuclear membrane is typical, suggesting an indirect association. **Table 3.1** shows the amount of investigated cells and IBs with their respective location.

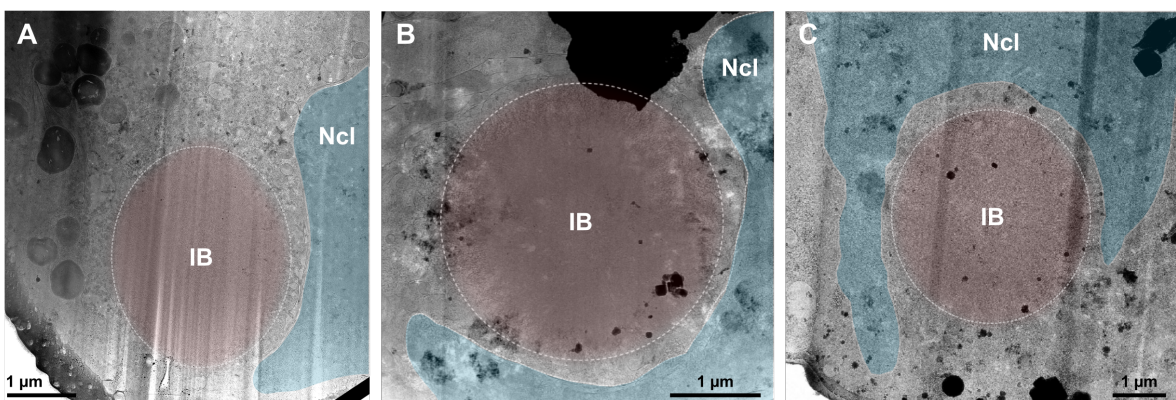


**Figure 3.6: Nuclear embracement of IBs.**

Shown are three different examples of IBs in typical close association to the nucleus (Ncl). A gap of 100-200 nm is observed in-between nucleus and IB. Significant surface areas of the IB are covered by the nucleus, visible in different extent, increasing from A to C.

Condition (cell type; construct expressed)	Number of cells / IBs analyzed by cryo-ET	Number of tomograms / experiments
Neurons ; Htt97Q-GFP, of which	8 / 11	11 / 3
- contained a cytosolic IB	5 / 5	5
- contained a nuclear IB	3 / 6	6
HeLa ; Htt97Q-GFP, of which	9 / 10	29 / 5
- contained a cytosolic IB	6 / 10	18
- contained a nuclear IB	0 / 0	0
- showed diffuse fluorescence	3 / -	11
HeLa ; Htt97Q, of which	7 / 10	16 / 3
- contained a cytosolic IB	5 / 8	11
- contained a nuclear IB	2 / 2	5

**Table 3.1:** Sample size

### AGGREGATED SPECIES

For decades it has been discussed, if polyQ-stretched Htt species aggregate amorphous or polymerize in a structured manner (Davies et al., 1997; DiFiglia et al., 1997; Finkbeiner, 2011; Miller et al., 2010; Petrasch-Parwez et al., 2007; Qin et al., 2004; Waelter et al., 2001). **Figure 3.7** demonstrates conclusively that Htt97Q inclusion bodies are composed of a network of mostly radially arranged amyloid-like fibrils. The IBs' inner structure is not subdivided and fibrils are typically oriented on the axis from the center radially towards the surface. However, most of them don't originate from the IBs center, but still point in this direction. Interestingly fibrils were never observed individually but exclusively in the context of the fibril network of an IB.

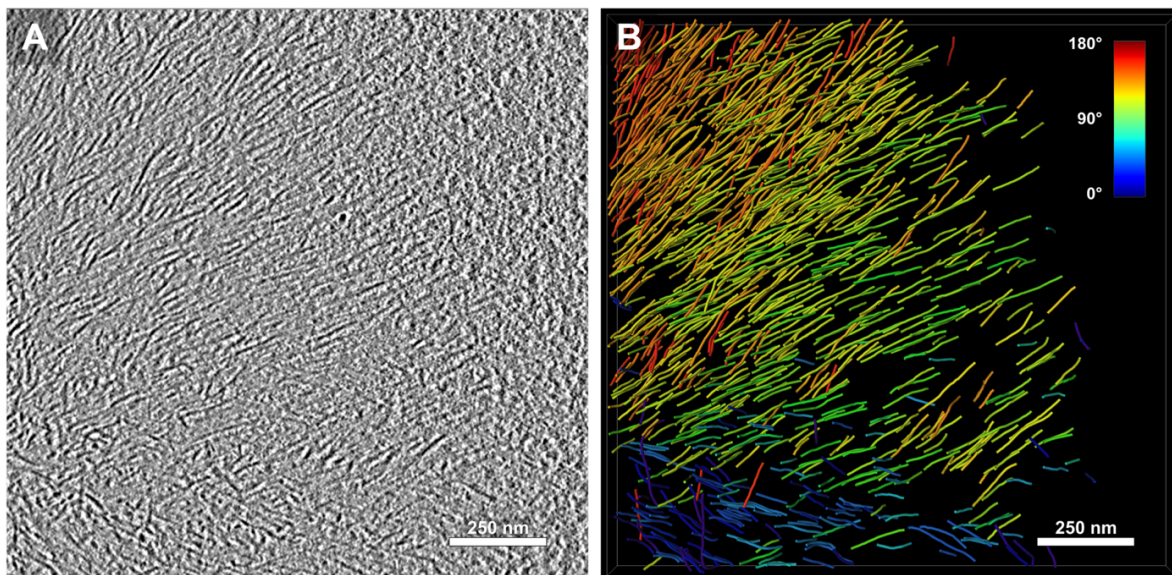


**Figure 3.7:** Htt97Q IBs are formed by radially arranged amyloid-like fibrils.

**A:** Tomographic slice of a Htt97Q-transfected HeLa cell showing the periphery of a cytosolic IB. Tomographic slice is 2.5 nm thick **B:** 3D rendering of Htt97Q fibrils automatically extracted from (A). The color of the fibrils indicates their orientation in the xy-plane.

### 3.2.2 FILAMENT CHARACTERIZATION

This section describes the morphology of fibrils of the different used constructs: Htt97Q-GFP, Htt97Q, Htt64Q-GFP and the difference in primary mouse neurons and HeLa cells:

#### HTT97Q-GFP IN NEURONS AND HELA

Htt97Q-GFP fibrils in neurons have a diameter of 7-8 nm similar to actin and a mean length of  $125 \pm 81$  nm, identical to Htt97Q-GFP fibrils in HeLa cells with the same diameter and  $129 \pm 85$  nm mean length (**Figure 3.8 A**). Interestingly, Htt97Q-GFP fibrils are decorated by regularly spaced globular densities of  $\sim 6$  nm in diameter consistent in size with GFP dimers (**Figure 3.8 C**). To further investigate the nature of these densities, HeLa cells were co-transfected with untagged 97Q Htt exon 1 (Htt97Q) and mCherry-ubiquitin. The latter can be conjugated to target proteins in a manner similar to wild-type ubiquitin (Qian et al., 2002) and its recruitment to IBs (Hipp et al., 2012) served as a surrogate fluorescent marker for Htt97Q IBs. Given the relatively low transfection rates obtained in neurons and the similarity of fibrils in the different species and cell types, these and further experiments are carried out in HeLa cells to increase the number of cells amenable to cryo-ET analysis.

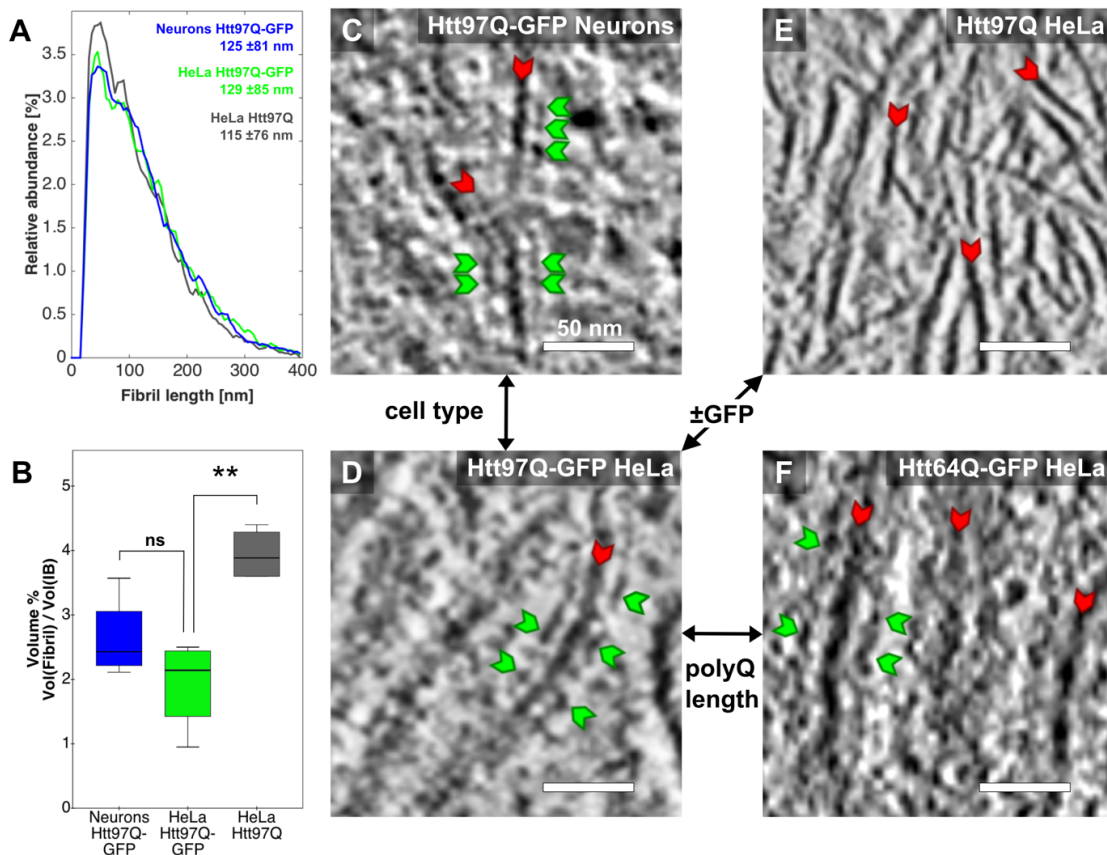


**Figure 3.8: Comparison of different Huntingtin exon 1 fibrils.**

**A:** Histograms of fibril length in mouse neurons expressing Htt97Q-GFP (blue), HeLa cells expressing Htt97Q-GFP (green), and HeLa cells expressing Htt97Q (gray) (number of fibrils:  $n = 11,481$  neurons and Htt97Q-GFP;  $n = 7,648$  HeLa and Htt97Q-GFP;  $n = 12,465$  HeLa and Htt97Q; 4 tomograms for



all conditions). **B**: Percentage of IB volume occupied by fibrils. The boxes and whiskers, respectively, indicate confidence intervals of 50% and 95% around the mean (solid line inside each box). \*\* indicates  $p < 0.01$ ; ns, not significant in an ANOVA analysis with Bonferroni post hoc test. **C-F**: Representative high-magnification tomographic slices of fibrils, compared in three ways: different cell type (neuron vs. HeLa), different polyQ length (97Q vs. 64Q) and concerning the GFP-label (with vs. without covalently bound GFP). **C**: High-magnification image of Htt97Q-GFP fibrils (red arrowheads) in a primary mouse neuron decorated by globular densities (green arrowheads). **D**: High-magnification image of Htt97Q-GFP fibrils (red arrowheads) in a HeLa cell decorated by globular densities (green arrowheads). **E**: High-magnification image of Htt97Q (without GFP tag) fibrils (red arrowheads) in a HeLa cell. **F**: High-magnification image of Htt64Q-GFP fibrils (red arrowheads) in a HeLa cell decorated by globular densities (green arrowheads). Tomographic slices are 1.7 nm thick. (Modified from (Bauerlein et al., 2017). Reprinted, with permission from Elsevier.)

### HTT97Q IN HELA

Htt97Q and Htt97Q-GFP IBs in HeLa cells were almost identical to those in neurons in terms of overall architecture and fibril morphology (**Figure 3.8C,D,E**). Htt97Q fibrils in HeLa cells have a diameter of 7-8 nm and a mean length of  $115 \pm 76$  nm.

Although Htt97Q-GFP and untagged Htt97Q fibrils were similar in diameter and length (**Figure 3.8A**), untagged Htt97Q fibrils were not decorated by additional densities (**Figure 3.8E**). This demonstrates that the fibrils consisted of Htt97Q, and suggests a molecular organization in which the polyQ regions form the fibril core, whereas the flexible C-terminal sequence protrudes outwards in a bottlebrush fashion (Isas et al., 2015).

### HTT64Q-GFP IN HELA

Huntingtin exon 1 with a repeat of 97 Glutamines (Htt97Q-GFP, Htt97Q) is used in this study because of its favorable aggregation kinetics (aggregation occurs mainly 24-48h after transfection), but has also a rather long polyQ stretch for regular human disease cases (**Figure 1.4A**). A repeat length of 97 Glutamines is found in rather rare juvenile disease cases, but nevertheless shorter polyQ-lengths are typically found in the regular disease.

It is essential to yield enough cells that contain an IB on a single EM grid at one time-point after transfection, since only a proportion of these is finally suitable for lamella preparation. The chance for this occurrence is in the sub-percent region with  $\sim 5$ -15 cells containing IBs per 2000-4000 HeLa cells on the grid and is substantially lower for shorter polyQ repeat lengths. Thus, the majority of analyses are performed with Htt97Q to yield sufficient numbers for cryo-ET.

To investigate a polyQ version closer to the typical disease situation and furthermore to explore the dependence of IB architecture and fibril morphology on the polyQ length, a construct with 64 repeats (Htt64Q-GFP) is analyzed in the following. A repeat of 64 Glutamines is still long compared to the typical repeat-lengths in HD (see **Figure 1.4A**) but it is substantially shorter than 97 Glutamines.

Htt64Q-GFP fibrils in HeLa cells appear similar to Htt97Q-GFP in HeLa cells and neurons. In total the IB architecture and fibril morphology of Htt64Q-GFP is indistinguishable to Htt97Q-GFP in HeLa cells as well as in neurons, justifying the general use of the longer polyQ construct (Htt97Q-GFP, Htt97Q).

### 3.2.3 VOLUME OCCUPATION OF IBs

Inclusion bodies are composed of a polymer network of polyQ expanded Htt exon 1 fibrils, that can be interpreted as a gel. Diffusion of proteins in a gel can be hindered due to interaction with the polymer network, depending on their hydrodynamic radius. IBs occupy an unneglectable portion of the cytoplasm and thus have the potential for sequestering cellular components (Olzscha et al., 2011; Park et al., 2013) either passively by lowering the diffusion coefficient or by direct interaction with the Huntingtin fibrils. Despite the dense appearance of the network, the fibrils occupy around 4% of the IB volume in the case of the untagged Htt97Q (**Figure 3.8B**), the globular densities of the GFP-labelled version, act as spacers between the filaments and result in a reduced density around 2% of the IB volume (**Figure 3.8B**).

Although only a small fraction of the IB volume was occupied by fibrils, the core of the aggregates was largely devoid of macromolecules like ribosomes, which accumulated at the IB periphery (**Figure 3.20**).

### 3.2.4 PERSISTENCE LENGTH OF IB FILAMENTS

Although tomograms of IBs in frozen hydrated cells show a static snapshot of the cellular processes and cytosolic movements at a single time point, it is possible to derive elastic parameters of cellular polymers: the persistence length, which is a measure of the stiffness. Since flexible polymers in the cytosol are permanently deformed by Brownian motion - this physical strain is captured at one moment in time by vitrification and the persistence length ( $L_p$ ) of the Huntingtin exon 1 fibrils can be calculated from the static tomogram - after segmentation of the fibrils - by (Nagashima and Asakura, 1980):

$$\langle \cos(\theta) \rangle = \langle \cos(\theta_0 - \theta_l) \rangle = e^{-l/L_p}$$

$\langle \cos(\theta) \rangle$  is the expectation value of the angle  $\theta = \theta_0 - \theta_l$  between the starting point 0 and a point on the filament after the distance  $l$ . For details of the data processing see **Appendix 6.3**. The persistence length is proportional to the Young's Modulus  $E$ , which defines the relation between applied force ( $F$ ) and deformation of the fibrils' length ( $\Delta L/L$ ) with the cross-sectional area ( $A$ ) by:

$$E = \frac{L_p}{l} k_B T = \frac{F/A}{\Delta L/L}$$

$I$ : area moment of inertia – in the case of a uniform rod  $I = \pi a^4/4$ .

The results of the calculation for persistence length and Young's Modulus are presented in **Figure 3.9**.

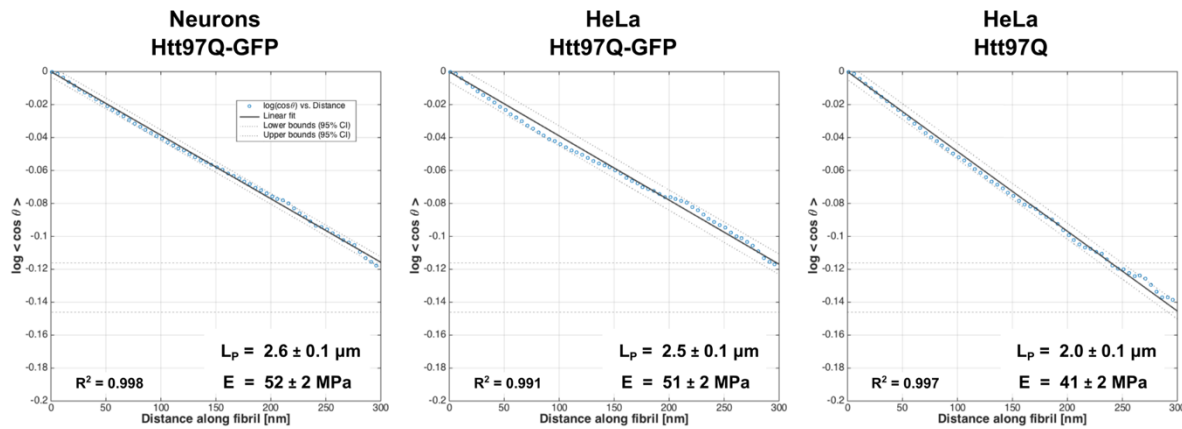


**Figure 3.9: Persistence length analysis of polyQ fibrils.**

Linear fit for the total persistence length for all tomograms analyzed (Number of fibrils: N = 11,481, neurons; Htt97Q-GFP; N = 7,648, HeLa; Htt97Q-GFP; N = 12,465, HeLa; Htt97Q; 4 tomograms for all conditions). 95% confidence lines and the values of the persistence length ( $L_p$ ), Young's modulus ( $E$ ) and coefficients of determination ( $R$ ) are indicated. The dashed lines mark the values of the fitting line at a distance along the filament of 300 nm as indication of the slope of the line, from which  $L_p$  is calculated. Note that the values are identical for Htt97Q-GFP in HeLa cells and neurons, but different from Htt97Q in HeLa cells. (Modified from (Bauerlein et al., 2017). Reprinted, with permission from Elsevier.)

The persistence length and Young's Modulus of Htt97Q-GFP fibrils were identical in neurons and HeLa with  $2.5 \pm 0.1 \mu\text{m}$  [ $52 \pm 2 \text{ MPa}$ ] vs.  $2.6 \pm 0.1 \mu\text{m}$  [ $51 \pm 2 \text{ MPa}$ ] ( $p = \text{ns}$ ). This provides further evidence that Htt97Q-GFP fibrils are indeed identical in mouse neurons and human HeLa cells – not only morphologically but also in the light of elastic properties. Untagged Htt97Q fibrils in HeLa have a slightly lower persistence length with  $2.0 \pm 0.1 \mu\text{m}$  and a Young's Modulus of  $41 \pm 2 \text{ MPa}$ . The presence of GFP seems to increase fibril stiffness by 25%.

The stiffness of Huntingtin exon 1 fibrils is invariant to the species (human vs. mouse) and to the cell origin (neuron vs. HeLa). The elastic properties are comparable to actin filaments: persistence length  $2.8 \mu\text{m}$  and a Young's Modulus of  $101 \text{ MPa}$  (Mahamid et al., 2016).

### 3.3 CELLULAR INTERACTIONS OF IBs

The cause of neurodegeneration in Huntington's Disease, as in most other neurodegenerative diseases, has yet to be identified. Oligomeric, soluble Huntingtin species have been shown to contribute to cytotoxic effects (Arrasate and Finkbeiner, 2012; Finkbeiner, 2011; MacDonald et al., 1993; Scherzinger et al., 1997), but the role of inclusion bodies in cytopathology, which consist of insoluble, polymerized Huntingtin, still remains open and has been poorly characterized. Inclusion bodies are often described and believed to be inert and thus a protective protein deposit for the toxic proven oligomeric species (Arrasate and Finkbeiner, 2012; Bucciantini et al., 2002; Haass and Selkoe, 2007; Leitman et al., 2013). This chapter describes the investigation of the interaction of inclusion bodies with their cellular environment.

### 3.3.1 STRUCTURAL ASSOCIATION OF IBs WITH ENDOMEMBRANES

#### INTERACTION OF IBs WITH THE ENDOPLASMIC RETICULUM

Cryo-ET of the periphery of inclusion bodies revealed surprisingly a strong interaction of the IB network with the endoplasmic reticulum (**Figure 3.10A,B**).

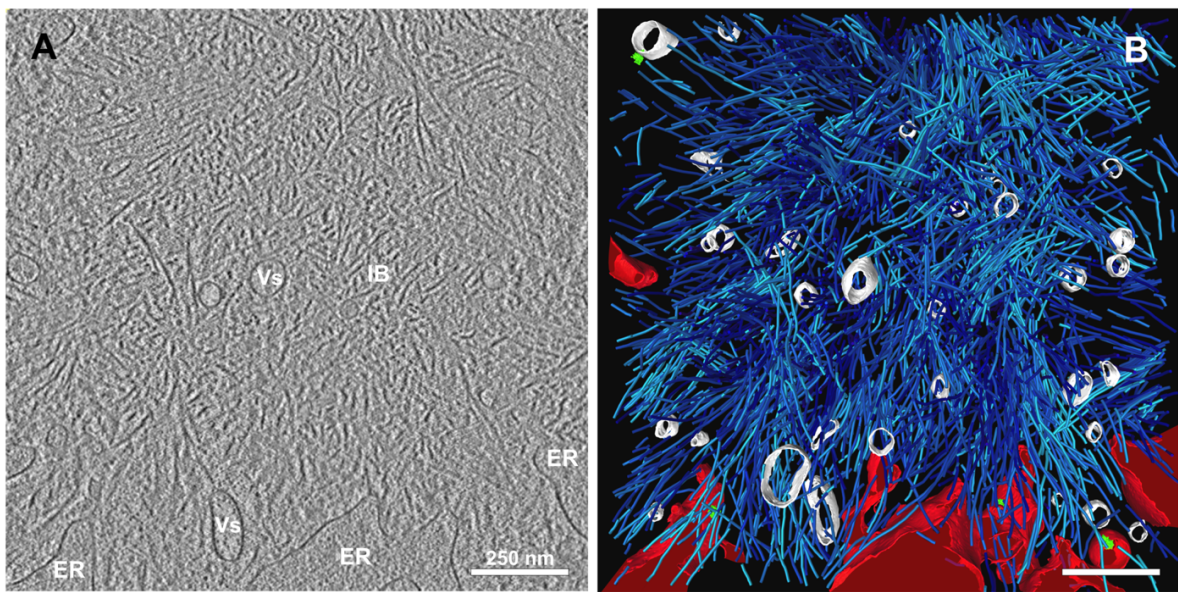


**Figure 3.10: Htt97Q IBs interact with cellular membranes.**

**A:** Tomographic slice from the interaction zone between an IB and cellular membranes in an Htt97Q-transfected HeLa cell. ER, endoplasmic reticulum; IB, Htt97Q inclusion body; Vs, vesicles. Tomographic slice is 2.5 nm thick **B:** 3D rendering of the tomogram shown in (A). ER membranes (red), ER-bound ribosomes (green), Htt97Q fibrils (cyan), vesicles inside the IB (white). (Modified from (Bauerlein et al., 2017). Reprinted, with permission from Elsevier.)

ER tubes often protruded into the IB, apparently interacting extensively with the fibrillar network: the ER-tubes are fully engulfed by the network and multiple fibrils touch the membranes. The electron densities of membranes and fibrils often appear continuous at points of contact (**Figure 3.10A and Figure 3.15**), indicating that the fibril-membrane distance is shorter than the pixel size (1.7 nm).

The high resolution of cryo-ET enables to uncover these interactions on a molecular level, but it also restricts the field of view: only < 5 % of the IB volume and surface are represented in the tomogram because of the limited detector size and thickness of the sample. To confirm the association of the ER with the IB on a more global scale, we used spinning disc confocal light microscopy. The ER is marked by KDEL-mCherry, where the KDEL amino acid sequence causes the retention of the fluorescent protein in the ER lumen. **Figure 3.11** demonstrates the intense accumulation of ER volume at the IB's boundary surface compared to the rest of the cell, indicating a non-local phenomenon that affects most of the IB's surface.

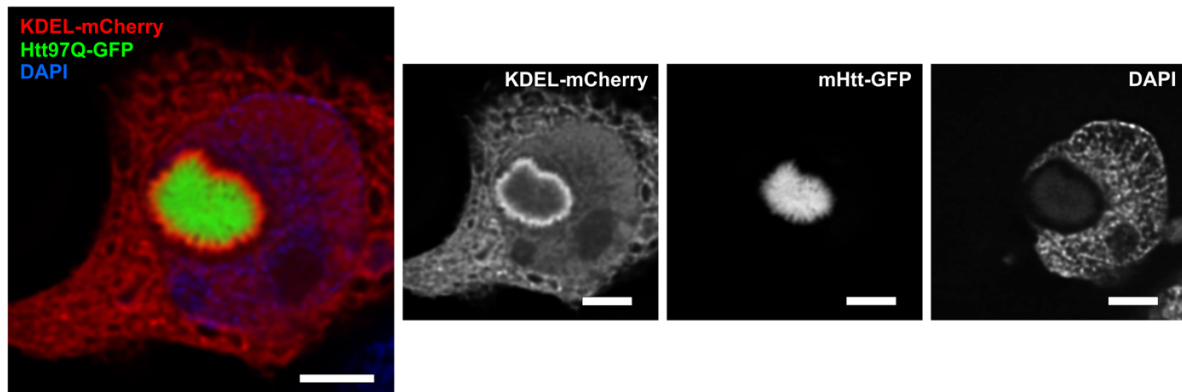


**Figure 3.11: ER association with Htt97Q-GFP IB in LM.**

HeLa cell co-expressing mHtt-GFP (green) and the ER luminal marker KDEL-mCherry (red). Spinning-disc confocal fluorescence imaging – micrographs deconvoluted. Note the accumulation of ER around the IB.

Interestingly, a heterogeneous population of vesicles is embedded in most cytosolic IBs (100%, neurons, Htt97Q-GFP | 94%, HeLa, Htt97Q-GFP | 82%, HeLa, Htt97Q) at sites of interaction with organelles (**Figure 3.10A,B**). Many of these vesicles were highly irregular in shape and are often in contact with fibrils. High membrane curvatures are observed at the site of contact, suggesting that the vesicles resulted from the disruption of organellar membranes upon interaction with the fibrils. Supporting this hypothesis is the occasional observation of vesicles – trapped with fibril-membrane contacts in the fibril network – with ribosomes bound to their membrane (**Figure 3.12**), suggesting that they originated from ruptured ER membranes.

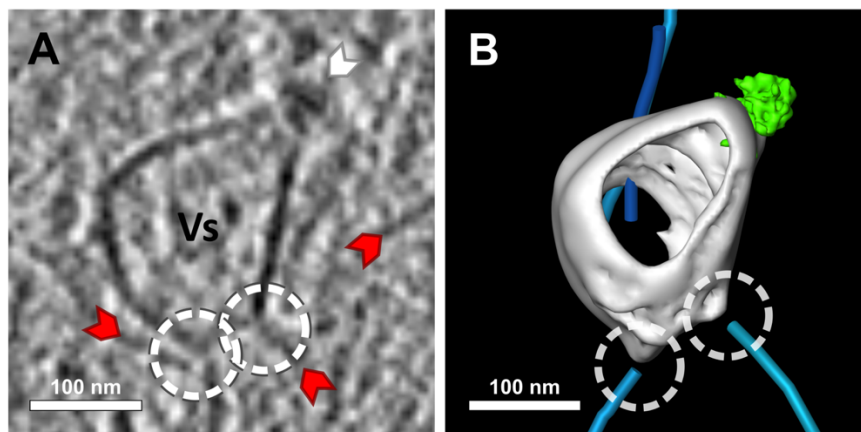


**Figure 3.12: Fibril associated vesicles with membrane-bound ribosomes trapped in IBs.**

**A:** Magnified tomographic slice of a membrane-bound ribosome (white arrowhead) on a small vesicle contacted (white circles) by the Htt97Q-GFP fibrils of an IB. Tomographic slice is 1.7 nm thick

**B:** 3D rendering of the vesicle shown in (A). Note the high curvature of the vesicle membrane at the sites of interaction with fibrils. (Modified from (Bauerlein et al., 2017). Reprinted, with permission from Elsevier.)

### INTERACTION OF IBs WITH OTHER ORGANELLES

Since Htt97Q±GFP IBs interact strongly with the endoplasmic reticulum, the question arises if other organelles are also affected and maybe trapped inside the IB. By light-microscopic imaging of HeLa cells loaded with Mito-Tracker, mitochondria are visible in the vicinity of IBs and more important are also trapped deep inside the IB (**Figure 3.13A**). In tomograms acquired by cryo-EM, mitochondria are observed at the IB's periphery in 35% - trapped mitochondria inside the IB (**Figure 3.13B**) are cached rarely and fibril-membrane contacts are not clearly identifiable, but the low number of observations does not exclude the possibility.

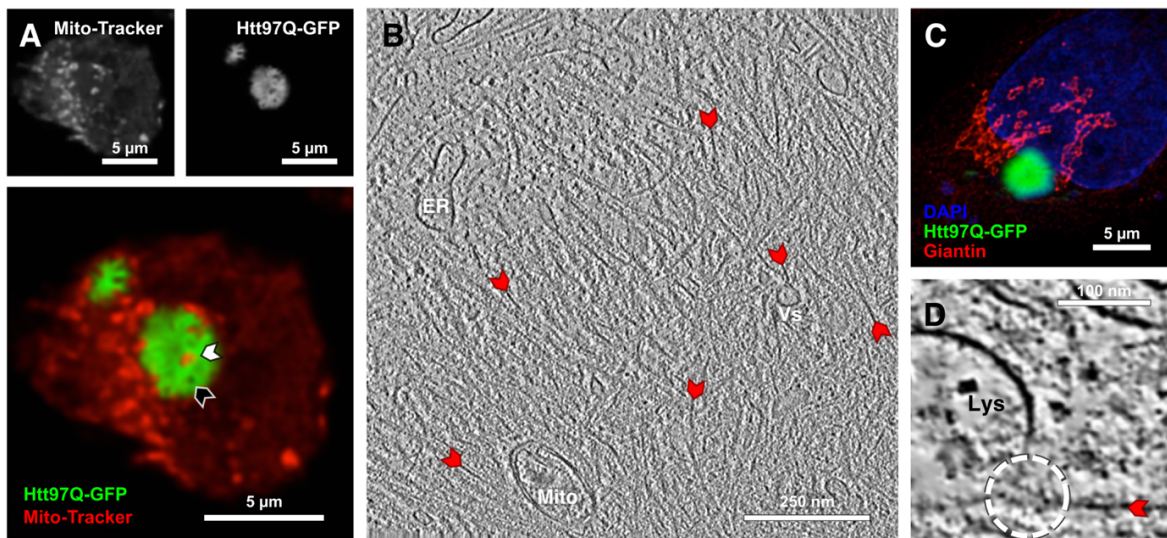


**Figure 3.13: Interactions of Htt97Q-GFP IBs with various organelles in HeLa cells.**

**A:** HeLa cell expressing Htt97Q-GFP (green) and loaded with Mito-Tracker (red). Note the mitochondria-positive structure inside the IB (white arrowhead). Other empty regions inside the IB are Mito-Tracker negative (black arrowhead) and may correspond to other organelles. **B:** Tomographic slice showing a mitochondrion (Mito) embedded inside an IB in an Htt97Q-GFP-transfected HeLa cell. ER, endoplasmic reticulum; red arrowheads, Htt97Q-GFP fibrils; Vs, vesicle. Tomographic slice is 2.5 nm thick **C:** HeLa cell expressing Htt97Q-GFP (green) and stained with antibodies against the Golgi marker giantin (red). **D:** Tomographic slice on the interaction (white circle) between an Htt97Q-GFP fibril and the membrane of a lysosome (Lys). (Modified from (Bauerlein et al., 2017). Reprinted, with permission from Elsevier.)

The Golgi apparatus was never observed to obviously interact with IBs by light microscopy of HeLa cells. Also by cryo-EM, the Golgi was only exceptionally seen in the vicinity of IBs, presumably due to its lower abundance.

Lysosomes are seen to be trapped inside IBs and fibrils clearly interact with the lysosome's membrane (**Figure 3.13D**) indicating a non-specificity of fibril-membrane contacts solely to the endoplasmic reticulum.

### POLYQ REPEAT LENGTH HAS NO STRONG INFLUENCE ON MEMBRANE INTERACTIONS

As described in chapter 3.2.2, the IB's architecture and the fibril morphology are independent of the length of the expanded polyQ tract. Since the length of the polyQ tract correlates negatively with the age of onset of symptoms in patients (**Figure 1.4B**), the interaction of fibrils with the ER - as a potential deleterious effect - needs to be investigated as a function of polyQ length. So far the interaction of IBs with endomembranes was investigated with Htt97Q±GFP. Here, HeLa cells expressing Htt64Q-GFP are analyzed concerning their IB's interaction with the endoplasmic reticulum. **Figure 3.14A,B** demonstrates the comparable effects of IB-membrane interactions with Htt64Q-GFP as seen with the longer polyQ version Htt97Q-GFP: the ER is closely associated to the IB's periphery, fibrils impinge on these membranes, ER tubes emerge deep into the fibril network and vesicles are also trapped inside the IB. However, the extent of ER association appeared to be slightly reduced in terms of overall occurrence.

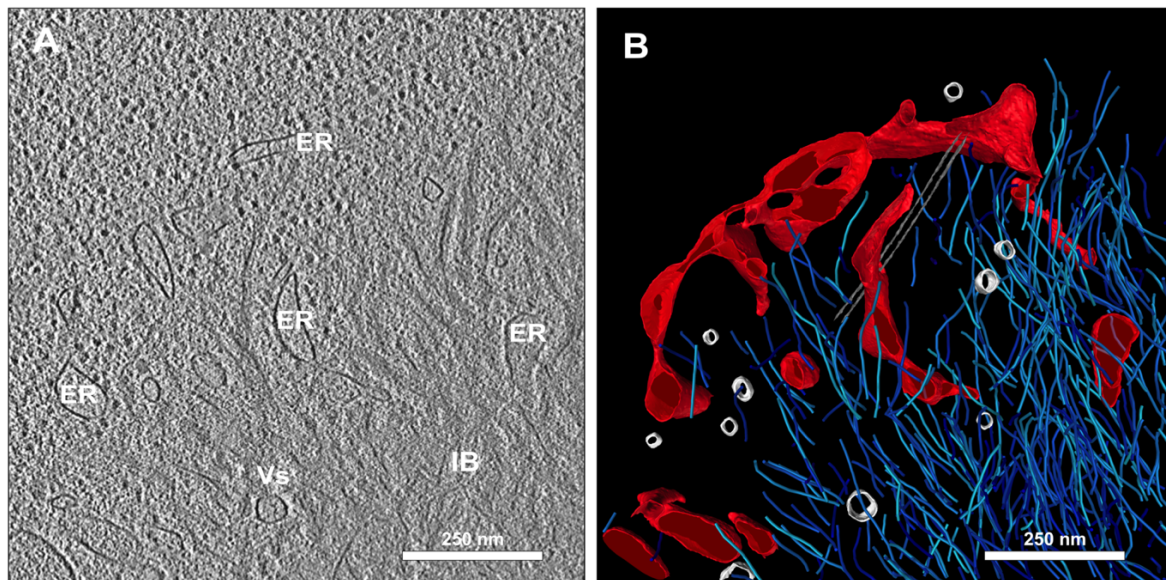


**Figure 3.14: Interactions of Htt64Q-GFP IBs with the ER in HeLa cells**

**A:** 2.5 nm thick tomographic slice of an Htt64Q-GFP IBs in a HeLa cell. Tomographic slice is 2.5 nm thick **B:** 3D rendering of the tomogram shown in (A). ER membranes (red), Htt97Q fibrils (cyan), membrane-bound vesicles (white), microtubule (gray parallel lines). Scale bars, 250 nm. (Modified from (Bauerlein et al., 2017). Reprinted, with permission from Elsevier.)

### 3.3.2 FILAMENT-MEMBRANE INTERACTIONS

This study shows for the first time in situ, that fibrils of Htt97Q±GFP interact strongly with endomembranes (**Figure 3.15**). **Figures 3.15A,C** present fibrils that contact ER membranes with their ends and sides – but also with lysosomes (**Figure 3.15B**). Often observed are spherical and asymmetric vesicles in contact with the fibrillar network (**Figure 3.15D-I**). Strong membrane deformations and atypically high membrane curvatures are noticed at the site of contact with the fibrils sides and ends in many cases (**Figure 3.15A-C,F-H**). Remarkable are also the extreme cases in **Figure 3.15A,B,F**, which show tube-like extrusions of the membrane at the site of fibril contact with almost rectangle edges in the membrane. The GFP-dependent decoration of fibrils - seen in Htt97Q-GFP fibrils - didn't change the affinity of the fibrils to membranes (**Figure 3.15G**).

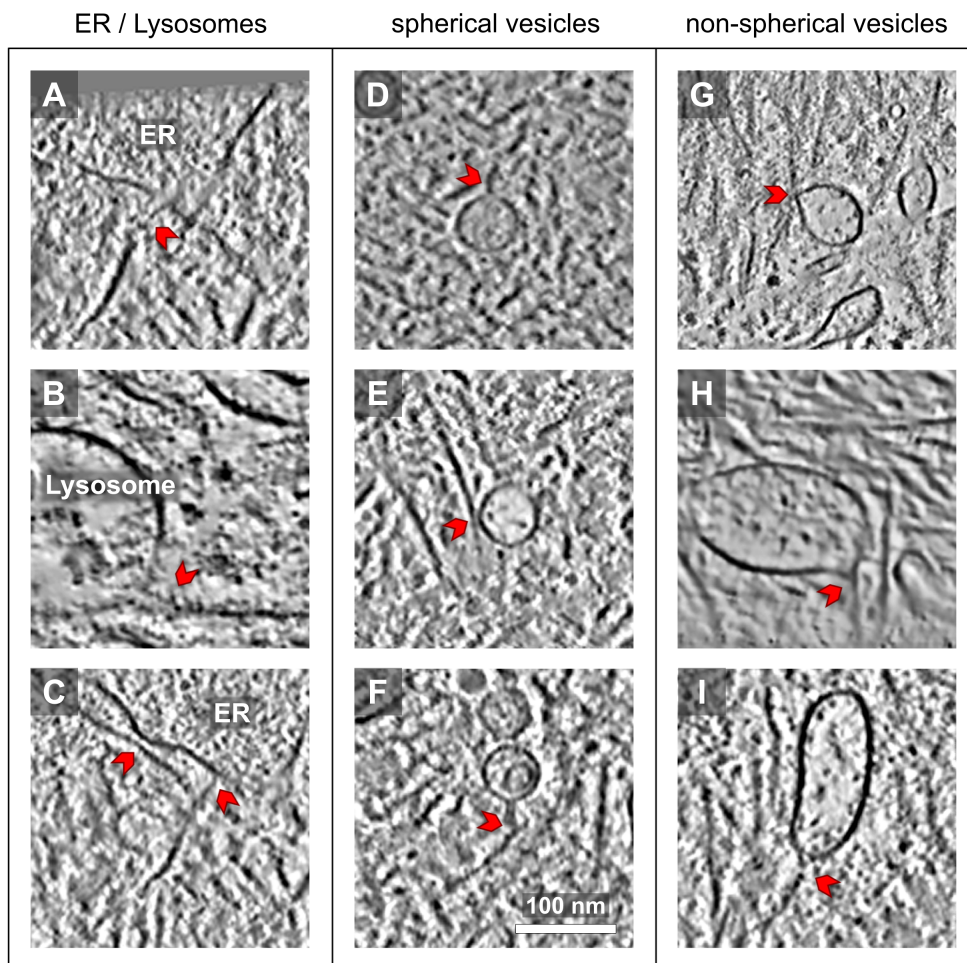


**Figure 3.15: Interaction of Htt97Q±GFP fibrils with endomembranes.**

This panel shows different interactions of Htt97Q±GFP fibrils with endomembranes. In the left column, ER membranes and a lysosome are shown, that are in contact with fibrils – strong deformations of the membrane are visible. The central / left column present spherical / non-spherical vesicles, trapped in the IB's volume. Also here high membrane curvatures are observable. Tomographic slices are 1.7 nm thick.



### 3.3.3 DEPENDENCE OF ER-DEFORMATION ON FILAMENTS

Sites of high membrane curvature and membrane deformation are seen at the point of contact between fibrils and membrane. To prove the causality of Huntingtin exon 1 fibrils inducing this effect, the following control cases are investigated:

- ER structures *distal from an IB* in HeLa cells containing a Htt97Q-GFP IB :

This control situation should prove the hypothesis that the direct local presence of Htt97Q-GFP fibrils is necessary to observe these high curvature regions in the ER membrane. **Figure 3.17A,B** exemplary demonstrates smooth ER membranes in the local absence of Htt97Q-GFP fibrils.

- ER structures in HeLa cells expressing *diffuse Htt97Q-GFP* without an IB :

The analysis of HeLa cells expressing diffuse Htt97Q-GFP should prove the hypothesis that high concentrations of the soluble species of Htt97Q-GFP are not causative for the high curvature regions in the ER membrane. This control also addresses the question if mono- and oligomers that could potentially diffuse off at the filament ends (Carulla et al., 2005) are causative. **Figure 3.17C,D** exemplary demonstrates smooth ER membranes in the presence of high concentrations of diffuse Htt97Q-GFP in the absence of fibrils.

- ER structures in HeLa cells expressing *Htt25Q-GFP* :

Htt25Q-GFP has a polyQ repeat length that is typical for physiological, non-pathogenic Huntingtin. As expected, no aggregation was observed for Htt25Q-GFP and **Figure 3.17E,F** exemplary demonstrates, that also in the non-pathological situation ER membranes are smooth and high curvature sites are not observed.

Since all performed experiments are based on overexpression of Huntingtin exon 1 after transient transfection, the question could arise, if these observed membrane deformations and high curvatures are an effect just of the overexpression of these proteins. To address this hypothesis, relative expression levels of the three huntingtin exon 1 constructs are measured by FACS analysis. **Figure 3.16** shows that the non-pathogenic Htt25Q-GFP is expressed at much higher levels than the pathogenic constructs Htt64Q-GFP and Htt97Q-GFP. However, no ER membrane deformations were observed in Htt25Q-GFP expressing cells (**Figure 3.17E,F**), suggesting that such deformations result specifically from the interactions of membranes with Htt64Q-GFP and Htt97Q-GFP fibrils and are not a mere consequence of overexpression.

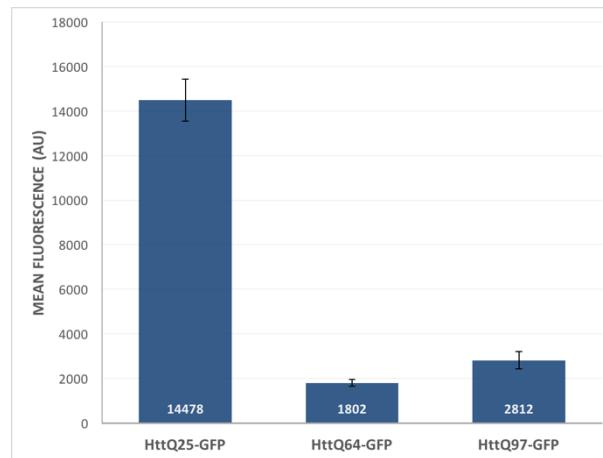


**Figure 3.16: Relative expression levels of the huntingtin exon 1 constructs.**

HeLa cells were transfected with Htt25QGFP, Htt64Q-GFP and Htt97Q-GFP. 24 hours after transfection cells were harvested, washed with PBS and analyzed by flow cytometry. Mean GFP fluorescence was computed. The average of triplicates was plotted showing mean (white numbers) and SD.

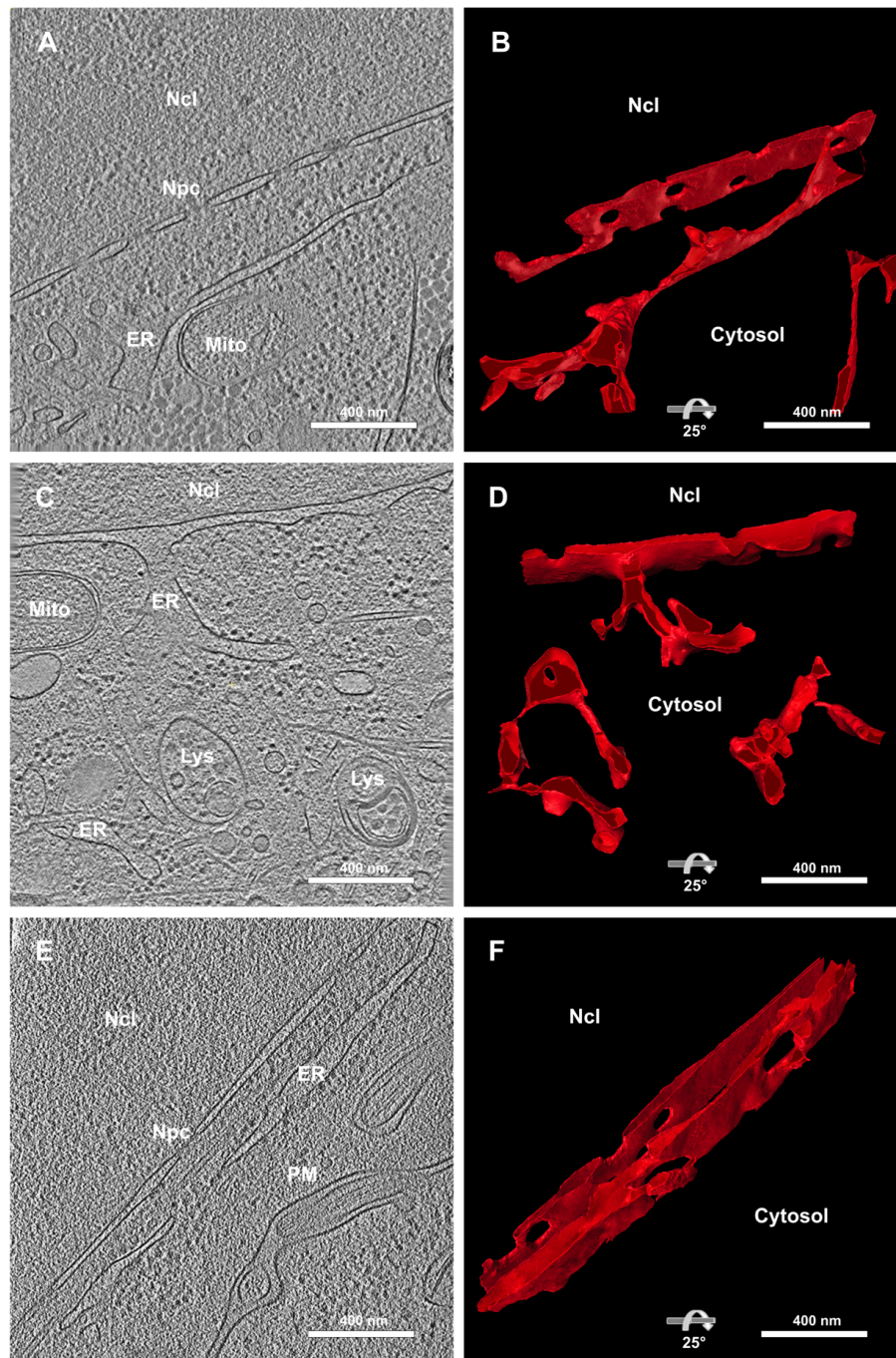


**Figure 3.17: Normal perinuclear ER morphology in HeLa cells in the absence of polyQ IBs.**

**A:** Tomographic slice of an area of the nuclear periphery distal from the IB in a HeLa cell containing an Htt97Q-GFP IB. **C:** Tomographic slice of the nuclear periphery of a HeLa cell expressing diffuse Htt97Q-GFP and no visible IB. **E:** Tomographic slice of the nuclear periphery of a HeLa cell expressing Htt25Q-GFP. **B,D,F:** 3D renderings of the tomograms shown in (A), (C) and (E) respectively, tilted 25° around the x-axis. ER membranes (red). In all cases, note the smooth ER membranes, in contrast to the deformed ER membranes observed in the vicinity of polyQ IBs (Figs. 1, 2, 3). ER, Endoplasmic reticulum; Lys, Lysosome; Mito, Mitochondria; Ncl, Nucleus; Npc: nuclear pore complex, PM: plasma membrane. Tomographic slices are 2.5 nm thick. Scale bars, 400 nm. (Reprinted from (Bauerlein et al., 2017), with permission from Elsevier.)

### Membrane Curvature

The qualitative observation of higher ER membrane curvatures in the vicinity of IBs was quantified in the following to be then compared statistically. For the purpose of quantification, an algorithm was developed (by Maria Kalemanov) that uses the segmentations of the ER membranes and calculates the local surface curvature (curvedness). Due to the lamella preparation, artificial membrane-boarders are exposed that are not present in the intact cell: the originally continuous membrane is artificially cut by FIB-milling and thus these membrane-cut sites bear high-curvatures that need to be neglected for the curvature calculation - this is realized in the algorithm. In **Figure 3.18** the curvedness of ER membranes in the vicinity of IBs were compared to ER membranes of control cells: the distributions of the normalized histograms differ significantly ( $p < 0.001$  by Kolmogorov–Smirnov test) and show higher curvedness of ER membranes in the vicinity of IBs. Note that sites with curvatures above  $1/10 \text{ nm}^{-1}$  were 20%–60% more abundant in the vicinity of inclusions.

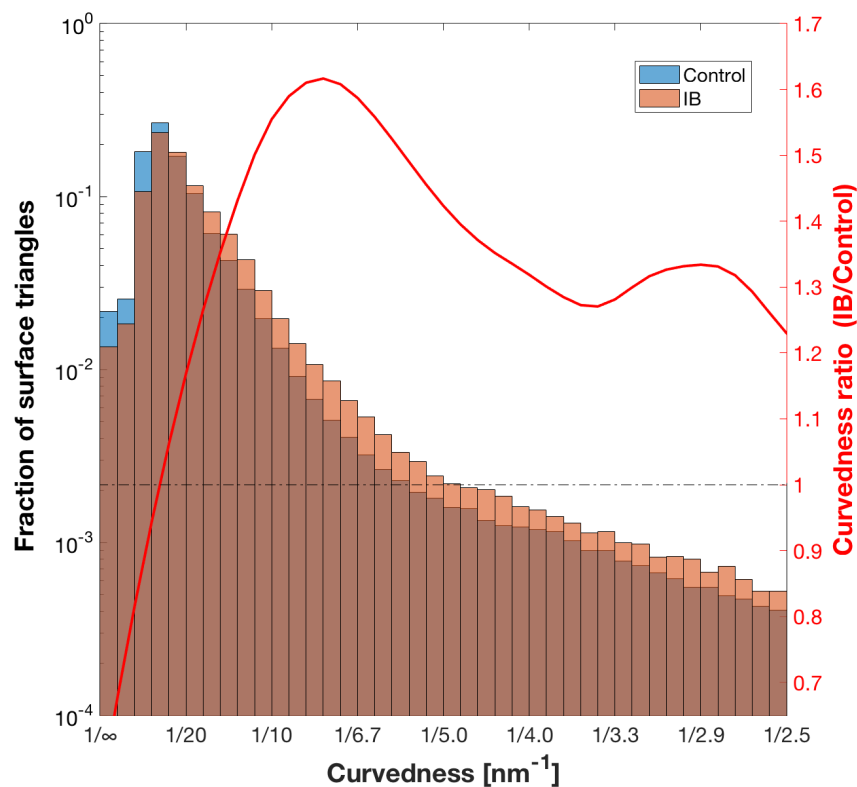


**Figure 3.18: Analysis of membrane curvature**

Histograms of ER membrane curvedness values as a measure of curvature. Curvedness was calculated for ER membranes in the vicinity of inclusions ( $n = 4$  tomograms, including two Htt97Q inclusions in HeLa cells, one Htt97Q-GFP IB in a neuron and one Htt64Q-GFP IB in a HeLa cell) and in control conditions ( $n = 3$  tomograms, including one of a Htt97Q-GFP IB-containing HeLa cell in an area distal from the IB, one of a HeLa cell expressing diffuse Htt97Q-GFP without visible IB and one of a HeLa cell expressing non-pathogenic Htt25Q-GFP; see Figure 3.17). The distributions of curvedness around inclusions and in control cells were significantly different ( $p < 0.001$  by Kolmogorov–Smirnov test). The red line shows the ratio between ER membrane curvatures around inclusions and in control cells. (Reprinted from (Bauerlein et al., 2017), with permission from Elsevier.)

### 3.3.4 ER-DYNAMICS AT IBs PERIPHERY

Based on the molecular resolution in cryo-EM tomograms, the previous three chapters showed that Huntingtin exon 1 fibrils touch and interact with ER membranes. Light microscopy of HeLa cells with an ER-luminal fluorescent protein (KDEL-mCherry) revealed an accumulation of ER volume at the IB's periphery. This static imaging allows no definite conclusion about the strength of the fibril-membrane association. The following analysis investigates the interaction between Htt97Q-GFP fibrils and ER membranes by live-cell imaging of the highly dynamic, molecular motor driven (Joensuu and Jokitalo, 2015; Pendin et al., 2011; Shibata et al., 2009) ER network (marked by KDEL-mCherry) in the whole cell compared to the vicinity of the IB.

**Figure 3.19A** presents the first image of a live cell movie. As a measure for the local dynamics of the ER, the variance of the pixel intensity is calculated over time (**Figure 3.19B,D**). Strikingly, this revealed a complete “freezing” of ER dynamics in the vicinity of Htt97Q-GFP IBs indicating a strong interaction between the fibrils and the ER. Thus the binding energy must be at least  $E_{\text{fibril-ER}} > k_B T$ , since thermal noise couldn't break this association, otherwise ER dynamics wouldn't be as dramatically reduced. This effect was not merely steric, as the ER was highly dynamic around other large cellular structures or the nucleus (**Figure 3.19A,B**).

This finding in individual cells is substantiated by averaging these measurements over a larger number of ER movies in different cells (N=44). For this, both ER abundance (pixel intensity of KDEL-mCherry) and ER dynamics (variance of pixel intensity) were radially averaged and normalized (**Figure 3.19C**, for details of the algorithm see **Appendix 6.4**). Note the substantial accumulation of ER (red curve) at the IB periphery ( $x = 0$ ) consistent over the whole population (narrow 95% CI) although there was some cell-to-cell variability on the extent of IB wrapping by the ER (see **Figure 6.1** in **Appendix 6.4**). Membrane dynamics were markedly slower in this ER domain – down to 30-50% at the region of maximal accumulation - than in more distal regions. This demonstrates that ER accumulation and reduced ER dynamics in the IB's periphery are indeed effects that are a typical feature in the presence of IBs and also remain after statistical averaging.

Thus this strong interaction between IB fibrils and the ER membrane may explain how vesicles result from the disruption of ER membranes.

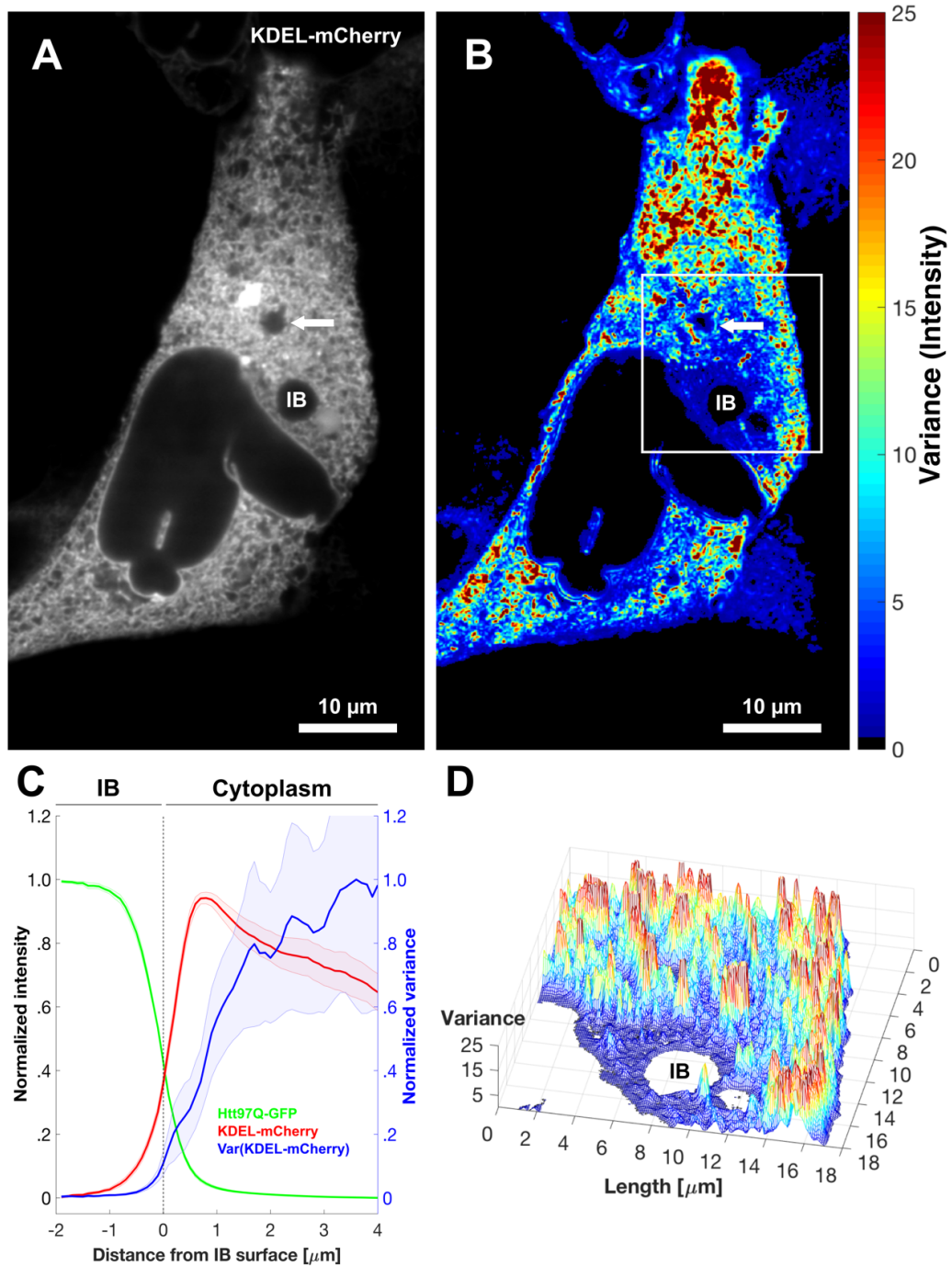


**Figure 3.19: Htt97Q-GFP IBs locally alter ER organization and dynamics.**

**A:** Additional example of a HeLa cell co-expressing Htt97Q-GFP and KDEL-mCherry. A white arrow points to an Htt97Q-GFP-negative large cytoplasmic structure around which ER dynamics are normal. **B:** ER dynamics of the cell shown in (A) quantified as the variance of KDEL-mCherry pixel intensity over time for 20 s. **C:** Quantification of ER membrane dynamics in the vicinity of Htt97Q-GFP IBs ( $N = 44$  cells). Note the substantial accumulation of ER (red curve; radial average of KDEL-mCherry pixel intensity) at the IB periphery ( $x = 0$ ). Membrane dynamics, assessed by the variance of KDEL-mCherry pixel intensity over time (blue curve), were markedly slower in this ER domain than in more distal regions. Radial averages (solid lines) and 95% confidence intervals (shaded areas) are shown. See **Appendix 6.4** for individual traces. **D:** 3D representation of the boxed region in (B) around the IB. (Modified from (Bauerlein et al., 2017). Reprinted, with permission from Elsevier.)

### 3.3.5 RELOCALIZATION OF ERAD COMPONENTS AND OTHER ER PROTEINS

Chapter 3.3.1 and 3.3.4 offered evidence that the endoplasmic reticulum typically accumulates at the IB's vicinity. This conclusion is drawn from imaging of KDEL-mCherry, which freely diffuses in the ER lumen and thus represents a measure of local ER volume.

The consequences of the interaction between IB's fibrils and the ER membrane were further investigated by immunostaining for a variety of ER-resident proteins: ER chaperones, components of the ER associated degradation (ERAD) machinery (Vembar and Brodsky, 2008) and some other important ER proteins.

#### ER CHAPERONES (CALNEXIN, CALRETICULIN, BiP, PDI)

ER chaperones detect misfolded proteins in the ER lumen and help them reach their native conformation. Calnexin is a membrane bound chaperone with luminal activity, Calreticulin is a luminal, soluble chaperone – both are  $\text{Ca}^{2+}$ -dependent and involved in  $\text{Ca}^{2+}$ -homeostasis. BiP is a luminal chaperone and also an essential component of the translocation machinery.

Calnexin was intensely enriched in the ER domain surrounding IBs whereas the soluble Calreticulin, BiP and PDI did not show this pattern (**Figure 3.20**). However, calnexin knock-out HeLa cells showed similar accumulation of the ER surrounding IBs.

#### ERAD (ERLIN-2, SEL1L, P97, OS9)

Terminally misfolded proteins in the ER are ubiquitinated and transported into the cytoplasm to be degraded by the ubiquitin-proteasome system – this pathway is called ER associated degradation (ERAD). ERLIN-2 and Sel1L are components of the ER membrane located ubiquitin ligase complex, OS9 is a luminal substrate binding protein, associating with Sel1L at the ER membrane, and p97 is involved in proteasomal targeting and located in the cytoplasm. It was shown that polyQ expanded huntingtin causes drastic defects in the ERAD machinery (Duennwald and Lindquist, 2008).

The ERAD components ERLIN-2 and Sel1L both accumulate in the ER domain surrounding IBs whereas p97 and OS9 did not show this pattern (**Figure 3.20**).

#### OTHER ER PROTEINS (SEC61, SERCA)

Sec61 is the ER translocon of the ribosome. SERCA is an ATP-dependent  $\text{Ca}^{2+}$ -pump localized in the ER membrane.

Interestingly Sec61 is not only not enriched but it is largely excluded from the IB's vicinity (**Figure 3.20**). SERCA is not seen to be enriched around IBs.

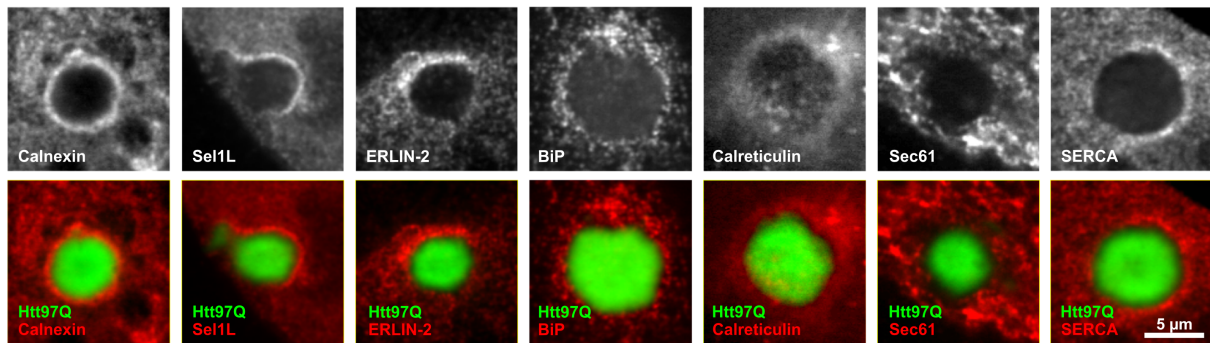


**Figure 3.20: Relocalization of ERAD components and other ER proteins at the interface of Htt97Q-GFP IBs.**

HeLa cells expressing Htt97Q-GFP (green) and stained with antibodies against the ER-proteins (red) calnexin, Sel1L, ERLIN-2, BiP, calreticulin, Sec61 and SERCA. (Modified from (Bäuerlein et al., 2017). Reprinted, with permission from Elsevier.)

### 3.3.6 DEPLETION OF MEMBRANE BOUND RIBOSOMES AT IB-ER INTERFACE

Cryo-EM tomograms of the IB periphery visualizing the interaction with the ER suggest that ER membrane regions in contact with fibrils are depleted of ribosomes (**Figure 3.11**). Supporting this is the observation in the previous chapter, that Sec61 – the translocon of the ribosome – appears to be depleted in the vicinity of IBs.

Template matching of membrane bound ribosomes revealed indeed a significant depletion of ribosomes attached to ER membrane regions in contact with the IB (**Figure 3.21**). A gradient of ribosomes is identifiable over the ER membrane from proximal to distal regions in **Figure 3.21A**. To better visualize the ribosome distribution on the ER membrane, a density metric was developed (by Maria Kalemanov) and applied (**Figure 3.21B**). The density metric sums for each voxel the distances on the membrane surface to all ribosomes, to yield a continuous measure. A further example is presented in **Figure 3.21C,D** which shows ER membranes almost completely engulfed in the fibril network and membrane bound ribosomes are completely depleted.

The loss of ER-bound ribosomes together with the translocase component Sec61, largely excluded from the IB vicinity suggests that translation is halted in this region.



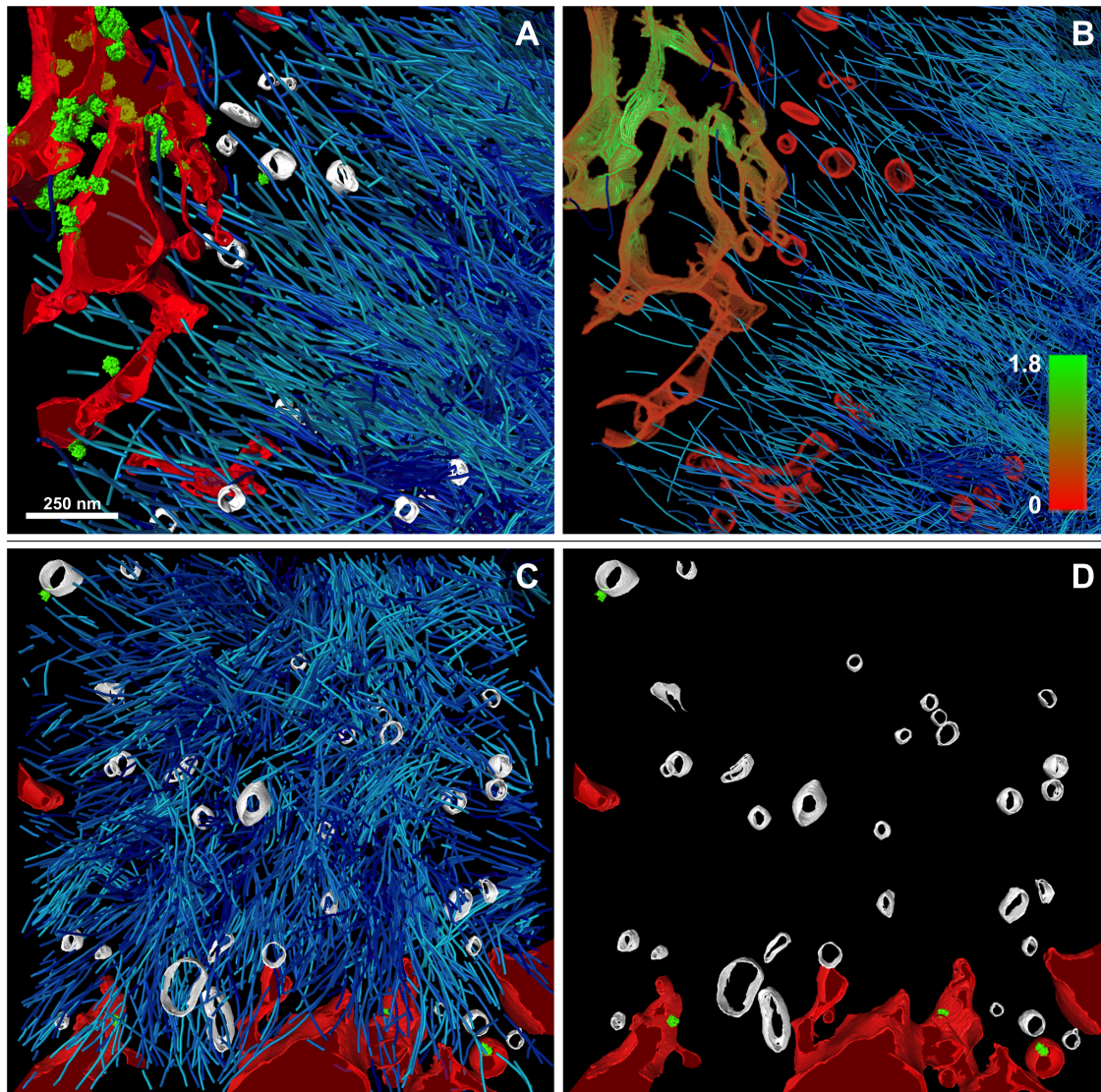


**Figure 3.21: Depletion of ER-bound ribosomes at the IB's periphery.**

**A:** 3D rendering of the tomogram from the interaction zone between an IB and cellular membranes in an Htt97Q-transfected HeLa cell. ER membranes (red), ER-bound ribosomes (green), Htt97Q fibrils (cyan), and vesicles inside the IB (white). **B:** Visualization of the density of membrane-bound ribosomes in (A). Ribosome density is indicated by color and is lower (red) on ER membranes in direct contact with fibrils. **C:** 3D rendering of ER membranes and ER-bound ribosomes in the vicinity of Htt97Q fibrils in a different cell. Note that ER-bound ribosomes are almost completely depleted from ER membranes directly interacting with Htt97Q fibrils. **D:** Same 3D rendering as in (C), but with Htt97Q-fibrils removed for better visibility of the very few ribosomes, that are present in the interaction zone. Scale bar for A-D shown in (A). (Modified from (Bauerlein et al., 2017). Reprinted, with permission from Elsevier.)

## 3.4 HUNTINGTIN AGGREGATION IN PRIMARY HIPPOCAMPAL NEURONS

Huntington's Disease is a predominantly neurodegenerative disease, and the most serious and prominent symptoms are results of cytotoxic effects of neurons in specific brain regions. However, huntingtin is expressed ubiquitarily in all tissues and HD patients develop multiple non-neurological symptoms like heart insufficiency and diabetes mellitus. IBs can be found in these and other tissues of HD mice and HD patients, including cardiac and skeletal muscle, pancreas and liver (Björkqvist et al., 2005; Ciammola et al., 2006; Jansen et al., 2017; Moffitt et al., 2009; Orth et al., 2003; Sathasivam et al., 1999; van der Burg et al., 2009).

The comparison of Htt97Q-GFP fibrils in this study revealed identical morphology (chapter 3.2.2) and elastic properties (chapter 3.2.4) in HeLa cells and neurons. These aspects justified the analysis of Htt97Q-GFP aggregation in HeLa cells, as it is possible to investigate a larger number of cells with IBs in this system.

Finally, to examine the neuronal relevance of the cellular interactions found in HeLa cells as described in chapter 3.3, we investigated these interactions as well in primary hippocampal mouse neurons transfected with Htt97Q-GFP.

### 3.4.1 CELLULAR INTERACTIONS OF IBs IN NEURONS

Primary hippocampal mouse neurons were transfected after 6 days in culture with Htt97Q-GFP. After 24h of expression neurons were vitrified. **Figure 3.22A,B** demonstrates a Htt97Q-GFP inclusion body in a primary hippocampal neuron: the overall IB architecture is indistinguishable from the ones observed in HeLa cells – fibrils are radially oriented, the fibril density is comparable and fibrils are similar in morphology and elastic properties. Also here, the ER is accumulating at the IB's periphery and ribosome-free ER tubes protrude into the IB, apparently interacting extensively with the fibril network. **Figure 3.22C** visualizes this situation with multiple fibrils in contact with the ER membrane, presumably preventing this structure from retraction. Many vesicular membrane structures are seen to be trapped inside the fibril network. In the shown example (**Figure 3.22B**) 45 vesicles are visible in the tomogram, which represents ~ 9% of the IB's total volume – extrapolated ~ 500 vesicles can be expected to be trapped in the entire IB. Many of the trapped vesicles and surrounding ER membranes show contact with fibrils (**Figure 3.22C,D**).

Both in primary neurons and HeLa cells, large macromolecules like ribosomes are not found inside the IB volume, although there would be space in between the fibrils. Template matching for cytosolic and membrane bound ribosomes revealed a complete depletion in the IB volume (**Figure 3.22A,B**). The free diffusion of macromolecules with a hydrodynamic radius of ribosomes is obviously hindered inside the IB's gel-forming fibrillary network.

In total, all observed cellular interactions and morphological features observed in HeLa cells are recapitulated in primary hippocampal neurons, proving the legitimacy and applicability of the investigations in HeLa cells.

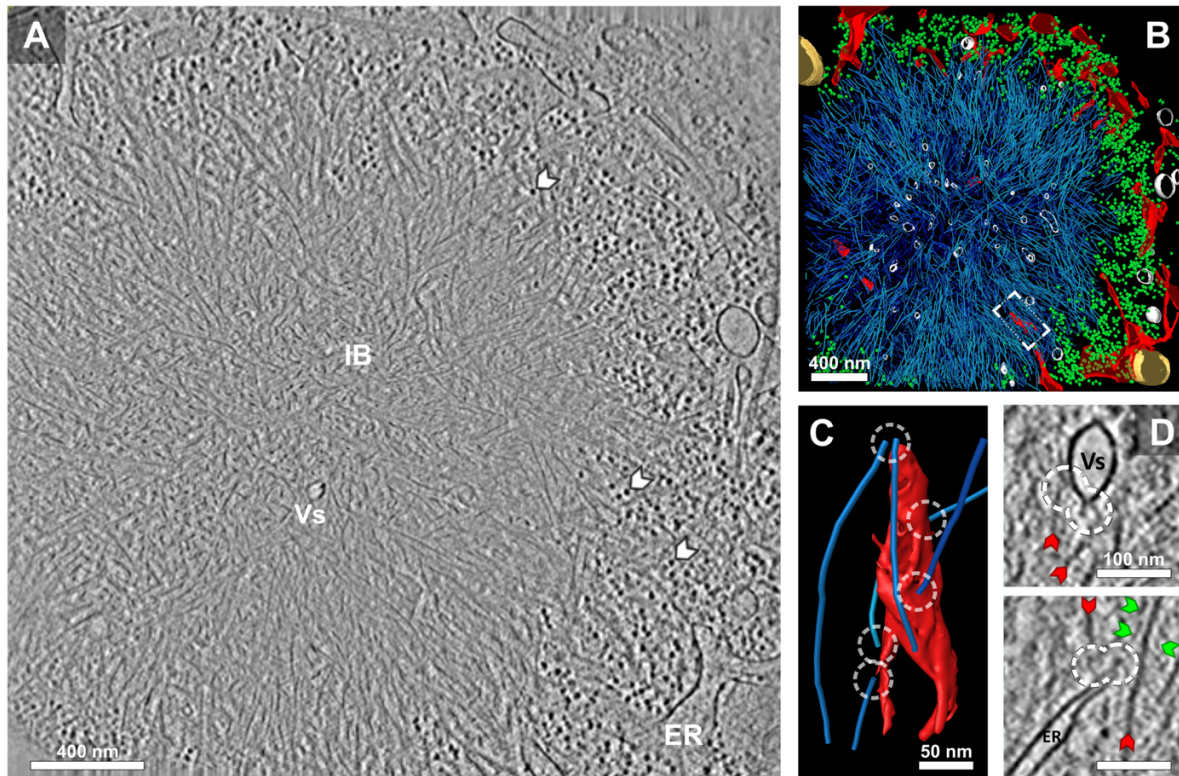


**Figure 3.22: Htt97Q-GFP IBs in primary hippocampal neurons.**

**A:** Tomographic slice of an IB in a Htt97Q-GFP-transfected mouse primary neuron. The cytoplasmic electron dense particles represent ribosomes (white arrowheads). ER, endoplasmic reticulum; Vs, vesicle. **B:** 3D rendering of the tomogram shown in (A). ER membranes (red), Htt97Q-GFP fibrils (cyan), ribosomes (green), vesicles (white), mitochondria (gold). Note that the core of the IB is largely devoid of ribosomes, which accumulate at the IB periphery. **C:** Magnified rendering of the region marked in (B) showing interaction sites (white circles) between the sides and the ends of Htt97Q-GFP fibrils and the ER membrane. **D:** Magnified tomographic slices showing Htt97Q-GFP fibrils (red arrowheads) decorated by globular densities (green arrowheads) interacting with cellular membranes in Htt97Q-GFP transfected neurons. Tomographic slices are 2.8 nm thick. (Modified from (Bauerlein et al., 2017). Reprinted, with permission from Elsevier.)

### 3.4.2 NUCLEAR IBs

Nuclear IBs are described to occur in higher frequencies in neurons than in other cell types (Jansen et al., 2017). Their role versus cytosolic IBs in cytopathology is unclear and interpreted differently in context of their structure (André et al., 2013; Hoffner and Djian, 2015).

Cryo-EM tomograms of primary hippocampal neurons showed a fraction of nuclear vs. cytosolic IBs of  $55 \pm 9\%$  (**Table 3.1**) and in HeLa cells  $10 \pm 5\%$ . The uncertainty about their structure in neurons can be specified: nuclear IBs are not amorphous - aggregation occurs ordered and results in amyloid-like fibrils, that are comparable to fibrils of cytosolic IBs in neurons (**Figure 3.23**). The overall architecture is also similar. Nuclear IBs are surrounded by chromatin, which is excluded from the IB's volume. Interestingly, no interaction was observed between fibrils and the inner nuclear membrane, nor were vesicles trapped inside the nuclear IBs indicating differential mechanisms of cellular interaction (Benn et al., 2005; Gu et al., 2015; Liu et al., 2015).

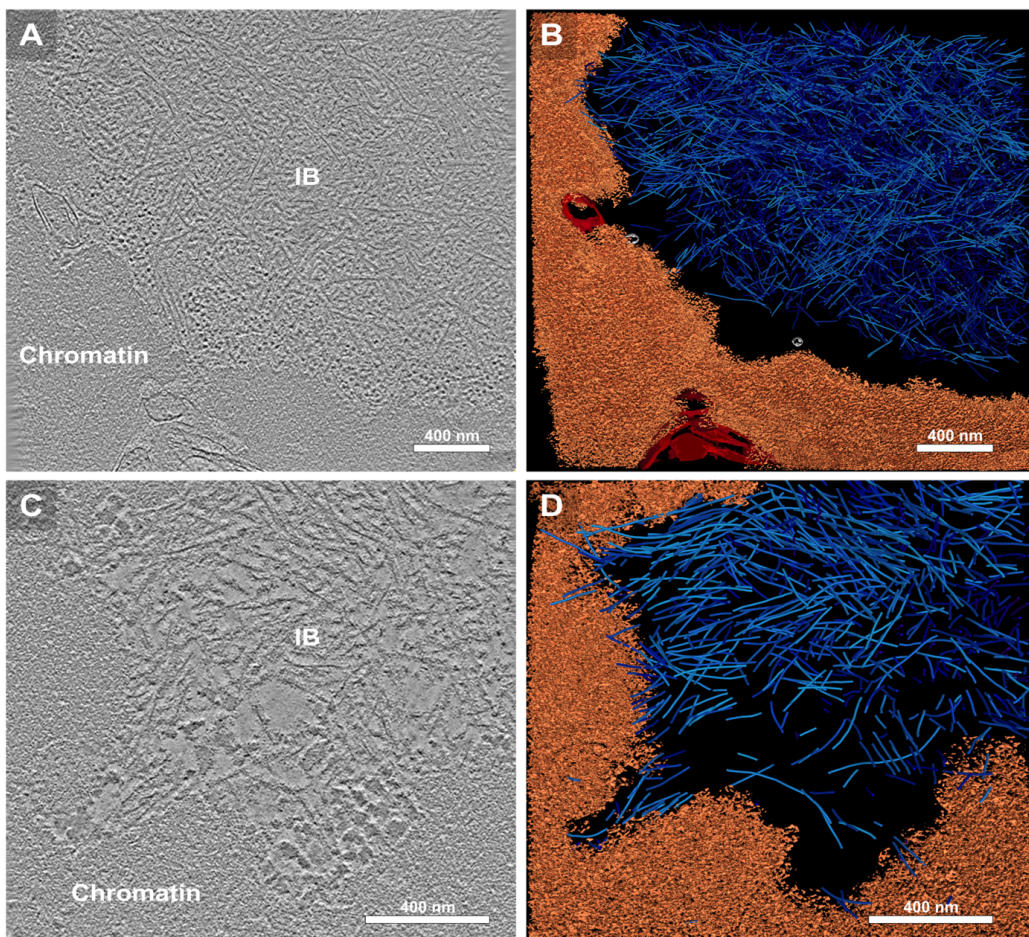


**Figure 3.23: Nuclear Htt97Q-GFP IBs in primary hippocampal neurons.**

**A,C:** 1.7 nm thick tomographic slices of nuclear IBs in mHtt-GFP-transfected neurons. **B,D:** 3D renderings respectively corresponding to (A) and (C). Chromatin (orange), nuclear envelope membranes (red), membrane-bound vesicles in the periphery of the IB (white), mHtt fibrils (cyan). (Modified from (Bauerlein et al., 2017). Reprinted, with permission from Elsevier.)



## 4

## DISCUSSION

4.1 POLYQ EXPANDED HUNTINGTIN EXON 1 FORMS  
FIBRILLARY IB'SHOW IS THE MOLECULAR ARRANGEMENT IN IB'S? ARE IB'S STRUCTURED OR  
AMORPHOUS?

While polyQ-expanded Htt exon 1 forms fibrils in vitro (Scherzinger et al., 1997), it has remained controversial for decades whether Htt in cellular IBs is present in granular or fibrillar form (Davies et al., 1997; DiFiglia et al., 1997; Finkbeiner, 2011; Petrasch-Parwez et al., 2007; Qin et al., 2004; Waelter et al., 2001).

These studies tried to identify the ultrastructural organization of Huntingtin IBs inside cells with classical electron microscopy. They described the IBs substantially as amorphous granular and less fibrillar, while the resolution was often too low to answer this question with certainty. The ultrastructure of IBs in the brains of HD patient brains shown by (DiFiglia et al., 1997) is indistinguishable from that of IBs found in HD mice expressing only exon 1 (Davies et al., 1997), as it was reported in the latter paper. The IBs found in HD mice brain expressing exons 1-15 (Petrasch-Parwez et al., 2007) were furthermore described as both granular and fibrillar.

Study	System	construct	IB appearance (classical EM)
Miller et al. 2010	-Primary striatal culture (rat)	HttQ64,72,97-GFP exon 1	granular / amorphous
Petrasch-Parwez et al. 2007	-tgHD rats -R6/2 mice	Q51 Htt exon 1-15 Q141-157 Htt exon 1	granular & fibrillar
Qin et al. 2004	-MCF-7	FH969-100Q	granular & fibrillar
Waelter et al. 2001	-293 Tet-Off	Hdq83 exon 1	fibrillar
DiFiglia et al. 1997	-HD patients	endogenous Htt	granular & fibrillar
Davies et al. 1997	-R6/2 mice	Q141-157 Htt exon 1	granular (occasional fibrillar)

**Table 4.1: Overview of studies investigating the molecular structure of IBs**

In contrast to the existing findings, we were able to show based on high resolution imaging that mutant Huntingtin Exon 1 gives rise to purely fibrillar IBs. The mentioned studies all used conventional preparation techniques for electron microscopy: due to dehydration, plastic embedding and heavy metal staining, they are all likely to cause structural alterations. Thus, these methods are inapt for molecular resolution imaging of biological specimens. Furthermore, the fibrils in heavy-metal stained preparations appeared substantially thicker than Htt97Q fibrils (Qin et al., 2004). The great advantage of cryo-electron tomography over conventional electron microscopy is its high molecular resolution that even visualizes GFP dependent tags on the fibrils and therefore offers an unperturbed view into these IBs in their cellular environment.

## WHAT IS THE IMPACT OF THE POLYQ REPEAT LENGTH ON IB FORMATION AND FIBRIL PROPERTIES?

The onset of symptoms in HD is highly correlated with the polyQ repeat length (Finkbeiner, 2011; Gusella and MacDonald, 2007), while disease progression in terms of duration of disease, from onset till death (Gusella and MacDonald, 2007), as well as the metabolic decline over time in the caudate (Clarke et al., 2000) are not related to the polyQ length. Aggregation kinetics in vitro have also been shown to strongly depend on polyQ length (Scherzinger et al., 1997) with longer polyQ repeats aggregating earlier than shorter ones. Therefore, it is likely that different polyQ lengths give rise to similar mechanisms of cellular toxicity, but with different kinetics.

We investigated the impact of polyQ length (Htt64Q-GFP, Htt97Q-GFP, Htt150Q-GFP) on IB formation and fibril properties. Our observations conformed to the existing research findings that in vivo IBs formed earlier with longer polyQ length. Our data show that Htt64Q-GFP, Htt97Q-GFP and Htt150Q-GFP IBs were structurally very similar, as these are formed by amyloid-like and radially arranged fibrils that interact with cellular membranes. The stiffness of Huntingtin exon 1 fibrils is invariant to the species (human vs. mouse) and to the cell origin (neuron vs. HeLa) – the presence of GFP increases fibril stiffness by 25%.

In summary, IB architecture and membrane interactions are comparable in cells expressing Htt64Q-GFP or Htt97Q-GFP. This argues against a strong influence of the exact length of the expanded polyQ tract on fibril structure and arrangement.

---

## WHAT CAN BE DERIVED FROM THE ARCHITECTURE OF IBs ?

This study showed the polymeric nature of the IBs to be fibrillar and that fibrils are not randomly arranged but have a higher order organization. The overall shape of the IBs is typically spherical to ellipsoidal. The architecture of IBs generally shows a radial arrangement of fibrils, most of them pointing to the IBs center. As the mean length of the fibrils is smaller than 1/10 of the IBs diameter, most of them don't originate from the IBs center, but still point in this direction. This suggests an initial nucleation core in the center of the IB and an outward growth of fibrils towards the surface. Another strong indication for this mechanism is the lack of trapped macro molecules like ribosomes in the fibrils network and an accumulation in the IBs periphery. This finding indicates that ribosomes are being pushed aside, while the fibril network grows from the center. The radial alignment of fibrils could not be explained by the hypothesis of a secondary assembly of preformed smaller fibrillar aggregates, but rather points to an IB nucleation and growth at site. (Johnston et al., 1998) proposed a model of regulated IB formation based on light microscopy data: the transport of aggregated species along microtubules towards the MTOC results in an inclusion body called 'aggresome' – that analysis was repeated with other proteins, amongst others also Htt104Q-GFP exon 1 (Lelouard et al., 2004; Muchowski et al., 2002; Shimohata et al., 2002), and interpreted similarly. This interesting model was not supported by our data - primarily due to the typical radial arrangement of the fibrillar network, but also due to the missing coincidence of IBs and the MTOC. Admittedly, the MTOC was rarely observed (3/201 tomograms), but never inside of IBs.

Supporting the idea of a nucleated growth at site rather than a transport is the observation that fibrils are exclusively seen in the bulk of an IB but never 'free' in the cytoplasm. Single fibrils of Htt97Q-GFP would be identifiable by the GFP tags lining the fibril, but have never been observed in the cytosolic fractions of the tomograms, suggesting that 'free' fibrils are not very common, if present at all.

The radial arrangement is the typical order that was observed in a large majority of the IBs. Occasionally the architecture deviates from this alignment and fibrils are packed together in a rather only locally oriented or patchy way, suggesting multiple nucleation centers – alternatively these rare forms could have formed by the aggresome-model.



## 4.2 CELLULAR INTERACTIONS OF IBs

### DO IBs INTERACT WITH THEIR CELLULAR ENVIRONMENT AND WHICH CELLULAR STRUCTURES ARE AFFECTED?

Physiological wild type Htt is known to interact with cellular membranes (Kegel-Gleason, 2013) and about half of it is found in association with these (DiFiglia et al., 1995; Kegel et al., 2000; Velier et al., 1998).

Fibrils of polyQ expanded Htt exon 1 and other amyloids associate with and cause membrane disruption in vitro (Milanesi et al., 2012; Pieri et al., 2012). So far there was no evidence that this also happens inside intact cells. (Milanesi et al., 2012) investigated the interaction of amyloid-like fibrils ( $\beta$ -microglobulin) with liposomes by cryo-electron tomography: the authors found strong interactions of these fibrils with liposomes (**Figure 4.1**), causing strong distortion and furthermore extraction of lipids at these high curvature sites. This observation is highly interesting in the light of neurodegenerative diseases, in which the different disease proteins form amyloid-like fibrils: if this observation could be proven in situ and shown to be significant between IBs and cellular membranes, this could explain a new, so far not-envisioned, possible mechanism of toxicity in neurodegeneration.

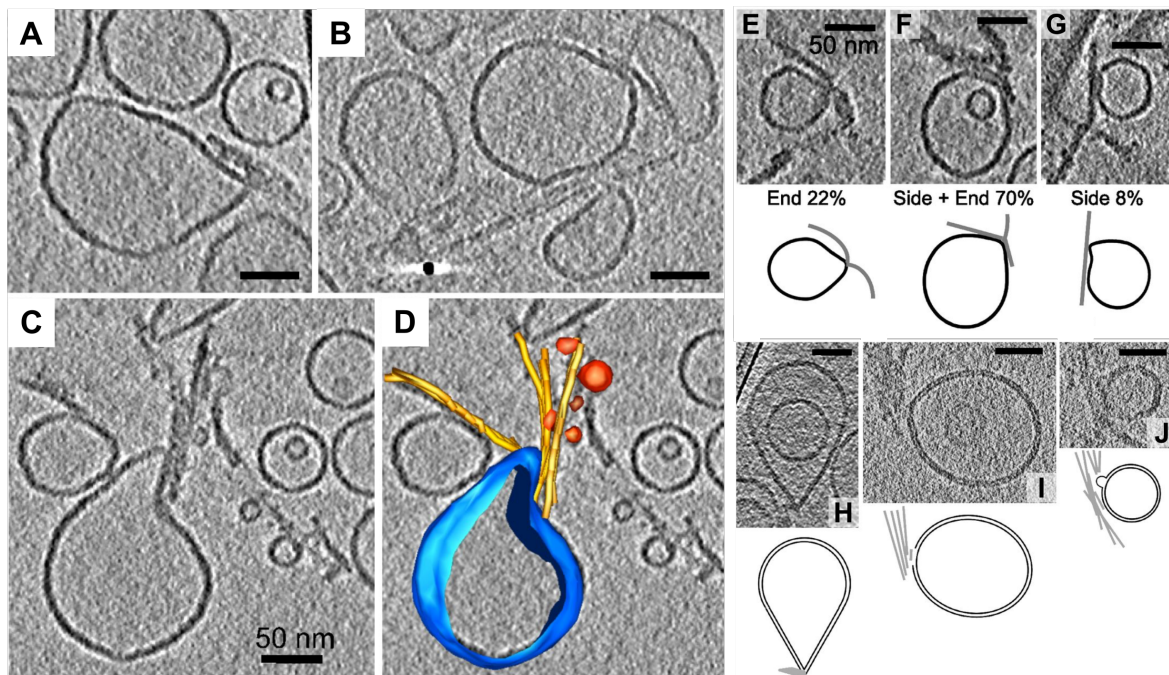


**Figure 4.1: In-Vitro Cryo-Electron Tomography of Liposome–Fibril Interactions.**

**A–C:** Sections of tomograms showing liposomes clustered and distorted by short fibrils. **D:** A rendered 3D model of a distorted liposome, surrounding fibrils and adjacent small vesicles from (C). Scale bar: 50 nm.

**E–J:** Distortions of liposomes in the vicinity of fibril ends. **E–G:** Examples and cartoons of the different types of fibril–liposome interactions observed, with the percentage of each type measured by counting examples in four tomograms. **H–J:** Sections of tomograms taken closer to focus, showing examples of the disruption of the lipid bilayer in the region of fibril ends, including **H:** formation of a sharp point, **I:** a break in the outer leaflet of the membrane, and **J:** a bubble forming in the outer leaflet, with corresponding cartoons showing membranes as black lines and fibrils as gray lines. Scale bar: 50 nm. (from (Milanesi et al., 2012), with permission)

We were able to show for the first time that IBs of fibrillar polyQ expanded Htt exon 1 associate in vivo with endomembranes in their native cellular environment. Our results suggest that Htt exon 1 IB fibrils impinge on and disrupt cellular endomembranes.

Most prominently this interaction occurred with the endoplasmic reticulum: our cryo-EM tomograms showed on a regular basis that ER tubes protrude into IBs, are fully engulfed by the network and multiple fibrils touch the membranes. This phenomenon has been observed in the vast majority of all tomograms showing an IB close to the ER. Therefore, these ER tubes protruding into the IB do not seem to be merely thermal fluctuations of the ER membrane. They are rather fibril membrane contacts that are at least stronger than  $k_B T$  and thus are holding these membrane structures in place. This is supported by the observation of local high membrane curvatures at these contact sites. These tubes inside the IB are only observed, when fibrils impinged on them.

Using fluorescence LM these local observations were shown to happen globally at most of the IB's surface: – the ER is intensely accumulating at the IB's boundary surface compared to the rest of the cell.

Since the interaction with the ER is very prominent, we wondered whether this interaction is specific to the ER membrane or if other organelles are also affected.

With fluorescence LM, mitochondria were also seen to accumulate in the IB's vicinity. More importantly they were also trapped inside the fibril network, without structurally communicating with the mitochondrial network. In 35% of the tomograms Cryo-EM tomography showed mitochondria in close contact with the IB's surface. Mitochondria that were trapped inside the IB were rarely found and fibril membrane contacts were not clearly identifiable.

The Golgi apparatus was never observed to interact with the IB, neither in cryo-EM tomography nor in fluorescence LM. Presumably this is due to its low abundance in the cell.

In contrast, lysosomes were seen to be trapped inside IB's and fibrils clearly interacted with lysosomal membranes. This indicates that fibril-membrane contacts do not exclusively occur with the endoplasmic reticulum.

The frequent observation of this interaction could be explained by the high presence of ER membranes especially at the site of the typical peri-nuclear occurrence of IBs. Also a large number of spherical and non-spherical vesicles are found in the IBs network, that interact strongly the fibrils.

As the vast majority of fibril-membrane interactions were seen to happen with the ER membrane, the question arises, if this interaction is rather lipideous or proteinaceous.

The association of wild type Htt with membranes is shown to be lipid based and has a particular affinity for cardiolipin and phosphatidylinositol phosphates (Kegel et al., 2009; Kegel-Gleason, 2013). PolyQ expanded mutant Huntingtin associates significantly more with phosphatidylethanolamine and PI(3,4,5)P<sub>3</sub> than wild-type huntingtin does and it associates with other phospholipids not recognized by wild-type huntingtin (Kegel et al., 2009). Htt has two putative membrane-binding domains (Kegel-Gleason, 2013), one of which is present in the Htt exon 1 construct used in this study: the N-terminal 17 amino acids form an amphiphatic helix (Michalek et al., 2013).

Fibril-membrane interactions are assumed to be largely lipid-mediated (Burke et al., 2013; Kegel et al., 2005; Trevino et al., 2012). Whether any specificity for ER membranes exists (Atwal et al., 2007) remains to be determined.

## WHAT ARE THE CONSEQUENCES OF THE IB-MEMBRANE INTERACTION?

We were able to show that IBs of fibrillar polyQ expanded Htt exon 1 associate in intact cells with endomembranes in their native environment. Our results show that Htt exon 1 IB fibrils impinge on cellular endomembranes: most prominently the ER, but also on Lysosomes. Interestingly, at the site of contact between fibril and membrane, typically a very high membrane curvature can be observed. These very high curvature membrane deformations of the ER are less often observed in the absence of fibrils:

- ER structures in HeLa cells, overexpressing a non-pathological and non-aggregating Htt exon 1 version with a polyQ length of 25 glutamine repeats (Htt25Q-GFP)
- ER structures in HeLa cells, overexpressing diffuse Htt97Q-GFP, but didn't form yet an IB and
- ER structures, distal from an IB in HeLa cells containing an Htt97Q-GFP IB.

In all these conditions with overexpression of polyQ-stretched or non-pathological Htt exon 1, the presence of fibrils and their contact with membranes caused local correlated high curvature membrane deformations. It could be discarded that overexpression was a cause for this phenomenon, since expression levels were significantly higher for Htt25Q-GFP than for Htt97Q-GFP and high curvature membrane deformations were not increased in this case.

Although it is possible that not the fibrils directly cause this phenomenon, but oligomers dissociating from the fibril ends (Carulla et al., 2005; Martins et al., 2008) contribute to these effects, high concentrations of soluble Htt97Q-GFP did not disturb membrane morphology in the absence of IBs.

Almost all investigated cytosolic IBs accumulated ER in their periphery (observed by fluorescence LM) and fibrils impinged regularly on the ER membranes (observed by cryo-ET). Interestingly, vesicles were almost always trapped in the IB's fibril network close to the interface between fibril and ER membrane in contrast to nuclear IBs that were not interacting with the inner nuclear membrane and not presenting trapped vesicles. Many of these vesicles were highly irregular in shape and were often in contact with fibrils at regions of high membrane curvature, suggesting that they resulted from the disruption of organellar membranes upon interaction with the fibrils. Fluorescence LM revealed puncta positive for ER markers trapped inside some IBs but disconnected from the ER network. Remarkable is the observation that some trapped vesicles carried ribosomes, suggesting that they originated from ruptured ER membranes. This hypothesis is supported by *in vitro* experiments, in which fibrils of polyQ expanded Htt exon 1 and other amyloids caused membrane disruption (Milanesi et al., 2012; Pieri et al., 2012).

To augment these static observations with kinetic information concerning the interaction of IBs with ER membranes, HeLa cells with IBs were investigated by live cell imaging. Strikingly, this revealed that the region of the ER surrounding the IBs was in general dramatically reduced in membrane dynamics, suggesting that a wide variety of cellular processes that depend on the dynamic behavior of the ER (Zhang and Hu, 2016) might also be affected. This effect was not merely steric, as the ER was highly dynamic around other large cellular structures or the nucleus – indicating a definitive adhesive interaction with the fibrils.

The complete “freezing” of ER dynamics in the vicinity of Htt97Q-GFP IBs is indicating a strong adhesion between the fibrils and the ER. Thus the binding energy can be expected to be at least  $E_{\text{fibril-ER}} > k_B T$ , since the association resists thermal noise.

Prerequisite for this is, that the filaments can tolerate these forces. From the static cryo-EM tomograms, elastic properties like the persistence length, bending stiffness and Young’s Modulus can be directly derived, and the tolerance against these forces can be estimated. The elastic properties are close to the ones from actin and thus can well tolerate and mediate forces applied by molecular motors and are sufficiently stiff to deform membranes (Roux, 2013).

In summary, these observations offer a hypothesis, how the interaction of IBs with ER membranes could result in disruption of these membranes:

The ER typically accumulates significantly around the IBs as seen in fluorescence LM and cryo-EM. Fibrils impinge on ER membranes and cause local high curvature deformations. The strength of the association of fibrils with ER membranes is demonstrated by the complete “freezing” of ER dynamics at the IB’s surface. The association is probably at least in the range or greater than ATP-driven molecular motors ( $24 k_B T$ ) that are responsible for ER dynamics, since this is completely inhibited at the interface. The measured elastic properties indicate that the fibrils of the IB can easily tolerate these forces and thus constrain the attached ER in its mobility, as observed. Due to its continued dynamics the surrounding distal ER network applies force on the proximal ER membranes in contact with fibrils and thus could cause disruption of these. The results are fibril-impinged, irregular vesicles trapped in the fibril network that occasionally carry membrane-bound ribosomes. The amount of many hundred trapped vesicles in a typical IB suggests that this is a frequent event.

Another consequence of the interaction of IBs with the ER that was observed in this study is a stress-response and relocalization of several ER resident proteins in the vicinity of the IB. Remarkably, in the region surrounding the IBs, translation is halted as the translocase component Sec61 was largely excluded from the IB’s vicinity, consistent with the observation by cryo-ET that ER membranes in contact with the IB were essentially devoid of ribosomes. In contrast to this depletion, we found that calnexin, a membrane bound chaperone with luminal activity, was intensely enriched in the ER domain surrounding IBs, suggesting that cytosolic IBs locally induce misfolding of ER luminal proteins. That this probably causes an ER stress response is reflected by the local accumulation of components of the ER-associated degradation (ERAD) machinery - ERLIN-2 and Sel1L. These results are consistent with previous findings that polyQ expression compromises ER function by perturbing ERAD and the ER redox state, leading to ER stress in cellular and animal models and upregulation of ER stress genes in HD patients (Jiang et al., 2016; Kirstein et al., 2015; Labbadia and Morimoto, 2013; Leitman et al., 2013).

## HOW DO NUCLEAR AND CYTOSOLIC IBs DIFFER IN THEIR CELLULAR INTERACTION?

In this study, the subcellular location of inclusion bodies in HeLa cells was typically cytosolic and rarely in the nucleus (9%) – in contrast to neurons, in which the occurrence of nuclear inclusion bodies was more frequent (38%).

Nuclear IBs have been reported in neurons of HD patient post mortem brains (Becher et al., 1998; DiFiglia et al., 1997; Gourfinkel-an et al., 1998), consistent with studies in transgenic mice expressing exon 1 of the HD gene (Davies et al., 1997). Cytosolic inclusion bodies are described to be prevalent in human brain (DiFiglia et al., 1997; Gutekunst et al., 1999) and especially these are reported to be more common. In a recent study (Jansen et al., 2017) it could be shown that nuclear IBs are present in 0.13%/4.91% of neurons in adult/juvenile HD patients, but also in astrocytes, microglia and oligodendrocytes in substantial percentages consistent with three different transgenic mouse models. (Gutekunst et al., 1999) showed that cytosolic IBs are alongside nuclear ones predominant in human neurons. It is diversely discussed (Becher et al., 1998), if the presence of nuclear IBs contributes to (Davies et al., 1997; Gourfinkel-an et al., 1998) or may not play a causative role in HD (Gutekunst et al., 1999; Liu et al., 2015).

Our results demonstrate that the overall architecture of nuclear IBs was comparable to the ones observed in the cytosol as well as the fibril density and, remarkably, also that the fibril morphology was indistinguishable. Thus one could expect similar observations as made with the cytosolic IBs. But conversely, our results show that nuclear IBs seem to act differently: they did not contact the inner nuclear membrane, they did not cause local high membrane curvatures and not a single vesicle was observed to be trapped in the fibril network of nuclear IBs. These remarkable differences between cytosolic and nuclear IBs - with identical fibrillar architecture - indicate differential mechanisms of cellular interaction (Benn et al., 2005; Gu et al., 2015; Liu et al., 2015). A potential explanation for the different behavior of nuclear IBs is the surrounding chromatin, which was seen to shield these from accessing the inner nuclear membrane and thus restrain nuclear IBs from exerting the potential deleterious effects that were observed with inclusion bodies in the cytosol.

Importantly, fibril formation is thought to be required for neurodegeneration in mice (Gu et al., 2009). Concluding, our results suggest that a cytopathological consequence of these phenomena is that Htt exon 1 IB fibrils impinge on and disrupt cellular endomembranes, most prominently those of the ER. As a result, IBs drive a reorganization of the ER network in their periphery.

## CAN PROTEINS BE TRAPPED INSIDE IB'S?

In this study we could show that polyQ expanded Htt exon 1 formed fibrillar inclusion bodies comparable in human cells and mouse neurons. Proteins could be trapped either passively in the dense network of the IB or actively due to protein interactions with the aggregated huntingtin. The latter point was investigated by (Kim et al., 2016): the authors found that the interaction propensity depends on the surface-volume ratio of the aggregated species and so 10-times less proteins were found to interact with the IB compared to the soluble oligomers, but chaperones and UPS components were specially enriched. The passive trapping of proteins needs to be investigated further, but a preliminary

---

interpretation should be presented here. The three-dimensional network of fibrils can be seen as the polymer basis for a gel. The diffusion of proteins could be expected to be constrained dependent of their size and consecutively be trapped inside the fibril network. The space in a typical IB occupied by fibrils, measures only 2-4%, leaving >96% of the IBs volume capable for trapping proteins. As an easy detectable representative of the cellular macro molecules, cytosolic ribosomes (~25 nm) were investigated in the tomograms and found to be largely excluded from the IBs volume and occur in high abundance in the IBs periphery. This is indicating that ribosomes cannot diffuse freely inside the fibril network and that they are pushed aside while the IB grows. It has been shown that particles with sizes in the range of the mesh dimension in actin networks exhibit anomalous sub-diffusive behavior (Wong et al., 2004) and this sub-diffusive motion is trap-like for particles >42% of the mesh size. The fibrils found in IBs in the present study are very similar to actin, concerning their morphology and flexibility, thus the model of Wong et al. (2004) could be applicable. The mesh dimension of Htt97Q fibrils is roughly in the size of 10-30 nm, suggesting that proteins >4-13 nm could be passively trapped. Ribosomes were not trapped in the IB, indicating that large macro molecules are rather pushed aside while growth than being trapped.

## 4.4 IMPROVEMENTS OF THE NEW-GENERATION CRYO-EM METHODS

### HOW APT IS VITRIFICATION BY PLUNGE FREEZING AND HOW FAR COULD IT BE IMPROVED?

Vitrification is essential to preserve the biological structure of the cellular components besides the important technical aspects: elimination of the vapor pressure of water in the electron microscope's vacuum, minimization of Brownian motion, reduction of beam damage in the sample and prevention of diffraction artifacts due to crystalline ice. This is achieved by very rapid cooling of the sample below the glass transition temperature, where the increased viscosity of liquid water prevents all rearrangements of the molecules and thus adopts qualities of a glassy solid, lacking any long-range order. Proper vitrification is a crucial premise to interpret physiological as well as pathological processes in biological systems.

The thickness of the sample is critical: for pure water, the maximum depth of vitrification was determined to be 1  $\mu\text{m}$  (Dubochet and McDowell, 1981). Due to cytoplasmic solutes acting as intrinsic cryoprotectants, cells are expected to be vitrified in larger depths. This hypothesis could not be verified for plunge-frozen cells before the invention of the cryo-FIB method (Bauerlein, 2010; Rigort and Bauerlein et al., 2012), since structures deep inside the cell were not accessible.

Now, being able to open windows into cells, it could be proven in this study (chapter 3.1.3) that HeLa cells regularly are not entirely vitrified and that major structural changes due to that can lead to wrong interpretations. Cortical regions of HeLa cells, 1-2  $\mu\text{m}$  close to the cells surface, were well vitrified, while deeper structures showed gradually increasing alterations. The outer mitochondrial membrane showed a depth-dependent wrinkling that could be interpreted as a pathological feature dependent on IBs, since they are often located deep inside the cell, and mitochondria showed stronger aberrations the closer they were located to the IB. Rarely, the IB was located closer to the cell surface: in this case the outer mitochondria membrane did not show a distance-dependence to the IB. Also the fibrils of Htt97Q IBs appeared to occur in a second conformation that appeared as a sludge of proteins sticking to them.

Both alterations were not observed anymore in following 130 tomograms after cryoprotection with 10% glycerol in DMEM medium.

Thus it has to be concluded that plunge freezing of large cells like HeLa with an improved cryogen (37% ethane + 63% propane; (Tivol et al., 2008)), cooled to  $-196^\circ\text{C}$ , is able only to vitrify cortical regions that are close to the cells' surface, but not regions deep inside the cell. Therefore, it is necessary to improve this process. Moreover, the sensitivity of testing for proper vitrification by diffraction seems to be limited and is not indicative in every case.

Consequently, the vitrification process has to be improved, by either improving the heat transfer rate in the cell or by hindering nucleation processes. The cryogen around the sample while plunge freezing takes up the thermal energy at the cells surface, but the transport of heat inside the cell is mainly determined by the heat transfer rate, following  $\frac{dQ}{dt} = \lambda \cdot A \cdot \frac{dT}{dx}$ . The heat conductivity  $\lambda$ , the cell surface  $A$  and the distance  $dx$  to the surface are invariant intrinsic factors. The temperature difference

can't be increased, since there are no organic compounds that are liquid below  $-196^{\circ}\text{C}$ . The inorganic substances (Ne,  $\text{H}_2$ , He) whose boiling point is lower, could maximally improve the heat transfer rate by not more than 31% but with the disadvantage of a much lower heat capacity.

High pressure freezing at 2100 bar delays the onset of nucleation due to a  $22^{\circ}\text{C}$  lowered freezing point and a nucleation temperature ( $-92^{\circ}\text{C}$ ) that is much closer (instead of  $-41^{\circ}\text{C}$  at normal pressure) to the glass transition temperature of  $-136^{\circ}\text{C}$  and thus can vitrify much thicker samples. However, samples vitrified by high pressure freezing are too thick to be thinned by cryo-FIB.

Another way to delay nucleation is to use a cryoprotectant that interspaces the water molecules and therefore has to pass the cell membrane. Since they are used regularly as cryoprotective agents, glycerol and DMSO were tested here for toxicity as additives to the cell medium and for the question, if vitrification is improved. DMSO surprisingly turned out to exert a strong cytotoxic effect in the first few minutes, while cells accepted glycerol by far better. Glycerol enters the cell via the aquaporin very quickly at  $37^{\circ}\text{C}$  (Kantha, 1985, p. 33). With an exposure for 2 min in a concentration of 10%, glycerol was able to entirely vitrify cells reproducibly without any obvious effects on cellular structures and inhibited any kind of alterations that were seen as described before.

#### HOW FAR IS VPP IMAGING COMPATIBLE WITH FIB-LAMELLAS?

Phase plate imaging of native FIB prepared lamellas regularly causes anisotropic image distortions and loss of phase contrast in substantial parts of the image, comparable to a “tunnel-vision” effect. This is caused by the local removal of the electrically conductive carbon film by the lamella preparation that could drain the electrical charge applied while imaging. Thus wide areas of the lamella build up an electrical field that acts as an additional, artificial electrostatic lens.

While this effect is not obviously disturbing classical defocus-imaging, it is interfering strongly with VPP imaging. The electron beam needs to be precisely and steadily focused on the phase plate in the back focal plane (on-plane condition). Due to the charged lamella the additional artificial electrostatic lens moves the focus away from that “on-plane condition”. The beam is widened in the back focal plane - larger than the original VPP spot – and therefore only a small part of the image receives phase contrast, the rest of the image shows almost no contrast.

This problem could be resolved reproducibly, if an electrically conductive surface layer is applied by sputtering metallic platinum on the FIB-lamella. Titrating the amount of sputtered platinum indicates a non-linear relationship between the amount of platinum and the electrical resistance of the surface, presumably due to the inhomogeneous growth of the platinum in islands.

Additionally, the island-like growth of the sputtered platinum causes strong contrast gradients in that layer because of the limited tilt range, as this is known from fiducial gold markers – in the 3D reconstruction these gradients are the source of “rays” corresponding to the highest tilt angles. The interference of a large number of such strong contrast gradient sites causes a z-dependent wave-like artifact that declines image quality. In the Fourier-space of the x-y plane of the tomogram, a narrow bright frequency band can be observed: its inverse frequency (wavelength of the artifact wave) increases linearly with the distance to the platinum layer.

An in-house developed cleaning-procedure (Fernandez et al., 2016) was applied to remove the platinum layer and consecutively this artifact very effectively from the tomogram. After reconstruction this procedure results in an artifact-cleaned tomogram with a considerably increased image quality. Also, in Fourier-space the noticeable bright frequency bands are strongly reduced asymptotically.

As we could show, VPP imaging is well compatible with FIB-lamellas after creating a conductive



surface layer by Pt sputtering. Thereby induced artifacts can be effectively reduced and the resulting image contrast and quality are therefore superior to defocus imaging.

# 5

## METHODS

The extent of this project was only possible due to a fruitful collaborative setting at the Max-Planck-Institutes for Biochemistry and Neurobiology with the following persons that substantially and perseveringly contributed with their individual expertise:

**Itika Saha** from the Department of Cellular Biochemistry (Prof. Ulrich Hartl):

HeLa cell culture; extensive optimization of transfection with all used constructs; antibody-staining of cells for immunofluorescence

**Archana Mishra** from the Department of Molecules, Signaling and Development (Prof. Rüdiger Klein):

Primary hippocampal neuron culture; optimization of the transfection of neurons with Htt97Q-GFP

**Maria Kalemanov** with support of **Antonio Martínez-Sánchez** from our Department of Structural Biology (Prof. Wolfgang Baumeister):

Ribosome template matching and calculation of ER-bound ribosome density; determination of ER membrane curvature

This methods section is a modification of the methods part of (Bauerlein et al., 2017).

## 5.1 EXPERIMENTAL MODEL

### HELA CELL CULTURE (PERFORMED BY ITIKA SAHA)

HeLa cells (female; ATCC® CCL-2™; RRID:CVCL\_0030) were freshly obtained from ATCC and no unusual DAPI staining was observed, indicating no mycoplasma contamination. Cells were seeded on holey carbon-coated 200 mesh gold EM grids (Quantifoil Micro Tools, Jena, Germany) within ibidi  $\mu$ -dishes (ibidi, Munich) containing Dulbecco's MEM (Biochrom) supplemented with 10% fetal bovine serum, 2mM L-Glutamine, 100 Units/mL penicillin, 100 $\mu$ g/mL streptomycin and non-essential amino acids cocktail (Gibco) and cultured at 37°C with 10% CO<sub>2</sub>. The cells were transfected by lipofection using Lipofectamine 2000 (Invitrogen) with either Htt25Q-GFP, Htt64Q-GFP, Htt97Q-GFP or Htt97Q together with mCherry-ubiquitin as per manufacturer's protocol. In co-transfected cells mCherry-ubiquitin formed a ring around Htt97Q inclusions that facilitated correlative microscopy (Hipp et al., 2012). 30 min prior to imaging the cells were stained with Annexin V conjugated to Alexa Fluor 594 (LifeTechnologies) to exclude cells undergoing apoptosis from further analysis.

### HIPPOCAMPAL NEURON CULTURE AND TRANSFECTION (PERFORMED BY ARCHANA MISHRA)

Holey carbon-coated 200 mesh gold EM grids were sterilized in ethanol for 10 min, washed several times in double distilled water and transferred to culture dishes containing water. Grids and dishes were coated with poly-D-lysine (Sigma-Aldrich; 1 mg/ml in borate buffer) and laminin (Thermo Fisher; 7.5  $\mu$ g/ml in PBS) for 24 h each, washed with PBS three times and placed in neurobasal medium supplemented with B27 containing 0.5 mM Glutamine (all reagents from Thermo Fisher). During washes and medium exchange steps, grids were transferred into another dish containing appropriate liquid to prevent grids from drying.

Mice (C57BL/6 background, either sex; RRID:CVCL\_9115) 561 were housed in a specific pathogen free facility with 12:12 h light/dark cycle and food/water available ad libitum. All animal experiments were performed in compliance with institutional policies approved by the government of upper Bavaria. For preparation of neurons, hippocampi from embryonic day 17 mice were separated from diencephalic structures and digested individually with 0.25% trypsin containing 1 mM 2, 2', 2'', 2''' - (ethane-1,2-diyldinitrilo) tetraacetic acid (EDTA) for 20 min at 37°C. Neurons were plated on the coated grids within 24-well plates (60,000 per well). After 6 days in culture at 37°C in 5% CO<sub>2</sub>, neurons were transfected with Htt97Q-GFP using DNA-In™ Neuro (GlobalStem) according to the manufacturer's protocol.

## 5.2 METHOD DETAILS

### PLASMIDS AND ANTIBODIES (APPLIED BY ITIKA SAHA)

The plasmids expressing myc-tagged Htt25Q exon 1-GFP, Htt64Q exon 1-GFP, Htt97Q exon 1 and Htt97Q exon 1-GFP have been described previously (Bence et al., 2001; Holmberg et al., 2004; Schaffar et al., 2004; Woerner et al., 2016). The plasmid expressing mCherry-Ubiquitin was a kind gift

from Eric J. Bennett & Ron R. Kopito. To generate the KDEL-mCherry construct (kind gift from Lisa Vincenz-Donnelly), the signal peptide of human pulmonary surfactant-associated protein B (MAESHLLQWLLLLLPTLCGPGTA) followed by one alanine residue and a myc tag was fused upstream to mCherry by PCR amplification. A C-terminal KDEL sequence, as well as a 5' BamH1 and a 3' Not1 digestion site were also added by PCR amplification. The purified PCR product was then inserted into the pcDNA3.1+ plasmid via BamH1/Not1.

The following primary antibodies were used for immunofluorescence:

BiP (AbCam ab21685; RRID:AB\_2119834),  
calnexin (AbCam ab10286; RRID:AB\_2069009),  
calreticulin (AbCam ab14234; RRID:AB\_2228460),  
giantin (AbCam ab24586; RRID:AB\_448163),  
p97/VCP (Cell Signalling 2468; RRID:AB\_2214632),  
PDIA6 (AbCam ab154820),  
Sec61A (AbCam ab183046; RRID:AB\_2620158),  
SEL1L (Sigma S3699; RRID:AB\_1856660) and  
SPFH2/ERLIN2 (AbCam ab128924; RRID:AB\_11150974).

The following secondary antibodies were used:

Anti-Rabbit Cy3 (Dianova 111-584 165-045) and Anti-Chicken Alexa Fluor 633 conjugate (Thermo Fisher A21103; RRID:AB\_2535756).

## IMMUNOFLUORESCENCE

HeLa cells were seeded on poly-L-lysine coated glass coverslips (NeuVibro), transfected with Htt97Q-GFP and fixed 24-48 h post-transfection using 4% formaldehyde in PBS for 10 min, permeabilized with 0.1% (v/v) Triton X-100 in PBS (Gibco) for 5 min and blocked in 5% milk in PBS for 1 h at room temperature. The cells were then washed and primary antibodies were applied overnight at a dilution of 1:500 to 1:1000 in blocking solution at 4°C, washed in PBS and incubated with secondary antibodies at a dilution of 1:5000 in PBS at room temperature for 1-2 h. Coverslips were stained with 500 nM DAPI in PBS for 5 min, washed several times with PBS and mounted in fluorescence mounting medium (Dako).

To investigate the identity of the membranous structures contained inside inclusions, HeLa cells were transfected with Htt97Q-GFP and loaded with either ER-Tracker Red or Mito-Tracker Red (Thermo Fischer) 24h after transfection. The cells were subsequently fixed and imaged as described below.

## CORRELATIVE LIGHT MICROSCOPY AND LIVE CELL IMAGING

To locate cells containing polyQ inclusions and suitable for cryo-ET, cells were imaged in an atmosphere of 37°C and 10% CO<sub>2</sub> using a CorrSight light microscope (FEI, Hillsboro, USA) equipped with bright field and spinning disc confocal laser illumination (405/488/561/640 nm), 20x (air, NA 0.8) and 63x (oil, NA 1.4) Plan Achromat objectives (Carl Zeiss, Jena, Germany) and a 1344 x 1024 pixel camera with a pixel size of 6.4 µm (Hamamatsu Digital Camera C10600 ORCA-R2). For correlative microscopy a map of the EM grid was acquired with 20x magnification (object pixel size 323 nm) in spinning disc confocal mode. Htt97Q and Htt97Q-GFP-expressing HeLa cells and primary neurons were imaged 24 h after transfection, as this yielded the best compromise between cell death and formation of IB. Protein expression was allowed for 48-72h in Htt64Q-GFP-expressing HeLa cells, as IB formation was slower.

For investigation of ER dynamics, HeLa cells were co-transfected with Htt97Q-608 GFP and KDEL-mCherry and imaged at 5-10 Hz with 63x magnification (object pixel size 102 nm) in spinning disk confocal mode for 20-30 s. The z slice containing the maximum IB diameter was analyzed further for each movie. Movies were first bleach-corrected using the exponential fit tool of Fiji ((Schindelin et al., 2012), RRID:SCR\_002285) and further processed using in-house Matlab (MathWorks) scripts. The IB boundary ( $x = 0$  in Figure 4E and Figure S 3F-H) was estimated as the line where Htt97Q-GFP intensity dropped to 40 % of its maximum value in each IB. A radial average of KDEL-mCherry pixel intensity was calculated from this mask within the cytoplasm. The radial variance of KDEL-mCherry pixel intensity was calculated over time, and normalized by pixel intensity to account for different KDEL-mCherry expression levels in different cells. The maximum of the curve was scaled to 1. The normalized variance was used as readout for ER membrane dynamics (blue curves in Figure 3.19C and Appendix 6.4).

## CELL VITRIFICATION

After light microscopy the cells were incubated for 1-5 min in DMEM containing 10% glycerol as a cryo-protectant to ensure full vitrification. The grids were then mounted on a manual plunger, blotted from the back side using Whatman paper #1 (Sigma-Aldrich) and plunged into a 2:1 ethane:propane mixture cooled down to liquid nitrogen temperature.

## CRYO-FOCUSED ION BEAM MILLING

To prepare thin electron transparent lamellae containing polyQ inclusions and surrounding cellular structures, plunge-frozen grids were first mounted into Autogrid frames (FEI). Autogrids were mounted into a dual-beam Quanta 3D focused ion beam (FIB) / scanning electron microscope (SEM) (FEI) using a custom-built transfer shuttle and a cryo-transfer system (PP3000T, Quorum). The samples were kept at  $-180^{\circ}$  C throughout FIB milling by the microscope's cryo stage. To target cells containing inclusions an overview map of the EM grid was acquired by SEM at 10 kV at 100x magnification (object pixel size 1.1  $\mu$ m) and correlated with the light microscopy map using MAPS software (FEI). Thereby, the fluorescence signal was overlaid on the correlated SEM micrograph. For Htt97Q/mCherry-ubiquitin co-transfected cells a custom-made Matlab algorithm was applied to the correlated light microscopy/SEM image to select inclusions as ring-shaped structures and classify them according to their size and usability in terms of distance to the grid bars. To protect the milling front of the lamellae, gaseous organic platinum was frozen on top of the grid using a gas injection system. 15-30  $\mu$ m wide lamellae were prepared in target cells using a Ga<sup>+</sup> ion beam at 30 kV at shallow angles (8-14 $^{\circ}$ ) in four consecutive steps: initially cells were abraded in 500 nm steps from the top down with 500-1000 pA and imaged consecutively by SEM at 2.5 kV, 4.1 pA in integration mode to identify inclusions. Further rectangular patterns were defined above and below the intended lamella with 2  $\mu$ m spacing for the rough milling step (ion beam current of 500-1000 pA), followed by fine milling with 800 nm spacing (200 pA) and a final polishing step down to the final lamella thickness of 150-250 nm (50 pA). To reduce lamella charging during phase plate cryo-ET data acquisition a thin layer of pure metallic Pt was sputtered onto the lamella under cryo conditions at the PP3000T transfer system with the following parameters: 5 mA sputtering current, 500 V between stage and sputtering target and 10 s of exposure at  $4.5 \times 10^{-2}$  mbar.

## CRYO-ELECTRON TOMOGRAPHY

Cryo-FIB lamellas were imaged using a Titan cryo-transmission electron microscope (TEM) (FEI) equipped with a field emission gun operated at 300 kV, a Volta phase plate (Danev et al., 2014), a post-column energy filter (Gatan, Pleasanton, CA, USA) operated at zero-loss and a K2 Summit direct electron detector (Gatan). Low magnification images of lamellas were recorded at 11,500 x (object pixel size 1.312 nm) and stitched using ICE (Microsoft Research) to produce complete lamella overviews. Phase plate alignment and operation was carried out as described (Fukuda et al., 2015). Upon phase plate conditioning, high magnification (19,500x, object pixel size 0.710 nm for Figure 1A; 33,000x, object pixel size 0.421 nm for all other tomograms) tilt series were recorded at locations of interest using the SerialEM (Mastrorade, 2005) low dose acquisition scheme with a tilt increment of 2°, typically spanning an angular range from -52° to 70°. Target defocus was set to -0.5 μm. The K2 camera was operated in dose fractionation mode recording frames every 0.2 s. For each tilt series, a new spot on the phase plate was selected. The total dose was limited to 70-150 e-/Å<sup>2</sup>.

## TOMOGRAM RECONSTRUCTION AND ANALYSIS

Raw K2 camera frames were aligned using an in-house software following previously developed procedures (Li et al., 2013). The resulting tilt series were aligned using the patch tracking option of the IMOD package (Kremer et al., 1996) and reconstructed by weighted back projection. After reconstruction, the tilt series were cleaned of surface contamination (ice crystals and sputtered metallic Pt) using the MaskTomRec software (Fernandez et al., 2016), realigned and reconstructed again. Membranes were automatically segmented using the TomoSegMemTV package (Martinez-Sanchez et al., 2014) and refined manually when necessary using Amira (FEI Visualization Sciences Group; RRID:SCR\_014305). PolyQ fibrils were automatically detected using the XTracing Module in Amira (Rigort et al., 2012b). In brief, tomograms were denoised by a non-local means filter and searched for a cylindrical template of 8 nm in diameter and 42 nm in length. The resulting cross-correlation fields were thresholded at an empirical value of 0.68-0.72 that produced optimal numbers of true positives and negatives. The thresholded correlation fields were used as starting point for the filament tracing process. The length and orientation distribution of the resulting fibrils was then measured. The total volume occupied by fibrils was calculated by multiplying the total length of all fibrils by  $\pi r^2$ , where  $r$  is the radius of the fibrils, here 4 nm. The fraction of IB occupied by fibrils was determined by dividing the total fibril volume by the volume of a manually traced envelope of the IB.

## 5.3 QUANTIFICATION AND STATISTICAL ANALYSIS

### PERSISTENCE LENGTH ANALYSIS

The persistence length ( $L_p$ ) was determined using an in-house script.  $L_p$  is a measure of the stiffness of polymers that can be defined as the average distance for which a filament is not bent. It is calculated as the expectation value of  $\cos \theta$ , where  $\theta$  is the angle between two tangents to the fibril at positions 0 and  $l$  (Roux, 2013)(Nagashima and Asakura, 1980):

$$\langle \cos(\theta_0 - \theta_l) \rangle = e^{-l/L_p}$$

Intuitively, the larger  $\theta$  (i.e. the smaller  $L_p$ ) the more flexible is the fibril.

The Young's modulus  $E$  defines the relation between applied force and deformation of the fibril and can be calculated from  $L_p$  as:

$$E = \frac{L_p k_B T}{I}$$

where  $k_B$  is the Boltzmann constant ( $1.38 \times 10^{-23} \text{ m}^2 \text{ kg s}^{-2} \text{ K}^{-1}$ ),  $T$  is the absolute temperature (here 295 K) and  $I$  is the momentum of inertia, which for a solid rod can be calculated from its radius  $r$  as:

$$I = \frac{\pi r^4}{4}$$

The force necessary to deform the cell membrane into filopodia-like extensions or to drive membrane fission by dynamin has been estimated in the order of 20 pN (Roux, 2013), which would result in only a 1 % axial deformation of an Htt97Q fibril according to:

$$E = \frac{\sigma(\varepsilon)}{\varepsilon} = \frac{F/A_0}{\Delta L/L_0}$$

where  $\sigma$  is the stress applied (force  $F$  divided by the cross section of the fibril  $A_0$ ) and  $\varepsilon$  the resulting strain or deformation (the increase in length  $\Delta L$  divided by the initial length  $L_0$ ). Therefore, we conclude that Htt97Q fibrils could easily withstand or exert the forces necessary to deform cellular membranes without rupturing.

### RIBOSOME TEMPLATE MATCHING AND CALCULATION OF ER-BOUND RIBOSOME DENSITY (PERFORMED BY MARIA KALEMANOV WITH SUPPORT OF ANTONIO MARTÍNEZ-SÁNCHEZ)

ER-bound ribosomes were analyzed by template matching using PyTom and TOM software (Hrabe et al., 2012; Nickell et al., 2005). In brief, tomograms were searched for the structure of a membrane-bound ribosome (Pfeffer et al., 2012) (Electron Microscopy Data Bank, EMDB, accession number

2099) downsampled to 40 Å resolution in a volume limited to < 100 nm distance from previously segmented ER membranes. The top cross-correlation hits were screened visually and further filtered to discard ribosomes whose center was located more than 18 nm away from the ER membrane. The remaining particles were aligned by real space alignment and classified into six groups using constrained principle component analysis and k-means clustering. One of those classes yielded non-membrane bound ribosomes and was discarded, whereas the others contained mainly true positives and were pooled.

Each membrane-bound ribosome center coordinate was mapped to a central voxel on the membrane plane of the ribosome template and overlapped with the membrane segmentation using in-house Matlab scripts to discard particles with wrong orientation. The membrane segmentation was transformed into a graph (Deo 2016) using the graph-tool python library (<https://git.skewed.de/count0/graph-tool>) as follows: All voxels of the ER or vesicle membranes were added to the set of vertices. Then, all pairs of vertices representing neighboring voxels were connected by edges, resulting in a fully-connected graph. The shortest distances via the membrane (geodesic distance) from each membrane voxel to the ribosome center voxels on the membrane ( $d$ ) were calculated using the graph-tool python library. The ribosome density ( $D$ ) for each membrane voxel was defined as:

$$D = \sum_{(\text{reachable ribosomes})} \frac{1}{d + 1}$$

Thus, for every membrane voxel, the higher the number of reachable ribosomes and the shorter the distances to them, the higher  $D$  value.

The cytosolic ribosomes shown in Figure 1B were detected by template matching using the structure of a cytosolic ribosome (Anger et al., 2013) (EMDB accession number 5592).

#### DETERMINATION OF ER MEMBRANE CURVATURE (WITH MARIA KALEMANOV)

First, ER membrane segmentations were pre-processed with morphological operations to remove small holes. ER membrane segmentations were then transformed into a signed, single-layer surface using in-house python software. This procedure was based on the Visualization Toolkit library (<http://www.vtk.org>; RRID:SCR\_015013) implementation of Hoppe's surface reconstruction algorithm (<http://hhoppe.com/proj/thesis/>). A graph for recovering surface mesh topology was then constructed using the graph-tool python library, so that every vertex represented a triangle center, and every edge connected two adjacent triangles. For each triangle, a local neighborhood of 9 nm radius was defined using the graph surface representation to measure geodesic distances between triangles. For each neighborhood, the maximal and minimal principal curvatures ( $\kappa_1$  and  $\kappa_2$ , respectively) were estimated by an in-house implementation of the normal vector voting algorithm (Page et al., 2002). The total ER membrane curvature was calculated from its curvedness (Koenderink and van Doorn, 1992), defined as:

$$\text{Curvedness} = \sqrt{\frac{\kappa_1^2 + \kappa_2^2}{2}}$$



## STATISTICAL ANALYSIS

The number of cells analyzed for each condition is shown in Table S 1. Tomograms of poor technical quality or showing signs of cell death were excluded. For optimal fibril tracing and subsequent analysis (fibril length, density, persistence length, Young’s modulus), the 4 tomograms with best signal-to-noise ratio were selected for each condition as this procedure can be affected by noise (Rigort et al., 2012b). This resulted in a large number of fibrils analyzed: N = 11,481, neurons, Htt97Q GFP; N = 7,648, HeLa, Htt97Q-GFP; N = 12,465, HeLa, Htt97Q. For the fibril density analysis, statistical significance was calculated by ANOVA analysis with Bonferroni post-hoc-test. The distributions of ER membrane curvature in the vicinity of inclusions and in control cells were compared by the Kolmogorov–Smirnov test. The red line in Figure S 2D was calculated as the IB/control ratio of curvedness for each bin and smoothed using robust LOESS. ER dynamics were analyzed in 44 cells from 2 independent experiments. The analysis included all cells in which IB size was in the range of those observed by cryo-ET, which was the case for the large majority of IB-containing cells.

## 5.4 DATA AND SOFTWARE AVAILABILITY

The Matlab and Python scripts used to calculate the density of membrane-bound ribosomes and measure

ER membrane curvature are available at <https://github.com/anmartinezs/polyqIB>.

The Matlab scripts used for the analysis of light microscopy data and quantification of fibril persistence length and ER membrane curvature measurements are available at

<https://github.com/FJBauerlein/Huntington.git> and also in the Appendix of this manuscript.

## 5.5 KEY RESOURCES TABLE

REAGENT or RESOURCE	SOURCE	IDENTIFIER
<b>Antibodies</b>		
Rabbit polyclonal anti-GRP78 BiP	Abcam	Cat# ab21685; RRID: AB_2119834
Rabbit polyclonal anti-Calnexin	AbCam	Cat# ab10286; RRID:AB_2069009
Chicken polyclonal anti-Calreticulin	AbCam	Cat# ab14234; RRID:AB_2228460
Rabbit polyclonal anti-Giantin	AbCam	Cat# ab24586; RRID:AB_448163
Rabbit monoclonal anti-PDIA6	AbCam	Cat# ab154820
Rabbit monoclonal anti-Sec61A	AbCam	Cat# ab183046; RRID:AB_2620158
Rabbit polyclonal anti-SEL1L	Sigma	Cat# S3699; RRID:AB_1856660
Rabbit monoclonal anti- SPFH2/ERLIN2	AbCam	Cat# ab128924; RRID:AB_11150974
Rabbit polyclonal anti-VCP	Cell Signalling	Cat# 2648; RRID:AB_2214632
Goat anti-Rabbit Cy3	Dianova	Cat# 111-165-045
Goat anti-Chicken Alexa Flour 633	Thermo Fisher	Cat# A-21103; RRID:AB_2535756

<b>Chemicals, Peptides, and Recombinant Proteins</b>		
Dulbecco's modified Eagle medium (DMEM)	Biochrom	Cat# F0435
Fetal Bovine Serum (FBS)	Gibco	Cat# 10270-106
L-Glutamine	Gibco	Cat# 25030-024
Penicillin / Streptomycin	Gibco	Cat# 15140-122
Non-essential amino acids	Gibco	Cat# 11140-035
Trypsin	Gibco	Cat# 12605-010
PBS	Gibco	Cat# 20012-068
Lipofectamine® 2000	Thermo Fisher Scientific	Cat# 11668027
16% Formaldehyde	Thermo Fisher Scientific	Cat# 28908
Fluorescence mounting medium	Dako	Cat# S3023
Poly-D-Lysine hydrobromide	Sigma-Aldrich	Cat# P7886
Laminin Mouse Protein, Natural	Thermo Fisher Scientific	Cat# 23017015
Neurobasal Medium	Thermo Fisher Scientific	Cat# 21103-049
B27 Serum-free Supplement	Thermo Fisher Scientific	Cat# 17504044
L-Glutamine (100x)	Thermo Fisher Scientific	Cat# 25030081
Trypsin-EDTA	Thermo Fisher Scientific	Cat# 25200056
DNA-In™ Neuro	MTI-GlobalStem	Cat# GST-2101
Laminin Mouse Protein, Natural	Thermo Fisher Scientific	Cat# 23017015
Neurobasal Medium	Thermo Fisher Scientific	Cat# 21103-049
Triton X-100	Sigma	Cat# T9284
DAPI	Thermo Fisher Scientific	Cat# D1306
<b>Critical Commercial Assays</b>		
Annexin V, Alexa Fluor 594 conjugate	Thermo Fisher Scientific	Cat# A13203
ER-Tracker Red	Thermo Fisher Scientific	Cat# E34250
Mito-Tracker Red	Thermo Fisher Scientific	Cat# M22425
<b>Deposited Data</b>		
Cryo-EM structure of membrane-bound ribosome	Pfeffer et al., 2012	EMDB 2099
Cryo-EM structure of non membrane-bound ribosome	Anger et al., 2013	EMDB 5592
<b>Experimental Models: Cell Lines</b>		
Human: HeLa cells	ATCC	ATCC® CCL-2™; RRID:CVCL_0030
<b>Experimental Models: Organisms/Strains</b>		
Mouse primary neuronal culture: C57BL/6 (E17)	MPI-Biochemistry	RRID:CVCL_9115
<b>Recombinant DNA</b>		
Plasmid: Htt25Q-GFP	Bence et al., 2001	N/A
Plasmid: Htt97Q-GFP	Bence et al., 2001	N/A
Plasmid: Htt97Q	Schaffar et al., 2004	N/A
Plasmid: Htt64Q-GFP	Holmberg et al., 2004	N/A

Plasmid: mCherry-Ubiquitin	Eric J. Bennett & Ron R. Kopito	N/A
Plasmid: KDEL-mCherry	This study	N/A
<b>Software and Algorithms</b>		
Fiji	Schindelin et al., 2012	<a href="https://fiji.sc/">https://fiji.sc/</a> RRID:SCR_002285
SerialEM	Mastronarde, 2005	<a href="http://bio3d.colorado.edu/SerialEM/">http://bio3d.colorado.edu/SerialEM/</a>
MaskTomRec	Fernandez et al., 2016	<a href="https://sites.google.com/site/3demim-ageprocessing/masktomrec">https://sites.google.com/site/3demim-ageprocessing/masktomrec</a>
TomoSegMemTV	Martinez-Sanchez et al., 2014	<a href="https://sites.google.com/site/3demim-ageprocessing/tomosegmentv">https://sites.google.com/site/3demim-ageprocessing/tomosegmentv</a>
Amira	N/A	<a href="https://www.fei.com/software/amira-3d-for-life-sciences/">https://www.fei.com/software/amira-3d-for-life-sciences/</a> RRID:SCR_014305
Amira XTTracing Module	Rigort et al., 2012b	<a href="http://www.zib.de/software/actin-segmentation">http://www.zib.de/software/actin-segmentation</a>
Pytom	Hrabe et al., 2012	<a href="http://pytom.org/">http://pytom.org/</a>
TOM toolbox	Nickell et al., 2005	<a href="https://www.biochem.mpg.de/tom">https://www.biochem.mpg.de/tom</a>
VTK	N/A	<a href="http://www.vtk.org">http://www.vtk.org</a> RRID:SCR_015013
Matlab and Python scripts used to calculate the density of membrane-bound ribosomes and measure ER membrane curvature	This study	<a href="https://github.com/anmartinezs/polyqIB">https://github.com/anmartinezs/polyqIB</a>
Matlab scripts used for the analysis of light microscopy data and quantification of fibril persistence length and ER membrane curvature measurements	This study	<a href="https://github.com/FJBauerlein/Huntington.git">https://github.com/FJBauerlein/Huntington.git</a>
<b>Other</b>		
ibidi 35 mm $\mu$ -Dishes	ibidi	Cat# 81158
Poly-L-Lysine coverslips	NeuVITRO	Cat# GG-12-PLL
Quantifoil grids 200 mesh Gold R2/1	Quantifoil Micro Tools	N/A
Whatman paper #1	Sigma-Aldrich	Cat# WHA10010155

# 6

## APPENDIX

### 6.1 AGGREGATE DETECTION ALGORITHM (AGDA)

This Matlab script analyses light microscopy data acquired with the FEI CorrSight microscope using the MAPS-Software: the script analyses the EM-grid overview taken with x times y tiles, identifies inclusion bodies by their fluorescent signal and marks the detected IBs in the bright field micrographs by a surrounding rectangle. Finally, an Excel list is written, with location, morphological properties, the distance of IBs to the grid bars and a quality score to optimize the selection for FIB lamella preparation.

Find the **AGDA.m** script under: <https://github.com/EJBauerlein/Huntington.git>

### 6.2 RING SHAPE DETECTION ALGORITHM (RSDA)

This Matlab script analyses light microscopy data acquired with the FEI CorrSight microscope using the MAPS-Software: the script analyses the EM-grid overview taken with x times y tiles, identifies inclusion bodies by detecting ring-like structures that are formed by mCherryUb around the IB and marks the detected IBs in the bright field micrographs by a surrounding rectangle. Finally, an Excel list is written, with location, morphological properties, the distance of IBs to the grid bars and a quality

score to optimize the selection for FIB lamella preparation.

Find the **RSDA.m** script under: <https://github.com/FJBauerlein/Huntington.git>

## 6.3 PERSISTENCE LENGTH CALCULATION OF FIBRILS

### PERSISTENCE LENGTH CALCULATION

This Matlab script was developed to calculate the persistence length of fibrils traced in cryo-EM data with Amira 6.0.1, using the XTracing module.

Needed data is the „Attribute“-dataset derived from the XTracing module saved as .xml file. After manually transforming to .xls format, the data is first transformed by the `Persistencelength_full.m` script with the `Amira_lineset_conversion.m` script (see below) and by scripts previously developed by M. Jasnin & E. Villa (Jasnin et al., 2013) to space the datapoints equidistantly and following the persistence length is calculated with the core script `Persistencelength.m`.

Find the scripts **Persistencelength\_full.m** and **Persistencelength.m** under: <https://github.com/FJBauerlein/Huntington.git>

### AMIRA LINESET CONVERSION

Matlab script, that aggregates data from the Amira 6.0.1 file. Amira 6.0.1 saves the necessary data in separate tables, that need to be merged.

Find the **Amira\_lineset\_conversion.m** script under: <https://github.com/FJBauerlein/Huntington.git>

## 6.4 MEASUREMENT OF LOCAL ER DYNAMICS/MOBILITY

### ER MOBILITY ANALYSIS PACKAGE

Matlab script in three parts to calculate the radially averaged accumulation and variance of the endoplasmic reticulum around inclusion bodies (IB).

- **Part 1:** loads all ER-movies, identifies individual IBs, defines IB borders and creates FIJI script for bleach correction
- run FIJI script for bleach correction of the ER-movies before continuing with part2
- **Part 2:** calculates ER-variance, defines extracellular and nuclear regions to exclude from averaging, calculates rotational averages and saves analyses to output files
- **Part 3:** cohort analysis for all IBs found and plotting of radial averages of ER and IB signal plus ER variance

Necessary data:

1. single exposure in the GFP-channel to identify Htt-GFP inclusion bodies
2. 10Hz time series of the ER-channel over 20-30s

Find the **ER\_mobility\_analysis** package (with the three subscripts) under:

<https://github.com/FJBauerlein/Huntington.git>

## INDIVIDUAL TRACES

The following figure shows the result of the result of the ER mobility analysis for the individual traces and the average measurements.

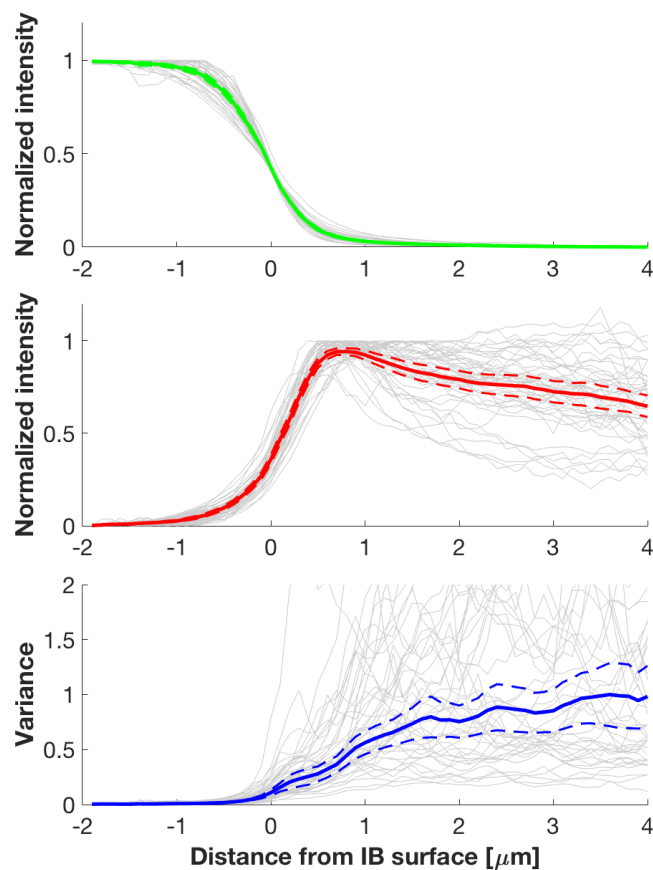


**Figure 6.1: Individual Traces**

Individual traces (gray), radial averages (solid lines) and 95% confidence intervals (dashed lines) of Htt97Q-GFP IB intensity (green), KDEL-mCherry ER intensity (red) and the variance of KDEL-mCherry intensity over time (blue) for all live cell movies analyzed (N=44) in Figure 3.19C. (Modified from (Bauerlein et al., 2017), with permission from Elsevier.)



## ACRONYMS

°C	degree Celsius
2D	Two-dimensional
3D	Three-dimensional
Å	Ångstrom
AFM	Atomic force microscopy
AGDA	Aggregate detection algorithm
CCD	Charge-coupled device
CET	Cryo-electron tomography
CT	Computer tomography
CTF	Contrast-transfer function
DDD	Direct detection device
DQE	Detective quantum efficiency
e <sup>-</sup>	Electron
eV	Electron-Volt
EM	Electron microscopy
ER	Endoplasmic reticulum
ERAD	Endoplasmic reticulum associated degradation
FIB	Focused Ion Beam
GFP	Green fluorescent protein
GIS	Gas-injection system
Golgi	Golgi Apparatus
Htt	Huntingtin
Htt97Q±GFP	Htt97Q & Htt97Q-GFP
IB	Inclusion body
K	Kelvin (Temperature scale)
kV	Kilo-Volt
LM	Light Microscope
MGy	Mega Gray
Mito	Mitochondria
MRI	Magnetic resonance imaging
OPS	Object pixel size
polyQ	repetitive sequence of glutamines
Pt	Platinum
Q	Glutamine
RDA	Ring detection algorithm
SEM	Scanning-electron microscope
SNR	Signal-to-noise ratio
TEM	Transmission Electron Microscope
VPP	Volta phase plate
WBP	Weighted back-projection
XY	XY-dimension (Image-plane)
Z	atomic number / Z-dimension (3 <sup>rd</sup> dimension)





## BIBLIOGRAPHY

- Aguzzi, A., Rajendran, L., 2009. The Transcellular Spread of Cytosolic Amyloids, Prions, and Prionoids. *Neuron* 64, 783–790. <https://doi.org/10.1016/j.neuron.2009.12.016>
- Al-Amoudi, A., Studer, D., Dubochet, J., 2005. Cutting artefacts and cutting process in vitreous sections for cryo-electron microscopy. *J. Struct. Biol.* 150, 109–121. <https://doi.org/10.1016/j.jsb.2005.01.003>
- Almqvist, E., Elterman, D., MacLeod, P., Hayden, M., 2001. High incidence rate and absent family histories in one quarter of patients newly diagnosed with Huntington disease in British Columbia. *Clin. Genet.* 60, 198–205. <https://doi.org/10.1034/j.1399-0004.2001.600305.x>
- André, W., Sandt, C., Dumas, P., Djian, P., Hoffner, G., 2013. Structure of Inclusions of Huntington's Disease Brain Revealed by Synchrotron Infrared Microspectroscopy: Polymorphism and Relevance to Cytotoxicity. *Anal. Chem.* 85, 3765–3773. <https://doi.org/10.1021/ac400038b>
- Anger, A.M., Armache, J.-P., Berninghausen, O., Habeck, M., Subklewe, M., Wilson, D.N., Beckmann, R., 2013. Structures of the human and *Drosophila* 80S ribosome. *Nature* 497, 80. <https://doi.org/10.1038/nature12104>
- Arnold, J., Mahamid, J., Lucic, V., de Marco, A., Fernandez, J.-J., Laugks, T., Mayer, T., Hyman, A.A., Baumeister, W., Plitzko, J.M., 2016. Site-Specific Cryo-focused Ion Beam Sample Preparation Guided by 3D Correlative Microscopy. *Biophys. J.* 110, 860–869. <https://doi.org/10.1016/j.bpj.2015.10.053>
- Arrasate, M., Finkbeiner, S., 2012. Protein aggregates in Huntington's disease. *Exp. Neurol.*, Special issue: Mechanisms of protein misfolding in stressors 238, 1–11. <https://doi.org/10.1016/j.expneurol.2011.12.013>
- Asano, S., Fukuda, Y., Beck, F., Aufderheide, A., Förster, F., Danev, R., Baumeister, W., 2015. A molecular census of 26S proteasomes in intact neurons. *Science* 347, 439–442. <https://doi.org/10.1126/science.1261197>
- Atwal, R.S., Xia, J., Pinchev, D., Taylor, J., Epand, R.M., Truant, R., 2007. Huntingtin has a membrane association signal that can modulate huntingtin aggregation, nuclear entry and toxicity. *Hum. Mol. Genet.* 16, 2600–2615. <https://doi.org/10.1093/hmg/ddm217>
- Baker, L.A., Smith, E.A., Bueler, S.A., Rubinstein, J.L., 2010. The resolution dependence of optimal exposures in liquid nitrogen temperature electron cryomicroscopy of catalase crystals. *J. Struct. Biol.* 169, 431–437. <https://doi.org/10.1016/j.jsb.2009.11.014>
- Balchin, D., Hayer-Hartl, M., Hartl, F.U., 2016. In vivo aspects of protein folding and quality control. *Science* 353, aac4354. <https://doi.org/10.1126/science.aac4354>
- Bammes, B.E., Jakana, J., Schmid, M.F., Chiu, W., 2010. Radiation damage effects at four specimen temperatures from 4 to 100K. *J. Struct. Biol.* 169, 331–341. <https://doi.org/10.1016/j.jsb.2009.11.001>
- Bammes, B.E., Rochat, R.H., Jakana, J., Chen, D.-H., Chiu, W., 2012. Direct electron detection yields cryo-EM reconstructions at resolutions beyond 3/4 Nyquist frequency. *J. Struct. Biol.* 177, 589–601. <https://doi.org/10.1016/j.jsb.2012.01.008>
- Bartesaghi, A., Merk, A., Banerjee, S., Matthies, D., Wu, X., Milne, J.L.S., Subramaniam, S., 2015. 2.2 Å resolution cryo-EM structure of  $\beta$ -galactosidase in complex with a cell-permeant inhibitor. *Science* 348, 1147–1151. <https://doi.org/10.1126/science.aab1576>
- Bartesaghi, A., Subramaniam, S., 2009. Membrane protein structure determination using cryo-electron

- tomography and 3D image averaging. *Curr. Opin. Struct. Biol., Membranes / Engineering and design* 19, 402–407. <https://doi.org/10.1016/j.sbi.2009.06.005>
- Bates, G.P., Dorsey, R., Gusella, J.F., Hayden, M.R., Kay, C., Leavitt, B.R., Nance, M., Ross, C.A., Scahill, R.I., Wetzel, R., Wild, E.J., Tabrizi, S.J., 2015. Huntington disease. *Nat. Rev. Dis. Primer* 1, nrdp20155. <https://doi.org/10.1038/nrdp.2015.5>
- Bäuerlein, F.J.B., 2010. Neue Wege der Probenpräparation für die zelluläre Kryoelektronentomographie (Systematische Untersuchungen zum Dünnen eiseingebetteter biologischer Proben mittels fokussiertem Ionenstrahl (FIB)) (Diplomarbeit). Ludwig-Maximilians-Universität & Max-Planck-Institut für Biochemie, München.
- Bäuerlein, F.J.B., Saha, I., Mishra, A., Kalemánov, M., Martínez-Sánchez, A., Klein, R., Dudanova, I., Hipp, M.S., Hartl, F.U., Baumeister, W., Fernández-Busnadiego, R., 2017. In Situ Architecture and Cellular Interactions of PolyQ Inclusions. *Cell* 171, 179–187.e10. <https://doi.org/10.1016/j.cell.2017.08.009>
- Baumeister, W., 2005a. A voyage to the inner space of cells. *Protein Sci.* 14, 257–269. <https://doi.org/10.1110/ps.041148605>
- Baumeister, W., 2005b. From proteomic inventory to architecture. *FEBS Lett.* 579, 933–937. <https://doi.org/10.1016/j.febslet.2004.10.102>
- Becher, M.W., Kotzük, J.A., Sharp, A.H., Davies, S.W., Bates, G.P., Price, D.L., Ross, C.A., 1998. Intranuclear Neuronal Inclusions in Huntington's Disease and Dentatorubral and Pallidolusian Atrophy: Correlation between the Density of Inclusions and IT15CAG Triplet Repeat Length. *Neurobiol. Dis.* 4, 387–397. <https://doi.org/10.1006/nbdi.1998.0168>
- Bence, N.F., Sampat, R.M., Kopito, R.R., 2001. Impairment of the Ubiquitin-Proteasome System by Protein Aggregation. *Science* 292, 1552–1555. <https://doi.org/10.1126/science.292.5521.1552>
- Benn, C.L., Landles, C., Li, H., Strand, A.D., Woodman, B., Sathasivam, K., Li, S.-H., Ghazi-Noori, S., Hockly, E., Faruque, S.M.N.N., Cha, J.-H.J., Sharpe, P.T., Olson, J.M., Li, X.-J., Bates, G.P., 2005. Contribution of nuclear and extranuclear polyQ to neurological phenotypes in mouse models of Huntington's disease. *Hum. Mol. Genet.* 14, 3065–3078. <https://doi.org/10.1093/hmg/ddi340>
- Bertram, L., Lill, C.M., Tanzi, R.E., 2010. The Genetics of Alzheimer Disease: Back to the Future. *Neuron* 68, 270–281. <https://doi.org/10.1016/j.neuron.2010.10.013>
- Björkqvist, M., Fex, M., Renström, E., Wierup, N., Petersén, Å., Gil, J., Bacos, K., Popovic, N., Li, J.-Y., Sundler, F., Brundin, P., Mulder, H., 2005. The R6/2 transgenic mouse model of Huntington's disease develops diabetes due to deficient  $\beta$ -cell mass and exocytosis. *Hum. Mol. Genet.* 14, 565–574. <https://doi.org/10.1093/hmg/ddi053>
- Böck, D., Medeiros, J.M., Tsao, H.-F., Penz, T., Weiss, G.L., Aistleitner, K., Horn, M., Pilhofer, M., 2017. In situ architecture, function, and evolution of a contractile injection system. *Science* 357, 713–717. <https://doi.org/10.1126/science.aan7904>
- Bollschweiler, D., Schaffer, M., Lawrence, C.M., Engelhardt, H., 2017. Cryo-electron microscopy of an extremely halophilic microbe: technical aspects. *Extremophiles* 21, 393–398. <https://doi.org/10.1007/s00792-016-0912-0>
- Bracewell, R.N., Riddle, A.C., 1967. Inversion of Fan-Beam Scans in Radio Astronomy. *Astrophys. J.* 150, 427. <https://doi.org/10.1086/149346>
- Brettschneider, J., Tredici, K.D., Lee, V.M.-Y., Trojanowski, J.Q., 2015. Spreading of pathology in neurodegenerative diseases: a focus on human studies. *Nat. Rev. Neurosci.* 16, nrm3887. <https://doi.org/10.1038/nrn3887>

- Brilot, A.F., Chen, J.Z., Cheng, A., Pan, J., Harrison, S.C., Potter, C.S., Carragher, B., Henderson, R., Grigorieff, N., 2012. Beam-induced motion of vitrified specimen on holey carbon film. *J. Struct. Biol.* 177, 630–637. <https://doi.org/10.1016/j.jsb.2012.02.003>
- Brookmeyer, R., Johnson, E., Ziegler-Graham, K., Arrighi, H.M., 2007. Forecasting the global burden of Alzheimer's disease. *Alzheimers Dement.* 3, 186–191. <https://doi.org/10.1016/j.jalz.2007.04.381>
- Brüggeller, P., Mayer, E., 1980. Complete vitrification in pure liquid water and dilute aqueous solutions. *Nature* 288, 569–571. <https://doi.org/10.1038/288569a0>
- Bucciantini, M., Giannoni, E., Chiti, F., Baroni, F., Formigli, L., Zurdo, J., Taddei, N., Ramponi, G., Dobson, C.M., Stefani, M., 2002. Inherent toxicity of aggregates implies a common mechanism for protein misfolding diseases. *Nature* 416, 507. <https://doi.org/10.1038/416507a>
- Burke, K.A., Hensal, K.M., Umbaugh, C.S., Chaibva, M., Legleiter, J., 2013. Huntingtin disrupts lipid bilayers in a polyQ-length dependent manner. *Biochim. Biophys. Acta BBA - Biomembr.* 1828, 1953–1961. <https://doi.org/10.1016/j.bbamem.2013.04.025>
- Campbell, M.G., Cheng, A., Brilot, A.F., Moeller, A., Lyumkis, D., Veessler, D., Pan, J., Harrison, S.C., Potter, C.S., Carragher, B., Grigorieff, N., 2012. Movies of Ice-Embedded Particles Enhance Resolution in Electron Cryo-Microscopy. *Structure* 20, 1823–1828. <https://doi.org/10.1016/j.str.2012.08.026>
- Carulla, N., Caddy, G.L., Hall, D.R., Zurdo, J., Gairí, M., Feliz, M., Giral, E., Robinson, C.V., Dobson, C.M., 2005. Molecular recycling within amyloid fibrils. *Nature* 436, 554–558. <https://doi.org/10.1038/nature03986>
- Castaño-Díez, D., Al-Amoudi, A., Glynn, A.-M., Seybert, A., Frangakis, A.S., 2007. Fiducial-less alignment of cryo-sections. *J. Struct. Biol.* 159, 413–423. <https://doi.org/10.1016/j.jsb.2007.04.014>
- Cattaneo, E., Zuccato, C., Tartari, M., 2005. Normal huntingtin function: an alternative approach to Huntington's disease. *Nat. Rev. Neurosci.* 6, nrn1806. <https://doi.org/10.1038/nrn1806>
- Ciammola, A., Sassone, J., Alberti, L., Meola, G., Mancinelli, E., Russo, M.A., Squitieri, F., Silani, V., 2006. Increased apoptosis, huntingtin inclusions and altered differentiation in muscle cell cultures from Huntington's disease subjects. *Cell Death Differ.* 13, 2068. <https://doi.org/10.1038/sj.cdd.4401967>
- Cisbani, G., Cicchetti, F., 2012. An in vitro perspective on the molecular mechanisms underlying mutant huntingtin protein toxicity. *Cell Death Dis.* 3, e382. <https://doi.org/10.1038/cddis.2012.121>
- Clarke, G., Collins, R.A., Leavitt, B.R., Andrews, D.F., Hayden, M.R., Lumsden, C.J., McInnes, R.R., 2000. A one-hit model of cell death in inherited neuronal degenerations. *Nature* 406, 195–199. <https://doi.org/10.1038/35018098>
- Comolli, L.R., Downing, K.H., 2005. Dose tolerance at helium and nitrogen temperatures for whole cell electron tomography. *J. Struct. Biol.* 152, 149–156. <https://doi.org/10.1016/j.jsb.2005.08.004>
- Crowther, R.A., DeRosier, D.J., Klug, A., S, F.R., 1970. The reconstruction of a three-dimensional structure from projections and its application to electron microscopy. *Proc R Soc Lond A* 317, 319–340. <https://doi.org/10.1098/rspa.1970.0119>
- Danev, R., Baumeister, W., 2017. Expanding the boundaries of cryo-EM with phase plates. *Curr. Opin. Struct. Biol., Cryo electron microscopy • Biophysical methods* 46, 87–94.

- <https://doi.org/10.1016/j.sbi.2017.06.006>
- Danev, R., Buijsse, B., Khoshouei, M., Plitzko, J.M., Baumeister, W., 2014. Volta potential phase plate for in-focus phase contrast transmission electron microscopy. *Proc. Natl. Acad. Sci.* 111, 15635–15640. <https://doi.org/10.1073/pnas.1418377111>
- Danev, R., Glaeser, R.M., Nagayama, K., 2009. Practical factors affecting the performance of a thin-film phase plate for transmission electron microscopy. *Ultramicroscopy* 109, 312–325. <https://doi.org/10.1016/j.ultramic.2008.12.006>
- Davies, S.W., Turmaine, M., Cozens, B.A., DiFiglia, M., Sharp, A.H., Ross, C.A., Scherzinger, E., Wanker, E.E., Mangiarini, L., Bates, G.P., 1997. Formation of Neuronal Intranuclear Inclusions Underlies the Neurological Dysfunction in Mice Transgenic for the HD Mutation. *Cell* 90, 537–548. [https://doi.org/10.1016/S0092-8674\(00\)80513-9](https://doi.org/10.1016/S0092-8674(00)80513-9)
- De Rosier, D.J., Klug, A., 1968. Reconstruction of Three Dimensional Structures from Electron Micrographs. *Nature* 217, 130–134. <https://doi.org/10.1038/217130a0>
- DeBenedetti, P.G., 2003. Supercooled and glassy water. *J. Phys. Condens. Matter* 15, R1669. <https://doi.org/10.1088/0953-8984/15/45/R01>
- DiFiglia, M., Sapp, E., Chase, K., Schwarz, C., Meloni, A., Young, C., Martin, E., Vonsattel, J.-P., Carraway, R., Reeves, S.A., Boyce, F.M., Aronin, N., 1995. Huntingtin is a cytoplasmic protein associated with vesicles in human and rat brain neurons. *Neuron* 14, 1075–1081. [https://doi.org/10.1016/0896-6273\(95\)90346-1](https://doi.org/10.1016/0896-6273(95)90346-1)
- DiFiglia, M., Sapp, E., Chase, K.O., Davies, S.W., Bates, G.P., Vonsattel, J.P., Aronin, N., 1997. Aggregation of Huntingtin in Neuronal Intranuclear Inclusions and Dystrophic Neurites in Brain. *Science* 277, 1990–1993. <https://doi.org/10.1126/science.277.5334.1990>
- Domínguez, J.F.D., Egan, G.F., Gray, M.A., Poudel, G.R., Churchyard, A., Chua, P., Stout, J.C., Georgiou-Karistianis, N., 2013. Multi-Modal Neuroimaging in Premanifest and Early Huntington's Disease: 18 Month Longitudinal Data from the IMAGE-HD Study. *PLOS ONE* 8, e74131. <https://doi.org/10.1371/journal.pone.0074131>
- Driver, J.A., Logroscino, G., Gaziano, J.M., Kurth, T., 2009. Incidence and remaining lifetime risk of Parkinson disease in advanced age. *Neurology* 72, 432–438. <https://doi.org/10.1212/01.wnl.0000341769.50075.bb>
- Dubochet, J., Adrian, M., Chang, J.J., Homo, J.C., Lepault, J., McDowell, A.W., Schultz, P., 1988. Cryo-electron microscopy of vitrified specimens. *Q. Rev. Biophys.* 21, 129–228.
- Dubochet, J., McDowell, A. w., 1981. Vitrification of Pure Water for Electron Microscopy. *J. Microsc.* 124, 3–4. <https://doi.org/10.1111/j.1365-2818.1981.tb02483.x>
- Duennwald, M.L., Lindquist, S., 2008. Impaired ERAD and ER stress are early and specific events in polyglutamine toxicity. *Genes Dev.* 22, 3308–3319. <https://doi.org/10.1101/gad.1673408>
- Duff, K., Paulsen, J., Mills, J., Beglinger, L.J., Moser, D.J., Smith, M.M., Langbehn, D., Stout, J., Queller, S., Harrington, D.L., Group, O. behalf of the P.-H.I. and C. of the H.S., 2010. Mild cognitive impairment in prediagnosed Huntington disease. *Neurology* 75, 500–507. <https://doi.org/10.1212/WNL.0b013e3181eccfa2>
- Dunker, A.K., Silman, I., Uversky, V.N., Sussman, J.L., 2008. Function and structure of inherently disordered proteins. *Curr. Opin. Struct. Biol., Catalysis and regulation / Proteins* 18, 756–764. <https://doi.org/10.1016/j.sbi.2008.10.002>
- Edelmann, C., 1988. *Vakuumphysik*. Spektrum Akademischer Verlag, Heidelberg/Berlin.
- Engel, B.D., Schaffer, M., Albert, S., Asano, S., Plitzko, J.M., Baumeister, W., 2015a. In situ structural

- analysis of Golgi intracisternal protein arrays. *Proc. Natl. Acad. Sci.* 112, 11264–11269. <https://doi.org/10.1073/pnas.1515337112>
- Engel, B.D., Schaffer, M., Cuellar, L.K., Villa, E., Plitzko, J.M., Baumeister, W., 2015b. Native architecture of the *Chlamydomonas* chloroplast revealed by in situ cryo-electron tomography. *eLife* 4, e04889. <https://doi.org/10.7554/eLife.04889>
- Faruqi, A.R., 2009. Principles and prospects of direct high resolution electron image acquisition with CMOS detectors at low energies. *J. Phys. Condens. Matter* 21, 314004. <https://doi.org/10.1088/0953-8984/21/31/314004>
- Fernandez, J.-J., Laugks, U., Schaffer, M., Bäuerlein, F.J.B., Khoshouei, M., Baumeister, W., Lucic, V., 2016. Removing Contamination-Induced Reconstruction Artifacts from Cryo-electron Tomograms. *Biophys. J.* 110, 850–859. <https://doi.org/10.1016/j.bpj.2015.10.043>
- Ferrante, R.J., 2009. Mouse models of Huntington's disease and methodological considerations for therapeutic trials. *Biochim. Biophys. Acta BBA - Mol. Basis Dis.* 1792, 506–520. <https://doi.org/10.1016/j.bbadis.2009.04.001>
- Ferri, C.P., Prince, M., Brayne, C., Brodaty, H., Fratiglioni, L., Ganguli, M., Hall, K., Hasegawa, K., Hendrie, H., Huang, Y., Jorm, A., Mathers, C., Menezes, P.R., Rimmer, E., Sczufca, M., 2005. Global prevalence of dementia: a Delphi consensus study. *The Lancet* 366, 2112–2117. [https://doi.org/10.1016/S0140-6736\(05\)67889-0](https://doi.org/10.1016/S0140-6736(05)67889-0)
- Finkbeiner, S., 2011. Huntington's Disease. *Cold Spring Harb. Perspect. Biol.* 3, a007476. <https://doi.org/10.1101/cshperspect.a007476>
- Förster, F., Hegerl, R., 2007. Structure Determination In Situ by Averaging of Tomograms, in: *Methods in Cell Biology, Cellular Electron Microscopy*. Academic Press, pp. 741–767. [https://doi.org/10.1016/S0091-679X\(06\)79029-X](https://doi.org/10.1016/S0091-679X(06)79029-X)
- Frangakis, A.S., Böhm, J., Förster, F., Nickell, S., Nicastro, D., Typke, D., Hegerl, R., Baumeister, W., 2002. Identification of macromolecular complexes in cryoelectron tomograms of phantom cells. *Proc. Natl. Acad. Sci.* 99, 14153–14158. <https://doi.org/10.1073/pnas.172520299>
- Friedrich, H., de Jongh, P.E., Verkleij, A.J., de Jong, K.P., 2009. Electron Tomography for Heterogeneous Catalysts and Related Nanostructured Materials. *Chem. Rev.* 109, 1613–1629. <https://doi.org/10.1021/cr800434t>
- Fukuda, Y., Beck, F., Plitzko, J.M., Baumeister, W., 2017. In situ structural studies of tripeptidyl peptidase II (TPPII) reveal spatial association with proteasomes. *Proc. Natl. Acad. Sci.* 114, 4412–4417. <https://doi.org/10.1073/pnas.1701367114>
- Fukuda, Y., Laugks, U., Lučić, V., Baumeister, W., Danev, R., 2015. Electron cryotomography of vitrified cells with a Volta phase plate. *J. Struct. Biol.* 190, 143–154. <https://doi.org/10.1016/j.jsb.2015.03.004>
- Georgiou-Karistianis, N., Gray, M.A., Domínguez D, J.F., Dymowski, A.R., Bohanna, I., Johnston, L.A., Churchyard, A., Chua, P., Stout, J.C., Egan, G.F., 2013. Automated differentiation of pre-diagnosis Huntington's disease from healthy control individuals based on quadratic discriminant analysis of the basal ganglia: The IMAGE-HD study. *Neurobiol. Dis.*, Mitochondrial dynamics and quality control in neuropsychiatric diseases 51, 82–92. <https://doi.org/10.1016/j.nbd.2012.10.001>
- Gilbert, P.F.C., 1972. The reconstruction of three-dimensional structure from projections and its application to electron microscopy II. Direct methods. *Proc R Soc Lond B* 182, 89–102. <https://doi.org/10.1098/rspb.1972.0068>
- Glaeser, R.M., 2013. Invited Review Article: Methods for imaging weak-phase objects in electron

- microscopy. *Rev. Sci. Instrum.* 84, 111101. <https://doi.org/10.1063/1.4830355>
- Global Burden of Disease Study 2015, 2016. Global, regional, and national incidence, prevalence, and years lived with disability for 310 diseases and injuries, 1990–2015: a systematic analysis for the Global Burden of Disease Study 2015. *The Lancet* 388, 1545–1602. [https://doi.org/10.1016/S0140-6736\(16\)31678-6](https://doi.org/10.1016/S0140-6736(16)31678-6)
- Goedert, M., 2001. Alpha-synuclein and neurodegenerative diseases. *Nat. Rev. Neurosci.* 2, 35081564. <https://doi.org/10.1038/35081564>
- Gourfinkel-an, I., Cancel, G., Duyckaerts, C., Faucheux, B., Hauw, J., Trotter, Y., Brice, A., Agid, Y., Hirsch, E.C., 1998. Neuronal distribution of intranuclear inclusions in Huntington's disease with adult onset. *Neuroreport* 9, 1823–1826.
- Gray, M., Shirasaki, D.I., Cepeda, C., André, V.M., Wilburn, B., Lu, X.-H., Tao, J., Yamazaki, I., Li, S.-H., Sun, Y.E., Li, X.-J., Levine, M.S., Yang, X.W., 2008. Full-Length Human Mutant Huntingtin with a Stable Polyglutamine Repeat Can Elicit Progressive and Selective Neuropathogenesis in BACHD Mice. *J. Neurosci.* 28, 6182–6195. <https://doi.org/10.1523/JNEUROSCI.0857-08.2008>
- Gu, X., Cantele, J.P., Greiner, E.R., Lee, C.Y.D., Barth, A.M., Gao, F., Park, C.S., Zhang, Z., Sandoval-Miller, S., Zhang, R.L., Diamond, M., Mody, I., Coppola, G., Yang, X.W., 2015. N17 Modifies Mutant Huntingtin Nuclear Pathogenesis and Severity of Disease in HD BAC Transgenic Mice. *Neuron* 85, 726–741. <https://doi.org/10.1016/j.neuron.2015.01.008>
- Gu, X., Greiner, E.R., Mishra, R., Kodali, R., Osmand, A., Finkbeiner, S., Steffan, J.S., Thompson, L.M., Wetzel, R., Yang, X.W., 2009. Serines 13 and 16 Are Critical Determinants of Full-Length Human Mutant Huntingtin Induced Disease Pathogenesis in HD Mice. *Neuron* 64, 828–840. <https://doi.org/10.1016/j.neuron.2009.11.020>
- Guo, Q., Huang, B., Cheng, J., Seefelder, M., Engler, T., Pfeifer, G., Oeckl, P., Otto, M., Moser, F., Maurer, M., Pautsch, A., Baumeister, W., Fernández-Busnadiego, R., Kochanek, S., 2018. The cryo-EM structure of huntingtin. *Nat. Press.*
- Gusella, J.F., MacDonald, M., 2007. Genetic criteria for Huntington's disease pathogenesis. *Brain Res. Bull., Proceedings of the Second World Congress on Huntington's Disease held in Manchester, England, 11-13 September 2005* 72, 78–82. <https://doi.org/10.1016/j.brainresbull.2006.10.014>
- Gutekunst, C.-A., Li, S.-H., Yi, H., Mulroy, J.S., Kuemmerle, S., Jones, R., Rye, D., Ferrante, R.J., Hersch, S.M., Li, X.-J., 1999. Nuclear and Neuropil Aggregates in Huntington's Disease: Relationship to Neuropathology. *J. Neurosci.* 19, 2522–2534.
- Haass, C., Selkoe, D.J., 2007. Soluble protein oligomers in neurodegeneration: lessons from the Alzheimer's amyloid  $\beta$ -peptide. *Nat. Rev. Mol. Cell Biol.* 8, 101. <https://doi.org/10.1038/nrm2101>
- Hagen, C., Dent, K.C., Zeev-Ben-Mordehai, T., Grange, M., Bosse, J.B., Whittle, C., Klupp, B.G., Siebert, C.A., Vasishtan, D., Bäuerlein, F.J.B., Cheliski, J., Werner, S., Guttman, P., Rehbein, S., Henzler, K., Demmerle, J., Adler, B., Koszinowski, U., Schermelleh, L., Schneider, G., Enquist, L.W., Plitzko, J.M., Mettenleiter, T.C., Grünwald, K., 2015. Structural Basis of Vesicle Formation at the Inner Nuclear Membrane. *Cell* 163, 1692–1701. <https://doi.org/10.1016/j.cell.2015.11.029>
- Hagen, W.J.H., Wan, W., Briggs, J.A.G., 2017. Implementation of a cryo-electron tomography tilt-scheme optimized for high resolution subtomogram averaging. *J. Struct. Biol., SI:Electron Tomography* 197, 191–198. <https://doi.org/10.1016/j.jsb.2016.06.007>
- Haines, J.L., Conneally, P.M., Rao, D.C., 1986. Causes of death in huntington disease as reported on

- death certificates. *Genet. Epidemiol.* 3, 417–423. <https://doi.org/10.1002/gepi.1370030606>
- Harreveld, A.V., Crowell, J., Malhotra, S.K., 1965. A Study of Extracellular Space in Central Nervous Tissue by Freeze-Substitution. *J Cell Biol* 25, 117–137.
- Hayles, M.F., Stokes, D.J., Phifer, D., Findlay, K.C., 2007. A technique for improved focused ion beam milling of cryo-prepared life science specimens. *J. Microsc.* 226, 263–269. <https://doi.org/10.1111/j.1365-2818.2007.01775.x>
- Heemskerk, A.-W., Roos, R. a. C., 2010. E04 Causes of death in Huntington's disease. *J. Neurol. Neurosurg. Psychiatry* 81, A22–A22. <https://doi.org/10.1136/jnnp.2010.22638.4>
- Hegerl, R., Hoppe, W., 1976. Influence of Electron Noise on Three-dimensional Image Reconstruction. *Z. Für Naturforschung A* 31, 1717–1721. <https://doi.org/10.1515/zna-1976-1241>
- Hell, S.W., Wichmann, J., 1994. Breaking the diffraction resolution limit by stimulated emission: stimulated-emission-depletion fluorescence microscopy. *Opt. Lett.* 19, 780–782. <https://doi.org/10.1364/OL.19.000780>
- Hely, M.A., Reid, W.G.J., Adena, M.A., Halliday, G.M., Morris, J.G.L., 2008. The Sydney multicenter study of Parkinson's disease: The inevitability of dementia at 20 years. *Mov. Disord.* 23, 837–844. <https://doi.org/10.1002/mds.21956>
- Hipp, M.S., Park, S.-H., Hartl, F.U., 2014. Proteostasis impairment in protein-misfolding and -aggregation diseases. *Trends Cell Biol.* 24, 506–514. <https://doi.org/10.1016/j.tcb.2014.05.003>
- Hipp, M.S., Patel, C.N., Bersuker, K., Riley, B.E., Kaiser, S.E., Shaler, T.A., Brandeis, M., Kopito, R.R., 2012. Indirect inhibition of 26S proteasome activity in a cellular model of Huntington's disease. *J. Cell Biol.* 196, 573–587. <https://doi.org/10.1083/jcb.201110093>
- Hoffner, G., Djian, P., 2015. Polyglutamine Aggregation in Huntington Disease: Does Structure Determine Toxicity? *Mol. Neurobiol.* 52, 1297–1314. <https://doi.org/10.1007/s12035-014-8932-1>
- Holmberg, C.I., Staniszewski, K.E., Mensah, K.N., Matouschek, A., Morimoto, R.I., 2004. Inefficient degradation of truncated polyglutamine proteins by the proteasome. *EMBO J.* 23, 4307–4318. <https://doi.org/10.1038/sj.emboj.7600426>
- Hoogeveen, A.T., Willemsen, R., Meyer, N., Roolj, K.E. de, Roos, R.A.C., Ommen, G.-J.B. van, Galjaard, H., 1993. Characterization and localization of the Huntington disease gene product. *Hum. Mol. Genet.* 2, 2069–2073. <https://doi.org/10.1093/hmg/2.12.2069>
- Hoop, C.L., Lin, H.-K., Kar, K., Magyarfalvi, G., Lamley, J.M., Boatz, J.C., Mandal, A., Lewandowski, J.R., Wetzel, R., Wel, P.C.A. van der, 2016. Huntingtin exon 1 fibrils feature an interdigitated  $\beta$ -hairpin-based polyglutamine core. *Proc. Natl. Acad. Sci.* 113, 1546–1551. <https://doi.org/10.1073/pnas.1521933113>
- Hoppe, W., 1969. The finity postulate and the sampling theorem of the three dimensional electron microscopical analysis of aperiodic structures. *Optik* 29, 617–621.
- Hrabe, T., Chen, Y., Pfeiffer, S., Kuhn Cuellar, L., Mangold, A.-V., Förster, F., 2012. PyTom: A python-based toolbox for localization of macromolecules in cryo-electron tomograms and subtomogram analysis. *J. Struct. Biol., Special Issue: Electron Tomography* 178, 177–188. <https://doi.org/10.1016/j.jsb.2011.12.003>
- Hsieh, C.-E., Leith, A., Mannella, C.A., Frank, J., Marko, M., 2006. Towards high-resolution three-dimensional imaging of native mammalian tissue: electron tomography of frozen-hydrated rat liver sections. *J. Struct. Biol.* 153, 1–13. <https://doi.org/10.1016/j.jsb.2005.10.004>



- Isas, J.M., Langen, R., Siemer, A.B., 2015. Solid-State Nuclear Magnetic Resonance on the Static and Dynamic Domains of Huntingtin Exon-1 Fibrils. *Biochemistry (Mosc.)* 54, 3942–3949. <https://doi.org/10.1021/acs.biochem.5b00281>
- Jansen, A.H.P., van Hal, M., op den Kelder, I.C., Meier, R.T., de Ruiter, A.-A., Schut, M.H., Smith, D.L., Grit, C., Brouwer, N., Kamphuis, W., Boddeke, H. w. g. m., den Dunnen, W.F.A., van Roon, W.M.C., Bates, G.P., Hol, E.M., Reits, E.A., 2017. Frequency of nuclear mutant huntingtin inclusion formation in neurons and glia is cell-type-specific. *Glia* 65, 50–61. <https://doi.org/10.1002/glia.23050>
- Jasnin, M., Asano, S., Gouin, E., Hegerl, R., Plitzko, J.M., Villa, E., Cossart, P., Baumeister, W., 2013. Three-dimensional architecture of actin filaments in *Listeria monocytogenes* comet tails. *Proc. Natl. Acad. Sci.* 110, 20521–20526. <https://doi.org/10.1073/pnas.1320155110>
- Jasnin, M., Ecke, M., Baumeister, W., Gerisch, G., 2016. Actin Organization in Cells Responding to a Perforated Surface, Revealed by Live Imaging and Cryo-Electron Tomography. *Structure* 24, 1031–1043. <https://doi.org/10.1016/j.str.2016.05.004>
- Jernigan, T.L., Salmon, D.P., Butters, N., Hesselink, J.R., 1991. Cerebral structure on MRI, part II: Specific changes in Alzheimer's and Huntington's diseases. *Biol. Psychiatry* 29, 68–81. [https://doi.org/10.1016/0006-3223\(91\)90211-4](https://doi.org/10.1016/0006-3223(91)90211-4)
- Jiang, Y., Chadwick, S.R., Lajoie, P., 2016. Endoplasmic reticulum stress: The cause and solution to Huntington's disease? *Brain Res., ER stress and neurodegenerative diseases: From disease mechanism to therapies* 1648, 650–657. <https://doi.org/10.1016/j.brainres.2016.03.034>
- Joensuu, M., Jokitalo, E., 2015. ER sheet–tubule balance is regulated by an array of actin filaments and microtubules. *Exp. Cell Res., Cell Biology at High Resolution* 337, 170–178. <https://doi.org/10.1016/j.yexcr.2015.04.009>
- Johnston, J.A., Ward, C.L., Kopito, R.R., 1998. Aggresomes: A Cellular Response to Misfolded Proteins. *J. Cell Biol.* 143, 1883–1898. <https://doi.org/10.1083/jcb.143.7.1883>
- Kalia, L.V., Lang, A.E., 2015. Parkinson's disease. *The Lancet* 386, 896–912. [https://doi.org/10.1016/S0140-6736\(14\)61393-3](https://doi.org/10.1016/S0140-6736(14)61393-3)
- Kanno, H., Speedy, R.J., Angell, C.A., 1975. Supercooling of Water to -92°C Under Pressure. *Science* 189, 880–881. <https://doi.org/10.1126/science.189.4206.880>
- Kartha, 1985. *Cryopreservation of Plant Cells and Organs*. CRC Press.
- Karuppasamy, M., Karimi Nejadasl, F., Vulovic, M., Koster, A.J., Ravelli, R.B.G., 2011. Radiation damage in single-particle cryo-electron microscopy: effects of dose and dose rate. *J. Synchrotron Radiat.* 18, 398–412. <https://doi.org/10.1107/S090904951100820X>
- Kegel, K.B., Kim, M., Sapp, E., McIntyre, C., Castaño, J.G., Aronin, N., DiFiglia, M., 2000. Huntingtin Expression Stimulates Endosomal–Lysosomal Activity, Endosome Tubulation, and Autophagy. *J. Neurosci.* 20, 7268–7278.
- Kegel, K.B., Sapp, E., Alexander, J., Valencia, A., Reeves, P., Li, X., Masso, N., Sobin, L., Aronin, N., DiFiglia, M., 2009. Polyglutamine expansion in huntingtin alters its interaction with phospholipids. *J. Neurochem.* 110, 1585–1597. <https://doi.org/10.1111/j.1471-4159.2009.06255.x>
- Kegel, K.B., Sapp, E., Yoder, J., Cuiffo, B., Sobin, L., Kim, Y.J., Qin, Z.-H., Hayden, M.R., Aronin, N., Scott, D.L., Isenberg, G., Goldmann, W.H., DiFiglia, M., 2005. Huntingtin Associates with Acidic Phospholipids at the Plasma Membrane. *J. Biol. Chem.* 280, 36464–36473. <https://doi.org/10.1074/jbc.M503672200>
- Kegel-Gleason, K.B., 2013. Huntingtin Interactions with Membrane Phospholipids: Strategic Targets

- for Therapeutic Intervention? *J. Huntingt. Dis.* 2, 239–250. <https://doi.org/10.3233/JHD-130068>
- Kiernan, M.C., Vucic, S., Cheah, B.C., Turner, M.R., Eisen, A., Hardiman, O., Burrell, J.R., Zoing, M.C., 2011. Amyotrophic lateral sclerosis. *The Lancet* 377, 942–955. [https://doi.org/10.1016/S0140-6736\(10\)61156-7](https://doi.org/10.1016/S0140-6736(10)61156-7)
- Kim, M., 2013. Beta conformation of polyglutamine track revealed by a crystal structure of Huntingtin N-terminal region with insertion of three histidine residues. *Prion* 7, 221–228. <https://doi.org/10.4161/pri.23807>
- Kim, Y.E., Hosp, F., Frotin, F., Ge, H., Mann, M., Hayer-Hartl, M., Hartl, F.U., 2016. Soluble Oligomers of PolyQ-Expanded Huntingtin Target a Multiplicity of Key Cellular Factors. *Mol. Cell* 63, 951–964. <https://doi.org/10.1016/j.molcel.2016.07.022>
- Kirstein, J., Morito, D., Kakihana, T., Sugihara, M., Minnen, A., Hipp, M.S., Nussbaum-Krammer, C., Kasturi, P., Hartl, F.U., Nagata, K., Morimoto, R.I., 2015. Proteotoxic stress and ageing triggers the loss of redox homeostasis across cellular compartments. *EMBO J.* 34, 2334–2349. <https://doi.org/10.15252/embj.201591711>
- Klar, T.A., Engel, E., Hell, S.W., 2001. Breaking Abbe's diffraction resolution limit in fluorescence microscopy with stimulated emission depletion beams of various shapes. *Phys. Rev. E* 64, 066613. <https://doi.org/10.1103/PhysRevE.64.066613>
- Knoll, M., Ruska, E., 1932. Das Elektronenmikroskop. *Z. Für Phys.* 78, 318–339. <https://doi.org/10.1007/BF01342199>
- Koenderink, J.J., van Doorn, A.J., 1992. Surface shape and curvature scales. *Image Vis. Comput.* 10, 557–564. [https://doi.org/10.1016/0262-8856\(92\)90076-F](https://doi.org/10.1016/0262-8856(92)90076-F)
- Koster, A.J., Grimm, R., Typke, D., Hegerl, R., Stoschek, A., Walz, J., Baumeister, W., 1997. Perspectives of Molecular and Cellular Electron Tomography. *J. Struct. Biol.* 120, 276–308. <https://doi.org/10.1006/jsbi.1997.3933>
- Kremer, J.R., Mastrorade, D.N., McIntosh, J.R., 1996. Computer Visualization of Three-Dimensional Image Data Using IMOD. *J. Struct. Biol.* 116, 71–76. <https://doi.org/10.1006/jsbi.1996.0013>
- Krivanek, O.L., Mooney, P.E., 1993. Applications of slow-scan CCD cameras in transmission electron microscopy. *Ultramicroscopy* 49, 95–108. [https://doi.org/10.1016/0304-3991\(93\)90216-K](https://doi.org/10.1016/0304-3991(93)90216-K)
- Kühlbrandt, W., 2014a. Microscopy: Cryo-EM enters a new era. *eLife* 3, e03678. <https://doi.org/10.7554/eLife.03678>
- Kühlbrandt, W., 2014b. The Resolution Revolution. *Science* 343, 1443–1444. <https://doi.org/10.1126/science.1251652>
- Labbadia, J., Morimoto, R.I., 2015. The Biology of Proteostasis in Aging and Disease. *Annu. Rev. Biochem.* 84, 435–464. <https://doi.org/10.1146/annurev-biochem-060614-033955>
- Labbadia, J., Morimoto, R.I., 2013. Huntington's disease: underlying molecular mechanisms and emerging concepts. *Trends Biochem. Sci.* 38, 378–385. <https://doi.org/10.1016/j.tibs.2013.05.003>
- Langmore, J.P., Smith, M.F., 1992. Quantitative energy-filtered electron microscopy of biological molecules in ice. *Ultramicroscopy* 46, 349–373. [https://doi.org/10.1016/0304-3991\(92\)90024-E](https://doi.org/10.1016/0304-3991(92)90024-E)
- Leapman, R.D., Sun, S., 1995. Cryo-electron energy loss spectroscopy: observations on vitrified hydrated specimens and radiation damage. *Ultramicroscopy, Proceedings of the 2nd international workshop on Electron Energy Loss Spectroscopy and Imaging* 59, 71–79.

- [https://doi.org/10.1016/0304-3991\(95\)00019-W](https://doi.org/10.1016/0304-3991(95)00019-W)
- Lebbink, M.N., Geerts, W.J.C., van der Krift, T.P., Bouwhuis, M., Hertzberger, L.O., Verkleij, A.J., Koster, A.J., 2007. Template matching as a tool for annotation of tomograms of stained biological structures. *J. Struct. Biol.* 158, 327–335. <https://doi.org/10.1016/j.jsb.2006.12.001>
- Leitman, J., Hartl, F.U., Lederkremer, G.Z., 2013. Soluble forms of polyQ-expanded huntingtin rather than large aggregates cause endoplasmic reticulum stress. *Nat. Commun.* 4, 2753. <https://doi.org/10.1038/ncomms3753>
- Lelouard, H., Ferrand, V., Marguet, D., Bania, J., Camosseto, V., David, A., Gatti, E., Pierre, P., 2004. Dendritic cell aggresome-like induced structures are dedicated areas for ubiquitination and storage of newly synthesized defective proteins. *J. Cell Biol.* 164, 667–675. <https://doi.org/10.1083/jcb.200312073>
- Lesage, S., Brice, A., 2009. Parkinson's disease: from monogenic forms to genetic susceptibility factors. *Hum. Mol. Genet.* 18, R48–R59. <https://doi.org/10.1093/hmg/ddp012>
- Li, S.-H., Schilling, G., Young, W.S., Li, X.-, Margolis, R.L., Stine, O.C., Wagster, M.V., Abbott, M.H., Franz, M.L., Ranen, N.G., Folstein, S.E., Hedreen, J.C., Ross, C.A., 1993. Huntington's disease gene (IT15) is widely expressed in human and rat tissues. *Neuron* 11, 985–993. [https://doi.org/10.1016/0896-6273\(93\)90127-D](https://doi.org/10.1016/0896-6273(93)90127-D)
- Li, X., Mooney, P., Zheng, S., Booth, C.R., Braunfeld, M.B., Gubbens, S., Agard, D.A., Cheng, Y., 2013. Electron counting and beam-induced motion correction enable near-atomic-resolution single-particle cryo-EM. *Nat. Methods* 10, 584–590. <https://doi.org/10.1038/nmeth.2472>
- Lidke, D.S., Lidke, K.A., 2012. Advances in high-resolution imaging – techniques for three-dimensional imaging of cellular structures. *J Cell Sci* 125, 2571–2580. <https://doi.org/10.1242/jcs.090027>
- Liu, K.-Y., Shyu, Y.-C., Barbaro, B.A., Lin, Y.-T., Chern, Y., Thompson, L.M., Shen, C.-K.J., Marsh, J.L., 2015. Disruption of the nuclear membrane by perinuclear inclusions of mutant huntingtin causes cell-cycle re-entry and striatal cell death in mouse and cell models of Huntington's disease. *Hum. Mol. Genet.* 24, 1602–1616. <https://doi.org/10.1093/hmg/ddu574>
- Liu, W., Yang, J., Burgunder, J., Cheng, B., Shang, H., 2016. Diffusion imaging studies of Huntington's disease: A meta-analysis. *Parkinsonism Relat. Disord.* 32, 94–101. <https://doi.org/10.1016/j.parkreldis.2016.09.005>
- MacDonald, M.E., Ambrose, C.M., Duyao, M.P., Myers, R.H., Lin, C., Srinidhi, L., Barnes, G., Taylor, S.A., James, M., Groot, N., MacFarlane, H., Jenkins, B., Anderson, M.A., Wexler, N.S., Gusella, J.F., Bates, G.P., Baxendale, S., Hummerich, H., Kirby, S., North, M., Youngman, S., Mott, R., Zehetner, G., Sedlacek, Z., Poustka, A., Frischauf, A.-M., Lehrach, H., Buckler, A.J., Church, D., Doucette-Stamm, L., O'Donovan, M.C., Riba-Ramirez, L., Shah, M., Stanton, V.P., Strobel, S.A., Draths, K.M., Wales, J.L., Dervan, P., Housman, D.E., Altherr, M., Shiang, R., Thompson, L., Fielder, T., Wasmuth, J.J., Tagle, D., Valdes, J., Elmer, L., Allard, M., Castilla, L., Swaroop, M., Blanchard, K., Collins, F.S., Snell, R., Holloway, T., Gillespie, K., Datson, N., Shaw, D., Harper, P.S., 1993. A novel gene containing a trinucleotide repeat that is expanded and unstable on Huntington's disease chromosomes. *Cell* 72, 971–983. [https://doi.org/10.1016/0092-8674\(93\)90585-E](https://doi.org/10.1016/0092-8674(93)90585-E)
- Mahamid, J., Pfeffer, S., Schaffer, M., Villa, E., Danev, R., Cuellar, L.K., Förster, F., Hyman, A.A., Plitzko, J.M., Baumeister, W., 2016. Visualizing the molecular sociology at the HeLa cell nuclear periphery. *Science* 351, 969–972. <https://doi.org/10.1126/science.aad8857>
- Majounie, E., Renton, A.E., Mok, K., Dopper, E.G., Waite, A., Rollinson, S., Chiò, A., Restagno, G., Nicolaou, N., Simon-Sanchez, J., van Swieten, J.C., Abramzon, Y., Johnson, J.O., Sendtner,

- M., Pamphlett, R., Orrell, R.W., Mead, S., Sidle, K.C., Houlden, H., Rohrer, J.D., Morrison, K.E., Pall, H., Talbot, K., Ansorge, O., Hernandez, D.G., Arepalli, S., Sabatelli, M., Mora, G., Corbo, M., Giannini, F., Calvo, A., Englund, E., Borghero, G., Floris, G.L., Remes, A.M., Laaksovirta, H., McCluskey, L., Trojanowski, J.Q., Van Deerlin, V.M., Schellenberg, G.D., Nalls, M.A., Drory, V.E., Lu, C.-S., Yeh, T.-H., Ishiura, H., Takahashi, Y., Tsuji, S., Le Ber, I., Brice, A., Drepper, C., Williams, N., Kirby, J., Shaw, P., Hardy, J., Tienari, P.J., Heutink, P., Morris, H.R., Pickering-Brown, S., Traynor, B.J., 2012. Frequency of the C9orf72 hexanucleotide repeat expansion in patients with amyotrophic lateral sclerosis and frontotemporal dementia: a cross-sectional study. *Lancet Neurol.* 11, 323–330. [https://doi.org/10.1016/S1474-4422\(12\)70043-1](https://doi.org/10.1016/S1474-4422(12)70043-1)
- Mangiarini, L., Sathasivam, K., Seller, M., Cozens, B., Harper, A., Hetherington, C., Lawton, M., Trotter, Y., Leach, H., Davies, S.W., Bates, G.P., 1996. Exon 1 of the HD Gene with an Expanded CAG Repeat Is Sufficient to Cause a Progressive Neurological Phenotype in Transgenic Mice. *Cell* 87, 493–506. [https://doi.org/10.1016/S0092-8674\(00\)81369-0](https://doi.org/10.1016/S0092-8674(00)81369-0)
- Marko, M., Hsieh, C., Moberlychan, W., Mannella, C.A., Frank, J., 2006. Focused ion beam milling of vitreous water: prospects for an alternative to cryo-ultramicrotomy of frozen-hydrated biological samples. *J. Microsc.* 222, 42–47. <https://doi.org/10.1111/j.1365-2818.2006.01567.x>
- Martinez-Sanchez, A., Garcia, I., Asano, S., Lucic, V., Fernandez, J.-J., 2014. Robust membrane detection based on tensor voting for electron tomography. *J. Struct. Biol.* 186, 49–61. <https://doi.org/10.1016/j.jsb.2014.02.015>
- Martins, I.C., Kuperstein, I., Wilkinson, H., Maes, E., Vanbrabant, M., Jonckheere, W., Gelder, P.V., Hartmann, D., D'Hooge, R., Strooper, B.D., Schymkowitz, J., Rousseau, F., 2008. Lipids revert inert A $\beta$  amyloid fibrils to neurotoxic protofibrils that affect learning in mice. *EMBO J.* 27, 224–233. <https://doi.org/10.1038/sj.emboj.7601953>
- Mastrorade, D.N., 2005. Automated electron microscope tomography using robust prediction of specimen movements. *J. Struct. Biol.* 152, 36–51. <https://doi.org/10.1016/j.jsb.2005.07.007>
- Mastrorade, D.N., 1997. Dual-Axis Tomography: An Approach with Alignment Methods That Preserve Resolution. *J. Struct. Biol.* 120, 343–352. <https://doi.org/10.1006/jsbi.1997.3919>
- McDowell, A.W., Chang, J.J., Freeman, R., Lepault, J., Walter, C.A., Dubochet, J., 1983. Electron microscopy of frozen hydrated sections of vitreous ice and vitrified biological samples. *J. Microsc.* 131, 1–9.
- McMullan, G., Chen, S., Henderson, R., Faruqi, A.R., 2009. Detective quantum efficiency of electron area detectors in electron microscopy. *Ultramicroscopy* 109, 1126–1143. <https://doi.org/10.1016/j.ultramic.2009.04.002>
- McMullan, G., Faruqi, A.R., Clare, D., Henderson, R., 2014. Comparison of optimal performance at 300keV of three direct electron detectors for use in low dose electron microscopy. *Ultramicroscopy* 147, 156–163. <https://doi.org/10.1016/j.ultramic.2014.08.002>
- Meents, A., Gutmann, S., Wagner, A., Schulze-Briese, C., 2010. Origin and temperature dependence of radiation damage in biological samples at cryogenic temperatures. *Proc. Natl. Acad. Sci.* 107, 1094–1099. <https://doi.org/10.1073/pnas.0905481107>
- Mehta, P., 2016. Prevalence of Amyotrophic Lateral Sclerosis — United States, 2012–2013. *MMWR Surveill. Summ.* 65. <https://doi.org/10.15585/mmwr.ss6508a1>
- Merk, A., Bartesaghi, A., Banerjee, S., Falconieri, V., Rao, P., Davis, M.I., Pragani, R., Boxer, M.B., Earl, L.A., Milne, J.L.S., Subramaniam, S., 2016. Breaking Cryo-EM Resolution Barriers to Facilitate Drug Discovery. *Cell* 165, 1698–1707. <https://doi.org/10.1016/j.cell.2016.05.040>
- Michalek, M., Salnikov, E.S., Bechinger, B., 2013. Structure and Topology of the Huntingtin 1–17

- Membrane Anchor by a Combined Solution and Solid-State NMR Approach. *Biophys. J.* 105, 699–710. <https://doi.org/10.1016/j.bpj.2013.06.030>
- Milanesi, L., Sheynis, T., Xue, W.-F., Orlova, E.V., Hellewell, A.L., Jelinek, R., Hewitt, E.W., Radford, S.E., Saibil, H.R., 2012. Direct three-dimensional visualization of membrane disruption by amyloid fibrils. *Proc. Natl. Acad. Sci.* 109, 20455–20460. <https://doi.org/10.1073/pnas.1206325109>
- Miller, J., Arrasate, M., Shaby, B.A., Mitra, S., Masliah, E., Finkbeiner, S., 2010. Quantitative Relationships between Huntingtin Levels, Polyglutamine Length, Inclusion Body Formation, and Neuronal Death Provide Novel Insight into Huntington's Disease Molecular Pathogenesis. *J. Neurosci.* 30, 10541–10550. <https://doi.org/10.1523/JNEUROSCI.0146-10.2010>
- Mochel, M.E., Mochel, J.M., 1986. A CCD imaging and analysis system for the VG HB5 STEM. *Proc 44 Th Ann Meet EMSA* 616–617.
- Moffitt, H., McPhail, G.D., Woodman, B., Hobbs, C., Bates, G.P., 2009. Formation of Polyglutamine Inclusions in a Wide Range of Non-CNS Tissues in the HdhQ150 Knock-In Mouse Model of Huntington's Disease. *PLOS ONE* 4, e8025. <https://doi.org/10.1371/journal.pone.0008025>
- Moor, H., 1964. Die Gefrier-Fixation lebender Zellen und ihre Anwendung in der Elektronenmikroskopie. *Z. Für Zellforsch. Mikrosk. Anat.* 62, 546–580. <https://doi.org/10.1007/BF00338850>
- Moor, H., Kistler, J., Muller, M., 1976. Freezing in a Propane Jet. *Experientia* 32, 805–805.
- Moor, H., Riehle, U., 1968. Snap-freezing under high pressure: A new fixation technique for freeze-etching. *Proc 4th Eur Reg Conf Electron Microsc Rome* 2, 33–44.
- Moore, E.B., Molinero, V., 2011. Structural transformation in supercooled water controls the crystallization rate of ice. *Nature* 479, 506–508. <https://doi.org/10.1038/nature10586>
- Moussavi, F., Heitz, G., Amat, F., Comolli, L.R., Koller, D., Horowitz, M., 2010. 3D segmentation of cell boundaries from whole cell cryogenic electron tomography volumes. *J. Struct. Biol.* 170, 134–145. <https://doi.org/10.1016/j.jsb.2009.12.015>
- Muchowski, P.J., Ning, K., D'Souza-Schorey, C., Fields, S., 2002. Requirement of an intact microtubule cytoskeleton for aggregation and inclusion body formation by a mutant huntingtin fragment. *Proc. Natl. Acad. Sci.* 99, 727–732. <https://doi.org/10.1073/pnas.022628699>
- Müller, M., Meister, N., Moor, H., 1980. Freezing in a propane jet and its application in freeze-fracturing. *Mikroskopie* 36, 129–140.
- Nagashima, H., Asakura, S., 1980. Dark-field light microscopic study of the flexibility of F-actin complexes. *J. Mol. Biol.* 136, 169–182. [https://doi.org/10.1016/0022-2836\(80\)90311-3](https://doi.org/10.1016/0022-2836(80)90311-3)
- Neueder, A., Landles, C., Ghosh, R., Howland, D., Myers, R.H., Faull, R.L.M., Tabrizi, S.J., Bates, G.P., 2017. The pathogenic exon 1 HTT protein is produced by incomplete splicing in Huntington's disease patients. *Sci. Rep.* 7, 1307. <https://doi.org/10.1038/s41598-017-01510-z>
- Nickell, S., Förster, F., Linaroudis, A., Net, W.D., Beck, F., Hegerl, R., Baumeister, W., Plitzko, J.M., 2005. TOM software toolbox: acquisition and analysis for electron tomography. *J. Struct. Biol.* 149, 227–234. <https://doi.org/10.1016/j.jsb.2004.10.006>
- Nurgaliev, D., Gatanov, T., Needleman, D.J., 2010. Chapter 25 - Automated Identification of Microtubules in Cellular Electron Tomography, in: Cassimeris, L., Tran, P. (Eds.), *Methods in Cell Biology, Microtubules: In Vivo*. Academic Press, pp. 475–495. [https://doi.org/10.1016/S0091-679X\(10\)97025-8](https://doi.org/10.1016/S0091-679X(10)97025-8)

- Olzscha, H., Schermann, S.M., Woerner, A.C., Pinkert, S., Hecht, M.H., Tartaglia, G.G., Vendruscolo, M., Hayer-Hartl, M., Hartl, F.U., Vabulas, R.M., 2011. Amyloid-like Aggregates Sequester Numerous Metastable Proteins with Essential Cellular Functions. *Cell* 144, 67–78. <https://doi.org/10.1016/j.cell.2010.11.050>
- Onofrij, M., Thomas, A., Bonanni, L., 2007. New approaches to understanding hallucinations in Parkinson's disease: phenomenology and possible origins. *Expert Rev. Neurother.* 7, 1731–1750. <https://doi.org/10.1586/14737175.7.12.1731>
- Orr, H.T., Zoghbi, H.Y., 2007. Trinucleotide Repeat Disorders. *Annu. Rev. Neurosci.* 30, 575–621. <https://doi.org/10.1146/annurev.neuro.29.051605.113042>
- Orth, M., Cooper, J.M., Bates, G.P., Schapira, A.H.V., 2003. Inclusion formation in Huntington's disease R6/2 mouse muscle cultures. *J. Neurochem.* 87, 1–6. <https://doi.org/10.1046/j.1471-4159.2003.02009.x>
- Orth, M., Handley, O.J., Schwenke, C., Dunnett, S.B., Craufurd, D., Ho, A.K., Wild, E., Tabrizi, S.J., Landwehrmeyer, G.B., Network, T. investigators of the E.H.D., 2010. Observing Huntington's Disease: the European Huntington's Disease Network's REGISTRY. *PLOS Curr. Huntingt. Dis.* <https://doi.org/10.1371/currents.RRN1184>
- Owen, R.L., Rudiño-Piñera, E., Garman, E.F., 2006. Experimental determination of the radiation dose limit for cryocooled protein crystals. *Proc. Natl. Acad. Sci. U. S. A.* 103, 4912–4917. <https://doi.org/10.1073/pnas.0600973103>
- Page, D.L., Sun, Y., Koschan, A.F., Paik, J., Abidi, M.A., 2002. Normal Vector Voting: Crease Detection and Curvature Estimation on Large, Noisy Meshes. *Graph. Models* 64, 199–229. <https://doi.org/10.1006/gmod.2002.0574>
- Park, S.-H., Kukushkin, Y., Gupta, R., Chen, T., Konagai, A., Hipp, M.S., Hayer-Hartl, M., Hartl, F.U., 2013. PolyQ Proteins Interfere with Nuclear Degradation of Cytosolic Proteins by Sequestering the Sis1p Chaperone. *Cell* 154, 134–145. <https://doi.org/10.1016/j.cell.2013.06.003>
- Penczek, P., Marko, M., Buttle, K., Frank, J., 1995. Double-tilt electron tomography. *Ultramicroscopy* 60, 393–410. [https://doi.org/10.1016/0304-3991\(95\)00078-X](https://doi.org/10.1016/0304-3991(95)00078-X)
- Pendin, D., McNew, J.A., Daga, A., 2011. Balancing ER dynamics: shaping, bending, severing, and mending membranes. *Curr. Opin. Cell Biol., Membranes and organelles* 23, 435–442. <https://doi.org/10.1016/j.ceb.2011.04.007>
- Petrasch-Parwez, E., Nguyen, H.-P., Löbbecke-Schumacher, M., Habbes, H.-W., Wiczorek, S., Riess, O., Andres, K.-H., Dermietzel, R., Von Hörsten, S., 2007. Cellular and subcellular localization of Huntington aggregates in the brain of a rat transgenic for Huntington disease. *J. Comp. Neurol.* 501, 716–730. <https://doi.org/10.1002/cne.21272>
- Pfeffer, S., Brandt, F., Hrabe, T., Lang, S., Eibauer, M., Zimmermann, R., Förster, F., 2012. Structure and 3D Arrangement of Endoplasmic Reticulum Membrane-Associated Ribosomes. *Structure* 20, 1508–1518. <https://doi.org/10.1016/j.str.2012.06.010>
- Pfeffer, S., Dudek, J., Schaffer, M., Ng, B.G., Albert, S., Plitzko, J.M., Baumeister, W., Zimmermann, R., Freeze, H.H., Engel, B.D., Förster, F., 2017. Dissecting the molecular organization of the translocon-associated protein complex. *Nat. Commun.* 8, ncomms14516. <https://doi.org/10.1038/ncomms14516>
- Pieri, L., Mадiona, K., Bousset, L., Melki, R., 2012. Fibrillar  $\alpha$ -Synuclein and Huntingtin Exon 1 Assemblies Are Toxic to the Cells. *Biophys. J.* 102, 2894–2905. <https://doi.org/10.1016/j.bpj.2012.04.050>

- Polymenidou, M., Cleveland, D.W., 2012. Prion-like spread of protein aggregates in neurodegeneration. *J. Exp. Med.* 209, 889–893. <https://doi.org/10.1084/jem.20120741>
- Powers, E.T., Morimoto, R.I., Dillin, A., Kelly, J.W., Balch, W.E., 2009. Biological and Chemical Approaches to Diseases of Proteostasis Deficiency. *Annu. Rev. Biochem.* 78, 959–991. <https://doi.org/10.1146/annurev.biochem.052308.114844>
- Qian, S.-B., Ott, D.E., Schubert, U., Bennink, J.R., Yewdell, J.W., 2002. Fusion Proteins with COOH-terminal Ubiquitin Are Stable and Maintain Dual Functionality in Vivo. *J. Biol. Chem.* 277, 38818–38826. <https://doi.org/10.1074/jbc.M205547200>
- Qin, Z.-H., Wang, Y., Sapp, E., Cuiffo, B., Wanker, E., Hayden, M.R., Kegel, K.B., Aronin, N., DiFiglia, M., 2004. Huntingtin Bodies Sequester Vesicle-Associated Proteins by a Polyproline-Dependent Interaction. *J. Neurosci.* 24, 269–281. <https://doi.org/10.1523/JNEUROSCI.1409-03.2004>
- Querfurth, H.W., LaFerla, F.M., 2010. Alzheimer's Disease. *N. Engl. J. Med.* 362, 329–344. <https://doi.org/10.1056/NEJMra0909142>
- Radon, J., 1917. Über die Bestimmung von Funktionen durch ihre Integralwerte längs gewisser Mannigfaltigkeiten. *Math.-Phys. Kl., Berichte über die Verhandlungen der Königlich Sächsischen Gesellschaft der Wissenschaften zu Leipzig* 69, 262–277.
- Ramos-Arroyo, M.A., Moreno, S., Valiente, A., 2005. Incidence and mutation rates of Huntington's disease in Spain: experience of 9 years of direct genetic testing. *J. Neurol. Neurosurg. Psychiatry* 76, 337–342. <https://doi.org/10.1136/jnnp.2004.036806>
- Reimer, L., Kohl, H., 2008. *Transmission Electron Microscopy: Physics of Image Formation*, 5th ed. 2008. ed. Springer, New York, NY.
- Riehle, U., Höchli, M., 1973. The theory and technique of high pressure freezing. Presented at the Freeze-Etching. Techniques and Applications. E. L.Benedetti, and P.Favard, eds. *Societe Francais de Microscopie Electronique*, Paris, pp. 31–61.
- Rigort, A. and Bäuerlein, F.J.B., Villa, E., Eibauer, M., Laugks, T., Baumeister, W., Plitzko, J.M., 2012. Focused ion beam micromachining of eukaryotic cells for cryoelectron tomography. *Proc. Natl. Acad. Sci.* 109, 4449–4454. <https://doi.org/10.1073/pnas.1201333109>
- Rigort, A., Günther, D., Hegerl, R., Baum, D., Weber, B., Prohaska, S., Medalia, O., Baumeister, W., Hege, H.-C., 2012b. Automated segmentation of electron tomograms for a quantitative description of actin filament networks. *J. Struct. Biol., Ueli Aebi Festschrift* 177, 135–144. <https://doi.org/10.1016/j.jsb.2011.08.012>
- Rigort, A., Villa, E., Bäuerlein, F.J.B., Engel, B.D., Plitzko, J.M., 2012c. Chapter 14 - Integrative Approaches for Cellular Cryo-electron Tomography: Correlative Imaging and Focused Ion Beam Micromachining, in: Thomas Müller-Reichert and Paul Verkade (Ed.), *Methods in Cell Biology*. Academic Press, pp. 259–281.
- Rochet, J.-C., Lansbury, P.T., 2000. Amyloid fibrillogenesis: themes and variations. *Curr. Opin. Struct. Biol.* 10, 60–68. [https://doi.org/10.1016/S0959-440X\(99\)00049-4](https://doi.org/10.1016/S0959-440X(99)00049-4)
- Ross, C.A., Poirier, M.A., 2004. Protein aggregation and neurodegenerative disease. *Publ. Online* 01 July 2004 [Doi101038nm1066](https://doi.org/10.1038/nm1066) 10, S10–S17. <https://doi.org/10.1038/nm1066>
- Roux, A., 2013. The physics of membrane tubes: soft templates for studying cellular membranes. *Soft Matter* 9, 6726–6736. <https://doi.org/10.1039/C3SM50514F>
- Rowland, L.P., 2001. How Amyotrophic Lateral Sclerosis Got Its Name: The Clinical-Pathologic Genius of Jean-Martin Charcot. *Arch. Neurol.* 58, 512–515. <https://doi.org/10.1001/archneur.58.3.512>

- Rubinsztein, D.C., Wytenbach, A., Rankin, J., 1999. Intracellular inclusions, pathological markers in diseases caused by expanded polyglutamine tracts? *J. Med. Genet.* 36, 265–270. <https://doi.org/10.1136/jmg.36.4.265>
- Russo, C.J., Passmore, L.A., 2016. Progress towards an optimal specimen support for electron cryomicroscopy. *Curr. Opin. Struct. Biol., Theory and simulation • Macromolecular machines* 37, 81–89. <https://doi.org/10.1016/j.sbi.2015.12.007>
- Rusu, M., Starosolski, Z., Wahle, M., Rigort, A., Wriggers, W., 2012. Automated tracing of filaments in 3D electron tomography reconstructions using Sculptor and Situs. *J. Struct. Biol., Special Issue: Electron Tomography* 178, 121–128. <https://doi.org/10.1016/j.jsb.2012.03.001>
- Sánchez, I., Mahlke, C., Yuan, J., 2003. Pivotal role of oligomerization in expanded polyglutamine neurodegenerative disorders. *Nature* 421, 373. <https://doi.org/10.1038/nature01301>
- Sandberg, K., Brega, M., 2007. Segmentation of thin structures in electron micrographs using orientation fields. *J. Struct. Biol.* 157, 403–415. <https://doi.org/10.1016/j.jsb.2006.09.007>
- Sartori, A., Gatz, R., Beck, F., Rigort, A., Baumeister, W., Plitzko, J.M., 2007. Correlative microscopy: Bridging the gap between fluorescence light microscopy and cryo-electron tomography. *J. Struct. Biol.* 160, 135–145. <https://doi.org/10.1016/j.jsb.2007.07.011>
- Sathasivam, K., Hobbs, C., Turmaine, M., Mangiarini, L., Mahal, A., Bertaux, F., Wanker, E.E., Doherty, P., Davies, S.W., Bates, G.P., 1999. Formation of Polyglutamine Inclusions in Non-CNS Tissue. *Hum. Mol. Genet.* 8, 813–822. <https://doi.org/10.1093/hmg/8.5.813>
- Sathasivam, K., Neueder, A., Gipson, T.A., Landles, C., Benjamin, A.C., Bondulich, M.K., Smith, D.L., Faull, R.L.M., Roos, R.A.C., Howland, D., Detloff, P.J., Housman, D.E., Bates, G.P., 2013. Aberrant splicing of HTT generates the pathogenic exon 1 protein in Huntington disease. *Proc. Natl. Acad. Sci.* 110, 2366–2370. <https://doi.org/10.1073/pnas.1221891110>
- Saxton, W.O., Baumeister, W., Hahn, M., 1984. Three-dimensional reconstruction of imperfect two-dimensional crystals. *Ultramicroscopy* 13, 57–70. [https://doi.org/10.1016/0304-3991\(84\)90057-3](https://doi.org/10.1016/0304-3991(84)90057-3)
- Schaffar, G., Breuer, P., Boteva, R., Behrends, C., Tzvetkov, N., Strippel, N., Sakahira, H., Siegers, K., Hayer-Hartl, M., Hartl, F.U., 2004. Cellular Toxicity of Polyglutamine Expansion Proteins: Mechanism of Transcription Factor Deactivation. *Mol. Cell* 15, 95–105. <https://doi.org/10.1016/j.molcel.2004.06.029>
- Schaffer, M., Engel, B.D., Laugks, T., Mahamid, J., Plitzko, J.M., Baumeister, W., 2015. Cryo-focused Ion Beam Sample Preparation for Imaging Vitreous Cells by Cryo-electron Tomography. *Bio-Protoc.* 5.
- Scherzinger, E., Lurz, R., Turmaine, M., Mangiarini, L., Hollenbach, B., Hasenbank, R., Bates, G.P., Davies, S.W., Lehrach, H., Wanker, E.E., 1997. Huntingtin-Encoded Polyglutamine Expansions Form Amyloid-like Protein Aggregates In Vitro and In Vivo. *Cell* 90, 549–558. [https://doi.org/10.1016/S0092-8674\(00\)80514-0](https://doi.org/10.1016/S0092-8674(00)80514-0)
- Schindelin, J., Arganda-Carreras, I., Frise, E., Kaynig, V., Longair, M., Pietzsch, T., Preibisch, S., Rueden, C., Saalfeld, S., Schmid, B., Tinevez, J.-Y., White, D.J., Hartenstein, V., Eliceiri, K., Tomancak, P., Cardona, A., 2012. Fiji: an open-source platform for biological-image analysis. *Nat. Methods* 9, 676. <https://doi.org/10.1038/nmeth.2019>
- Schwartz, C.L., Sarbash, V.I., Ataullakhanov, F.I., McIntosh, J.R., Nicastro, D., 2007. Cryo-fluorescence microscopy facilitates correlations between light and cryo-electron microscopy and reduces the rate of photobleaching. *J. Microsc.* 227, 98–109. <https://doi.org/10.1111/j.1365-2818.2007.01794.x>



- Shibata, Y., Hu, J., Kozlov, M.M., Rapoport, T.A., 2009. Mechanisms Shaping the Membranes of Cellular Organelles. *Annu. Rev. Cell Dev. Biol.* 25, 329–354. <https://doi.org/10.1146/annurev.cellbio.042308.113324>
- Shimohata, T., Sato, A., Burke, J.R., Strittmatter, W.J., Tsuji, S., Onodera, O., 2002. Expanded polyglutamine stretches form an ‘aggresome.’ *Neurosci. Lett.* 323, 215–218. [https://doi.org/10.1016/S0304-3940\(02\)00162-3](https://doi.org/10.1016/S0304-3940(02)00162-3)
- Slow, E.J., van Raamsdonk, J., Rogers, D., Coleman, S.H., Graham, R.K., Deng, Y., Oh, R., Bissada, N., Hossain, S.M., Yang, Y.-Z., Li, X.-J., Simpson, E.M., Gutekunst, C.-A., Leavitt, B.R., Hayden, M.R., 2003. Selective striatal neuronal loss in a YAC128 mouse model of Huntington disease. *Hum. Mol. Genet.* 12, 1555–1567. <https://doi.org/10.1093/hmg/ddg169>
- Smith, R.S., Dohnálek, Z., Kimmel, G.A., Stevenson, K.P., Kay, B.D., 2000. The self-diffusivity of amorphous solid water near 150 K. *Chem. Phys.* 258, 291–305. [https://doi.org/10.1016/S0301-0104\(00\)00130-0](https://doi.org/10.1016/S0301-0104(00)00130-0)
- Spillantini, M.G., Schmidt, M.L., Lee, V.M.-Y., Trojanowski, J.Q., Jakes, R., Goedert, M., 1997.  $\alpha$ -Synuclein in Lewy bodies. *Nature* 388, 42166. <https://doi.org/10.1038/42166>
- Stefani, M., Dobson, C.M., 2003. Protein aggregation and aggregate toxicity: new insights into protein folding, misfolding diseases and biological evolution. *J. Mol. Med.* 81, 678–699. <https://doi.org/10.1007/s00109-003-0464-5>
- Taylor, K.A., Reedy, M.C., Córdova, L., Reedy, M.K., 1984. Three-dimensional reconstruction of rigor insect flight muscle from tilted thin sections. *Nature* 310, 285. <https://doi.org/10.1038/310285a0>
- Tivol, W.F., Briegel, A., Jensen, G.J., 2008. An Improved Cryogen for Plunge Freezing. *Microsc. Microanal.* 14, 375–379. <https://doi.org/10.1017/S1431927608080781>
- Trevino, R.S., Lauckner, J.E., Sourigues, Y., Pearce, M.M., Bousset, L., Melki, R., Kopito, R.R., 2012. Fibrillar Structure and Charge Determine the Interaction of Polyglutamine Protein Aggregates with the Cell Surface. *J. Biol. Chem.* 287, 29722–29728. <https://doi.org/10.1074/jbc.M112.372474>
- Trottier, Y., Devys, D., Imbert, G., Saudou, F., An, I., Lutz, Y., Weber, C., Agid, Y., Hirsch, E.C., Mandel, J.-L., 1995. Cellular localization of the Huntington’s disease protein and discrimination of the normal and mutated form. *Nat. Genet.* 10, 104–110. <https://doi.org/10.1038/ng0595-104>
- van der Burg, J.M., Björkqvist, M., Brundin, P., 2009. Beyond the brain: widespread pathology in Huntington’s disease. *Lancet Neurol.* 8, 765–774. [https://doi.org/10.1016/S1474-4422\(09\)70178-4](https://doi.org/10.1016/S1474-4422(09)70178-4)
- van Harrevelde, A., Crowell, J., 1964. Electron microscopy after rapid freezing on a metal surface and substitution fixation. *Anat. Rec.* 149, 381–385. <https://doi.org/10.1002/ar.1091490307>
- Velier, J., Kim, M., Schwarz, C., Kim, T.W., Sapp, E., Chase, K., Aronin, N., DiFiglia, M., 1998. Wild-Type and Mutant Huntingtins Function in Vesicle Trafficking in the Secretory and Endocytic Pathways. *Exp. Neurol.* 152, 34–40. <https://doi.org/10.1006/exnr.1998.6832>
- Vembar, S.S., Brodsky, J.L., 2008. One step at a time: endoplasmic reticulum-associated degradation. *Nat. Rev. Mol. Cell Biol.* 9, 944–957. <https://doi.org/10.1038/nrm2546>
- von Campenhausen, S., Bornschein, B., Wick, R., Bötzel, K., Sampaio, C., Poewe, W., Oertel, W., Siebert, U., Berger, K., Dodel, R., 2005. Prevalence and incidence of Parkinson’s disease in Europe. *Eur. Neuropsychopharmacol., Size & Burden of Mental Disorders in Europe* 15, 473–490. <https://doi.org/10.1016/j.euroneuro.2005.04.007>

- Waelter, S., Boeddrich, A., Lurz, R., Scherzinger, E., Lueder, G., Lehrach, H., Wanker, E.E., 2001. Accumulation of Mutant Huntingtin Fragments in Aggresome-like Inclusion Bodies as a Result of Insufficient Protein Degradation. *Mol. Biol. Cell* 12, 1393–1407. <https://doi.org/10.1091/mbc.12.5.1393>
- Walker, F.O., 2007. Huntington's disease. *The Lancet* 369, 218–228. [https://doi.org/10.1016/S0140-6736\(07\)60111-1](https://doi.org/10.1016/S0140-6736(07)60111-1)
- Watanabe, N., Kouchi, A., 2008. Ice surface reactions: A key to chemical evolution in space. *Prog. Surf. Sci.* 83, 439–489. <https://doi.org/10.1016/j.progsurf.2008.10.001>
- Weber, B., Greenan, G., Prohaska, S., Baum, D., Hege, H.-C., Müller-Reichert, T., Hyman, A.A., Verbavatz, J.-M., 2012. Automated tracing of microtubules in electron tomograms of plastic embedded samples of *Caenorhabditis elegans* embryos. *J. Struct. Biol., Special Issue: Electron Tomography* 178, 129–138. <https://doi.org/10.1016/j.jsb.2011.12.004>
- Webster, R.E., Osborn, M., Weber, K., 1978. Visualization of the same PtK2 cytoskeletons by both immunofluorescence and low power electron microscopy. *Exp. Cell Res.* 117, 47–61. [https://doi.org/10.1016/0014-4827\(78\)90426-3](https://doi.org/10.1016/0014-4827(78)90426-3)
- Wimo, A., Winblad, B., Aguero-torres, H., Strauss, E. von, 2003. The magnitude of dementia occurrence in the world. *Alzheimer Dis. Assoc. Disord.* 17, 63–67.
- Woerner, A.C., Frottin, F., Hornburg, D., Feng, L.R., Meissner, F., Patra, M., Tatzelt, J., Mann, M., Winklhofer, K.F., Hartl, F.U., Hipp, M.S., 2016. Cytoplasmic protein aggregates interfere with nucleocytoplasmic transport of protein and RNA. *Science* 351, 173–176. <https://doi.org/10.1126/science.aad2033>
- Wong, I.Y., Gardel, M.L., Reichman, D.R., Weeks, E.R., Valentine, M.T., Bausch, A.R., Weitz, D.A., 2004. Anomalous Diffusion Probes Microstructure Dynamics of Entangled F-Actin Networks. *Phys. Rev. Lett.* 92, 178101. <https://doi.org/10.1103/PhysRevLett.92.178101>
- Wright, H.H., Still, C.N., Abramson, R.K., 1981. Huntington's Disease in Black Kindreds in South Carolina. *Arch. Neurol.* 38, 412–414. <https://doi.org/10.1001/archneur.1981.00510070046005>
- Zeitlin, S., Liu, J.-P., Chapman, D.L., Papaioannou, V.E., Efstratiadis, A., 1995. Increased apoptosis and early embryonic lethality in mice nullizygous for the Huntington's disease gene homologue. *Nat. Genet.* 11, ng1095-155–155. <https://doi.org/10.1038/ng1095-155>
- Zernike, F., 1955. How I Discovered Phase Contrast. *Science* 121, 345–349. <https://doi.org/10.1126/science.121.3141.345>
- Zhang, H., Hu, J., 2016. Shaping the Endoplasmic Reticulum into a Social Network. *Trends Cell Biol.* 26, 934–943. <https://doi.org/10.1016/j.tcb.2016.06.002>
- Zhang, X., Sun, P., Yan, T., Huang, Y., Ma, Z., Zou, B., Zheng, W., Zhou, J., Gong, Y., Sun, C.Q., 2015. Water's phase diagram: From the notion of thermodynamics to hydrogen-bond cooperativity. *Prog. Solid State Chem.* 43, 71–81. <https://doi.org/10.1016/j.progsolidstchem.2015.03.001>
- Zheng, Q.S., Braunfeld, M.B., Sedat, J.W., Agard, D.A., 2004. An improved strategy for automated electron microscopic tomography. *J. Struct. Biol.* 147, 91–101. <https://doi.org/10.1016/j.jsb.2004.02.005>



## CURRICULUM VITAE

### Felix Jan Benedict Bäuerlein

- 30. April 1982** Born in Heidelberg
- July 2001** A-Levels (Gymnasium München-Fürstenried-West, Munich)
- Sept. 01 – June 02** Civilian service at Großhadern Medical Center (LMU), Munich
- July 02 – Jan. 09** Student assistant at Großhadern Medical Center of LMU  
2<sup>nd</sup> Medical clinic (Professor Reinhart Zachoval) Munich
- Oct. 2002** Matriculation for physics at Ludwig-Maximilians-University, Munich
- Apr. 2005** Intermediate diploma in physics (LMU Munich)
- Sept./Oct. 2006** Georgia Institute of Technology (Professor Bridget Barry), Atlanta, USA
- since Jan. 2005** Research project „*Survival and Complications after Liver Transplantation – Medical Center Munich, Campus Großhadern (LMU)*“  
(Professor Reinhart Zachoval)
- Feb. 09 – Apr. 10** Diploma thesis at the Max-Planck-Institute of Biochemistry – Department of Molecular Structural Biology (Professor Wolfgang Baumeister)  
„*New ways of the sample preparation for cellular cryo-electron tomography (CET) – systematic study on the thinning of frozen-hydrated biological specimens with Focused-Ion-Beam technology*“
- 30. April 2010** Diploma in Physics and Biophysics of LMU Munich
- July – Dec 2010** Scientific assistant at Großhadern Medical Center  
2<sup>nd</sup> Medical clinic (Professor Reinhart Zachoval) - LMU, Munich
- since Oct. 2010** Matriculation for human medicine at Ludwig-Maximilians-University, Munich
- since Oct. 2010** PhD thesis (Dr. med.) in medicine at Großhadern Medical Center of LMU, Munich (Professor Reinhart Zachoval)  
„*Survival and Complications after Liver Transplantation between 1997-2012 at the Medical Center Großhadern of LMU Munich*“
- since Dec. 2010** PhD thesis (Dr. rer. nat.) in physics (TUM, Munich) at the Max-Planck-Institute of Biochemistry – Department of Molecular Structural Biology (Professor Wolfgang Baumeister)  
„*In Situ Architecture and Cellular Interactions of PolyQ Inclusions*“
- 08. March 2013** pre-clinical medical examination at LMU/TUM Munich  
(following the requirements for the Licensing Regulations for physicians in Germany)



## ACKNOWLEDGEMENTS

I am deeply grateful to **Professor Wolfgang Baumeister**, who not only gave me the opportunity to do exciting research in his department as a physicist but who also kept faith in me and permitted me to study medicine in parallel. This fulfils my wish to bring these worlds together. By offering me the topic of this thesis, the two passions of my scientific life found a perfect symbiosis.

Similarly, I would like to express my gratitude to **Professor Jürgen Plitzko**, who offered me in 2009 to work on my future diploma-thesis project in the department and who was fundamentally involved in realizing my scientific life between biophysics and medicine. I'm very thankful for the great support!

Very special and cordial thanks I would like to express to **Rubén Fernández-Busnadiego**, my direct PhD advisor. It was very pleasant working together and I'm really very happy it happened! We had quite exciting times together and lived through all emotions in the 12 months of tough revision-time of our paper that concluded finally in great happiness. I really enjoyed very much working with you and I'm looking forward to working on new things with you...

This project was possible in this extent only due a fantastic and fruitful collaboration with the department of Cellular Biochemistry (Prof. F.U. Hartl) of the MPI of Biochemistry and the department of Molecules – Signaling – Development (Prof. R. Klein) of the MPI of Neurobiology.

I am very grateful to **Professor Ulrich Hartl** and **Dr. Mark Hipp** for their strong support, their belief in the project and their essential inputs.

I am more than thankful to my great colleague and collaborator **Itika Saha** from the Hartl-Department, who was indispensable for this project! Itika was the driving force behind the not-trivial cell-cultures – we had plenty of difficult issues with the transfection and toxicity of our cells... we discussed many problems and Itika always found a solution.

I would like to express my gratitude also to **Professor Rüdiger Klein**, **Dr. Irina Dudanova** and **Dr. Archana Misra** for their support to prove our findings from HeLa cells in neurons! Big thanks to Archana, who prepared the primary neuron cultures from mice and worked hard to optimize the transfection of the neurons (which was a big challenge). Also my honest thanks to **Dr. Tom Gaitanos** for the assistance with the confocal microscope in the Klein-department.

Without this fantastic support of our collaborators this project wouldn't have been possible in the way it developed – so again thank you very much!

I'm also very thankful to **Maria Kalemánov** and **Dr. Antonio Martínez-Sánchez** for their computational contribution, particularly the curvature algorithm, the ribosome template matching and membrane-density estimation. Maria also spent many hours of thorough membrane-segmentation.

Many thanks to my great friends and colleagues **Dr. Radostin Danev** and **Dr. Yoshiuki Fukuda**, that will soon start their Professor-positions in Japan. I will miss the deep physical discussions about cryo-EM and many other things and specially the numerous nice late evenings together with Luca in lab.

I would like to thank my amazing friends and colleagues **Andreas, Ben, Daniel, Eri, Fabian, Inga, Jan, Jonathan, Luca, Marc, Maria, Marion, Maryam, Nico, Qiang, Saradha, Shoh, Tillman, Thomas, Ulrike, Victoria** for their friendship and without who my PhD-time wouldn't have been so enjoyable!

The department's functionality bases on a handful of important people: great thanks to **Jürgen Plitzko** and **Günter Pfeifer** – without them, the microscopes wouldn't stay long in a functional state. Special thanks also to the director's office managers **Birgit Book** and **Nathalie Leclercq** for their thorough and everlasting administrative support. Many thanks to **Dr. Harald Engelhardt**, who manages the department not only financially and administratively. I also want to mention and thank **Rudolf Gatz** and the extremely skilled precision mechanic **Thomas Matthes-Rösler** and also **Inga Wolf**, who always finds a solution for computer issues.

All my gratitude to my good friends and former colleagues **Dr. Elizabeth Villa, Dr. Julio Ortiz** and **Dr. Julia Mahamid**, with whom I had great times in Munich, that now have top positions in academia and that are deeply missed in Martinsried!

Great thanks to my good friend and great engineer **Tim Laugks**. We started almost at the same time in the lab and Tim was of exceptional help throughout – we worked very successfully together on the development of the cryo-FIB during my diploma-thesis. Also while my PhD time, Tim developed essential parts for a live cell imaging setup. We have already plenty of ideas together, how to improve methods in cryo-EM. I hope, we can start soon, to work on that...

I am sincerely grateful to my good friends **Dr. Marga Schüler** and **Professor Dirk Schüler**, who always provided me with valuable scientific advice – you are both very much missed in Munich! I also want to thank you both again for the reinforcement to stay persistent in what I believe in and for the “Paper-Submission-Whiskey” – it successfully did his job!

My deep gratitude to **Professor Reinhart Zachoval**, my medical mentor and PhD advisor, for his everlasting support and patience! With substantial aid, he was fundamentally involved in realizing my scientific life on the medical side! I'm very thankful for this great support!

The deepest appreciation is due to my parents **Cornelia Meinertz-Bäuerlein** und **Professor Edmund Bäuerlein**, who always supported my interests and decisions in life and made it possible as it developed! Very special thanks also to my great sister **Henrike Bäuerlein** for proofreading my thesis. It is awesome, to have such a great family!

Very special and warm thanks to my wonderful Dr. cand. **Aurore Menegaux** – you always supported me mentally as well as with very helpful scientific discussions. Your background in biology and your expertise in neuroimaging gave me useful inspiration and aside I learned a lot about MRI tomography from you. I'm a very happy person but you brighten my life further! It's wonderful to know you at my side!